

DEVELOPMENT AND APPLICATION OF AN OXIDATION FLOW REACTOR
TO STUDY SECONDARY ORGANIC AEROSOL FORMATION FROM AMBIENT AIR

by

BRETT BRIAN PALM

B.A., Dartmouth College, 2009

A thesis submitted to the
Faculty of the Graduate School of the
University of Colorado in partial fulfillment
of the requirement for the degree of
Doctor of Philosophy
Department of Chemistry and Biochemistry

2017

This thesis entitled:

Development and Application of an Oxidation Flow Reactor to Study

Secondary Organic Aerosol Formation from Ambient Air

written by Brett Brian Palm

has been approved for the Department of Chemistry and Biochemistry

Professor Jose-Luis Jimenez

Professor Steven S. Brown

Date_____

The final copy of this thesis has been examined by the signatories, and we find that both the content and the form meet acceptable presentation standards of scholarly work in the above mentioned discipline.

Palm, Brett Brian (Ph.D., Chemistry; Department of Chemistry and Biochemistry)

Development and Application of an Oxidation Flow Reactor to Study Secondary Organic Aerosol
Formation from Ambient Air

Thesis directed by Professor Jose-Luis Jimenez

ABSTRACT

Secondary organic aerosols (SOA) in the atmosphere play an important role in air quality, human health, and climate. However, the sources, formation pathways, and fate of SOA are poorly constrained. In this dissertation, I present development and application of the oxidation flow reactor (OFR) technique for studying SOA formation from OH, O₃, and NO₃ oxidation of ambient air. With a several-minute residence time and a portable design with no inlet, OFRs are particularly well-suited for this purpose.

I first introduce the OFR concept, and discuss several advances I have made in performing and interpreting OFR experiments. This includes estimating oxidant exposures, modeling the fate of low-volatility gases in the OFR (wall loss, condensation, and oxidation), and comparing SOA yields of single precursors in the OFR with yields measured in environmental chambers. When these experimental details are carefully considered, SOA formation in an OFR can be more reliably compared with ambient SOA formation processes.

I then present an overview of what OFR measurements have taught us about SOA formation in the atmosphere. I provide a comparison of SOA formation from OH, O₃, and NO₃ oxidation of ambient air in a wide variety of environments, from rural forests to urban air. In a rural forest, the SOA formation correlated with biogenic precursors (e.g., monoterpenes). In urban air, it correlated instead with reactive anthropogenic tracers (e.g., trimethylbenzene). In mixed-source regions, the SOA formation did not correlate well with any single precursor, but could be predicted by multilinear regression from several precursors. Despite these correlations, the concentrations of speciated ambient VOCs could only

explain approximately 10-50% of the total SOA formed from OH oxidation. In contrast, ambient VOCs could explain all of the SOA formation observed from O₃ and NO₃ oxidation. Evidence suggests that lower-volatility gases (semivolatile and intermediate-volatility organic compounds; S/IVOCs) were present in ambient air and were the likely source of SOA formation that could not be explained by VOCs. These measurements show that S/IVOCs likely play an important intermediary role in ambient SOA formation in all of the sampled locations, from rural forests to urban air.

Dedicated to
my family

ACKNOWLEDGEMENTS

I owe a debt of gratitude to my Ph.D. adviser, Professor Jose-Luis Jimenez, for his mentorship over the last seven years. I joined his research group because I saw an opportunity to work with top-tier scientists and get involved with influential science. I wanted an adviser who would hold me to the highest standard, and I was not disappointed. Professor Jimenez's constant pursuit to improve himself and those around him is admirable, and I am a better scientist for it.

I received immeasurable support from the members of the Jimenez group. In particular, I want to thank Doug Day, Pedro Campuzano-Jost, Weiwei Hu, and Amber Ortega, with whom I spent many hours thinking really hard about science in the field and in the office. Thank you also to laboratory managers Michael Lechner, Philip Handley, and Anne Handschy for their wonderful support.

I cannot thank my family and close friends enough for all of the support they have given me in my pursuits, academic and otherwise. I am extraordinarily proud to be the first in my extended family to earn a Ph.D., and I earned it by standing on your shoulders.

I am thankful to the many colleagues and friends that I made while participating in the BEACHON-RoMBAS, DC3, SOAS, SEAC⁴RS, and GoAmazon2014/5 field campaigns. Some campaigns were exhilarating, some were stressful, but all were unforgettable experiences.

Finally, I am grateful for financial support from a CIRES Graduate Student Fellowship, as well as an EPA STAR Graduate Fellowship. Their support allowed me to stay focused on my research.

CONTENTS

CHAPTERS

1. Introduction	1
1.1 Atmospheric aerosols	1
1.2 Secondary organic aerosol (SOA) formation.....	1
1.3 Techniques for studying SOA formation and properties	3
1.4 Dissertation focus	4
2. In situ secondary organic aerosol formation from ambient pine forest air using an oxidation flow reactor.....	6
2.1 Introduction	7
2.2 Experimental methods.....	11
2.2.1 BEACHON-RoMBAS campaign	11
2.2.2 Oxidation flow reactor	12
2.2.3 Sampling strategy and measurements	15
2.3 Results and discussion	21
2.3.1 OFR operation.....	21
2.3.2 VOC enhancement/depletion vs eq. age	23
2.3.3 Fate of condensable gases in an OFR.....	28
2.3.3.1 Modeled low-volatility organic compound (LVOC) fate	28
2.3.3.2 Model validation: sulfuric acid (H ₂ SO ₄) condensation.....	35
2.3.4 SOA mass enhancement vs. OH _{exp}	37
2.3.5 Condensation vs. nucleation in the OFR.....	41
2.3.6 Sources of SOA in ambient air	44
2.3.6.1 SOA mass formed vs. mass predicted from VOCs	44
2.3.6.2 SOA mass formed vs. predicted from S/IVOCs	48
2.3.6.3 Sensitivity to LVOC fate model parameters.....	52
2.4 Conclusions	54
2.5 Supplementary Information	56
2.5.1 Correction for particle diffusion to sampling line walls.....	56

2.5.2 Determination of AMS collection efficiency (CE).....	58
2.5.3 Determination of AMS aerodynamic lens transmission efficiency.....	62
2.5.4 In-canopy vs. 25 m height PTR-TOF-MS measurements.....	65
3. Secondary organic aerosol formation from in situ OH, O ₃ , and NO ₃ oxidation of ambient forest air in an oxidation flow reactor.....	72
3.1 Introduction	73
3.2 Experimental methods.....	76
3.2.1 BEACHON-RoMBAS field campaign	76
3.2.2 OFR methods	77
3.2.3 Particle and gas measurements.....	80
3.2.4 Modeling of SOA formation	82
3.3 Results and discussion	83
3.3.1 Modeled vs. measured NO ₃ and O ₃ exposures.....	83
3.3.2 SOA formed from oxidation of ambient air	88
3.3.2.1 OA enhancement vs. photochemical age	88
3.3.2.2 Measured vs. predicted OA enhancement	92
3.3.3 H:C and O:C ratios of SOA formed from oxidation of ambient air	94
3.3.4 Particulate organic nitrate (pRONO ₂) formation from NO ₃ oxidation of ambient air	102
3.4 Conclusions	106
3.5 Supplementary information.....	108
3.5.1 NO ₃ oxidant modeling.....	108
4. Secondary organic aerosol formation from ambient air in an oxidation flow reactor during GoAmazon2014/5.....	124
4.1 Introduction	125
4.2 Experimental methods.....	127
4.2.1 GoAmazon2014/5 field campaign	127
4.2.2 Oxidation flow reactor	128
4.2.3 Gas and particle measurements	129

4.2.4 Predicting SOA formation in the OFR	131
4.3 Results and Discussion	132
4.3.1 Using VOC decay to determine OH and O ₃ exposure	132
4.3.2 SOA formation from ambient biogenic and anthropogenic gases in the OFR.....	135
4.3.3 OA enhancement vs. photochemical age	138
4.3.4 Investigating SOA yields in an OFR using standard addition	141
4.3.5 Measured vs. predicted SOA formation	147
4.3.6 Positive Matrix Factorization (PMF) of SOA after OH oxidation.....	151
4.3.7 Hygroscopicity of the organic component of CCN after OH oxidation.....	154
4.3.8 Estimating source contributions to potential SOA using multi-linear regression analysis.....	158
4.4 Conclusions	167
4.5 Supplementary information.....	169
5. Conclusions and future work	175
5.1 Conclusions	175
5.2 Future work.....	177
5.2.1 OFR technique improvements	177
5.2.2 Measurement possibilities.....	180
References	182

LIST OF TABLES

Table 2.1: Glossary.....	8
Table 2.2: List of prominent compounds detected by PTR-TOF-MS in the OFR. Likely compound identifications are taken from previous measurements at the same research site, described in Kim et al. (2010) and Kaser et al. (2013b).....	24
Table 2.3: Low-NO _x SOA yield parameters using basis sets, used to estimate SOA yields from VOCs in the OFR (Sect. 2.3.6.1).....	45
Table 2.S1: Slope and correlation values for a comparison of AMS vs. SMPS volume, when applying aerodynamic lens transmission correction curves 0-5 (shown in Fig. 2.S5) or no correction (base case).....	62
Table 3.S1: List of reactions and parameters used in modeling of the oxidant chemistry in the OFR when performing NO ₃ oxidation. The rate constants are calculated using the modified Arrhenius equation $k = A \cdot \left(\frac{T(K)}{300}\right)^{-n} \cdot e^{-\frac{E}{RT(K)}}$ with pressure dependence as described in Sect. 2 of JPL (Sander et al., 2011). Parameter values are from JPL, with exceptions noted.....	110
Table 3.S2: List of reactions and parameters used in modeling of the oxidant chemistry in the OFR when performing O ₃ oxidation. The rate constants are calculated using the modified Arrhenius equation $k = A \cdot \left(\frac{T(K)}{300}\right)^{-n} \cdot e^{-\frac{E}{T(K)}}$. Parameter values are from IUPAC (Atkinson et al., 2006)..	111

LIST OF FIGURES

- Figure 1.1:** Pie charts showing the average mass concentration and chemical composition of non-refractory submicron particulate matter at various locations in the Northern Hemisphere, measured using an AMS. The label colors indicate the type of sampling location, where blue labels indicate urban areas, black indicates areas within 100 miles downwind of urban areas, and pink indicates rural/remote measurements. This figure is reproduced from Zhang et al. (2007)..... 2
- Figure 1.2:** Photographs of inlet (left) and output (right) of the OFR during the BEACHON-RoMBAS field campaign..... 4
- Figure 2.1:** Simplified schematic of the experimental setup. Ambient air was alternately sampled either directly or through the oxidation flow reactor (OFR). In the OFR, the concentration of OH was increased to simulate atmospheric aging from hours up to several weeks. 17
- Figure 2.2:** Continuous cycling of OH oxidation using the OFR185 method, compared to concurrent ambient measurements. The sawtooth pattern in the OFR results from OA mass enhancement at low–intermediate OH exposure (OH_{exp}) and decreases at the highest photochemical ages. SO_4 mass increased monotonically with OH_{exp} and at higher exposures, as expected from relatively slow $SO_2 + OH$ oxidation and lack of OH destruction of SO_4 23
- Figure 2.3:** The absolute changes (signal after OH oxidation in the reactor minus ambient signal) of molecules measured by the PTR-TOF-MS after 4 hours of eq. aging using the OFR185 method, shown as a difference mass spectrum and in a mass defect diagram. The mass spectra are 10-min averages (5 min from each of the two sample cycles used). The background-subtracted signals are shown in arbitrary units, not corrected for differences in sensitivity of each compound due to the large number of compounds and the inability to positively identify all of them. Prominent molecules are labeled by name or elemental formula assignments. Dashed lines representing molecules with varying double bond equivalents (DBE) or number of oxygen atoms are shown for reference. A red marker signifies that the signal decreased due to oxidation, while a black marker indicates where signal was greater after oxidation. The markers are sized by the square root of the absolute change in signal at each peak after oxidation (i.e., marker area is proportional to signal). Minor signals with absolute change of <0.2 arb. units or change of <20% of total ambient signal were removed. 25
- Figure 2.4:** Relative changes in prominent PTR-TOF-MS compounds as a function of photochemical age using the OFR185 method: a) toluene+*p*-cymene and terpene-related signals compared to nighttime OA enhancement using the OFR185 method (not LVOC fate corrected), and b) oxidation products formed in the OFR. For comparison, dashed lines indicate theoretical depletion of an equal mix of α -pinene, β -pinene, and 3-carene (the three major MT at this site; Kim et al., 2010; Ortega et al., 2014), a 74:26 mix of toluene+*p*-cymene (Kaser et al., 2013a), and methanol..... 27
- Figure 2.5:** Fractional fates of loss of LVOCs to OFR walls, condensation to aerosols, reaction with OH to produce volatile products, or exiting the OFR to be lost on sampling line walls as a function of photochemical age for a) high CS and b) low CS cases; c) LVOC lifetimes for each of these pathways. Lifetime for condensation to aerosols is shown for all data points (colored by OA enhancement after oxidation) using CS calculated from SMPS measurements. 33

Figure 2.6: Measured vs. predicted SO_4 formation after OH oxidation in an OFR. The data points are colored by the fraction of H_2SO_4 predicted to condense on aerosols, calculated using $\alpha = 0.65$ and the average of the SMPS size distributions measured before and after oxidation. Data are shown with the LVOC fate correction applied, along with linear fits to the corrected (red) and uncorrected (black) data. Ambient SO_2 concentrations <0.2 ppb have been excluded from this analysis..... 36

Figure 2.7: Comparison of absolute OA enhancement from OH oxidation using the OFR185 and OFR254-70 methods, binned by photochemical age and separated into daytime (08:00–20:00 local time) and nighttime (20:00–08:00 local time) to reflect the changes in ambient SOA precursors between day and night. Data are shown with (right axis, open symbols, and dashed lines) and without (left axis, closed symbols and solid lines) the LVOC fate correction described in Sect. 3.3. Inset: the maximum OA enhancement (all data 0.4–1.5 days eq. age) as a function of time of day, with (dashed) and without (solid) the LVOC fate correction. OFR254-70 measurements with positive OA enhancement were multiplied by the ratio of ambient MT concentrations measured during OFR185 vs. OFR254-70 sampling periods (ratio = 1.8). Negative OA enhancements were not normalized in this way since the amount of mass lost due to heterogeneous oxidation would not necessarily correlate with ambient MT concentrations..... 38

Figure 2.8: OA enhancement from OH oxidation of ambient air using the OFR185 method as a function of photochemical age. All data points (uncorrected only) are shown, shaded by in-canopy monoterpene (MT) concentrations. Average OA enhancements of age quantiles with equal number of data points with (right axis, dashed lines) and without (left axis, solid lines) the LVOC fate correction are also shown, separated into low (0 to 0.75 ppbv), medium (0.75 to 1.5 ppbv), and high (>1.5 ppbv) ambient MT concentration ranges. The inset shows the correlation ($R^2=0.56$) between the LVOC fate corrected maximum OA enhancement (0.4–1.5 eq. days aging) and in-canopy MT concentrations. 40

Figure 2.9: SMPS volume size distributions after OH oxidation using the OFR185 method, labeled by photochemical age and compared to concurrent ambient measurements. Each of the 6 OH-aged size distributions is an average of 6 SMPS scans from the night of 28–29 July, when relatively large OA enhancement was observed and the ambient aerosol dry surface area was in the range of $80\text{--}100 \mu\text{m}^2 \text{cm}^{-3}$. Dashed lines represent the approximate size distributions that were transmitted through the AMS aerodynamic lens (for which a correction was applied to reported OA values as discussed in Sect. S3). Scans with large OA enhancement were used in order to more clearly illustrate the condensation vs. nucleation behavior in the OFR, so the AMS lens transmission correction in this figure appears larger than average. All scans have been corrected for small particle losses to sampling lines (Sect. S1)..... 43

Figure 2.10: Measured vs. predicted SOA formation from OH oxidation of ambient air in an OFR using the OFR185 method. Only the range of photochemical ages with the highest SOA formation (0.4–1.5 eq. days) was used, and the LVOC fate correction was applied. Predicted SOA formation was calculated by applying OA concentration-dependent yields (average of 12.5%, 13.2%, 13.8%, and 3.2% for MT, SQT, toluene+*p*-cymene, and isoprene, respectively, with average OA concentration of $4.1 \mu\text{g m}^{-3}$) to VOCs reacted in the OFR (Tsimpidi et al., 2010). The amount of reacted VOCs was estimated using OH_{exp} and ambient VOC concentrations. If a non-zero y-intercept is allowed, the regression line becomes $y = 5.0x - 0.5$ 46

Figure 2.11: Top: diurnal maximum measured OA enhancement (all data from 0.4–1.5 eq. days aging, LVOC fate corrected) in the OFR from OH oxidation using the OFR185 method, and predicted OA

formation from measured VOCs (x4.4). Bottom: ambient MT, SQT (x5), toluene+p-cymene (x5), MBO+isoprene, and S/IVOC mass concentrations vs. time of day. 47

Figure 2.12: Measured vs. predicted SOA formation from OH oxidation of ambient air in an OFR using the OFR185 method. Only the range of photochemical ages with the highest SOA formation (0.4–1.5 eq. days) was used, and the LVOC fate correction was applied. Predicted SOA formation is estimated using VOCs (described in Sect. 2.3.6.1) with and without including an empirical 58% SOA yield from S/IVOCs measured by the TD-EIMS (a lower limit of total S/IVOCs). Inset: average S/IVOC concentrations as a function of the log of the saturation vapor concentration C^* . This comparison includes all data for which S/IVOCs and SOA formation in the OFR were concurrently measured (26, 28-29 July, and 9-10, 12-13 August). For some data points, PTR-TOF-MS data was not available, so the VOC contribution was estimated using the linear fit in Fig. 2.10. 49

Figure 2.13: Sensitivity of the slope of measured vs. predicted SOA formation from VOCs, and of the range of SOA yields estimated for bulk S/IVOCs (same curves, different Y axes), to parameters in the LVOC fate model. The change in slope and yields is calculated by changing only one parameter at a time while keeping the rest at the base case values of 5 reactions with OH, $k_{OH} = 1 \times 10^{-11} \text{ cm}^3 \text{ molec}^{-1} \text{ s}^{-1}$, average CS, $\alpha = 1$, $k_e = 0.0036 \text{ s}^{-1}$, and $D = 7 \times 10^{-6} \text{ m}^2 \text{ s}^{-1}$ 53

Figure 2.S1: Top: Average species mass fraction of ambient aerosol measured by the AMS, and inlet sampling line particle transmission efficiency. The transmission efficiency was estimated using the Max Planck Institute for Chemistry Particle Loss Calculator (von der Weiden et al., 2009). This transmission curve was used to correct SMPS size distributions for particle losses in the ambient and OFR sampling lines. Particle losses to surfaces inside the OFR are discussed in Sect. 2.5.3. Bottom: Average species mass size distribution of ambient aerosol measured by the AMS. 58

Figure 2.S2: Scatter plot of ambient aerosol volume measurements from AMS vs. SMPS with regression line. AMS data was calculated using CE=1. AMS volume was estimated using densities of 1.52 g cm^{-3} for chloride, 1.75 g cm^{-3} for sulfate, ammonium, and nitrate (DeCarlo et al., 2004; Salcedo et al., 2006; Lide, 2013), and a parameterization using elemental composition to estimate the density of OA (Kuwata et al., 2012). All data is shown without the LVOC fate correction. 59

Figure 2.S3: Scatter plot of aerosol volume and change in volume after OH aging from AMS vs. SMPS. AMS volume was estimated using densities of 1.52 for chloride, 1.75 for sulfate, ammonium, and nitrate (DeCarlo et al., 2004; Salcedo et al., 2006; Lide, 2013), and a parameterization using elemental composition to estimate the density of OA (Kuwata et al., 2012). Data is shown after correction for particle transmission losses in the AMS aerodynamic lens according to the case 2 correction in Fig. 2.S5. All data is shown without the LVOC fate correction. At the highest ages, heterogeneous oxidation led to fragmentation/volatilization of preexisting OA, resulting in a net loss of OA. 60

Figure 2.S4: Total particle volume enhancement as measured by the AMS and SMPS as a function of photochemical age, split into daytime (08:00–20:00 local time) and nighttime (20:00–08:00 local time) data. AMS volume was estimated using densities of 1.52 g cm^{-3} for chloride, 1.75 g cm^{-3} for sulfate, ammonium, and nitrate (DeCarlo et al., 2004; Salcedo et al., 2006; Lide, 2013), and a parameterization using elemental composition to estimate the density of OA (Kuwata et al., 2012). All data is shown without the LVOC fate correction. Error bars represent the standard error of the mean of each quantile of data. 61

- Figure 2.S5:** Potential AMS aerodynamic lens transmission efficiency curves used to evaluate small particle losses in the lens, as a function of vacuum aerodynamic diameter D_{va} and mobility diameter D_m . D_{va} was converted to D_m assuming a density of 1.45 g cm^{-3} (the campaign average). Case 0 is the recommended AMS lens transmission efficiency when no campaign-specific determination is possible (Knote et al., 2011). Case 2 was chosen as the best fit for the data under the conditions during BEACHON-RoMBAS. 63
- Figure 2.S6:** Scatter plot of aerosol volume and change in volume after OH aging from AMS vs. SMPS. AMS volume was estimated using densities of 1.52 g cm^{-3} for chloride, 1.75 g cm^{-3} for sulfate, ammonium, and nitrate (DeCarlo et al., 2004; Salcedo et al., 2006; Lide, 2013), and a parameterization using elemental composition to estimate the density of OA (Kuwata et al., 2012). Data is shown for base case (uncorrected) for particle transmission losses in the AMS aerodynamic lens according to Fig. 2.S5. All data is shown without the LVOC fate correction. At the highest ages, heterogeneous oxidation led to fragmentation/volatilization of preexisting OA, resulting in a net loss of OA. 64
- Figure 2.S7:** Time series of ambient OA, total OA, and OA enhancement for OFR185 and OFR254 methods, ambient MT (25 m inlet), and ambient S/IVOC mass concentrations measured by the TD-EIMS. The OA enhancements are not LVOC fate corrected here, and include all ages. 64
- Figure 2.S8:** Scatterplots of in-canopy (through OFR or 1 m inlet) vs. 25 m inlet for PTR-TOF-MS measurements of MT, SQT, MBO+isoprene, and toluene. In-canopy concentrations were 1.9, 5.9, 1.4, and 1.2 times higher than at 25 m, respectively. 66
- Figure 2.S9:** The absolute changes of ions (signal after OH oxidation in the reactor minus ambient signal) measured by the PTR-TOF-MS after 7 days of aging using the OFR185 method, shown as a difference mass spectrum and in a mass defect diagram. The mass spectra are 10-min averages (5 min from each of the two sample cycles used). The background-subtracted signals are shown in arbitrary units, not corrected for differences in sensitivity of each compound due to the large number of compounds and the inability to positively identify all of them. Prominent ions are labeled by name or elemental formula assignments. Dashed lines representing molecules with varying double bond equivalents (DBE) or number of oxygen atoms are shown for reference. A red marker signifies that the signal decreased due to oxidation, while a black marker indicates where signal was greater after oxidation. The markers are sized by the square root of the absolute change in signal at each peak after oxidation (i.e., marker area is proportional to signal). Minor signals with absolute change of <0.2 arb. units or change of $<20\%$ of total ambient signal are removed. 67
- Figure 2.S10:** Sensitivity study of the measured vs. predicted SO_4 formation after OH oxidation in the OFR vs. key uncertain parameters. The data points are colored by the fraction of H_2SO_4 predicted to condense on aerosols, calculated using $\alpha = 0.65$ and the average of the SMPS size distributions (SD) measured before and after oxidation. Data are shown without applying the LVOC fate correction, along with linear fits that result from applying various sets of corrections including $\alpha = 0.43-1$ and using the ambient (start), post-oxidation (end), or average SD to calculate the CS. Ambient SO_2 concentrations <0.2 ppb have been excluded from this analysis. 68
- Figure 2.S11:** Scatterplot of ambient MT vs. SQT concentrations measured by the PTR-TOF-MS at the 25 m inlet above the canopy. 69
- Figure 2.S12:** Measured vs. predicted SOA formation from OH oxidation of ambient air in an OFR using the OFR185 method. Only the range of photochemical ages with the highest SOA formation (0.4-

1.5 eq. days) was used. The LVOC fate correction was not applied. Predicted SOA formation was calculated by applying OA concentration-dependent yields (average of 10.9%, 11.1%, 11.5%, and 2.9% for MT, SQT, toluene, and isoprene, respectively, with average OA concentration of $2.9 \mu\text{g m}^{-3}$) to VOCs reacted in the OFR (Tsimpidi et al., 2010). The amount of reacted VOCs was estimated using OH_{exp} and ambient VOC concentrations. If a non-zero y-intercept is allowed, the regression line becomes $y = 4.0x - 0.8$ 70

Figure 2.S13: Scatterplot of mass concentration of ambient S/IVOCs (lower limit measured by TD-EIMS) vs. ambient MT measured by PTR-TOF-MS. Data are shown colored by local time of day. 71

Figure 3.1: Typical average mixing ratios and reactive fluxes for the major reactions in the NO_3 -OFR when injecting N_2O_5 to investigate SOA formation from NO_3 oxidation. These reactive fluxes resulted from running the model with inputs of 25°C , 50% RH, 50 ppb O_3 , 2 ppb NO_2 , 1.5 ppb NO_3 , 50 ppb N_2O_5 , 0.75 ppb total MT, and a rate constant for N_2O_5 uptake to aerosol surfaces of $3 \times 10^{-5} \text{ s}^{-1}$. Reaction arrow widths are sized relative to their average reactive fluxes. Reactions that were included in the model (shown in Table 3.S1) but with smaller average rates are not shown here. 85

Figure 3.2: Modeled vs. measured a) N_2O_5 , b) NO_2 , c) NO_3 , and d) fraction of ambient MT reacted with NO_3 in the output of the NO_3 -OFR. 86

Figure 3.3: Modeled vs. measured fraction MT reacted by O_3 oxidation in the O_3 -OFR..... 87

Figure 3.4: Ambient, measured remaining, and modeled remaining MT from O_3 oxidation on Aug. 23–24 (top) and NO_3 oxidation on Aug. 22–23 (bottom) in the OFR. Modeled O_3 and NO_3 exposures are also shown. The amount of oxidation was cycled from no added oxidant (no MT reacted) to maximum oxidation (most or all MT reacted) in repeated 2–3 h cycles. 88

Figure 3.5: OA enhancement from oxidation of ambient air by O_3 (left) and NO_3 (right) as a function of oxidant exposure. Data are colored by ambient in-canopy MT concentrations and include the LVOC fate correction. Binned averages for times when ambient MT concentrations were either below or above $3 \mu\text{g m}^{-3}$ (0.66 ppb) are also shown, illustrating the positive relationship between OA enhancement and MT concentrations at the higher oxidant concentrations..... 89

Figure 3.6: OA enhancement vs. age in eq. d for OH, O_3 , and NO_3 oxidation, separated into daytime (08:00–20:00 LT) and nighttime (20:00–08:00 LT) data. All data is LVOC fate corrected. OH oxidation produced several-fold more OA enhancement than O_3 and NO_3 oxidation. OH-aged OA enhancement data is taken from Palm et al. (2016), and shows data only for <5 eq. d aging where the LVOC fate correction could be applied..... 91

Figure 3.7: Measured vs. predicted SOA formation for O_3 and NO_3 oxidation in an OFR. The measured SOA formation includes the LVOC fate correction, and includes all ages greater than 0.7 eq. d for O_3 -PAM and greater than 0.3 eq. d for NO_3 -PAM. Predicted SOA formation was estimated by applying published chamber SOA yields to the mass of VOCs predicted by the model to be oxidized in the OFR (see Sect. 3.2.3 for details). 93

Figure 3.8: Scatter plots of $\mu\text{mol m}^{-3} \text{ O}$ and $\mu\text{mol m}^{-3} \text{ H}$ added per $\mu\text{mol m}^{-3} \text{ C}$ added from OH oxidation of ambient air in the OFR. Slopes are fit to the photochemical age ranges of 0.1–0.4 (avg.=0.18) d, 0.4–1.5 (avg.=0.9) d, 1.5–5 (avg.=2.7) d, and 5–15 (avg.=10) d, showing that the atomic O:C(H:C) ratios of the SOA mass formed in those ranges were 0.55 (1.60), 0.84 (1.44), 1.13

- (1.36), and 1.55 (1.22), respectively. At higher ages, heterogeneous oxidation led to loss of C and H and little to no loss of O. 95
- Figure 3.9:** Scatter plots of $\mu\text{mol m}^{-3}$ O and $\mu\text{mol m}^{-3}$ H added per $\mu\text{mol m}^{-3}$ C added from O_3 oxidation of ambient air in the OFR. Data are colored by eq. d of O_3 exposure. The slopes show that the atomic O:C (H:C) ratio of the SOA mass formed was 0.50 (1.61). The slopes did not change with increasing photochemical age. 96
- Figure 3.10:** Scatter plots of $\mu\text{mol m}^{-3}$ O and $\mu\text{mol m}^{-3}$ H added per $\mu\text{mol m}^{-3}$ C added from NO_3 oxidation of ambient air in the OFR. The amount of O added is shown without including the O from the $-\text{NO}_2$ group, since those O atoms do not affect the oxidation state of C. The slopes show that the atomic O:C(H:C) ratio of the SOA mass formed was 0.39 (1.60). The slopes did not change with increasing NO_3 exposure. Contrary to Figs. 3.8–3.9, data are not colored by NO_3 exposure. The ranges of NO_3 exposure achieved during daytime vs. nighttime were unequal (Figs. 3.5-3.6, 3.S12), obscuring any trend of OA enhancement vs. eq. age. 96
- Figure 3.11:** Van Krevelen diagrams of H:C vs. O:C ratios of OA after oxidation by a) NO_3 , b) O_3 , and c) OH along with concurrent ambient ratios. The H:C and O:C ratios of the new SOA mass formed in the OFR (i.e., the slopes from Figs. 3.8–3.10) are shown for each oxidant (diamonds), and are summarized in d) compared with all ambient measurements. For data where no net C addition was observed after OH oxidation, the slope along which heterogeneous OH oxidation transforms the ambient OA is shown (purple dashed line). 99
- Figure 3.12:** Example time series of OA, NH_4 , and NO_3 (split into pRONO_2 and NH_4NO_3) aerosol measurements after NO_3 oxidation in the OFR, compared to ambient aerosol, NO_2^+ to NO^+ ratio, model-derived eq. age of NO_3 oxidation, MT concentration, and RH measurements. Production of both NH_4NO_3 and pRONO_2 was observed at different times, which appears to depend on changes in experimental conditions. 104
- Figure 3.13:** Organic $-\text{ONO}_2$ mass added vs. OA added from OH, O_3 , and NO_3 oxidation in an OFR. No pRONO_2 formation was observed (or expected) from OH or O_3 oxidation under the experimental conditions. The slope of 0.10 from NO_3 oxidation is consistent with previous chamber measurements (shown in grey), which range from approximately 0.1–0.18 (Fry et al., 2009, 2011; Boyd et al., 2015). 106
- Figure 3.S1:** Normalized residence time distributions in the OFR as a function of normalized residence time (1 = avg. residence time of each distribution). The FLUENT model was used to calculate the residence time for the OFR configuration without the inlet plate used during BEACHON-RoMBAS. This distribution is compared to the bis(2-ethylhexyl) sebacate (BES) particle residence time distribution measured with the inlet plate on in Lambe et al. (2011a) and to the ideal plug flow distribution (where all particles have equal residence time calculated as the OFR volume divided by the total flow rate through the OFR). The residence time distribution without the inlet plate is much narrower than with the plate and is close to plug flow, though local winds will create a broader distribution than the model shows. 111
- Figure 3.S2:** Schematic of experimental setup of NO_3 -OFR and O_3 -OFR experiments. 112

- Figure 3.S3:** Modeled fractional fates of condensable low-volatility organic compounds (LVOCs) produced in the OFR, as a function of eq. age for O_3 oxidation (top) and NO_3 oxidation (bottom). For O_3 oxidation, on average 31% of LVOCs condensed onto particles, 34% condensed on OFR walls, and 35% exited the OFR to condense on sampling line walls. For NO_3 oxidation, on average 36% of LVOCs condensed onto particles, 34% condensed on OFR walls, and 30% exited the OFR to condense on sampling line walls. 113
- Figure 3.S4:** a) The wall loss rate constant of N_2O_5 and NO_3 vs. %RH, determined empirically in order to achieve agreement between modeled and measured N_2O_5 concentrations (Fig. 3.2a). b) Modeled vs. measured N_2O_5 remaining (analogous to Fig. 3.2a), shown if the N_2O_5 and NO_3 wall loss rate was assumed to be a constant 0.014 s^{-1} at all %RH. 114
- Figure 3.S5:** Calculated rate constant for reactive uptake of N_2O_5 onto particles, as a function of RH. The rate constant was calculated using the same method for condensation of gases onto aerosols described in Palm et al (2016), using the measured ambient aerosol condensational sink and using an organic-mass-fraction-corrected uptake efficiency $\gamma(N_2O_5)$ from Gaston et al. (2014).114
- Figure 3.S6:** Ambient, measured remaining, and modeled remaining MT from NO_3 oxidation in the OFR on Aug. 4–6 and Aug. 9–10, along with modeled NO_3 exposure (d). For these examples, the amount of injected N_2O_5 was held roughly constant (with a higher constant value injected on Aug. 9–10). 116
- Figure 3.S7:** Ambient, measured remaining, and modeled remaining MT from O_3 oxidation in the OFR on Aug. 7–8 and Aug. 8–9, along with modeled O_3 exposure (d). The amount of oxidation was cycled from no added oxidant (no MT reacted) to maximum oxidation (most or all MT reacted) in repeated 2–3 h cycles. Note that the ambient MT were sampled through a separate inlet within the canopy, several meters from the OFR. Short periods of higher MT concentrations measured through the OFR (at low O_3 exposures) may be due to brief spatial heterogeneity in ambient MT concentrations within the canopy. 117
- Figure 3.S8:** OA enhancement per ppbv ambient MT for OH, O_3 and NO_3 oxidation in the OFR as a function of ambient temperature. Enhancement is defined as the difference between the concentrations measured after oxidation and in ambient air, where positive enhancements signify formation in the OFR. Data are colored by ambient in-canopy MT concentrations, and include the LVOC fate correction. Quantile averages of OA enhancement per ppbv MT are shown for each oxidant, with error bars corresponding to the standard error of the mean of each quantile. 118
- Figure 3.S9:** Pearson's r for the correlation between maximum SOA formation for each oxidant and the available ambient VOC concentrations. Maximum SOA formation is defined as the ranges of 0.4–1.5 eq. d for OH-PAM, 0.7–5 eq. d for O_3 -PAM, 0.3–4 eq. d for NO_3 -PAM. Reaction rate constants are taken from Atkinson and Arey (2003) and the IUPAC database (Atkinson et al., 2006). The orange colored background denotes rate constants that are fast enough so that $\geq 20\%$ of the VOC can react to form SOA under the conditions of maximum SOA formation in the OFR for each oxidant. In contrast, the grey background shows rate constants where the molecules do not react in the OFR and cannot contribute to SOA formation, but could be useful as tracers. 119

- Figure 3.S10:** Elemental C, H, and O enhancements due to OH aging in the OFR, as a function of eq. OH age and exposure. Enhancement is defined as the difference between the concentrations measured after oxidation and in ambient air, where positive enhancements signify formation in the OFR. Data are colored by ambient in-canopy MT concentrations, and do not include the LVOC fate correction. 120
- Figure 3.S11:** Elemental C, H, and O enhancements due to O₃ aging in the OFR, as a function of eq. O₃ age and exposure. Enhancement is defined as the difference between the concentrations measured after oxidation and in ambient air, where positive enhancements signify formation in the OFR. Data are colored by ambient in-canopy MT concentrations, and do not include the LVOC fate correction. 121
- Figure 3.S12:** Elemental C, H, and O enhancements due to NO₃ aging in the OFR, as a function of eq. NO₃ age and exposure. Enhancement is defined as the difference between the concentrations measured after oxidation and in ambient air, where positive enhancements signify formation in the OFR. Data are colored by ambient in-canopy MT concentrations, and do not include the LVOC fate correction. 122
- Figure 3.S13:** Van Krevelen diagrams of H:C vs. O:C ratios of OA after OH oxidation of ambient air in an OFR, along with values for ambient OA. OH aged data are colored by the amount of OA enhancement observed after oxidation. The H:C and O:C ratios of the new SOA mass formed in the OFR (i.e., the slopes from Fig. 3.8) are shown (diamonds; see Fig. 3.11). For data where no net C addition was observed after OH oxidation, the slope along which heterogeneous OH oxidation transforms the ambient OA is shown (purple dashed line). Panel a) shows only data in the eq. range of 0.1–0.4 (avg.=0.18) d, while panel b) shows all data. 123
- Figure 4.1:** Fraction of ambient toluene, ambient MT, and injected CO remaining after OH oxidation in the OFR, as a function of equation-estimated photochemical age (Peng et al., 2015). Binned averages of the fraction remaining are also shown, compared to the amount predicted to remain assuming either plug flow or using the residence time distribution (RTD) for particles from Lambe et al. (2011a). 134
- Figure 4.2:** Fraction of ambient MT remaining after O₃ oxidation in the OFR, as a function of photochemical age. Binned averages of the fraction remaining are also shown, compared to the amount predicted to remain assuming either plug flow or using the RTD of particles from Lambe et al. (2011a). 135
- Figure 4.3:** An example of the time series of OA concentrations measured in ambient air and after OH oxidation of ambient air in the OFR, shown together with ambient copaene (a sesquiterpene, measured by SV-TAG) and monoterpenes (measured by PTR-TOF-MS before and after the OFR). Daytime hours are indicated with the yellow background. OH exposure in the OFR was held constant throughout this time at approximately 3 eq. days. The SOA formed in the OFR is shown as measured, without the LVOC fate correction. In this example, the SOA formation from OH oxidation closely follows the availability of ambient biogenic gases, though the amount of SOA formed was substantially larger than could be formed from the measured ambient gases. 136

- Figure 4.4:** An example of OA concentrations in ambient air and after OH oxidation of ambient air in the OFR at the T2 site, shown together with MT, xylenes, and trimethylbenzene (TMB) measured in ambient air and after OH oxidation. The OH exposure is also shown (in eq. days). OH age was cycled through a range of exposures, including no added exposure (black circles) where none of the VOCs were reacted in the OFR. This example illustrates how SOA formation in the OFR can come from anthropogenic (Period 1), biogenic (Period 3), or mixed (Period 2) precursors, depending on ambient conditions. 138
- Figure 4.5:** Absolute OA enhancement after OH oxidation in the OFR as a function of photochemical age, shown as binned averages for the wet and dry seasons at both the T2 and T3 measurement sites, and split into daytime (06:00–18:00 LT) and nighttime (18:00–06:00 LT) data. This data is not corrected for LVOC fate, in order to show measurement behavior at the highest OH_{exp} 139
- Figure 4.6:** Absolute OA enhancement after O_3 oxidation in the OFR as a function of photochemical age, shown as binned averages for the wet and dry seasons at the T3 measurement site, and split into daytime (06:00–18:00 LT) and nighttime (18:00–06:00 LT) data. The data is not corrected for LVOC fate. 140
- Figure 4.7:** SOA yields measured for individual VOCs in the OFR by standard addition into ambient air, as a function of OA concentration. Typical SOA yield parameterizations from environmental chamber experiments are also shown. The VOCs were injected into ambient air at the entrance to the OFR, and aged between 0–5 eq. days. Data are corrected for LVOC fate. 145
- Figure 4.8:** Measured SOA formation vs. the concentration of SOA predicted to form from the oxidation of ambient VOCs, shown for OH and O_3 oxidation during both wet and dry seasons. Data are colored by local time of day. Measured SOA formation is corrected for LVOC fate. 148
- Figure 4.9:** Measured SOA formation vs. local time of day and diurnal cycles of measured and predicted SOA formation, shown for OH oxidation during both wet and dry seasons. 150
- Figure 4.10:** Absolute and relative changes in PMF factors as a function of eq. days of OH aging in the OH-OFR, for the wet season (top panels) and the dry season (bottom panels)..... 153
- Figure 4.11:** Binned averages of hygroscopicity of OA (κ_{OA}) as a function of bulk O:C of the OA. The data includes ambient data, measurements after 1–3 eq. days OH aging (at both 100 and 160 nm) to sample maximum SOA formation, and measurements after 12–44 eq. days aging (at only 160 nm) sampled through a gas denuder in order to sample the result of heterogeneous oxidation of pre-existing OA. 156
- Figure 4.12:** Scatterplots of maximum measured SOA enhancement from OH oxidation at the T3 site during IOP1, vs. several ambient SOA precursor tracer gases. Correlation coefficients (R^2) are shown for each scatterplot. 159
- Figure 4.13:** Scatterplots of maximum measured SOA enhancement from OH oxidation at the T3 site during IOP2, vs. several ambient SOA precursor tracer gases. Correlation coefficients (R^2) are shown for each scatterplot. 160
- Figure 4.14:** Top: Maximum measured SOA enhancement from OH oxidation in the OFR during the wet season (IOP1), vs. the total amount predicted from multilinear regression analysis. Bottom: Diurnal average values of the maximum measured SOA formation from OH oxidation during the

- wet season, the amount attributed to each emission source, and the total amount predicted from all source. 162
- Figure 4.15:** Top: Maximum measured SOA enhancement from OH oxidation in the OFR at the T3 site during the dry season (IOP2), vs. the total amount predicted from multilinear regression analysis. Bottom: Diurnal average values of the maximum measured SOA formation from OH oxidation at the T3 site during the dry season, the amount attributed to each emission source, and the total amount predicted from all sources..... 163
- Figure 4.16:** Top: comparison of the average tracer concentrations and potential SOA formation during wet and dry seasons. Bottom: the amounts and fraction of the total SOA formation from OH oxidation in the OFR at the T3 site that were attributed to biogenic, anthropogenic, and biomass burning emission types using multilinear regression analysis..... 165
- Figure 4.S1:** Mean ambient OH reactivity used as a parameter in the equation to estimate OH exposure in the OFR, shown as a function of local time of day. This diurnal cycle of OH reactivity was adapted and smoothed from Williams et al. (2016)..... 169
- Figure 4.S2:** Aerosol volume measured in the AMS vs. in the SMPS for IOP1 and IOP2. The AMS mass was converted to volume using species densities of 1.75 g cm^{-3} for SO_4 , NO_3 , and NH_4 , 1.52 g cm^{-3} for Chl (DeCarlo et al., 2004; Salcedo et al., 2006; Lide, 2013), and the parameterization for OA density using elemental ratios described in Kuwata et al. (2012). AMS data was calculated using $\text{CE}=1$ during IOP1 and a composition-dependent CE (mostly $\text{CE}=0.5$; Middlebrook et al., 2012) during IOP2. 169
- Figure 4.S3:** High-resolution factor profiles for the PMF analysis of the wet season, normalized to a total sum of 1. 170
- Figure 4.S4:** High-resolution factor profiles for the PMF analysis of the dry season, normalized to a total sum of 1. 171
- Figure 4.S5:** Elemental O:C ratio of the bulk OA measured after OH oxidation in the OFR, as a function of eq. age of OH aging during the dry season. 172
- Figure 4.S6:** Scatterplots of maximum measured SOA enhancement from OH oxidation at the T3 site during IOP1, vs. several ambient SOA precursor tracer gases. Correlation coefficients (R^2) are shown for each scatterplot. 172
- Figure 4.S7:** Scatterplots of maximum measured SOA enhancement from OH oxidation at the T3 site during IOP2, vs. several ambient SOA precursor tracer gases. Correlation coefficients (R^2) are shown for each scatterplot. 173
- Figure 4.S8:** Diurnal average values of the maximum measured SOA formation from OH oxidation during IOP1 (top) and IOP2 (bottom), along with the amount attributed to each tracer, and the total amount predicted from all tracers. These results were calculated without including MT as a tracer, for comparison with the bottom panels in Figs. 4.12–4.13. 174
- Figure 5.1:** Possible design improvements for a future OFR. Condensational sink could be increased by injecting a seed aerosol through a permanent injection line designed to optimize mixing with

ambient air before passing through a mesh grid. A narrower and longer reactor could help to decrease the distribution of residence times. Finally, the particle and gas sampling lines could be moved along the length of the OFR in order to sample different ages (with oxidant concentration held roughly constant). 180

Chapter 1

Introduction

1.1 Atmospheric aerosols

Aerosols, liquid or solid particles that are suspended in the atmosphere, are important constituents of the Earth's atmosphere. In the troposphere, particles with diameters less than one μm (i.e., submicron particles) are particularly consequential. These particles impact climate by directly scattering light and by affecting cloud formation and lifetimes (IPCC, 2013). Due to a relatively poor ability to predict global aerosol distributions and their impacts on clouds, the aerosol radiative forcing is the most uncertain forcing in the climate system (Myhre et al., 2013). They can contribute to poor air quality and visibility (Godish et al., 2014), and substantially increase morbidity in affected human populations (Pope and Dockery, 2006).

Figure 1.1 illustrates the abundances and chemical composition of submicron aerosols (not including black carbon or refractory metals, which are typically minor components) measured at a variety of locations in the Northern Hemisphere (Zhang et al., 2007). These particles consist of inorganic nitrate (NO_3^-), sulfate (SO_4^{2-}), ammonium (NH_4^+), and chloride (Cl^-) components, as well as organic (OA) components. Inorganic aerosols, e.g., ammonium sulfate ($(\text{NH}_4)_2\text{SO}_4$) and ammonium nitrate (NH_4NO_3), have relatively few sources and sinks in the atmosphere, and are consequently better understood than the organic fraction. OA, which often comprises the majority of submicron aerosol mass concentrations, consists of thousands of different molecules with a large variety of sources and sinks. Simplified mechanisms to accurately simulate the global distribution of OA have so far proven elusive due to fundamental gaps in our understanding (Tsigaridis et al., 2014; Chen et al., 2015b).

1.2 Secondary organic aerosol (SOA) formation

OA can be split into two broad categories: primary and secondary. Primary OA (POA) is emitted directly into the atmosphere as particles, e.g., as smoke from biomass burning, vehicular combustion,

sea spray, and windblown dust. Typically, POA represents a relatively small fraction of total OA in the atmosphere (Jimenez et al., 2009). The majority of OA tends to be formed through secondary processes, where the organic molecules are emitted to the atmosphere as gases (or evaporated POA) and go through secondary degradation processes that convert them into particles. These processes include gas-phase oxidation (typically by reaction with hydroxyl radical (OH), ozone (O₃), or nitrate radical (NO₃)), photolysis, multiphase reactions, or condensed phase reactions within particles or in aerosol or cloud liquid water (Hallquist et al., 2009; Ervens et al., 2011).

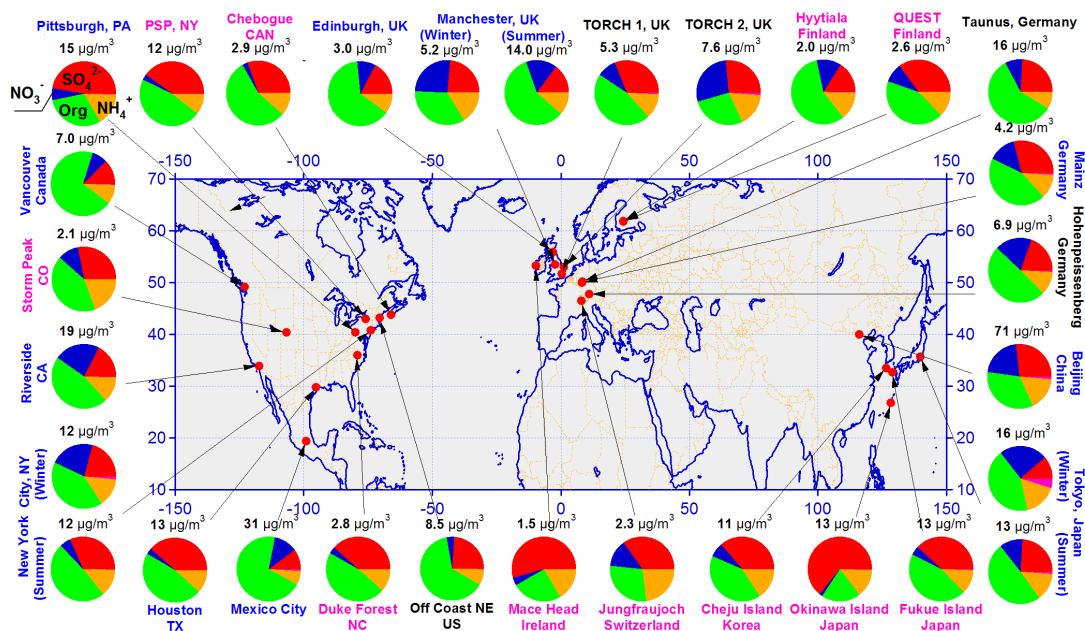


Fig. 1.1. Pie charts showing the average mass concentration and chemical composition of non-refractory submicron particulate matter at various locations in the Northern Hemisphere, measured using an AMS. The label colors indicate the type of sampling location, where blue labels indicate urban areas, black indicates areas within 100 miles downwind of urban areas, and pink indicates rural/remote measurements. This figure is reproduced from Zhang et al. (2007).

Exactly which gases in the atmosphere are responsible for SOA formation, and at which locations and times they are important, is still an open research question. Broadly, SOA-forming gases can be broken down into three source categories: biogenic, anthropogenic, and biomass burning (e.g., Goldstein and Galbally, 2007; Hallquist et al., 2009). They span approximately 10 orders of magnitude in vapor pressure (Donahue et al., 2006). The most volatile gases are called volatile organic compounds (VOCs), and many VOCs (e.g., isoprene, terpenes, aromatics) from each source type are widely

recognized to contribute to SOA formation in the atmosphere. Gases that are less volatile than VOCs, called semi-volatile and intermediate volatility organic compounds (S/IVOCs), have also emerged as important contributors to SOA formation (e.g., Robinson et al., 2007; Zhao et al., 2014). However, relatively little is known about the processes by which VOCs and S/IVOCs are transformed to SOA in the atmosphere.

1.3 Techniques for studying SOA formation and properties

SOA formation from VOCs and/or S/IVOCs has typically been studied using large environmental chambers in the laboratory (Hallquist et al., 2009, and references therein). These chambers allow gases to be oxidized under controlled conditions in order to measure the amount and properties of SOA formed after oxidation, and to study the mechanisms of SOA formation. SOA yields (mass of SOA formed per mass of VOC reacted) from laboratory chamber experiments are used to model SOA formation on local, regional, and global scales (e.g., Tsimpidi et al., 2010). However, these experiments suffer from substantial particle and gas losses to the chamber walls, which increases the uncertainties associated with using chamber results to model SOA formation in the atmosphere (Pierce et al., 2008; Matsunaga and Ziemann, 2010; Zhang et al., 2014; Krechmer et al., 2015). Also, large chambers are generally not suitable for conducting experiments with ambient air. Several “mobile” chambers have been developed for ambient or point source sampling; however, these chambers still typically require residence times on the order of hours to perform a single experiment, leading to possible wall loss effects and low time resolution (Tanaka et al., 2003; Presto et al., 2011; Platt et al., 2013; Peng et al., 2016a).

As an alternative to chambers, several varieties of oxidation flow reactors (OFRs) have been recently introduced, including the Potential Aerosol Mass (PAM) reactor used in this work (Kang et al., 2007). The OFR technique employs a small reactor with short residence times (typically several minutes), using elevated oxidant concentrations (10–1000s of times higher than the atmosphere) in order to achieve minutes to weeks of equivalent atmospheric oxidant exposure. OFRs are small and portable,

meaning they can be used in a laboratory or deployed to oxidize ambient air during field campaigns. They are logistically and financially easier to use than large chambers. Photographs of the PAM OFR used during a field campaign are shown in Fig. 1.2.

OFRs are versatile scientific tools. They can be used for studying SOA formation processes (e.g., Lambe et al., 2012) or to investigate heterogeneous oxidation (e.g., George et al., 2008; Smith et al., 2009). The amount of SOA formed from oxidation of gases can be measured to quantify SOA yields (e.g., Kang et al., 2007, 2011; Lambe et al., 2011a). The properties of the SOA formed in the OFR can be measured as well, e.g., cloud condensation nuclei (CCN) activity or oxidation level (e.g., George et al., 2008; Massoli et al., 2010; Saukko et al., 2012). However, as of the beginning of my thesis work, there had been no publications describing the oxidation of ambient air in OFRs. Furthermore, many questions remained about how well the OFR could really reproduce ambient SOA formation processes.



Fig. 1.2. Photographs of inlet (left) and output (right) of the OFR during the BEACHON-RoMBAS field campaign.

1.4 Dissertation focus

In this dissertation, I present development and field application of the OFR technique for the purpose of studying atmospheric SOA formation. I will discuss several advances that I have made in the interpretation of OFR measurements, which are particularly critical for proper quantification of SOA formed in the OFR. I also present the results of SOA formation from the oxidation of ambient air. These

measurements were made at two locations, including a rural, biogenically-dominated location (BEACHON-ROMBAS campaign in the Colorado Rockies, USA) and downwind of an urban area in a location with mixed biogenic, anthropogenic, and biomass burning sources of SOA-forming gases (GoAmazon2014/5 campaign in Amazonia, Brazil). The results at these contrasting locations provide information about the spatial heterogeneity of SOA-forming gases in the atmosphere.

In Chapter 2, OH-initiated oxidation of ambient pine forest air in an OFR during BEACHON-ROMBAS is discussed. I introduce a model to predict the fate of condensable gases in the OFR for the purpose of correcting for limitations of the technique. The sources of SOA-forming gases (a common theme of each chapter in this thesis) in an atmosphere dominated by biogenic emissions are explored.

In Chapter 3, the techniques for studying SOA formation from O_3 and NO_3 -initiated oxidation of ambient air are introduced for the first time. These oxidants were also used for the oxidation of ambient pine forest air, as in Chapter 2. I discuss chemical properties of the SOA formed from OH, O_3 , and NO_3 oxidation in the OFR. Further discussion about the amounts and sources of SOA-forming gases can also be found in this chapter.

In Chapter 4, the sources of SOA-forming gases in an Amazon forest atmosphere with mixed biogenic, anthropogenic, and biomass burning emissions are investigated as part of the GoAmazon2014/5 field campaign. SOA yields were measured under the conditions used during the oxidation of ambient air in the OFR to compare with published SOA yields in chambers. Properties of the SOA formed in the OFR are investigated, including CCN activity and the lifetimes and formation rates of the major components of SOA and POA. This analysis informs the investigation of sources of SOA-forming gases at this field site.

Finally, Chapter 5 summarizes the conclusions drawn from this dissertation as a whole. I also discuss possible future avenues of research using the OFR. I suggest possible upgrades to the technique, and share which science questions I believe could be answered by using them.

CHAPTER 2

In situ secondary organic aerosol formation from ambient pine forest air using an oxidation flow reactor

Adapted from Palm, B.B., Campuzano-Jost, P., Ortega, A.M., Day, D.A., Kaser, L., Jud, W., Karl, T., Hansel, A., Hunter, J.F., Cross, E.S., Kroll, J.H., Peng, Z., Brune, W.H., Jimenez, J.L., *Atmos. Chem. Phys.*, 16, 2943-2970, doi: 10.5194/acp-16-2943-2016, 2016.

Abstract

An oxidation flow reactor (OFR) is a vessel inside which the concentration of a chosen oxidant can be increased for the purpose of studying SOA formation and aging by that oxidant. During the BEACHON-RoMBAS field campaign, ambient pine forest air was oxidized by OH radicals in an OFR to measure the amount of SOA that could be formed from the real mix of ambient SOA-precursor gases, and how that amount changed with time as precursors changed. High OH concentrations and short residence times allowed for semi-continuous cycling through a large range of OH exposures ranging from hours to weeks of equivalent (eq.) atmospheric aging. A simple model is derived and used to account for the relative time scales of condensation of low volatility organic compounds (LVOCs) onto particles, condensational loss to the walls, and further reaction to produce volatile, non-condensing fragmentation products. More SOA production was observed in the OFR at nighttime (average $3 \mu\text{g m}^{-3}$ when LVOC fate corrected) compared to daytime (average $0.9 \mu\text{g m}^{-3}$ when LVOC fate corrected), with maximum formation observed at 0.4–1.5 eq. days of photochemical aging. SOA formation followed a similar diurnal pattern to monoterpenes, sesquiterpenes, and toluene+*p*-cymene concentrations, including a substantial increase just after sunrise at 7 AM local time. Higher photochemical aging (>10 eq. days) led to a decrease in new SOA formation and a loss of preexisting OA due to heterogeneous oxidation followed by fragmentation and volatilization. When comparing two different commonly used methods of OH production in OFRs (OFR185 and OFR254-70), similar amounts of SOA formation were

observed. We recommend the OFR185 mode for future forest studies. Concurrent gas-phase measurements of air after OH oxidation illustrate the decay of primary VOCs, production of small oxidized organic compounds, and net production at lower ages followed by net consumption of terpenoid oxidation products as photochemical age increased. New particle formation was observed in the reactor after oxidation, especially during times when precursor gas concentrations and SOA formation were largest. Approximately 4.4 times more SOA was formed in the reactor from OH oxidation than could be explained by the VOCs measured in ambient air. To our knowledge this is the first time that this has been shown when comparing VOCs and SOA formation measured at the same time, rather than comparing measurements made at different times. Several recently-developed instruments quantified ambient semi- and intermediate-volatility organic compounds (S/IVOCs) that were not detected by a PTR-TOF-MS. An SOA yield of 18-58% from those compounds can explain the observed SOA formation. This work suggests that these typically unmeasured gases play a substantial role in ambient SOA formation. Our results allow ruling out condensation sticking coefficients much lower than 1. These measurements help clarify the magnitude of potential SOA formation from OH oxidation in forested environments, and demonstrate methods for interpretation of ambient OFR measurements.

2.1 Introduction

Atmospheric aerosols play a complex and important role in air pollution, human health, and global climate. Exposure to fine particles has adverse effects on cardiopulmonary health (Pope and Dockery, 2006). Aerosols affect climate forcing by directly scattering or absorbing incoming solar radiation. They also act as cloud condensation nuclei (CCN; acronyms are listed in Table 2.1), affecting the reflectivity, lifetime, and precipitation of clouds (IPCC, 2013). Among all radiative forcings, the estimates for aerosols represent the largest uncertainty (Myhre et al., 2013).

Table 2.1. Glossary.

OFR	Oxidation flow reactor
SOA	Secondary organic aerosol
LVOC	Low volatility organic compound
OA	Organic aerosol
VOC	Volatile organic compound
S/IVOC	Semi- and intermediate-volatility organic compound
PTR-TOF-MS	Proton transfer reaction time-of-flight mass spectrometer
OH	Hydroxyl radical
O ₃	Ozone
NO ₃	Nitrate radical
MBO	2-methyl-3-buten-2-ol
MT	Monoterpenes
SQT	Sesquiterpenes
OHR _{ext}	External OH reactivity
OHR _{int}	Internal OH reactivity
OH _{exp}	OH exposure
eq.	Equivalent
SMPS	Scanning mobility particle sizer
AMS	Aerodyne High-Resolution Time-of-Flight Aerosol Mass Spectrometer
k_{OH}	Rate constant for reaction with OH
k_{O_3}	Rate constant for reaction with O ₃
TD-EIMS	Thermal desorption electron impact mass spectrometer
C^*	Effective saturation vapor concentration
τ_{aer}	Lifetime of LVOCs (or H ₂ SO ₄) for condensation onto aerosols
τ_{wall}	Lifetime of LVOCs (or H ₂ SO ₄) for loss to OFR walls
τ_{OH}	Lifetime of LVOCs for reaction with OH
τ_{total}	Total lifetime for loss of LVOCs (or H ₂ SO ₄)
CS	Condensational sink
D	Gas diffusion coefficient
r	Particle radius
$N(r)$	Particle number size distribution
α	Sticking coefficient
Kn	Knudsen number
λ_g	Mean free path of gas molecules
A/V	Surface-area-to-volume ratio of OFR
k_e	Coefficient of eddy diffusion
F_x	Fraction of LVOCs (or H ₂ SO ₄) lost to pathway x
SO ₄	Sulfate aerosol

Organic aerosols (OA) make up a substantial fraction of submicron aerosols (Murphy et al., 2006; Zhang et al., 2007; Jimenez et al., 2009). OA is composed of thousands of different molecules, of which only a small fraction has been speciated (Goldstein and Galbally, 2007). OA can be emitted directly in the particle phase as primary OA (POA), or it can be formed as secondary OA (SOA) through

gas-to-particle conversion. During gas-phase SOA formation, an oxidant (mainly OH, O₃, or NO₃) reacts with organic gases to produce either less-volatile functionalized products (e.g., reacting to add a hydroxyl group) or more-volatile fragmented products (e.g., breaking C-C bonds to produce smaller molecules). If the reaction products have sufficiently lower volatility, they can then partition into the particle phase to form SOA (Pankow, 1994; Donahue et al., 2006). In addition to gas-phase oxidation pathways, SOA formation can result from aqueous chemistry within aerosol water or in cloud droplets (e.g., Lim et al., 2010; Ervens et al., 2011; Ervens, 2015) or heterogeneous uptake reactions (e.g., Surratt et al., 2010). Oxidative aging of gases and particles continues until deposition occurs (or CO₂ is produced). The complexity of OA chemistry arises from this intricate mix of multiphase-multigenerational reaction pathways and physicochemical processes involving thousands of molecules.

Much progress has been made in the past decade towards identifying and quantifying the sources, formation, and aging mechanisms of SOA. Aerosol models using traditional (pre-2007) aerosol yields for volatile organic compounds (VOCs) from chamber studies generally underpredict SOA mass by a factor of 10 in urban areas (Volkamer et al., 2006; Hodzic et al., 2010; Hayes et al., 2015). More recent models are able to better predict SOA mass in urban areas by using higher VOC yields and adding previously ignored semivolatile and intermediate volatility organic compounds (S/IVOCs; Hodzic et al., 2010; Hayes et al., 2015). Model comparisons for biogenically-dominated areas have not shown such systematic underpredictions even when using older models (e.g., Tunved et al., 2006; Chen et al., 2009; Hodzic et al., 2009; Slowik et al., 2010). Recent measurements of the oxidation of biomass burning emissions, vehicle exhaust, and urban air have also found S/IVOCs to be important contributors to SOA formation (Grieshop et al., 2009; Miracolo et al., 2010; Zhao et al., 2014), building on the ideas of Robinson, et al. (2007). However, model parameterizations of SOA formation from S/IVOCs are based on large extrapolations and are still uncertain. The recent AeroCom intercomparison of 31 global OA models showed large variability between models and low temporal correlations between models and

measurements (Tsigaridis et al., 2014). Their work suggests that current model parameterizations of SOA formation, transport, and removal processes are inadequate.

SOA formation has traditionally been studied in large environmental “smog” chambers. These chamber experiments have provided the SOA yields for models, but recent evidence shows that chamber experiments are affected by large losses of semivolatile gases to chamber walls (Matsunaga and Ziemann, 2010; Zhang et al., 2014; Krechmer et al., 2015) in addition to well-known particle wall losses (Pierce et al., 2008). This is especially true at long (>1 day) residence times, making it difficult to study SOA formation and aging on longer time scales. Also, while chamber experiments have been performed using emissions from mesocosm (e.g., whole tree) systems in the laboratory (e.g., Wyche et al., 2014), it is difficult to perform field experiments with ambient air in chambers (Tanaka et al., 2003). To explore the sources of SOA on a rapid time scale and with a wide range of oxidant exposures, a variety of oxidation flow reactors (OFR) have been developed (Kang et al., 2007; George et al., 2008; Smith et al., 2009; Keller and Burtscher, 2012). OFRs employ higher oxidant concentrations than chambers while having a short residence time with reduced wall contact. This allows hours to months of equivalent (eq.) atmospheric aging, and the same experimental system can be used in both laboratory and field experiments.

Previous experiments have shown SOA yields from various precursor gases oxidized in an OFR to be similar to yields from large environmental chambers (Kang et al., 2007, 2011, Lambe et al., 2011b, 2015). OFRs have also been used to investigate SOA formation from pollution source emissions containing complex mixtures of precursors such as controlled biomass burning (Ortega et al., 2013; Bruns et al., 2015) and vehicular emissions in a tunnel (Tkacik et al., 2014). Ortega et al. (2016) pioneered the use of an OFR to study SOA formation from ambient air in an urban study in the Los Angeles area. Bruns et al. (2015) found that for a wood combustion system, the amount of SOA formed in an OFR compared to a large chamber agreed reasonably well. Tkacik et al. (2014) and Ortega et al.

(2013) showed substantially more SOA formation than could be explained from speciated VOCs. Despite relying on SOA yields measured in large chambers, which can be affected by the aforementioned wall losses of semivolatile gases, these results suggest that S/IVOCs contribute to SOA formation in biomass burning plumes and vehicle exhaust.

In this study, we used an OFR to expose ambient air to variable levels of OH in a ponderosa pine forest during the BEACHON-RoMBAS campaign. We extensively characterized both the gas and particle phase to investigate the formation and aging of SOA. Changes in aerosol formation with gas precursor concentrations, time of day, and OH exposure were explored. The fate of condensable organic gases in the OFR was modeled. This model was used to estimate how much SOA formation was missed in the OFR due to gas-phase wall losses, excessive OH reaction that led to gas-phase fragmentation prior to condensation, and inadequate time/particle surface area for condensation. The SOA mass produced via oxidation was compared to the amount of SOA predicted based on literature yields of measured VOCs. The role of S/IVOCs in SOA formation in a forest was also explored. These results are discussed in the context of improving our knowledge of SOA sources and formation processes in a biogenic-dominated environment.

2.2 Experimental Methods

2.2.1 BEACHON-RoMBAS Campaign

The BEACHON-RoMBAS field campaign (Bio-hydro-atmosphere interactions of Energy, Aerosols, Carbon, H₂O, Organics & Nitrogen – Rocky Mountain Biogenic Aerosol Study; <http://cires.colorado.edu/jimenez-group/wiki/index.php/BEACHON-RoMBAS>) took place at the Manitou Experimental Forest Observatory near Woodland Park, Colorado, in July–August 2011 (39.10° N, 105.10° W; 2370 m elevation). It was a collaboration of 27 institutions from the United States and Europe, focused on understanding primary and secondary biogenic aerosol emissions, formation and processing.

An overview of atmospheric chemistry research at the Manitou Experimental Forest Observatory, including the BEACHON-RoMBAS campaign, has been previously published (Ortega et al., 2014).

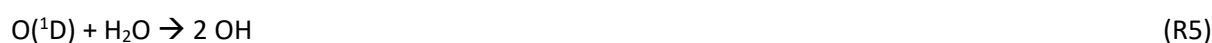
The sampling site was located in a ponderosa pine forest in a mountain valley. VOC concentrations were characterized by high 2-methyl-3-buten-2-ol (MBO) during the daytime and monoterpenes (MT) during the nighttime. VOCs at this site have been described in detail for previous campaigns during July–September 2008 (Kim et al., 2010) and August–September 2010 (Kaser et al., 2013a, 2013b), while Fry et al. (2013) discussed diurnal cycles of select biogenic and anthropogenic VOCs during this campaign. The diurnal cycle of the concentration of MBO+isoprene (detected as the same product ion in the proton transfer reaction time-of-flight mass spectrometer; PTR-TOF-MS) measured at an above-canopy 25 m inlet ranged from about 1.5 ppb during the day to 0.3 ppb at night, while MT concentrations were on average 0.1 ppb during the day and 0.5 ppb at night. The relative ratio of isoprene/(MBO + isoprene) at this field site was estimated using a combination of GC-MS, PTR-TOF-MS, and whole air sample measurements during summer 2010 (Kaser et al., 2013a) and using NO^+ ionization mass spectrometry during the BEACHON-RoMBAS campaign (Karl et al., 2012) to be approximately 20%. Isoprene concentrations are calculated in this study using that approximation, which gives values typically <300 ppt. While largely dominated by biogenic emissions, the site receives some airflow from the front range urban areas (Denver metropolitan area and Colorado Springs) on most days, as evidenced by moderate increases in NO_x , CO, and anthropogenic VOCs during late afternoon and into the evening (Fry et al., 2013; Ortega et al., 2014; Chan et al., 2016).

2.2.2 Oxidation flow reactor

The Potential Aerosol Mass (PAM) oxidation flow reactor (hereafter flow reactor or OFR) is a cylindrical tube 45.7 cm long and 19.7 cm ID with a volume of approximately 13 liters, previously described elsewhere (Kang et al., 2007, 2011; Lambe et al., 2011a; Ortega et al., 2013, 2016). Ambient air was sampled through the reactor with a residence time of 2–4 min (3.5–6.5 lpm total flow rate),

achieving oxidant exposures of hours to months of eq. atmospheric aging. The 14 cm diameter inlet plate was removed from the intake end of the OFR to reduce possible losses of semivolatile SOA precursors to the inlet plate inferred in a previous study (Ortega et al., 2013) and to reduce the width of the residence time distribution in the reactor (Ortega et al., 2016). Air was sampled into the reactor through this 14 cm diameter opening, which was covered with a coarse-grid mesh screen to reduce turbulence in the reactor and prevent insects and debris from entering the reactor. The mesh was coated with an inert silicon coating (Sulfinert by SilcoTek, Bellefonte, PA) to minimize gas and particle losses. OH radicals in the OFR were produced inside the reactor through one of two methods: OH production from photolysis of ambient H₂O, O₂, and concurrently produced O₃ using 185 and 254 nm light (referred to as the OFR185 method), or OH production from photolysis of injected (externally produced) O₃ using 254 nm light (referred to as the OFR254 method; Peng et al., 2015). O₃ and NO₃ oxidation were also investigated and will be the subject of a future manuscript.

For both methods, UV light was produced using two low-pressure mercury lamps (BHK, Inc., model no. 82-9304-03) mounted inside and on the upper part of the flow reactor. The lamps have discrete emission wavelengths of 185 and 254 nm. The following reactions produce the OH radicals:



In the OFR185 method, OH was produced by H₂O photolysis (R1) and also by O₃ photolysis (R4-5), as O₃ was formed in the reactor from O₂ photolysis (R2-3). In the OFR254 method, the mercury lamps were mounted inside Teflon-coated quartz sheaths, which blocked transmission of 185 nm light into the OFR, and only (R4-5) produced OH by photolysis of injected O₃. Following the terminology introduced by Peng

et al. (2015), the method used in this work can be referred to as OFR254-70, signifying that typically 70 ppm of O₃ was injected when using the OFR254 method. Note that both wavelengths (185 and 254 nm) may initiate chemistry not normally occurring in the troposphere, and O(³P) and O(¹D) are also present in the reactor at elevated concentrations. However, under the OFR conditions of our study neither of those non-OH reactants is a competitive reaction pathway (Peng et al., 2016b). O₃ oxidation, on the other hand, can be competitive in the OH oxidation experiments under certain conditions. According to Fig. 5 of Peng et al. (2016b), O₃ in the OFR185 method during this study likely contributed only a minor (< 20%) role in the oxidation of a few biogenic VOCs with the largest k_{O_3}/k_{OH} ratios (e.g., β -caryophyllene, α -terpinene, α -humulene), and only at the lowest OH exposures (OH_{exp}) equivalent to several hours of aging. With the OFR254-70 method though, the ratio of O₃ exposure to OH_{exp} was as high as 10⁶ for the lowest OH_{exp} in this study. Under these conditions, O₃ may have played a substantial role in the initial oxidation of a larger number of species of biogenic VOCs (e.g., reacting with ~100% of β -caryophyllene and α -terpinene, ~60% of α -pinene and limonene, ~20% of 3-carene and β -pinene, 10% of isoprene). Still, the relative importance of O₃ vs. OH oxidation in the OFR was over an order-of-magnitude lower than under typical daily-average atmospheric conditions (Peng et al., 2016b).

The OH exposure was stepped over a range of exposures by adjusting the mercury lamp intensities using programmable computer controls. A key parameter for interpreting the flow reactor aging was the total oxidant exposure, or oxidant concentration integrated over time, experienced by the sampled air. OH_{exp} for the OFR185 method was estimated in part based on a model-derived equation, which uses measurements of ambient water vapor concentration, O₃ produced in the reactor, and estimated external OH reactivity (OHR_{ext}) as equation parameters (Li et al., 2015). OHR_{ext} is the OH reactivity from ambient gases such as VOCs, CO, SO₂, and is accounted for separately from the “internal OH reactivity (OHR_{int})” from species such as HO_x/H₂O₂/O₃ that are greatly enhanced by this reactor. For this study, OH_{exp} was calculated using an estimated OHR_{ext} = 10 s⁻¹, based on measurements at the same

field site and season during previous campaigns (Kim et al., 2013; Nakashima et al., 2014). To provide the best estimate of OH_{exp} for this study, the output OH_{exp} from the model was divided by a factor of two (which is within the estimated model uncertainty of a factor of three) in order to bring it into better agreement with VOC decay rates measured during this campaign (Sect. 3.2). OH_{exp} for the OFR254-70 method was calculated from a different model-derived equation, using OHR_{ext} and a measurement of the amount of O_3 consumed as equation parameters (Peng et al., 2015), and was also divided by a factor of two. For both methods, OH_{exp} was converted to eq. days of atmospheric aging by dividing by a 24-h-average atmospheric concentration of $1.5 \times 10^6 \text{ molec cm}^{-3} \text{ OH}$ (Mao et al., 2009). All usage of hours/days of aging in this work refers to eq. ages calculated in this manner.

Oxidant exposure is not the only factor that determines aerosol chemistry. NO_x concentrations have been shown to affect oxidation products and aerosol yields in chamber studies, especially due to the competition of NO and HO_2/RO_2 to react with the RO_2 radicals formed during oxidation (e.g., Ng et al., 2007; Lim and Ziemann, 2009). In all OH oxidation experiments in the reactor, ambient NO_x was rapidly oxidized to HNO_3 in as little as a couple of seconds at the highest OH concentrations, while photolysis of HNO_3 back to NO_x was too slow to compete with oxidation (Li et al., 2015). Thus, the OH flow reactor experiments were assumed to occur under RO_2+HO_2 conditions.

2.2.3 Sampling strategy and measurements

An important advantage of the OFR technique is that the oxidant concentration inside the reactor can be rapidly and consistently controlled to achieve any desired amount of oxidation from hours up to many weeks of eq. atmospheric age. Stepping through a repeating cycle of several oxidant concentrations from no added OH to several weeks of eq. aging allowed continuous investigation of SOA formation as a function of this age. The time needed to complete one cycle was kept as short as possible ($\sim 2 \text{ h}$, limited by the number of steps and reactor residence time). This allows the potential of SOA

formation from OH oxidation to be studied over the whole range of exposures as functions of time of day and the concentration of precursors that change on that time scale.

In typical OFR185 and OFR254-70 exposure cycles during BEACHON-RoMBAS, the UV lamps inside the reactor were stepped through six 20-min-long settings of varying lamp intensities for a combined cycle length of 2 h, from both lamps off to both lamps at full intensity. Oxidant and product concentrations in the reactor were allowed 15 min (~4–7 reactor residence times) to reach a steady state at each light setting (mainly to allow the OFR to flush, as the lamp UV intensity stabilizes within seconds) before being sampled for the last 5 min of each cycle. Immediately after this 5 min sampling period, the lamp intensity was changed to prepare for the next oxidant concentration in the cycle. During the 15 min in which the OFR was not being sampled, ambient aerosols were sampled directly, through a thermodenuder (Huffman et al., 2008), and directly again, for 5 min each. In this method, all perturbation measurements (OFR or thermodenuder) are bracketed by unperturbed ambient measurements. The ambient AMS sampling has also been described in Fry et al. (2013).

Ambient aerosols and those after oxidation in the OFR were measured using a TSI 3936 Scanning Mobility Particle Sizer (SMPS) and an Aerodyne High-Resolution Time-of-Flight Aerosol Mass Spectrometer (HR-ToF-AMS, hereafter AMS; DeCarlo et al., 2006). A system of automated valves (Aerodyne AutoValve), controlled by a custom automation program written in Labview (National Instruments, Inc.), was used to multiplex the AMS and SMPS to alternate between measuring ambient air and air oxidized in the OFR (or heated by the thermodenuder). The flow rate through the OFR and all sampling lines was kept constant at all times by using make-up flows when not sampling from each of the inlet lines or reactors. The same custom software was used to control and schedule the UV lamp cycling as well as record relative humidity (RH), temperature and output O₃ concentrations in the OFR. Sampled air was dried to <30% relative humidity upstream of the SMPS and AMS using a Nafion membrane drier (Perma Pure, LLC; MD-110-24S-4). For OH_{exp} calculations in the OFR, O₃ was measured

using a 2B Technologies Model 205 Monitor and ambient water vapor was measured using a Vaisala HM70 probe. A schematic of the experimental setup is shown in Fig. 2.1. The SMPS consisted of a TSI 3080 Electrostatic Classifier, a 3081 long Differential Mobility Analyzer (DMA) column, and a 3010 Condensation Particle Counter (CPC). It was operated with sheath and aerosol flow rates of 3.0 and 0.3 lpm, respectively, with a TSI Kr-85 neutralizer and no impactor. The SMPS sampled the range of 14–626 nm mobility diameters, with one 4 min scan every five minutes, and synchronized with OFR and AMS sampling.

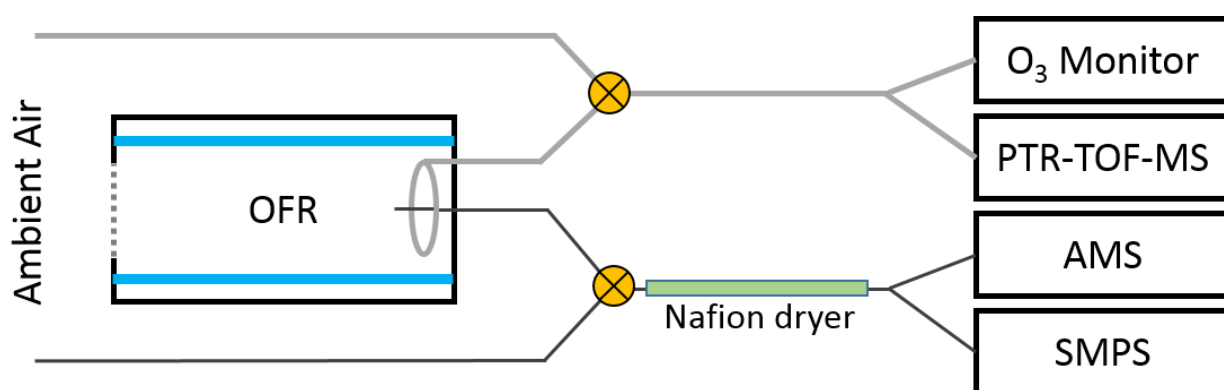


Fig. 2.1. Simplified schematic of the experimental setup. Ambient air was alternately sampled either directly or through the oxidation flow reactor (OFR). In the OFR, the concentration of OH was increased to simulate atmospheric aging from hours up to several weeks.

The AMS data used in this analysis was recorded as 2.5 min average mass spectra in “V-mode”. Instrument sensitivity was calibrated every 3 days with 400 nm monodisperse, dried, ammonium nitrate particles. The gas-phase N₂ signal, commonly referred to as the airbeam, was used to track changes in sensitivity between calibrations. The flow rate of air into the AMS was calibrated in the field before measurements began. A fluorocarbon standard was leaked into the ionization chamber in order to provide high m/z background peaks for improved m/z calibration up to approximately m/z 300 (DeCarlo et al., 2006). Corrections were applied to account for gas-phase CO₂ interference and water fragmentation patterns using daily aerosol-free background filters and continuous ambient CO₂ measurements. AMS and SMPS concentrations and SMPS size distributions were corrected to account for diffusion losses to the walls of the inlet sampling lines, described in Sect. S1. AMS data was

processed using a collection efficiency (CE) of 1, detailed in Sect. S2 and based on a comparison of the AMS and SMPS measurements of ambient aerosol volume (Fig. S2), OFR-oxidized aerosol volume and change in volume (Fig. S3), and total volume enhancement as a function of photochemical age (Fig. S4). AMS concentrations were also corrected for losses of small particles through the aerodynamic lens and to the OFR walls. Details for these corrections can be found in the Sect. S3. AMS data is reported at 293 K and 0.76 atm (typical ambient values at this research site). The time series, diurnal cycles, and average size distributions of ambient OA, sulfate (SO_4), nitrate (NO_3), and ammonium (NH_4) aerosol mass concentrations have been previously published (Ortega et al., 2014).

While both OH generation methods detailed above were used during the campaign, the analysis in this paper will mainly focus on the OFR185 mode for several reasons. The analysis of SOA mass formed vs. predicted in Sect. 3.6 was done using the age range that produced the maximum SOA formation (0.4–1.5 eq. days). However, determination of ages below approximately 1 eq. day using the OFR254-70 method was limited by the ability to accurately measure the amount of injected O_3 that was consumed in the reactor. The variability of the measurement of the initial concentration of O_3 inside the reactor was approximately ± 2 ppm (when reaching a total of about 70 ppm of O_3) due to variations in the mixing of injected O_3 with ambient air sampled into the OFR, especially when sampling in windy conditions. The model used to estimate eq. age for the OFR254-70 method estimated that 2 ppm of photolyzed O_3 produced an age of 0.5 eq. days, so that was the effective lower limit of detection of age with the OFR254-70 method under the experimental conditions used during this campaign. Measuring the decay of a compound that reacts relatively quickly with OH but does not react with O_3 could allow for better OH_{exp} quantification at low ages for OFR254-70. Also, the OFR254 method requires high concentrations of O_3 (up to 70 ppm in this study) to be injected in order to reach high ages. As discussed above, O_3 may play a role in the oxidation of some VOCs in the OFR254-70 method, while the role of O_3 oxidation in OFR185 is minor. This could further complicate the interpretation of the results of OH

oxidation for the lower measurable ages (hours–days) when using OFR254-70. In addition, the temporal data coverage of OFR185 oxidation (23 July–4 August, 9–14 and 24–26 August) was much greater than OFR254-70 (17–20 and 28–30 August). This short time period of OFR254-70 measurements combined with the difficulty of sampling at short eq. ages with this particular experimental setup meant that there were few OFR254-70 measurements relative to OFR185 measurements for the analysis in Sect. 3.6. Also, there were no concurrent measurements of S/IVOC concentrations and SOA formation using OFR254-70 available for the analysis in Sect. 3.6.2. If these analyses would have been performed on a combined dataset using both OH production methods, the results would be driven almost completely by OFR185 measurements. For these reasons, the analyses were performed and conclusions reached using only OFR185 measurements. Regardless, we document below that both OH oxidation methods gave consistent results for SOA production over the range of overlapping ages (~1–30 eq. days) used during this campaign (Sect. 3.4). The time series of OFR185 and OFR254-70 OA measurements are shown compared to ambient OA, MT, and S/IVOCs in Fig. S7.

This work focuses on the changes in OA mass due to SOA formation and OA aging as a result of exposure of ambient air to OH. OA enhancement is defined here as the difference between OA mass measured by the AMS after oxidation in the OFR and the average of the two ambient OA concentrations measured just before and after the oxidation data point. If SOA was produced in the reactor, the OA enhancement was positive; if oxidation led to a net loss of OA mass, then the OA enhancement was negative. As discussed in the results below, SOA formation in the OFR correlated with ambient precursor gas concentrations. If the ambient concentration of those gases was close to zero, then no SOA formation was observed (e.g., Fig 8). Therefore, any SOA formation from, e.g., gases desorbing from the OFR walls, was negligible.

Measurements of VOCs in ambient air and after OFR oxidation were made using a high-resolution PTR-TOF-MS (Kaser et al., 2013a). This technique can separate and identify isobaric

compounds with a mass resolution ($m/\Delta m$) of up to ~ 4000 . This allowed for tracking of the depletion of primary biogenic species in the OFR as well as the production of more oxygenated products. Signals from isotopes, internal standards, and possible artifacts (e.g., saturated hydrocarbons that correlate with O_3 concentration in the reactor) were removed from the analysis. When calculating predicted depletion for α -pinene, β -pinene, 3-carene, toluene, p -cymene, methanol, and sesquiterpenes (SQT; using longifolene as a representative compound) in the following analysis, the rate constants used were: $k_{OH} = 5.3 \times 10^{-11}$, 7.7×10^{-11} , 8.7×10^{-11} , 5.5×10^{-12} , 1.5×10^{-11} , 9.1×10^{-13} , and $4.8 \times 10^{-11} \text{ cm}^3 \text{ molec}^{-1} \text{ s}^{-1}$, respectively (Calvert et al., 2002; Atkinson and Arey, 2003; Alarcón et al., 2014). As an approximation of previous measurements at this site, MT are assumed to be an equal mix of α -pinene, β -pinene, and 3-carene for this analysis (Kim et al., 2010; Ortega et al., 2014). Likewise, the ratio of toluene: p -cymene used in calculations was taken from Kaser et al. (2013a) to be 74:26. Similar to the multiplexing scheme described above for particle sampling, a system of automated Teflon valves was used to alternate between measuring ambient air and air through the OFR, sampling from the OFR concurrently with the AMS+SMPS. PTR-TOF-MS measurements from the OFR were performed during 1-4 and 24-25 August, 2011, while using the OFR185 method. The analysis here focuses on two consecutive sampling cycles from 00:00–04:00 MDT (local time) on 3 August, 2011, when the concentration of MT was relatively high (0.8 ppbv) and the concentration of MBO+isoprene was relatively low (0.1 ppbv).

Ambient PTR-TOF-MS measurements are also used in this work to estimate how much SOA could form in the OFR. The continuous PTR-TOF-MS measurements during BEACHON-RoMBAS were made from an inlet at the top of a tower above the canopy at 25 m height, while the OFR was located on top of an instrument trailer within the canopy at approximately 4 m height. In-canopy gradients were accounted for by comparing the PTR-TOF-MS measurements at 25 m with measurements made through the OFR in the absence of oxidant and with measurements from a different nearby inlet at 1 m height. It was observed that the concentrations of MT, SQT, MBO+isoprene, and toluene+ p -cymene were

approximately 1.9, 5.9, 1.4, and 1.2 times higher in the canopy than at 25 m, respectively (discussed in Sect. S4). All analyses in this work were done using estimated in-canopy concentrations, which were inferred by applying these empirical relationships to the continuous 25 m inlet measurements. This scaling technique has been used before, producing similar results when applied to measurements during the summer 2010 BEACHON-ROCS campaign at the same field location (Kim et al., 2013; Wolfe et al., 2014).

Ambient SO₂ concentrations were measured using a Thermo Environmental Model 43C-TLE analyzer. Data were reported as 5 min averages from 6 different heights on a tower up to 25.1 m. We used only data measured at the 5 m height, to best match the height of the OFR on top of the trailer. The SO₂ instrument was automatically zeroed every 6 h, using scrubbed zero grade air. It was calibrated by a standard addition of 3 sccm of a 14 ppmv SO₂ in N₂ standard (Scott-Marrin) into the 3 slpm sample flow.

A novel thermal desorption electron impact mass spectrometer (TD-EIMS) was used to measure ambient concentrations of ensemble S/IVOCs with volatilities in the range of effective saturation vapor concentrations (C^*) of 10^1 - 10^7 $\mu\text{g}/\text{m}^3$. This method involved cryogenic collection of organic gases, temperature-programmed desorption into ultra-high-purity (UHP) helium, and measurement with a high-resolution time-of-flight mass spectrometer (Cross et al., 2013; Hunter et al., 2016). The TD-EIMS provided a time series of the gas-phase organic mass and composition in each volatility bin.

2.3 Results and discussion

2.3.1 OFR operation

Under typical operation, an OFR is used to study oxidation dominated by a single oxidant, similar to typical large chamber experiments. In the case of a field application (as in this study) the sample is a complex and time-varying mixture of ambient precursors that enter the OFR. Importantly, the OH:O₃:NO₃ oxidant ratios produced within the OFR are generally not the same as the changing ambient

ratios. Therefore SOA formation in the OFR does not, and is not meant to, reproduce in situ ambient SOA formation at each point in time. In other words, the OFR can be used as a tool to determine the amount of SOA from a single oxidant that would form upon oxidation of ambient gases (both identified and unidentified) at any time of day.

Typical OFR operation of OH oxidation using the OFR185 method is illustrated in Fig. 2.2, by an example of the evolution of OA and SO₄ aerosol mass concentrations as OH concentration was cycled through the range of eq. ages. As age increased over the first few lamp settings, OA mass increased due to production and condensation of low volatility species from the oxidation of gas-phase SOA precursors. SO₄ mass remained nearly the same as in ambient air for these lower ages. The increase of SOA mass at lower ages compared to SO₄ is thought to be due to the different rate constants for reaction of OH. The rates with biogenic VOCs, e.g., $k_{OH} = 5.3 \times 10^{-11} \text{ cm}^3 \text{ molec}^{-1} \text{ s}^{-1}$ for α -pinene (Atkinson and Arey, 2003), are generally much faster than the reaction of OH with SO₂, where $k_{OH} = 9.49 \times 10^{-13} \text{ cm}^3 \text{ molec}^{-1} \text{ s}^{-1}$ (Sander et al., 2011). As the eq. age continued to increase, OA mass enhancement decreased, eventually resulting in net OA loss. These high ages led to a lack of formation of SOA as well as heterogeneous oxidation of the preexisting OA, leading to fragmentation and evaporation (Ortega et al., 2016). The amount of SO₄ aerosol production increased with eq. age, and plateaued with no further production at ages above ~10 days. This behavior is consistent with theory, since SO₂ has a lifetime of ~8 days with respect to oxidation by OH (Sander et al., 2011). Also, as expected, SO₄ aerosol (and H₂SO₄ gas) was not consumed by excess OH_{exp} in the same way as OA (and SOA precursor gases).

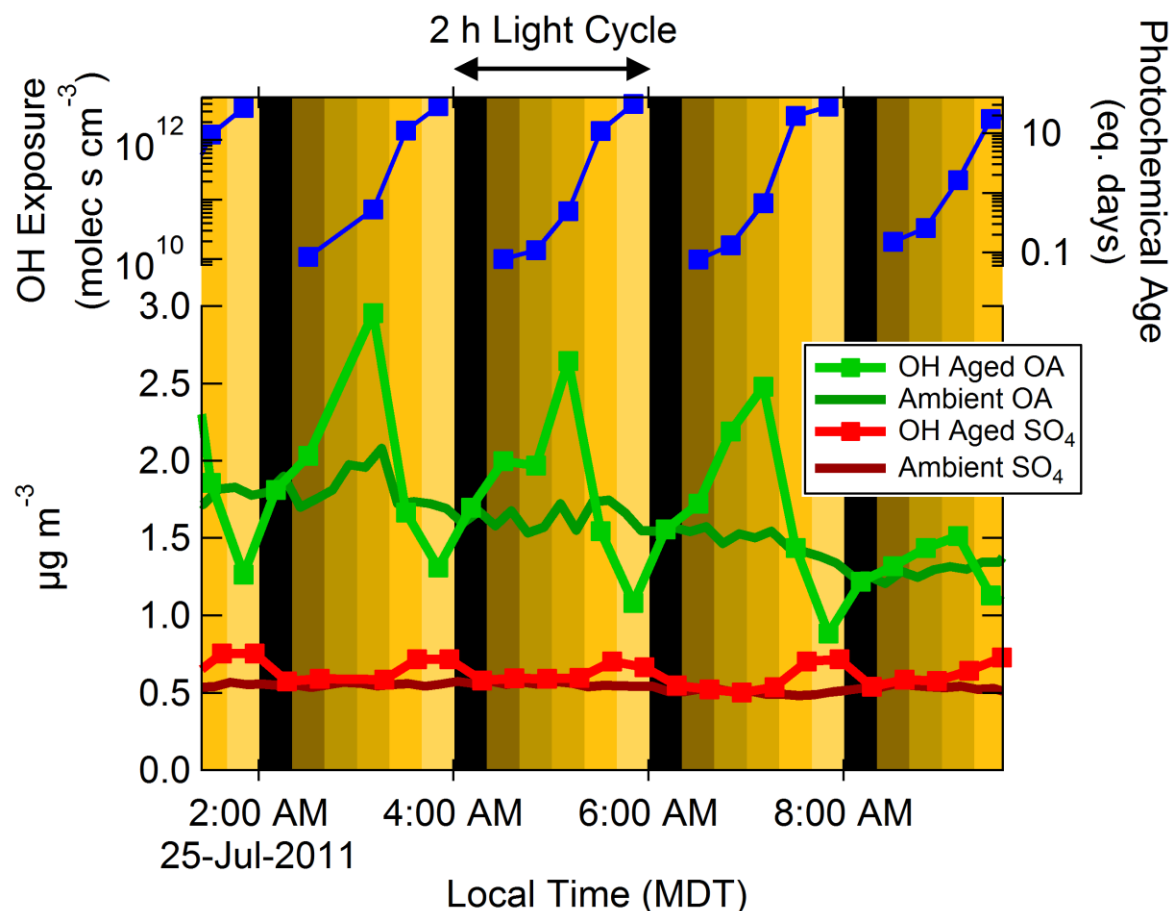


Fig. 2.2. Continuous cycling of OH oxidation using the OFR185 method, compared to concurrent ambient measurements. The sawtooth pattern in the OFR results from OA mass enhancement at low–intermediate OH exposure (OH_{exp}) and decreases at the highest photochemical ages. SO_4 mass increased monotonically with OH_{exp} and at higher exposures, as expected from relatively slow $\text{SO}_2 + \text{OH}$ oxidation and lack of OH destruction of SO_4 .

2.3.2 VOC enhancement/depletion vs eq. age

VOCs were measured before (in ambient air) and after OH oxidation in the OFR using a PTR-TOF-MS. This showed which VOCs were being depleted, potentially to form SOA, as well as which products were being formed. Also, the decay of VOCs after oxidation provided a direct measurement for validation of the model-derived age estimates. A number of likely compounds have been identified based on measurements from previous campaigns at the Manitou Experimental Forest Observatory site (Kim et al., 2010; Kaser et al., 2013b), as listed in Table 2.2.

Table 2.2. List of prominent compounds detected by PTR-TOF-MS in the OFR. Likely compound identifications are taken from previous measurements at the same research site, described in Kim et al. (2010) and Kaser et al. (2013b).

Protonated molecular formula	Likely compound(s)	Exact mass (<i>m/z</i>)
CH ₂ O-H ⁺	formaldehyde	31.02
CH ₄ O-H ⁺	methanol	33.03
C ₂ H ₄ O-H ⁺	acetaldehyde	45.03
CH ₂ O ₂ -H ⁺	formic acid	47.01
C ₃ H ₆ O-H ⁺	acetone	59.05
C ₂ H ₄ O ₂ -H ⁺	acetic acid	61.03
C ₅ H ₈ -H ⁺	MBO(~80%)+isoprene(~20%) ^a	69.07
C ₇ H ₈ -H ⁺	toluene(74%)+ <i>p</i> -cymene(26%) ^b	93.07
C ₁₀ H ₁₄ -H ⁺	<i>p</i> -cymene	135.12
C ₁₀ H ₁₆ -H ⁺	MT	137.13, 81.07
C ₉ H ₁₄ O-H ⁺	nopinone	139.11
C ₁₀ H ₁₄ O-H ⁺	pinonaldehyde(-H ₂ O), caronaldehyde(-H ₂ O)	151.11
C ₁₀ H ₁₆ O-H ⁺	camphor+ α -pinene oxide	153.13
C ₁₅ H ₂₄ -H ⁺	SQT	205.20

^a(Karl et al., 2012; Kaser et al., 2013a)

^b(Kaser et al., 2013a)

For an overview of PTR-TOF-MS measurements, the difference mass spectrum and mass defect (exact mass minus nominal mass) plots for 4 eq. hours of aging during nighttime are shown in Fig. 2.3. The greatest absolute magnitude of depletion in oxidized air compared to ambient nighttime air was observed for MT. Depletion was also observed for toluene+*p*-cymene, MBO+isoprene, SQT, pinonaldehyde+caronaldehyde, and camphor+ α -pinene oxide. Notably, formation of nopinone was observed after 4 eq. hours of aging. OH oxidation also led to substantial production of several relatively small oxidation product molecules, including formaldehyde, acetaldehyde, formic acid, acetone, and acetic acid, which have been commonly observed in similar photooxidation experiments (e.g., Lee et al., 2006; Ortega et al., 2013). Many other unidentified molecules were observed to be produced in smaller concentrations as a result of OH oxidation in the flow reactor. A similar plot is shown for higher eq. age

(7 days) in Fig. S9, for comparison to Fig. 2.3. At such a high age, species such as MT, SQT, and toluene+*p*-cymene were completely depleted, while many small oxidation products increased as much as 5-fold.

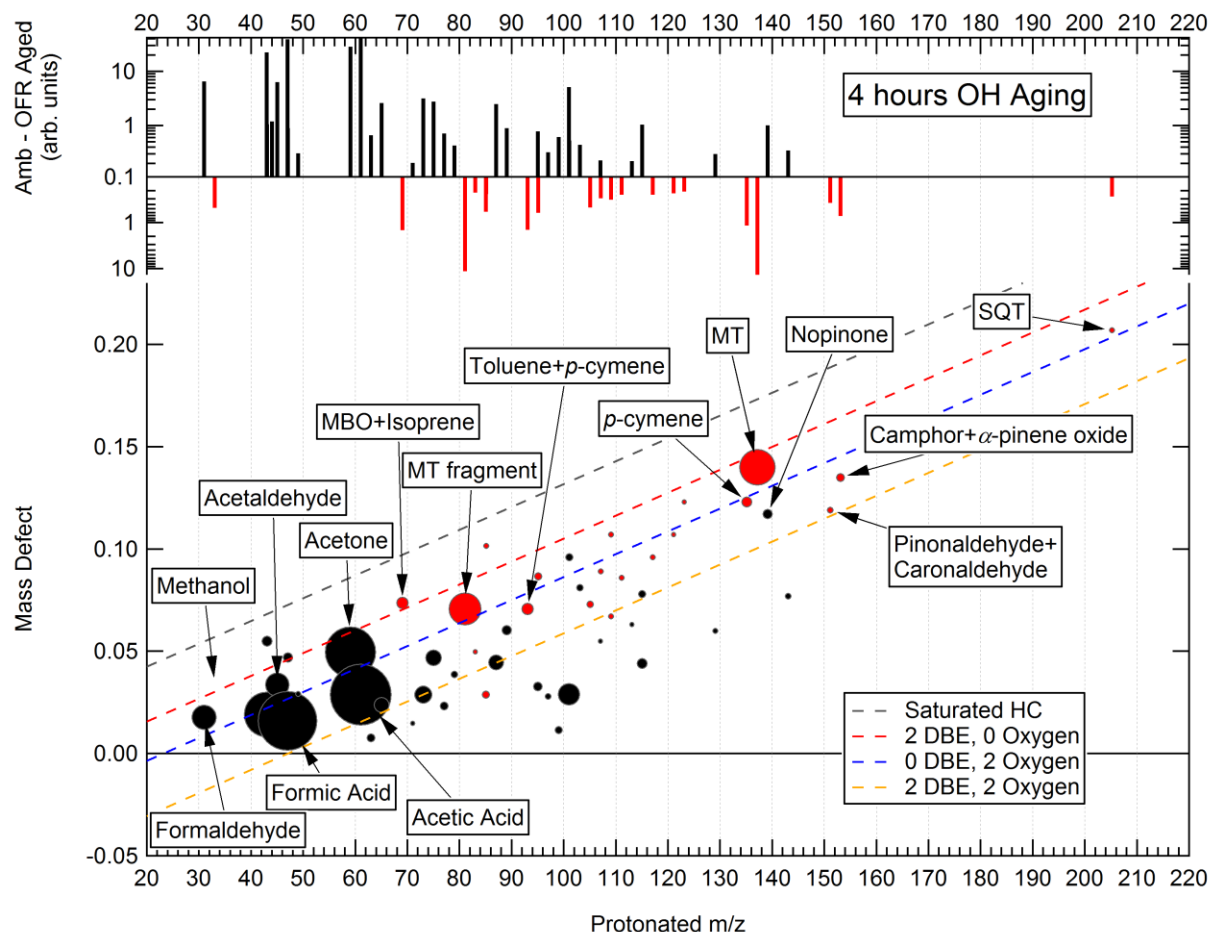


Fig. 2.3. The absolute changes (signal after OH oxidation in the reactor minus ambient signal) of molecules measured by the PTR-TOF-MS after 4 hours of eq. aging using the OFR185 method, shown as a difference mass spectrum and in a mass defect diagram. The mass spectra are 10-min averages (5 min from each of the two sample cycles used). The background-subtracted signals are shown in arbitrary units, not corrected for differences in sensitivity of each compound due to the large number of compounds and the inability to positively identify all of them. Prominent molecules are labeled by name or elemental formula assignments. Dashed lines representing molecules with varying double bond equivalents (DBE) or number of oxygen atoms are shown for reference. A red marker signifies that the signal decreased due to oxidation, while a black marker indicates where signal was greater after oxidation. The markers are sized by the square root of the absolute change in signal at each peak after oxidation (i.e., marker area is proportional to signal). Minor signals with absolute change of <0.2 arb. units or change of <20% of total ambient signal were removed.

In general for all degrees of oxidation, molecules with higher positive mass defects (corresponding to more chemically reduced species such as hydrocarbons) were depleted. Conversely, molecules with lower mass defect (more oxygenated compounds) were formed. This trend is consistent with what would be expected from gas-phase or heterogeneous OH oxidation chemistry. Also, Fig. 2.3 shows that monoterpenes constituted the majority of VOCs measured by the PTR-TOF-MS that were depleted after oxidation, while other compounds associated with terpenoid emissions and/or oxidation products were consumed or produced in smaller concentrations.

The relative changes of each of the compounds discussed above are shown as a function of OH_{exp} in Fig. 2.4. As previously discussed, nopinone is an example of a compound that increased in concentration at 4 hours eq. age, indicating that it was an oxidation product in the OFR. This signal showed net formation at low ages (earlier than the peak of maximum SOA formation in the OFR) and eventually decreased to net loss at high exposures, as expected due to its reactivity with OH. Fig. 2.4 also shows the net decay of several other terpene-related species and the formation of smaller, more volatile oxidation products as OH_{exp} increased. While the MBO+isoprene signal showed a substantial increase with increasing age, this is likely due to production of an isomeric interference, e.g., a fragment of an oxidation product.

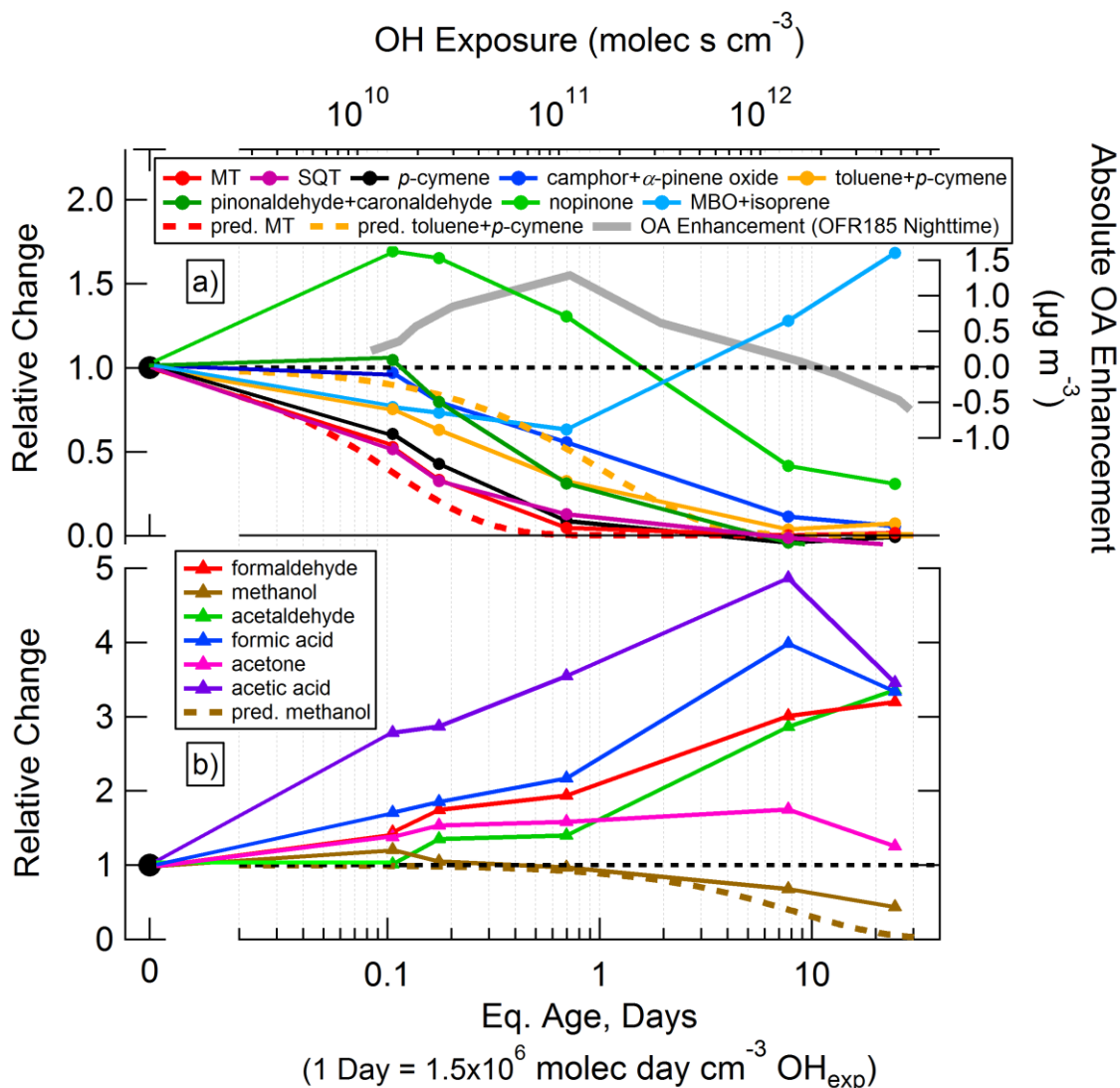


Fig. 2.4. Relative changes in prominent PTR-TOF-MS compounds as a function of photochemical age using the OFR185 method: a) toluene+*p*-cymene and terpene-related signals compared to nighttime OA enhancement using the OFR185 method (not LVOC fate corrected), and b) oxidation products formed in the OFR. For comparison, dashed lines indicate theoretical depletion of an equal mix of of α -pinene, β -pinene, and 3-carene (the three major MT at this site; Kim et al., 2010; Ortega et al., 2014), a 74:26 mix of toluene+*p*-cymene (Kaser et al., 2013a), and methanol.

An assessment of the reasonableness of the model-derived OH_{exp} (including the factor of two decrease discussed in Sect. 2.2) can be made by comparing the measured depletion of gases vs. expected depletion using published reaction rates with OH. This comparison is shown for an average speciated MT mixture, toluene+*p*-cymene, and methanol in Fig. 2.4. The MT and methanol signals decay slower than predicted, while the toluene+*p*-cymene signal decays slightly faster. These results are

consistent with the previous evaluation of the model-predicted OH_{exp} for laboratory and field studies (Li et al., 2015). Determination of OH_{exp} in the OFR is limited by many factors, including model uncertainties (Peng et al., 2015), the true non-plug-flow residence time distribution in the OFR, the difficulty of measuring a difference of signals using the PTR-TOF-MS in a perturbed environment, the possibility of competing production of the measured compounds (e.g., methanol), interferences and/or false identification of measured signal (e.g., fragments or different species with the same elemental composition interfering with the measured ions), and uncertainty in the relative composition of the MT and toluene+*p*-cymene mixtures. Despite these uncertainties, the PTR-TOF-MS is clearly measuring formation and decay of compounds that react with OH on the time scale of several hours of photochemical age. This is strong evidence that the OFR can be used to study a wide range of atmospherically-relevant time scales.

2.3.3 Fate of condensable gases in an OFR

2.3.3.1 Modeled Low-volatility organic compound (LVOC) Fate

In order to properly interpret SOA formation as a function of age in an OFR, the time scales of various competing processes need to be carefully considered in the context of the relative importance of those processes in the OFR vs the atmosphere. When organic gases are oxidized in the OFR, they can form LVOCs, a term used here to describe organic gases with volatilities that are low enough to (effectively) irreversibly condense onto particles or surfaces. In the atmosphere, the dominant fate of these LVOCs is to condense onto aerosols (lifetime of ~minutes), as dry and wet deposition of even fast-depositing species are generally slower sinks (lifetime of ~hours; Farmer and Cohen, 2008; Knote et al., 2015; Nguyen et al., 2015). However, due to the different time scales, the LVOCs formed in the OFR can have other fates besides condensation onto aerosols. These include condensational loss to the walls of the OFR, further reaction with OH to produce either condensable or non-condensable gas-phase products, or exiting the reactor in the gas-phase (where they will almost entirely condense on the

sampling tube walls, due to the large surface-area-to-volume ratio). If the LVOCs condense onto aerosols, then they are measured by the AMS+SMPS. However, if they are subject to one of the other three fates, then the AMS + SMPS measurements would underestimate the amount of SOA that would form in the atmosphere at the same level of OH exposure. Similar to loss of gases to large Teflon chamber walls (e.g., Matsunaga and Ziemann, 2010), these other three fates are experimental limitations of the OFR technique that need to be corrected in order to relate OFR measurements to real atmospheric SOA formation processes. As mentioned above, this correction takes into account that dry deposition of such LVOCs is not competitive with condensation onto particles in the atmosphere (Knote et al., 2015; Nguyen et al., 2015). Note that this section pertains to gas-phase losses, while a correction for particle losses to the OFR walls was also included as described in Sect. S3. The need for an LVOC correction to OFR measurements has been suggested before (Lambe et al., 2011a, 2015), but to our knowledge this work is the first attempt to apply one.

In this analysis, we calculate approximate lifetimes of LVOCs for condensation onto aerosols (τ_{aer}), loss to the walls of the OFR (τ_{wall}), and reaction with OH (τ_{OH}) as a function of OH_{exp} . Some semivolatile species (SVOC) will likely also be produced. However, we focus on irreversibly condensing LVOCs, both for simplicity and based on the observation that most of the OA has low volatility at this site, according to thermal denuder measurements (Hunter et al., 2016), and consistent with measurements at other locations (Cappa and Jimenez, 2010; Lopez-Hilfiker et al., 2016). If the low volatility of OA is a result of condensation of SVOC followed by fast particle-phase reactions to produce low-volatility species, then the distinction between LVOC and SVOC would be irrelevant for this analysis. The lifetimes of LVOCs against different processes are estimated as follows:

- τ_{aer} : Following Pirjola et al. (1999), the lifetime for LVOC condensation onto aerosols was calculated as

$$\tau_{aer} = \frac{1}{4\pi \cdot CS \cdot D} \quad (1)$$

with a diffusion coefficient $D = 7 \times 10^{-6} \text{ m}^2 \text{ s}^{-1}$ representative of an oxidized organic molecule with a molecular weight of approximately 200 g mol^{-1} at the field site ambient pressure (Tang et al., 2015). CS is the “condensational sink”

$$CS = \int_0^{\infty} r\beta(r)N(r)dr \quad (2)$$

which is the integral of the first moment of the particle size distribution, where r is the wet particle radius, $N(r)$ is the particle number size distribution, and

$$\beta(r) = \frac{Kn+1}{0.377Kn+1+\frac{4}{3}\alpha^{-1}Kn^2+\frac{4}{3}\alpha^{-1}Kn} \quad (3)$$

is the Fuchs-Sutugin correction for gas diffusion to a particle surface in the transition regime, calculated using the sticking coefficient α of the condensing species (Seinfeld and Pandis, 2006). CS was calculated using the average of the size distributions of ambient air entering the OFR and of air exiting the OFR after oxidation, as a best approximation of the actual CS experienced by LVOCs in the OFR. Since LVOC condensation in the OFR took place under ambient RH, the dried SMPS particle size distribution measurement was corrected to account for the increase in CS from hygroscopic particle growth as a function of RH. For each data point, a growth factor (gf) was calculated from the equation

$$\kappa = \sum \varepsilon_i \kappa_i = (gf^3 - 1)(1 - a_w)a_w^{-1} \quad (4)$$

from Petters and Kreidenweis (2007) and Nguyen et al. (2015), where ε_i is the volume fraction of aerosol species i , κ_i is the hygroscopicity parameter of aerosol species i , κ is the hygroscopicity parameter of the total aerosol, and a_w is water activity. We approximate a_w as being equal to RH, between 0 and 1. Total κ was estimated using $\kappa_{OA} = 0.13$ as previously reported for this site and campaign (Levin et al., 2014) and $\kappa_{inorganic} = 0.6$, using the volume mixing rule (Petters and Kreidenweis, 2007). The volume fractions were calculated from AMS measurements in ambient air or after OFR oxidation, using estimated component densities (Salcedo et al., 2006; Kuwata et al., 2012). The gf ranged between 1 and 2.3 with an average of 1.2. It was applied to the dry SMPS particle diameter before calculating CS . The correction $\beta(r)$ is a function of the Knudsen number

$$Kn = \frac{\lambda_g}{r} \quad (5)$$

where λ_g is the mean free path of the condensing gas. Based on previous modeling and measurements, we assume $\alpha = 1$ for LVOCs (Kulmala and Wagner, 2001; Julin et al., 2014; Krechmer et al., 2015). A sensitivity study on the values of D , the impact of deviations from $\alpha = 1$, and the choice of SMPS size distribution used to calculate CS is discussed below in Sect. 3.6.3.

- τ_{wall} : Following McMurry and Grosjean (1985), we estimate the first-order rate of LVOC loss to the walls of the OFR limited by eddy diffusion as

$$k_{wall} = \frac{1}{\tau_{wall}} = \frac{A}{V} \cdot \frac{2}{\pi} \cdot \sqrt{k_e D} \quad (6)$$

which is the version of this equation that is valid when α is sufficiently large (i.e., greater than $\sim 10^{-5}$). We used the measured OFR surface-area-to-volume ratio of $A/V = 25 \text{ m}^{-1}$ and a coefficient of eddy diffusion $k_e = 0.0036 \text{ s}^{-1}$ (much faster than the coefficient D estimated above), estimated by extrapolating values given in McMurry and Grosjean (1985). The choice of k_e is included in the sensitivity analysis in Sect. 3.6.3. Equation (6) results in an estimated wall loss rate of 0.0025 s^{-1} ($\tau_{wall} = 400 \text{ s}$), similar to the lifetime of $\sim 600 \text{ s}$ estimated for this type of OFR in Lambe et al. (2011a). In the absence of any CS and oxidant, an upper limit of approximately 30% of LVOCs would be lost to the walls and the balance would exit the reactor and be lost to the tubing walls. When including this campaign's average integrated dry particle surface area of $63 \mu\text{m}^2 \text{ cm}^{-3}$ (with number mode at $\sim 50 \text{ nm}$) in the calculation, the percentage lost to the walls decreases by only a few percent to 26%. If using an integrated particle surface area of $500 \mu\text{m}^2 \text{ cm}^{-3}$ that might be found in an urban, pollution source, or lab study, the percentage drops to 15%.

- τ_{OH} : To estimate the loss of LVOCs to non-condensable products due to continued reaction with OH, τ_{OH} , we make the assumption that LVOCs will remain available to condense on aerosols, walls, or exit the reactor for up to 5 generations of OH reaction. After they have reacted 5 times with OH, they are deemed lost by fragmentation into small oxidized molecules that are too volatile to condense. Further, we assume a rate constant for reaction with OH (of the order of that for an oxygenated molecule with

ten carbon atoms and no C=C double bonds) of $k_{OH} = 1 \times 10^{-11} \text{ cm}^3 \text{ molec}^{-1} \text{ s}^{-1}$ (Ziemann and Atkinson, 2012), so

$$\tau_{OH} = \frac{5}{k_{OH} \cdot [\text{OH}]} \quad (7)$$

Sensitivity studies for variations in parameters k_{OH} and the number of reactions with OH before LVOCs fragment to non-condensable products are also discussed in Sect. 3.6.3.

These three lifetimes are combined to determine the total lifetime of loss of LVOCs to these three combined pathways,

$$\tau_{total} = \left(\frac{1}{\tau_{aer}} + \frac{1}{\tau_{wall}} + \frac{1}{\tau_{OH}} \right)^{-1} \quad (8)$$

This total lifetime is compared to the average OFR residence time τ_{OFR} (OFR volume divided by flow rate) to determine the fraction of LVOCs that exits the OFR without reaching one of the three other fates (and thus condenses onto sampling line walls),

$$F_{exit} = e^{-\frac{\tau_{OFR}}{\tau_{total}}} \quad (9)$$

The fraction of LVOCs that is lost to each pathway inside the OFR is then

$$F_x = (1 - F_{exit}) \cdot \left(\frac{k_x}{k_{total}} \right) \quad (10)$$

where the rate constant $k_x = \tau_x^{-1}$ and $x = \text{wall, OH, or aerosol (aer)}$.

Figure 2.5c compares all of the LVOC lifetimes and fractional fates as a function of age and OH_{exp} , with a typical OFR residence time of 140 s shown for comparison. The fractional fates are shown using high (Fig. 2.5a) and low (Fig. 2.5b) rates of condensation to aerosol, based on typical higher and lower aerosol surface areas during this particular campaign. As discussed below (Sect. 2.3.5), OH oxidation leads to a substantial increase in the number of small particles when gas-phase precursors are available. This in turn increases the surface area available for condensation of LVOCs, and therefore τ_{aer} depends on the amount of SOA formed from OH oxidation in the OFR in addition to the ambient particle surface area. During times of low SOA formation ($<0.3 \mu\text{g m}^{-3}$), total dry surface area concentrations

after oxidation are similar to ambient concentrations in the range of $30\text{-}100\ \mu\text{m}^2\ \text{cm}^{-3}$, and τ_{aer} is estimated to be approximately 400 s or longer. However, during times with $>1.5\ \mu\text{g}\ \text{m}^{-3}$ SOA formation, total dry surface area concentrations increase to $100\text{-}400\ \mu\text{m}^2\ \text{cm}^{-3}$ or larger and τ_{aer} becomes <100 s.

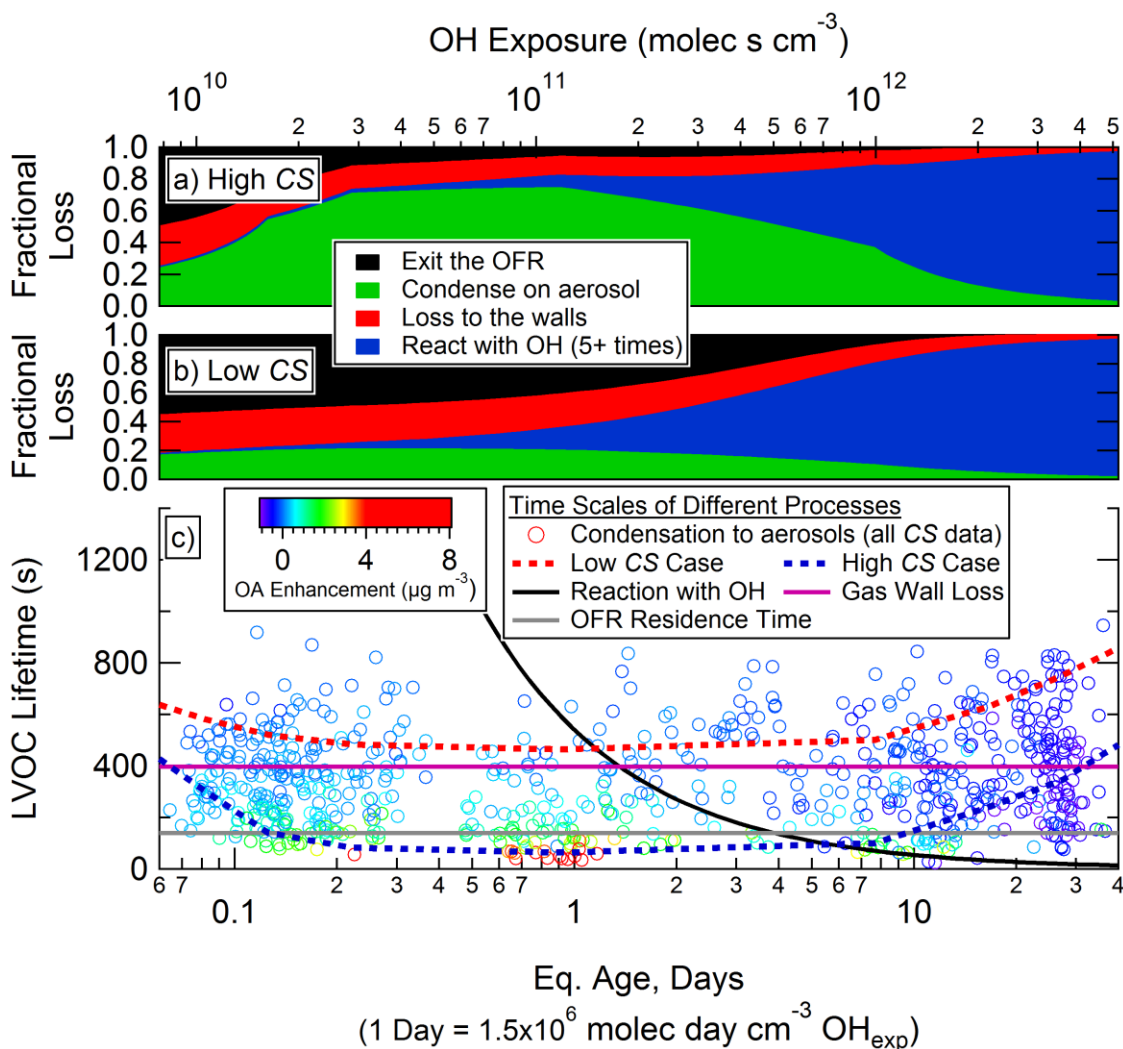


Fig. 2.5. Fractional fates of loss of LVOCs to OFR walls, condensation to aerosols, reaction with OH to produce volatile products, or exiting the OFR to be lost on sampling line walls as a function of photochemical age for a) high CS and b) low CS cases; c) LVOC lifetimes for each of these pathways. Lifetime for condensation to aerosols is shown for all data points (colored by OA enhancement after oxidation) using CS calculated from SMPS measurements.

For an eq. age of 0.1 day, as little as 20% of the LVOCs formed in the OFR are predicted to condense onto aerosols, with the rest being lost to the walls in or after the OFR. However, the majority of LVOCs are likely not produced until higher OH_{exp} , concurrent with the highest SOA production. As eq. age increases into the 0.2-3 day range, condensation onto aerosols can account for as much as 75% of

LVOC fate, provided there is enough SOA formation to sufficiently increase the total particle surface area. In this case, shown in Fig. 2.5a, the remaining 25% of LVOCs are approximately equally split between loss to the walls, exiting the OFR, and reacting with OH >5 times. However if sufficient particle surface area is not formed, as in Fig. 2.5b, then still only 20% of LVOCs will condense onto aerosols.

For the conditions analyzed here from the BEACHON-RoMBAS campaign, these calculations suggest that when there were enough gas-phase precursors to produce $>1.5 \mu\text{g m}^{-3}$ SOA, it is likely that the majority of this aerosol (up to $\sim 75\%$) would be produced and measured in the OFR despite the perturbed time scales. When there were relatively few gas-phase precursors and little SOA was formed, it is likely that a majority of the LVOCs were not able to condense into SOA during the reactor residence time. However, if there were few precursors to begin with, the absolute amount of potential SOA mass that would not have time to condense would still be relatively small, limiting the effect of this correction on the objectives of this study.

Another important conclusion from this analysis is that for high eq. ages >10 days, a very small fraction of the LVOC formed ($<10\%$) will condense to form new SOA. The remainder will react many times with OH before having a chance to condense, likely leading to smaller fragmentation products that are too volatile to condense into SOA. This is, of course, different from what occurs in the atmosphere, where LVOCs would typically have sufficient time for condensation to aerosols under most conditions. Since this rapid oxidation will remove any semi-volatile vapors from the gas phase, semi-volatile OA molecules will begin to evaporate to reestablish equilibrium partitioning. However, measurements of evaporation kinetics for ambient and lab-generated SOA suggest that evaporation is too slow to account for the changes measured during the short OFR residence time (Vaden et al., 2011). Furthermore, thermodenuder measurements have shown that only a small fraction ($\sim 20\%$) of ambient OA would be susceptible to evaporation due to removal of the gas phase molecules (Cappa and Jimenez, 2010; Ortega

et al., 2016). Therefore, heterogeneous oxidation of the preexisting OA by OH likely dominates the measured OA depletion at very high eq. ages (DeCarlo et al., 2008; Ortega et al., 2016).

2.3.3.2 Model validation: sulfuric acid (H₂SO₄) condensation

In addition to LVOCs, H₂SO₄ can also be produced in the OFR from OH oxidation of SO₂. H₂SO₄ molecules can also condense onto OFR or sampling line walls (but not be lost to further reaction with OH). These limitations of the OFR technique need to be corrected in order to relate OFR measurements to real atmospheric processes. H₂SO₄ formation is an analogous yet much simpler system compared to LVOC formation, so it can be used to validate the LVOC fate model. If the H₂SO₄ condenses onto aerosols, it will be measured as SO₄ aerosol by the AMS. SO₄ aerosol formation in the OFR was predicted by using estimated OH_{exp} to calculate how much ambient SO₂ would be oxidized into H₂SO₄. The LVOC fate model was then used to determine F_{aer} , F_{wall} , and F_{exit} for H₂SO₄, while F_{OH} was set equal to zero since gas-phase H₂SO₄ will not continue to react with OH to produce volatile fragments. We used $D = 1 \times 10^{-5} \text{ m}^2 \text{ s}^{-1}$ for an H₂SO₄ molecule hydrated by H₂O molecules in the gas phase at the relevant ambient pressure and humidity (Hanson and Eisele, 2000), and the best-fit value of $\alpha = 0.65$ from Pöschl et al. (1998). An additional minor correction was applied to account for the fact that the SO₂+OH reaction is relatively slow, so the effective τ_{OFR} for H₂SO₄ molecules in the reactor can be less than the full OFR residence time depending on OH_{exp}. Using the model results, the fraction of H₂SO₄ that does not condense onto aerosol was corrected for by dividing the newly produced SO₄ mass measured with the AMS by F_{aer} .

The measured vs. predicted SO₄ enhancement after OH oxidation in the OFR using the OFR185 method is shown in Fig. 2.6. The AMS measured 61% of the predicted SO₄ enhancement. After applying the correction for H₂SO₄ wall and sampling line losses as described in the previous paragraph, the measured and predicted SO₄ enhancements agreed well with a slope of 0.81, and R² slightly increased from 0.80 to 0.85. To illustrate the sensitivities of this model to key uncertain parameters, namely the

effects of using the range of $\alpha = 0.43-1$ given in Pöschl et al. (1998) and using the size distributions before or after oxidation in the OFR (as lower and upper bounds of CS) are illustrated in Fig. S10. Generally, the amount of SO_4 formed after applying the H_2SO_4 wall and sampling line loss correction was consistent with the expected amount within the uncertainties. The amount of scatter introduced by applying the correction was larger when the amount of SO_4 produced (and predicted) was close to zero, when the F_{aer} correction factor was less than ~ 0.3 . This suggests that the LVOC fate model becomes more uncertain when the correction factors are large and F_{aer} is close to zero. However, this analysis demonstrates that a correction can be successfully applied for H_2SO_4 condensation, and that a similar correction should also be applied for LVOC condensation to accurately interpret the results of SOA formation in an OFR.

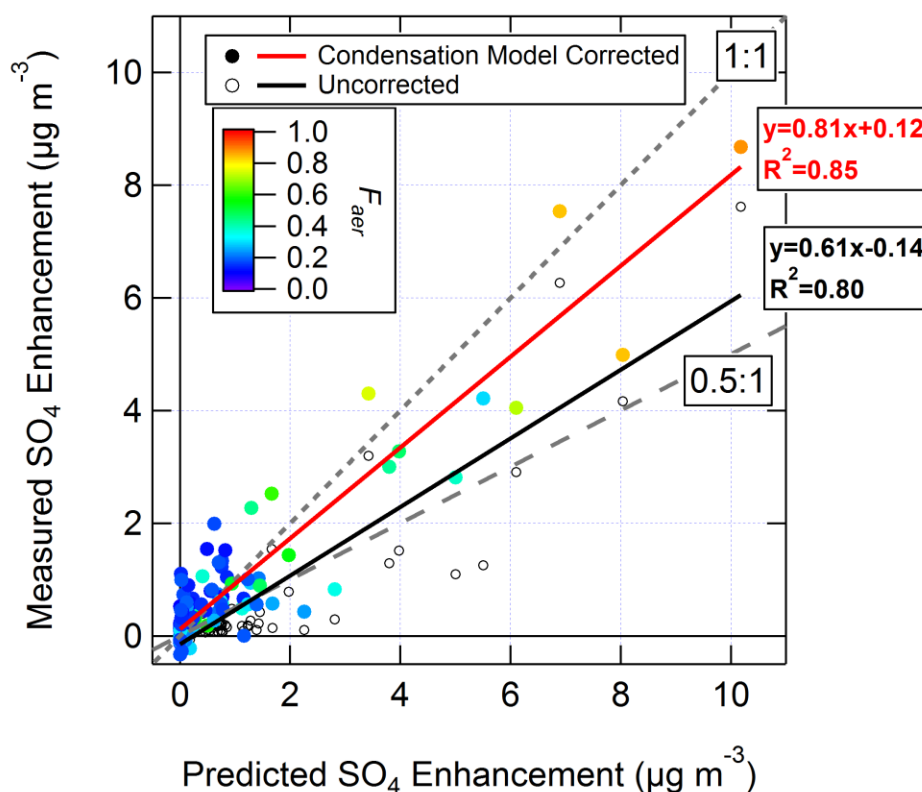


Fig. 2.6. Measured vs. predicted SO_4 formation after OH oxidation in an OFR. The data points are colored by the fraction of H_2SO_4 predicted to condense on aerosols, calculated using $\alpha = 0.65$ and the average of the SMPS size distributions measured before and after oxidation. Data are shown with the LVOC fate correction applied, along with linear fits to the corrected (red) and uncorrected (black) data. Ambient SO_2 concentrations < 0.2 ppb have been excluded from this analysis.

In the subsequent analyses, SOA formation is presented both with and without applying a correction to account for incomplete LVOC condensation to aerosol in the reactor. The correction, hereafter referred to as the “LVOC fate correction,” is applied by dividing the amount of SOA mass formed by F_{aer} . The correction is only applied for data with eq. age < 5 days. At higher exposures, it becomes unfeasible to apply the correction, because dividing small SOA mass formation by small fractions of condensation on aerosol results in large uncertainties. Instead, only uncorrected data is shown for eq. age > 5 days, and it is interpreted as being dominated by heterogeneous oxidation.

2.3.4 SOA mass enhancement vs. OH_{exp}

Both the concentrations and relative fractions of ambient SOA precursor gases changed between day and night. They were dominated by MBO+isoprene (under ambient OH chemistry) during the day, and by MT+SQT (under ambient O_3/NO_3 chemistry) at night (Fry et al., 2013). SOA will be formed in the OFR from these changing VOC mixtures and any other gases present in the ambient air that enters the reactor, so it might be expected that different amounts of SOA production would be observed during daytime vs. nighttime. Fig. 2.7 shows daytime and nighttime OA enhancement as a function of eq. age and OH_{exp} . During all times of the day, OA enhancement was largest in the range of 0.4–1.5 eq. days of photochemical aging, hereafter referred to as the age range of maximum OA enhancement. The diurnal profile of the OA enhancement in this range (inset of Fig. 2.7) shows that the maximum OA enhancement follows a pattern that is more nuanced than strictly daytime vs. nighttime, with a peak of SOA production in the early morning. Net loss of OA was observed above 10 eq. days of aging, consistent with the LVOC fate model and the interpretation that heterogeneous oxidation dominates at high eq. ages. This is also consistent with previous studies of heterogeneous OH oxidation of OA in a flow tube (George et al., 2008) and with results with the OFR in the Los Angeles urban area (Ortega et al., 2016).

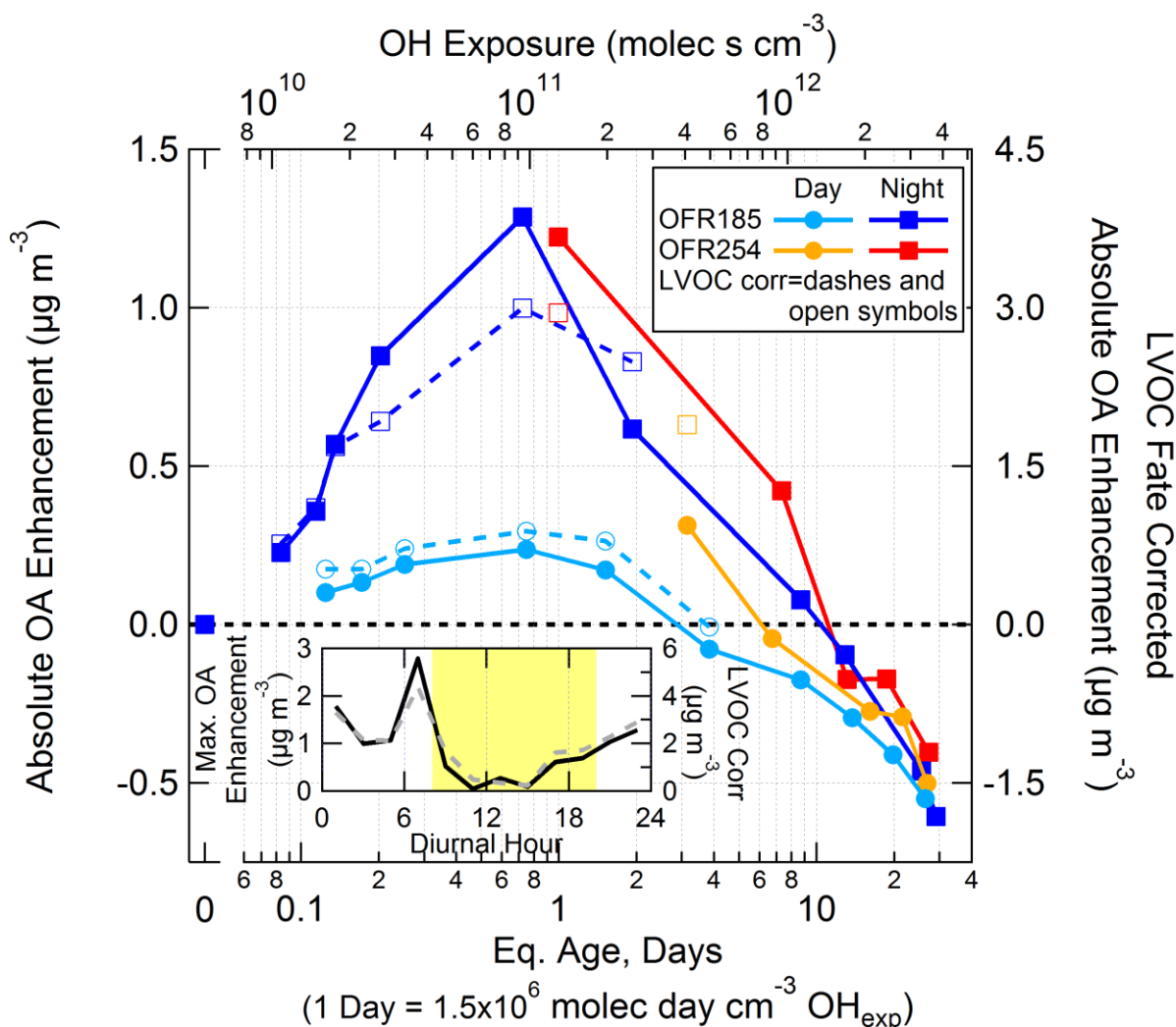


Fig. 2.7. Comparison of absolute OA enhancement from OH oxidation using the OFR185 and OFR254-70 methods, binned by photochemical age and separated into daytime (08:00–20:00 local time) and nighttime (20:00–08:00 local time) to reflect the changes in ambient SOA precursors between day and night. Data are shown with (right axis, open symbols, and dashed lines) and without (left axis, closed symbols and solid lines) the LVOC fate correction described in Sect. 3.3. Inset: the maximum OA enhancement (all data 0.4–1.5 days eq. age) as a function of time of day, with (dashed) and without (solid) the LVOC fate correction. OFR254-70 measurements with positive OA enhancement were multiplied by the ratio of ambient MT concentrations measured during OFR185 vs. OFR254-70 sampling periods (ratio = 1.8). Negative OA enhancements were not normalized in this way since the amount of mass lost due to heterogeneous oxidation would not necessarily correlate with ambient MT concentrations.

As shown in Fig. 2.7, OA enhancement shows a strong difference between daytime and nighttime. However, SOA formation potential in the OFR should not be a function of time of day itself. Rather, this is thought to be a coincidental dependence based on the SOA precursor gas concentrations

that change in a diurnal manner. In other words, this OH oxidation in the OFR is not meant to reproduce true ambient nighttime chemistry, rather it allows us to measure SOA formation from OH oxidation of the true mix of ambient gases as it evolves with time of day, including nighttime. In fact, the lack of ambient nighttime OH oxidation may help explain the increased SOA formation potential when nighttime air is oxidized by OH in the OFR.

These measurements were made in a pine forest dominated by MT (Ortega et al., 2014). As an alternative to separating by time of day, the data are separated by ambient MT concentrations in Fig. 2.8. The magnitude of SOA formation increased with ambient MT concentrations, ranging from no formation up to greater than $6 \mu\text{g m}^{-3}$ OA enhancement (up to $3 \mu\text{g m}^{-3}$ enhancement without the LVOC fate correction). For the range of ages with maximum OA enhancement (0.4–1.5 eq. days), a correlation is observed between OA enhancement and MT concentrations ($R^2=0.56$). Of course, MT may not be the only important precursors driving this correlation. Other gases that are correlated with MT, e.g. sesquiterpenes ($R^2=0.70$ with MT shown in Fig. S11) or MT reaction products, may also contribute to the observed correlations. Although MT emissions are strongest during daytime due to their positive temperature dependence, their concentrations are higher at night due to the shallower nighttime boundary layer and reduced oxidation rate (Kim et al., 2010).

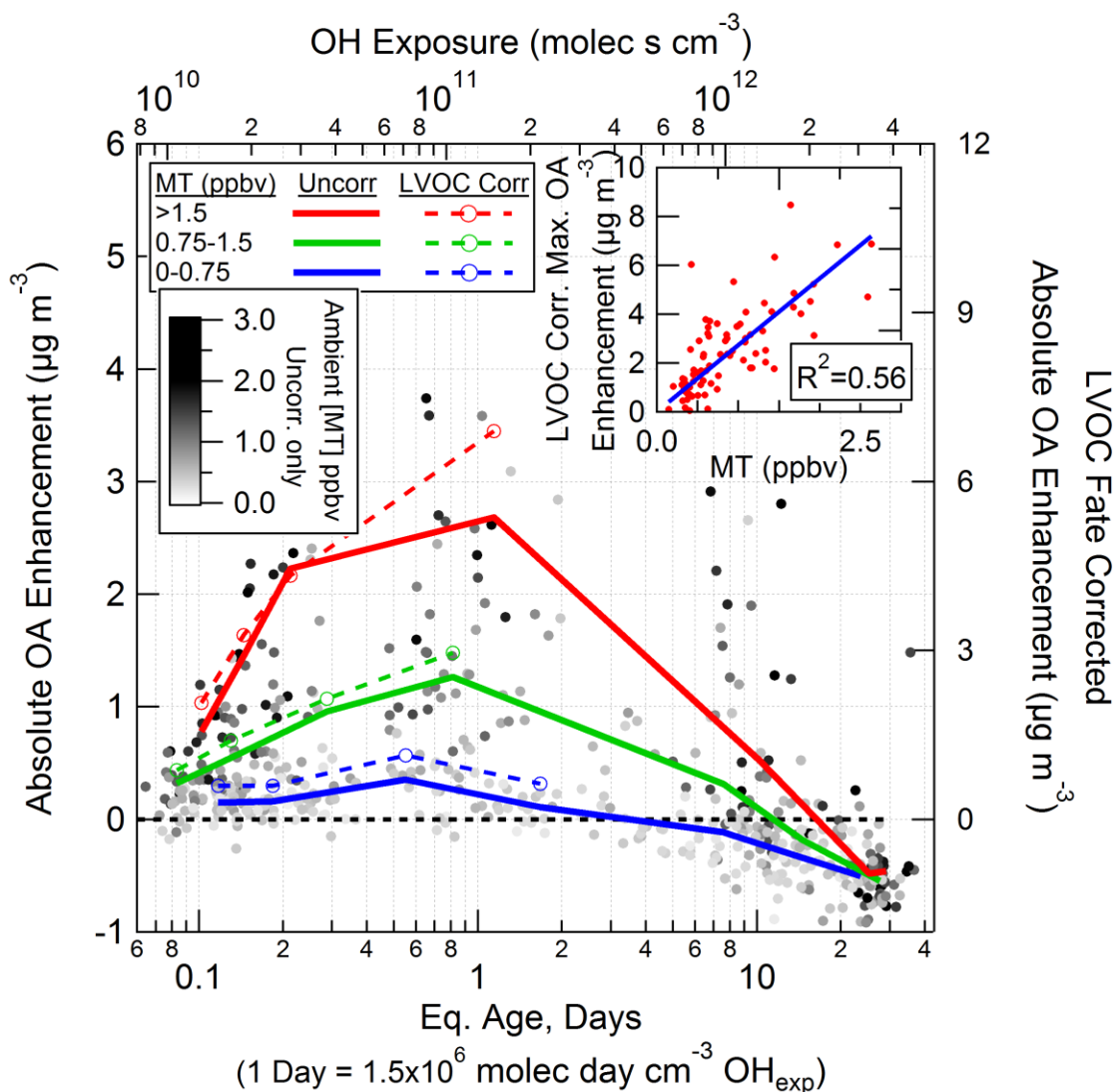


Fig. 2.8. OA enhancement from OH oxidation of ambient air using the OFR185 method as a function of photochemical age. All data points (uncorrected only) are shown, shaded by in-canopy monoterpene (MT) concentrations. Average OA enhancements of age quantiles with equal number of data points with (right axis, dashed lines) and without (left axis, solid lines) the LVOC fate correction are also shown, separated into low (0 to 0.75 ppbv), medium (0.75 to 1.5 ppbv), and high (>1.5 ppbv) ambient MT concentration ranges. The inset shows the correlation ($R^2=0.56$) between the LVOC fate corrected maximum OA enhancement (0.4–1.5 eq. days aging) and in-canopy MT concentrations.

We observed much less SOA formation during the daytime, when concentrations of MBO+isoprene peaked but MT concentrations were lower. We note that SOA formation mechanisms that involve heterogeneous uptake followed by multiphase reactions are not efficiently simulated by the OFR, as their time scales are not shortened proportionally to increased OH concentrations (Hu et al., 2016). This includes the IEPOX pathway from isoprene (Paulot et al., 2009) and the similar pathway

proposed for MBO (Zhang et al., 2012). While SOA formation from isoprene in an OFR has been demonstrated (Lambe et al., 2015), the total SOA formation potential from MBO + isoprene may be underestimated in our study.

OA enhancement from the OFR185 and OFR254-70 modes of operation are compared in Fig. 2.7. Because these were performed with the same physical reactor, we could only perform one of them at a time (see Fig. S7). Since ambient MT concentrations changed over the course of the campaign and they correlated with the amount of SOA formed in the reactor, this effect needed to be corrected before the results of the two reactor modes could be compared. The positive OA enhancement for the OFR254-70 data was multiplied by the ratio of average MT concentrations between the OFR185 and OFR254-70 periods (a factor of 1.8). From Fig. 2.7, we conclude that there were no major differences in the amount of SOA formation between the OFR185 and OFR254-70 methods over the range of ages measured in this campaign. Minor differences in SOA formation between the two methods are likely a result of limits on the ability to determine the proper eq. age (especially for low ages in OFR254-70 as discussed in Sect. 2.2.3) or due to real changes in ambient SOA precursor gases, since the measurements using each method were not simultaneous. Additional comparisons of both methods sampling the same air, carefully designed and controlled to more accurately determine low ages in OFR254-70, would be useful to further explore this issue. Since the OFR185 mode is experimentally simpler and does not require addition of O_3 (with associated issues of mixing, dilution, possible contamination, etc.), and since the OFR185 mode more faithfully simulates OH chemistry due to reduced O_3 concentrations (Peng et al., 2016b), we recommend the OFR185 mode of operation for future OFR studies of OH oxidation in forested areas.

2.3.5 Condensation vs. nucleation in the OFR

When gas-phase molecules are oxidized and achieve a low enough volatility, they can condense onto existing particles (or other surfaces) or nucleate/grow new particles. The difference can be

important experimentally because nucleation may produce some particles too small for the size range of the AMS, and it also increases surface area more efficiently than condensation to preexisting particles. Changes in the size distributions measured by the SMPS are used here to investigate the relative importance of these processes.

Particle volume size distributions of air oxidized over the full range of eq. photochemical ages in the flow reactor are shown in Fig. 2.9, during a period with relatively large OA enhancement in order to clearly demonstrate the behavior. OH oxidation in the reactor resulted in substantial new particle formation and growth, as well as growth of the preexisting ambient particles. The maximum enhancement in both particle modes occurred at an eq. age of ~ 1 day, consistent with AMS measurements of total mass enhancement. At higher ages, the new particle mode decreased in magnitude and diameter and eventually was not present at the highest ages. This is consistent with the results of the LVOC fate model, where at high eq. ages organic gases are rapidly oxidized into smaller volatile products that do not condense. The accumulation mode was also depleted at higher eq. ages, consistent with heterogeneous oxidation leading to fragmentation and evaporation of OA. The observed nucleation at lower eq. ages likely results from some combination of H_2SO_4 and extremely low-volatility organic compounds (ELVOCs; Kirkby et al., 2011; Ehn et al., 2014).

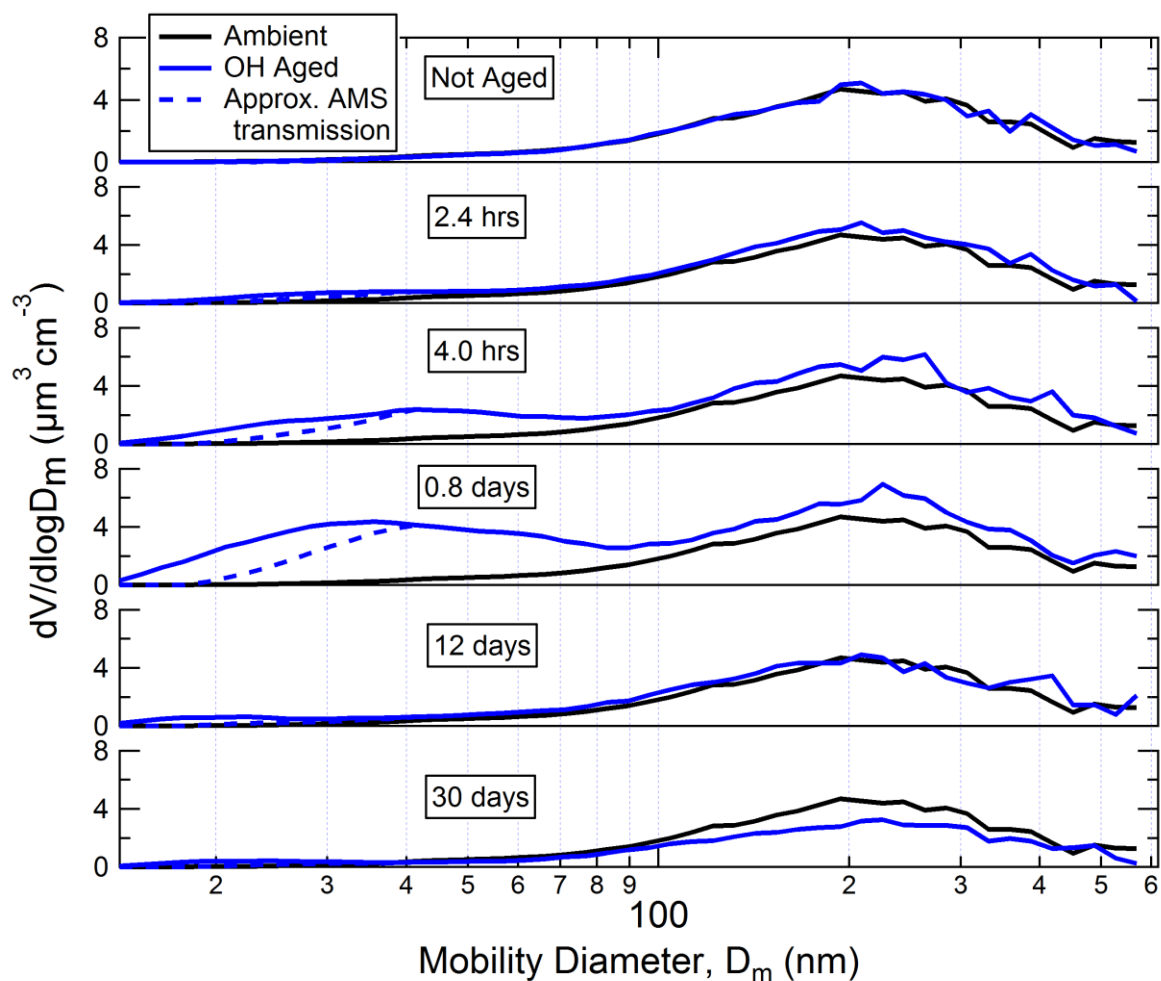


Fig. 2.9. SMPS volume size distributions after OH oxidation using the OFR185 method, labeled by photochemical age and compared to concurrent ambient measurements. Each of the 6 OH-aged size distributions is an average of 6 SMPS scans from the night of 28–29 July, when relatively large OA enhancement was observed and the ambient aerosol dry surface area was in the range of $80\text{--}100 \mu\text{m}^2 \text{cm}^{-3}$. Dashed lines represent the approximate size distributions that were transmitted through the AMS aerodynamic lens (for which a correction was applied to reported OA values as discussed in Sect. S3). Scans with large OA enhancement were used in order to more clearly illustrate the condensation vs. nucleation behavior in the OFR, so the AMS lens transmission correction in this figure appears larger than average. All scans have been corrected for small particle losses to sampling lines (Sect. S1).

For the data shown in Fig. 2.9, a larger fraction of SOA molecules condensed onto the freshly nucleated particle mode than onto the preexisting particles. This behavior likely depends on the availability and position of the CS in the size distribution. With the small aerosol concentrations during this campaign, the CS from the new small particles sometimes competed with the CS from ambient particles. During periods when the CS entering the OFR in ambient air was larger, it reduced the

condensation of SOA onto new particles, consistent with the lower importance of this mode for an OFR study in the Los Angeles area (Ortega et al., 2016). These results support the possibility of using flow reactors to study the potential for new particle formation and growth in different ambient airmasses and sources (Ezell et al., 2014; Chen et al., 2015a).

2.3.6 Sources of SOA in ambient air

2.3.6.1 SOA mass formed vs. mass predicted from VOCs

Many previous studies have measured the yields of SOA from oxidation of VOCs in chambers. Those experiments were generally performed under controlled conditions, with detailed information about the type and amount of VOCs available to form SOA at the beginning of the experiment. In this study, we also measured the yield of SOA from oxidation of organic gases, but in this case we started with a complex mixture of ambient organic gases, with some species not being directly measured or speciated. Therefore, the method used here provided a measure of the total SOA formation (or destruction) as a function of oxidant exposure from *all* ambient gases present, measured and unmeasured. The total SOA formation in the OFR was compared to the amount predicted from measured VOCs. SOA formation was predicted by applying low-NO_x, OA-concentration-dependent, chamber derived aerosol yields to the ambient VOC concentrations predicted to react in the OFR based on OH_{exp}. Estimated fractions reacted were >99% of ambient MT, SQT, and isoprene, and ~45% of toluene+*p*-cymene in the age range of 0.4–1.5 eq. days. The yields used to predict SOA formation were calculated for each individual data point as a function of the OA mass concentration measured after oxidation in the OFR, using the two- or four-product basis set parameterizations listed in Table 2.3 (Henze and Seinfeld, 2006; Tsimpidi et al., 2010). With an average post-oxidation OA concentration of 4.1 g m⁻³ with the LVOC fate correction applied, this resulted in campaign-average SOA yields of 12.5, 13.2, 13.8, and 3.2% for MT, SQT, toluene, and isoprene, respectively. Previous experiments have shown SOA yields from various precursor gases oxidized in the OFR to be of the same order as yields from large

environmental chambers (Kang et al., 2007, 2011, Lambe et al., 2011b, 2015). These yield values reflect the amount of SOA that forms after several generations of gas-phase oxidation of precursor gases. We do not include additional “aging” of the precursors through additional oxidation steps, as such parameterizations are not well-supported experimentally.

Table 2.3. Low-NO_x SOA yield parameters using basis sets, used to estimate SOA yields from VOCs in the OFR (Sect. 3.6.1).

SOA precursor	C* saturation vapor concentrations ($\mu\text{g m}^{-3}$ at 298K)			
	1	10	100	1000
MT ^a	0.107	0.092	0.359	0.600
SQT ^a	0.075	0.150	0.750	0.900
Toluene ^a	0.075	0.225	0.375	0.525
	C* saturation vapor concentrations ($\mu\text{g m}^{-3}$ at 295K)			
	0.6	116		
Isoprene ^b	0.0288	0.232		

^a(Tsimpidi et al., 2010), not including the chemical “aging” parameterization

^b(Henze and Seinfeld, 2006)

The comparison of maximum measured vs. predicted SOA formation in Fig. 2.10 shows that approximately 4.4 times more SOA was formed than predicted from MT, SQT, toluene+*p*-cymene, and isoprene. If the LVOC fate correction is not applied, still 3.1 times more SOA was measured than predicted (Fig. S12). Note that while the LVOC fate correction led to a factor of ~2.5 increase in OA enhancement (seen in Figs. 2.7–2.8), it causes only a factor of 1.4 increase in the slope in Fig. 2.10. This is because the higher OA concentrations also lead to higher predicted SOA formation due to increased SOA yields (resulting from increased partitioning to the particle phase).

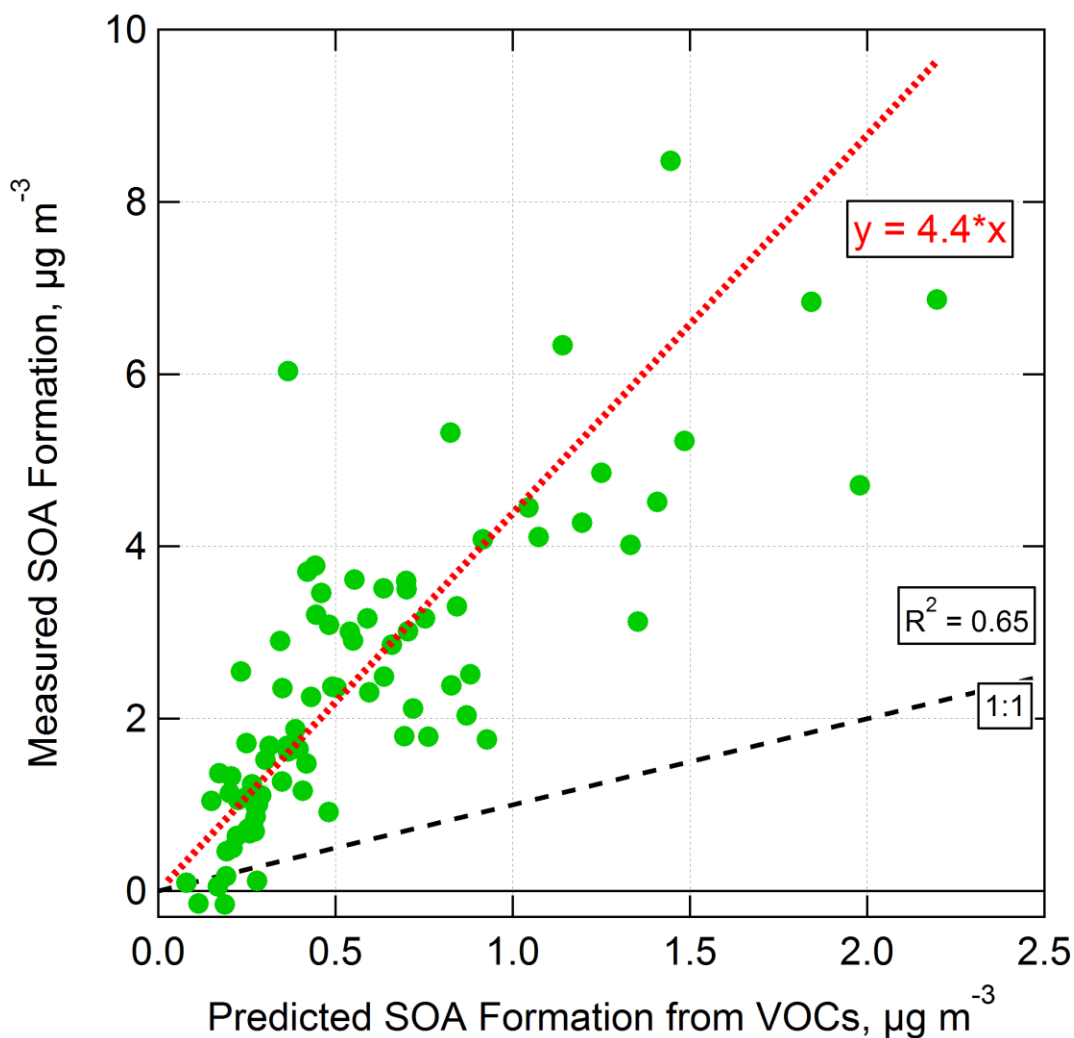


Fig. 2.10. Measured vs. predicted SOA formation from OH oxidation of ambient air in an OFR using the OFR185 method. Only the range of photochemical ages with the highest SOA formation (0.4–1.5 eq. days) was used, and the LVOC fate correction was applied. Predicted SOA formation was calculated by applying OA concentration-dependent yields (average of 12.5%, 13.2%, 13.8%, and 3.2% for MT, SQT, toluene+*p*-cymene, and isoprene, respectively, with average OA concentration of $4.1 \mu\text{g m}^{-3}$) to VOCs reacted in the OFR (Tsimpidi et al., 2010). The amount of reacted VOCs was estimated using OH_{exp} and ambient VOC concentrations. If a non-zero y-intercept is allowed, the regression line becomes $y = 5.0x - 0.5$.

MT were the dominant SOA precursors, contributing an average of 87% to predicted SOA formation, with SQT, toluene+*p*-cymene, and isoprene contributing 5%, 3%, and 5%, respectively. Other known VOCs that form SOA, such as benzene or xylenes, were present in such low concentrations that they would contribute even smaller percentages to predicted SOA formation, so they were not included in this analysis.

The correlation between measured and predicted SOA was $R^2 = 0.65$, indicating that SOA formation potential was controlled mainly by MT and other biogenic gases with similar concentration diurnal patterns, including SQT. Toluene also likely originated at least partially from biogenic sources at this site (Misztal et al., 2015). A diurnal plot of the measured maximum (0.4–1.5 eq. days age) and predicted SOA formation is shown in Fig. 2.11, along with ambient MT, SQT, toluene+*p*-cymene, and MBO+isoprene concentrations (and S/IVOC concentrations, discussed in Sect. 2.3.6.2). SOA formation followed a similar diurnal pattern to MT, SQT, and toluene+*p*-cymene, including a substantial increase just after sunrise at 7 AM local time. SOA formation in the OFR followed a very different diurnal pattern than ambient MBO+isoprene, supporting the conclusion that MBO+isoprene was an insignificant contributor to SOA formation in the OFR for the ambient conditions of this campaign.

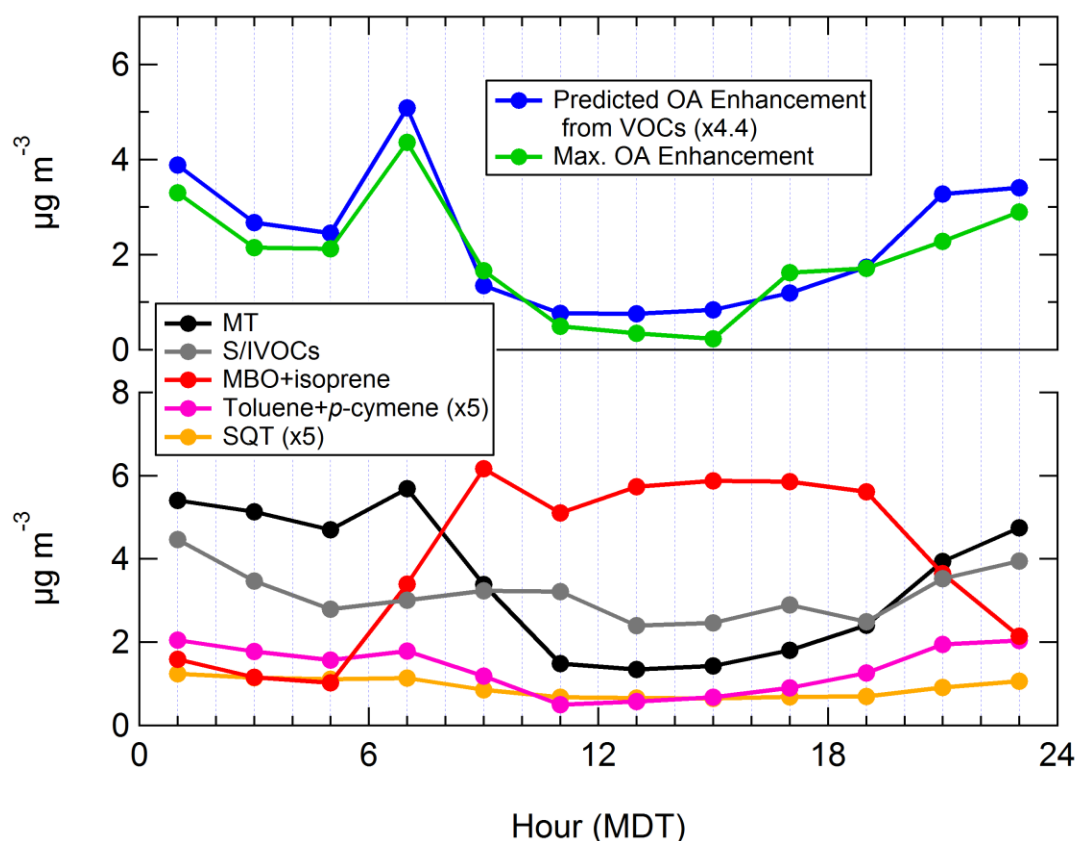


Fig. 2.11. Top: diurnal maximum measured OA enhancement (all data from 0.4–1.5 eq. days aging, LVOC fate corrected) in the OFR from OH oxidation using the OFR185 method, and predicted OA formation from measured VOCs (x4.4). Bottom: ambient MT, SQT (x5), toluene+*p*-cymene (x5), MBO+isoprene, and S/IVOC mass concentrations vs. time of day.

In order for SOA formation in the OFR to be fully explained by the ambient VOCs, the SOA yields would have needed to be approximately a factor of 4.4 larger than the values used in this analysis. This would mean, e.g., a 55% yield from MT with the OA concentrations of only $4.1 \mu\text{g m}^{-3}$ (34% at $2.9 \mu\text{g m}^{-3}$ if the LVOC fate correction is not applied), which is inconsistent with previous OFR and chamber studies that have only achieved such high SOA yields in experiments with over an order of magnitude higher OA concentrations (Kang et al., 2007, 2011; Tsimpidi et al., 2010; Lambe et al., 2011b, 2015). Accounting for S/IVOC wall losses in such experiments (Matsunaga and Ziemann, 2010; Zhang et al., 2014) or including aging parameterizations (Tsimpidi et al., 2010) might lessen this discrepancy, but is unlikely to be the entire answer. Therefore, this analysis strongly suggests that there are other gases in ambient air than the VOCs measured by the PTR-TOF-MS that make important contributions to SOA formation.

2.3.6.2 SOA mass formed vs. predicted from S/IVOCs

While the lowest-volatility organic matter (i.e., OA) is measured by the AMS and the highest-volatility range (VOCs and some IVOCs) is sampled by the PTR-TOF-MS, there is a substantial range of S/IVOCs between them. The gases that enter the OFR as S/IVOCs are the most likely source of SOA formation contributing to the factor of 4.4 discrepancy in Sect. 2.3.6.1. During the BEACHON-RoMBAS campaign, measurements were made using the TD-EIMS instrument to quantify the bulk (volatility-resolved) ambient S/IVOC mass (Hunter et al., 2016). Other techniques at the site identified and quantified various subsets of the S/IVOCs (Yatavelli et al., 2014; Chan et al., 2016). All of the measurements are compiled in Hunter et al. (2016) to determine the total average organic volatility distribution during the campaign, which shows that S/IVOCs were the only pool of gas-phase species that could possibly produce as much SOA mass as observed in our study.

The average bulk S/IVOC mass concentrations measured with the TD-EIMS are shown as a function of $\log(C^*)$ in the inset of Fig. 2.12. In Hunter et al. (2016), this mass was interpreted as being an approximate lower limit to S/IVOC mass, assuming the S/IVOCs measured by Yatavelli et al. (2014), Chan

et al. (2016), and by the PTR-TOF-MS were subsets of the TD-EIMS measurement. The upper limit is to assume that each instrument measured a different set of S/IVOCs with no overlap, and would be ~ 3.2 times larger than the mass shown in the inset of Fig. 2.12. With the substantial temporal overlap between OFR185 operation and TD-EIMS measurements, it is feasible to perform a point-by-point analysis using the full TD-EIMS time series (shown in Fig. S7) to determine what the SOA yield of the lower limit S/IVOC mass would need to be in order to fully explain the amount of SOA formed from OH oxidation in the OFR.

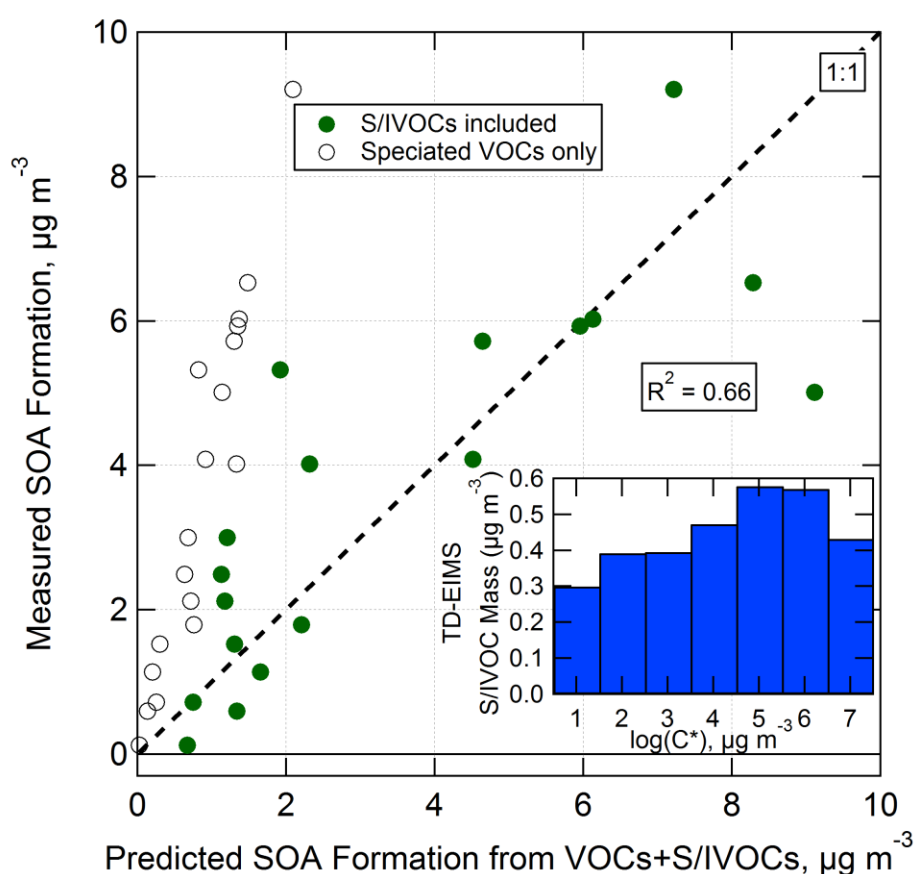


Fig. 2.12. Measured vs. predicted SOA formation from OH oxidation of ambient air in an OFR using the OFR185 method. Only the range of photochemical ages with the highest SOA formation (0.4–1.5 eq. days) was used, and the LVOC fate correction was applied. Predicted SOA formation is estimated using VOCs (described in Sect. 2.3.6.1) with and without including an empirical 58% SOA yield from S/IVOCs measured by the TD-EIMS (a lower limit of total S/IVOCs). Inset: average S/IVOC concentrations as a function of the log of the saturation vapor concentration C^* . This comparison includes all data for which S/IVOCs and SOA formation in the OFR were concurrently measured (26, 28–29 July, and 9–10, 12–13 August). For some data points, PTR-TOF-MS data was not available, so the VOC contribution was estimated using the linear fit in Fig. 2.10.

Ideally, the total mass of S/IVOCs at each data point that would be converted into SOA by oxidation would be determined by multiplying the mass in each volatility bin by the SOA yields of each bin. Since experimental measurements of the aerosol yields of such gases are generally not available and the ambient mixture of S/IVOCs was not fully speciated, we instead proceed under the assumption that all of the SOA formation that was not due to the previously discussed PTR-TOF-MS-measured VOCs came instead from the mass measured in the $C^* = 10^1\text{--}10^7 \mu\text{g m}^{-3}$ volatility bins, with one correction. Since SQT are typically in the $C^* = 10^5 \mu\text{g m}^{-3}$ range, we subtracted the SQT mass measured by the PTR-TOF-MS from the bulk S/IVOC mass (a subtraction of 6% of the total TD-EIMS measurement), to avoid double-counting due to this expected measurement overlap. While MT are in the $C^* = 10^7 \mu\text{g m}^{-3}$ volatility bin, that bin is at the upper volatility limit of the TD-EIMS measurement capability. Some gases in that bin were sampled, but MT were expected to be too volatile to be measured (Hunter et al., 2016). This was supported by the fact that the campaign-average mass in the $C^* = 10^7 \mu\text{g m}^{-3}$ bin was only $0.43 \mu\text{g m}^{-3}$, which would correspond to only approximately 0.1 ppbv MT, if there were no other gases in that bin. The campaign-average in-canopy MT concentration measured by the PTR-TOF-MS was approximately 0.8 ppbv.

For the lower limit S/IVOC mass case, the average SOA yield of the total S/IVOCs was determined by finding the yield value that made the slope of SOA measured vs. predicted from VOCs + S/IVOCs equal to one. As shown in Fig. 2.12, an average SOA yield of 58% for the bulk S/IVOC mass was required in order to bring the measured vs. predicted SOA formation into optimal agreement in this time series analysis. The correlation between measured and predicted SOA formation was $R^2=0.66$. Attempts were made to optimize the correlation between measured and predicted SOA formation by applying arbitrary C^* -dependent yields, but this did not result in significantly better correlations. Since speciated S/IVOC measurements as well as yields for each volatility bin (which may have varied with

diurnal changes in the composition of each bin) were not available, we concluded that further detailed interpretation of SOA production from the measured S/IVOCs would be under-constrained

As mentioned above, this average SOA yield for S/IVOCs of 58% was estimated by assuming the lower limit case where the total ambient S/IVOC mass was sampled by the TD-EIMS. The upper limit mass case in Hunter et al. (2016) assumed that the several instruments that measured S/IVOCs were measuring different subsets of total S/IVOCs, so the measurements needed to be summed in order to determine the total mass concentration. Due to limited temporal overlap between all instruments, the analysis in Hunter et al. (2016) was performed on campaign average measurements. For this reason, the average SOA yield of S/IVOCs for the upper limit case is also done using the campaign average values instead of the time series analysis that was possible for the lower limit case. The average upper and lower limit S/IVOC mass concentrations were 10 and $3.1 \mu\text{g m}^{-3}$. To estimate the SOA yield of S/IVOCs in the upper limit case, the TD-EIMS time series data was multiplied by 3.2, so that it reflected a campaign average of $10 \mu\text{g m}^{-3}$. Using this upper limit mass time series, an average SOA yield for S/IVOCs of 18% was needed to bring measured vs. predicted SOA formation in the OFR into agreement. This makes the assumption that the ratio of S/IVOC mass measured by each technique was always constant.

While measurements of SOA yields for speciated S/IVOCs are limited, especially for the relatively low OA concentrations in this study, previous work suggests that this range of 18-58% yield is reasonable. A yield of 51% was measured for n-heptadecane ($C^* = 10^4 \mu\text{g/m}^3$) with $\text{OA} = 15.4 \mu\text{g/m}^3$ under high- NO_x conditions (Presto et al., 2010). Yields can be even higher from cyclic compounds (Lim and Ziemann, 2009; Tkacik et al., 2012) and under low- NO_x conditions (Ng et al., 2007; Lane et al., 2008). SOA yields from several other IVOCs (naphthalene and alkylnaphthalenes) under low- NO_x conditions were determined to be 58-73% with OA concentrations of 10–40 $\mu\text{g/m}^3$ (Chan et al., 2009).

This analysis suggests that OH oxidation of organic gases in a parcel of ambient pine forest air can potentially produce approximately 3.4 times more SOA from S/IVOC gases than from VOCs. This

does not provide information about the sources of the lower volatility organic gases in this parcel. They may be directly emitted, formed as oxidation products of VOCs that were emitted upwind of this parcel, or some combination of these two options. Ambient MT and S/IVOC concentrations measured by the TD-EIMS exhibit a modest correlation ($R^2 = 0.43$, shown in Fig. S13), suggesting that the S/IVOCs may at least partially come from a biogenic source related to the emission of MT. For example, O_3 and NO_3 may react with the C=C-containing MT and SQT emissions during nighttime, leading to a buildup of oxidation product S/IVOCs that lack C=C double bonds and would generally not react further with O_3 and NO_3 (Atkinson, 1997). If this occurs, then OFR oxidation is merely starting with precursors that are partway through the “aging” process from VOC emission to SOA formation. Variations in the ratio of measured to predicted SOA formation in Figs. 2.10 and 2.12 could be due partly to variations in the ratio of the concentrations of S/IVOCs to VOCs due to changes in the meteorological or chemical conditions of the atmosphere, or from periodic changes in the biogenic and/or anthropogenic sources of S/IVOCs. However, as shown in Fig. 2.11, the diurnal profile of S/IVOC concentrations showed a relatively smaller increase in concentrations at night compared to MT or measured SOA formation. Since emissions generally change with time of day, it would not be unreasonable to expect the speciation and SOA formation potential of ambient S/IVOCs to also change with time of day. Until the S/IVOCs in a dataset such as this can be better speciated and quantified, these conclusions remain speculative.

2.3.6.3 Sensitivity to LVOC fate model parameters

The LVOC fate correction in this analysis led to a relatively large factor of 2.5 increase in OA enhancement and factor of 1.4 increase in measured vs. predicted SOA formation. As the values of several of the model parameters are not well constrained, in this section we investigate the sensitivity of the LVOC fate correction to these parameters. Fig. 2.13 shows the sensitivity of the slope of measured vs. predicted SOA formation from VOCs, as well as how that affected the range of SOA yields needed from S/IVOCs in order to explain the total SOA formation in the OFR. Sensitivity was tested for k_{OH} , the

number of reactions with OH before LVOCs are lost to volatile, non-condensable products, the SMPS size distribution used to calculate CS , α , k_e , and D .

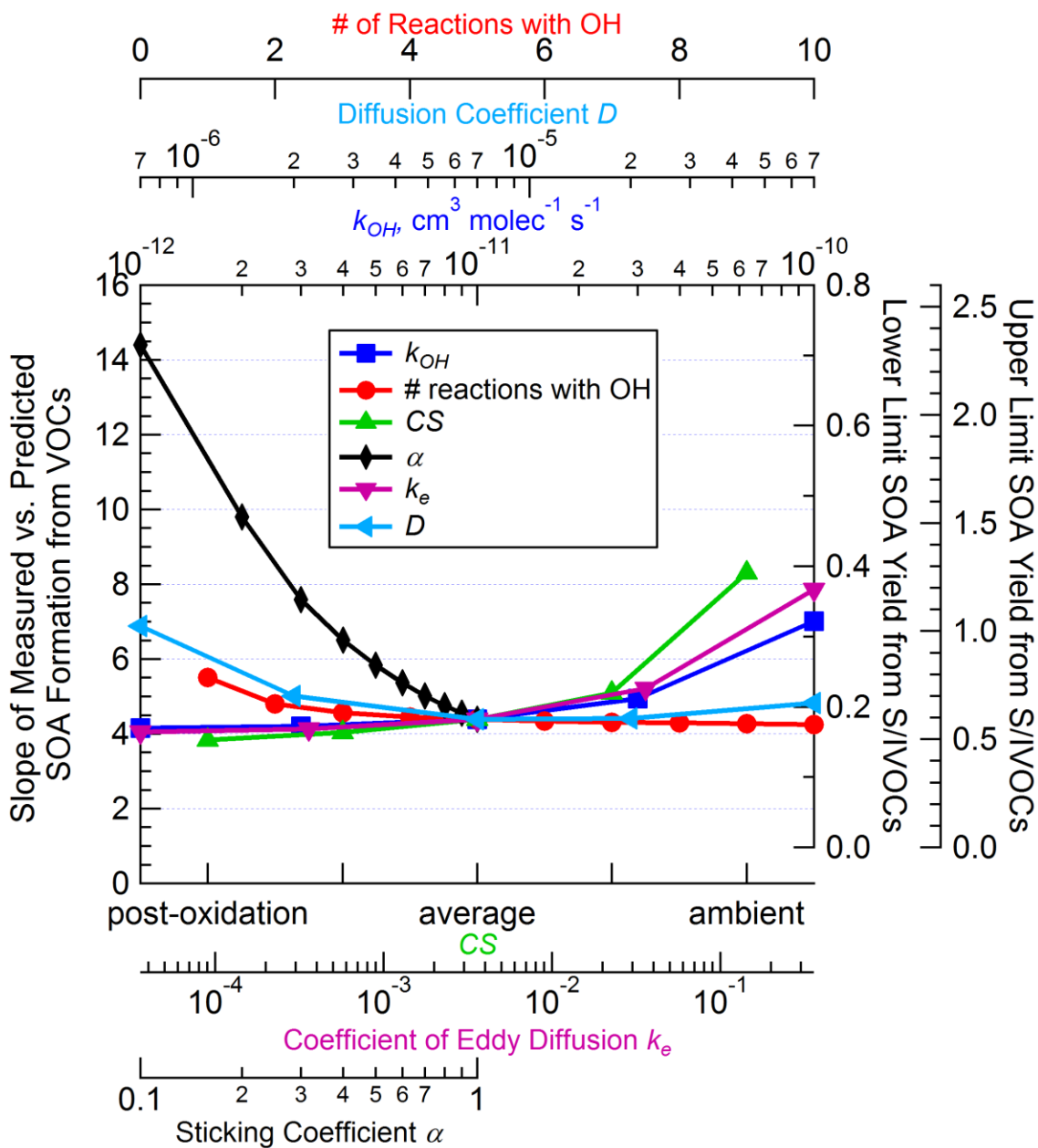


Fig. 2.13. Sensitivity of the slope of measured vs. predicted SOA formation from VOCs, and of the range of SOA yields estimated for bulk S/IVOCs (same curves, different Y axes), to parameters in the LVOC fate model. The change in slope and yields is calculated by changing only one parameter at a time while keeping the rest at the base case values of 5 reactions with OH, $k_{OH} = 1 \times 10^{-11} \text{ cm}^3 \text{ molec}^{-1} \text{ s}^{-1}$, average CS , $\alpha = 1$, $k_e = 0.0036 \text{ s}^{-1}$, and $D = 7 \times 10^{-6} \text{ m}^2 \text{ s}^{-1}$.

The least-well-defined parameters in the model were likely k_{OH} and the number of reactions with OH, especially since the analysis of H_2SO_4 condensation in Sect. 3.3.2 did not use them. However,

the LVOC fate correction was relatively insensitive to these parameters, specifically for values of k_{OH} less than $3 \times 10^{-11} \text{ cm}^3 \text{ molec}^{-1} \text{ s}^{-1}$ or when assuming 2+ reactions with OH. If we assume LVOCs always remain available to condense and never fragment, the slope reaches a lower asymptote of 4.1. The model also showed a relatively low sensitivity to k_e and D over several orders of magnitude.

The slope of measured vs. predicted SOA formation was more sensitive to the choice of CS and α . The slope is mainly sensitive to CS when approaching the ambient (smaller) value. Since using the average value of CS worked well for the H_2SO_4 analysis (and the ambient CS gave poor results there), it is likely that the average CS is at least close enough to the proper value as not to cause systematic biases. Using values of α less than 1 led to a rapid increase in the magnitude of the LVOC fate correction. Values less than approximately $\alpha = 0.1$ would require the SOA yield from S/IVOCs to approach 100% as a lower limit, which is unlikely to be the case. In other words, if the sticking coefficient was very low (e.g. $\alpha < 0.1$) it would be impossible to explain the amount of SOA formed from the carbon present in the gas-phase. This suggests that $\alpha = 1$ or close to 1 is a good approximation for the conditions in the OFR at this campaign, and allows us to rule out values much lower than 1.

It is noteworthy that none of the changes to these four parameters led to a substantial *decrease* in the slope of measured vs. predicted SOA formation. The parameters that can lead to a considerable increase in F_{aer} are the CS and residence time of the OFR (i.e., time allowed for condensation onto particles, which is controlled by flow rate). However, these values were among the best constrained parameters, since we had direct measurements of both during the campaign. This suggests that while the LVOC fate correction was relatively large, it was unlikely to be much smaller.

2.4 Conclusions

During the BEACHON-RoMBAS campaign, ambient air was oxidized by OH in an OFR to study in situ SOA formation from the ambient mixture of SOA precursors as they exist in a forest environment. SOA formation was measured semi-continuously, and the changes in both gas and particle phases were

documented as a function of photochemical age. The amount of SOA formation increased with age to a maximum at 0.4–1.5 days of eq. photochemical aging, coinciding with depletion of known SOA precursors measured with the PTR-TOF-MS. SOA formation in the OFR correlated with MT concentrations, both of which were typically larger during nighttime. Net SOA loss was observed at >10 days eq. age, consistent with heterogeneous oxidation processes being important only for the longest lived aerosol (e.g., free tropospheric aerosol). Similar amounts of SOA formation were observed from both the OFR185 and OFR254-70 methods for the overlapping range of eq. ages (~1-30 days). Comparison at shorter ages was not possible because the OFR254-70 method, especially as it was employed during this campaign, was not suitable for measuring <1 eq. day of OH aging. Condensation onto preexisting ambient particles and nucleation and growth of small particles were both observed.

A modeling analysis of the fate of LVOCs in the OFR was presented. The validity of this model was evaluated using the simpler process of SO₂ gas conversion to SO₄ aerosol. The fraction of LVOCs that condense onto aerosols, versus the other fates of LVOCs including condensing on the reactor walls, exiting the reactor to condense on sampling lines, or reacting with OH to produce volatile fragmentation products, depends strongly on the aerosol surface area available for condensation. Our measurements rule out sticking coefficients much lower than 1. For ambient experiments in rural areas with low CS, laboratory experiments without seed aerosol, or when sampling with a relatively short residence time, a large correction may be required. Addition of an aerosol seed to sample air with low aerosol CS (such as this study) would reduce the uncertainties associated with the LVOC fate correction. In urban areas or in laboratory studies with large seed aerosol surface area, the correction can be much smaller (<20%). In either case, the relative time scales of key processes in the OFR need to be carefully considered in order to properly interpret the results of measured SOA formation.

The amount of SOA that could be produced from OH oxidation of the major VOC species measured at this site (MT, SQT, toluene+*p*-cymene, and isoprene) was insufficient to explain the

measured SOA formation in the reactor by a factor of 4.4. To our knowledge, this is the first time this has been demonstrated by comparing simultaneous VOC measurements with in situ SOA formation, particularly in a biogenic environment. A discrepancy this large is unlikely to be completely explained by incorrect yields for the speciated VOCs or by experimental uncertainties. The correlation between measured and predicted SOA formation suggests that the unidentified SOA precursors were of biogenic origin with a similar diurnal pattern to MT, SQT, and toluene +*p*-cymene. Novel TD-EIMS measurements quantified the reservoir of *S*/IVOCs, which are not measured efficiently by a PTR-TOF-MS and represent the only pool of gas-phase carbon at the site that could possibly explain the observed SOA. An SOA yield of 18-58% for the total mass of *S*/IVOCs measured was required to account for all of the SOA formation from OH oxidation in the OFR. This research points to a need to improve our understanding and measurement capabilities of *S*/IVOCs.

We have demonstrated how an OFR can be used in combination with a variety of aerosol and gas instruments to provide information about the net SOA formation potential of forest air. The OFR technique allows investigating the quantity and variability of SOA precursor gases that are present in ambient air. These results could be used to inform the treatment of *S*/IVOCs, such as VOC oxidation products, in SOA models. Future OFR experiments could be designed with additional specialized instrumentation to determine the molecular identities of *S*/IVOCs and investigate their specific SOA yields.

2.5 Supplementary information

2.5.1 Correction for particle diffusion to sampling line walls

AMS and SMPS particle concentrations were corrected for diffusion losses to the walls of the inlet sampling lines, estimated using the Max Planck Institute for Chemistry's Particle Loss Calculator (von der Weiden et al., 2009). The sampling lines were constructed from a mixture of 3/8" and 1/4" OD copper tubing. The ambient air sampling line contained a PM_{2.5} cyclone impactor at the inlet. The total

length of tubing between the cyclone/OFR and AMS/SMPS was approximately 8 m, with a total residence time of about 9 s. The transmission curve used to correct for line losses is shown in Fig. 2.S1. Estimates for particle losses in the ambient sampling line and in the OFR sampling line were similar, so a single transmission curve is applied to all data. The transmission curve was applied to SMPS size distributions to determine particle volume lost to the inlet walls. This volume was added to the AMS species in the same ratio that the species volumes were measured by the AMS. As seen in Fig. 2.S1, there was on average only a slight size dependence to the species mass fractions of ambient aerosol. The mass fractions are also particularly noisy at smaller particle sizes due to small mass concentrations. Ideally, the species size distributions measured at each point in time could be used to allocate the sampling line particle losses to each species. In practice, the AMS size-distribution measurement mode is not sensitive enough at these concentrations to do such a correction at high time-resolution. Ambient AMS size distribution data could be averaged over long periods of time to increase the signal-to-noise, but this would not be possible for OFR measurements, since the OH exposure is changed between each successive data point. Thus, we have applied the best correction possible and expect that it should improve quantification. Regardless, the small size dependence of species mass fractions would have a minimal impact on this analysis since the correction is at most 20% at the smallest sizes. Mass was estimated from volume using densities of 1.52 g cm^{-3} for chloride and 1.75 g cm^{-3} for sulfate, ammonium, and nitrate AMS aerosol species (DeCarlo et al., 2004; Salcedo et al., 2006; Lide, 2013), and a parameterization using elemental composition to estimate the density of OA (Kuwata et al., 2012). The combination of the sampling line particle loss correction and the AMS lens transmission correction (discussed in Sect. 2.5.3) added an average of 4% to the ambient OA, and an average of 12% to the OA measured after 0.4–1.5 days of aging (when the corrections were largest).

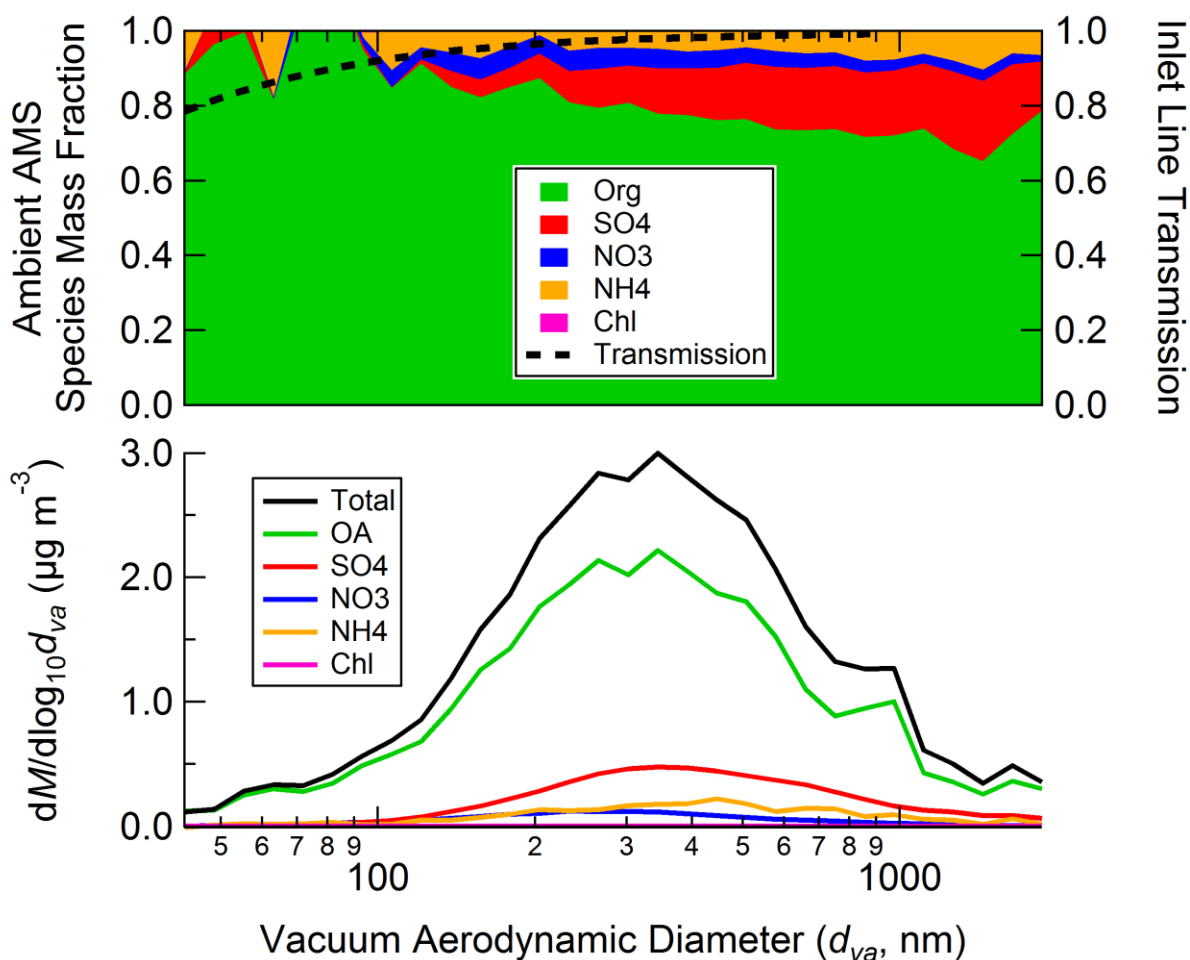


Fig. 2.S1. Top: Average species mass fraction of ambient aerosol measured by the AMS, and inlet sampling line particle transmission efficiency. The transmission efficiency was estimated using the Max Planck Institute for Chemistry Particle Loss Calculator (von der Weiden et al., 2009). This transmission curve was used to correct SMPS size distributions for particle losses in the ambient and OFR sampling lines. Particle losses to surfaces inside the OFR are discussed in Sect. 2.5.3. Bottom: Average species mass size distribution of ambient aerosol measured by the AMS.

2.5.2 Determination of AMS collection efficiency (CE)

CE is typically variable between 0.5 and 1, depending on composition, as detailed in Middlebrook et al. (2012). To our knowledge, ambient AMS measurements with a constant CE of ~ 1 have been reported in two prior studies in forested environments: during the wet season in the remote Amazon forest at the Amazonian Aerosol Characterization Experiment 2008 (Chen et al., 2015c), and South American Biomass Burning Analysis (SAMBBA) experiment during the dry season and dry-to-wet

transition period in the southwestern Amazon rainforest in 2012 (Brito et al., 2014). Here, we assessed CE by comparing AMS measurements with an SMPS that sampled from the same inlet. This SMPS measurement was validated by an intercomparison with four other calibrated and independently-operated SMPS instruments, as well as three CPC total particle number measurements, that sampled concurrently at the same research site. Fig. 2.S2 shows that CE = 1 was required to match the AMS and SMPS measurements.

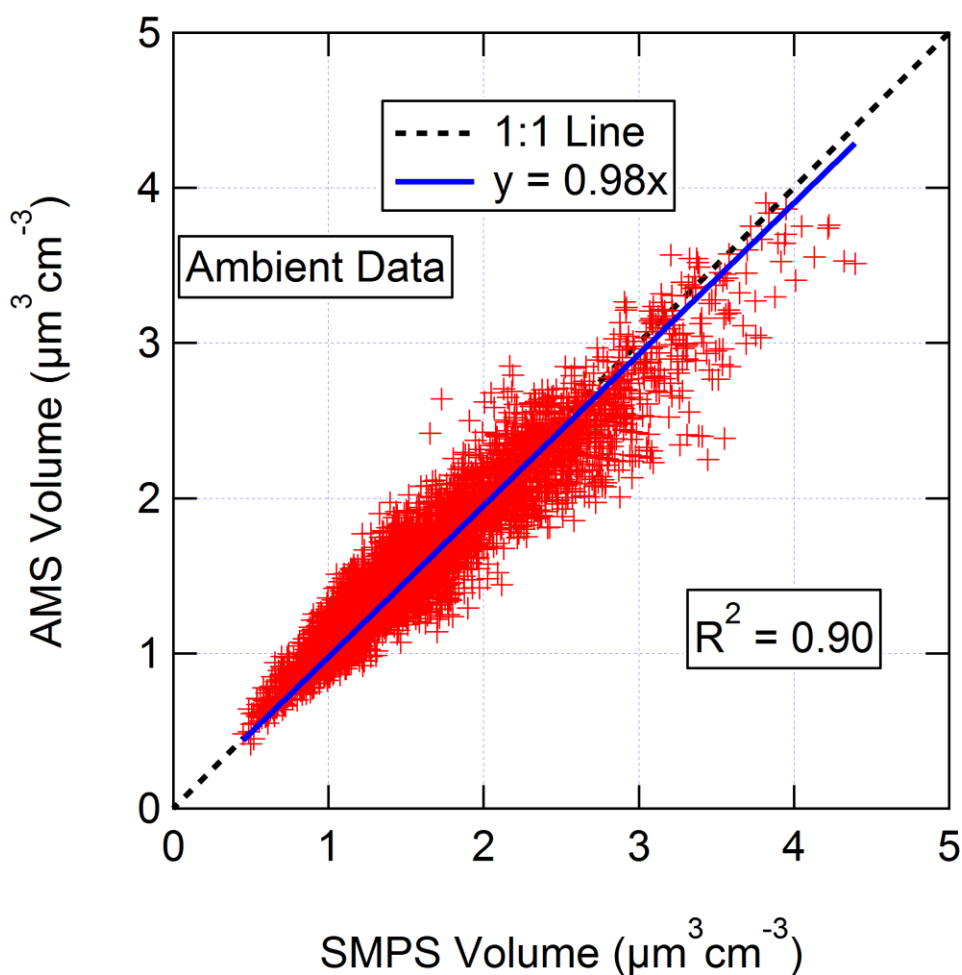


Fig. 2.S2. Scatter plot of ambient aerosol volume measurements from AMS vs. SMPS with regression line. AMS data was calculated using CE=1. AMS volume was estimated using densities of 1.52 g cm^{-3} for chloride, 1.75 g cm^{-3} for sulfate, ammonium, and nitrate (DeCarlo et al., 2004; Salcedo et al., 2006; Lide, 2013), and a parameterization using elemental composition to estimate the density of OA (Kuwata et al., 2012). All data is shown without the LVOC fate correction.

One concern was that the CE would change after oxidation in the OFR, due to changes in the aerosol composition and properties. A change in CE would result in a change in the slope of AMS vs. SMPS volume. However, we did not observe such a change, as seen in the comparison of total aerosol volume measured after the OFR in the left panel of Fig. 2.S3. Occasionally, high concentrations of NH_4NO_3 were produced in the OFR from OH oxidation. During those times, the AMS measured up to several times more volume than the SMPS (implying a $\text{CE} \gg 1$). This is likely due to evaporation of the NH_4NO_3 in the SMPS, as the SMPS sample flow was diluted inside the DMA column, as well as between the DMA and the CPC. For this reason, these data are not included in the analysis of CE.

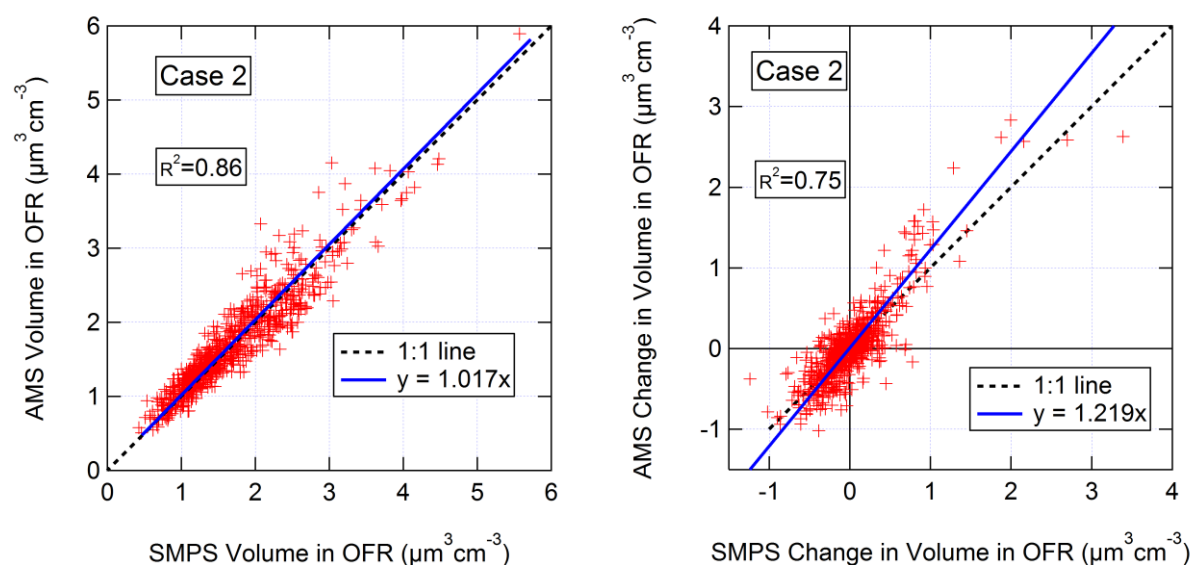


Fig. 2.S3. Scatter plot of aerosol volume and change in volume after OH aging from AMS vs. SMPS. AMS volume was estimated using densities of 1.52 for chloride, 1.75 for sulfate, ammonium, and nitrate (DeCarlo et al., 2004; Salcedo et al., 2006; Lide, 2013), and a parameterization using elemental composition to estimate the density of OA (Kuwata et al., 2012). Data is shown after correction for particle transmission losses in the AMS aerodynamic lens according to the case 2 correction in Fig. 2.S5. All data is shown without the LVOC fate correction. At the highest ages, heterogeneous oxidation led to fragmentation/volatilization of preexisting OA, resulting in a net loss of OA.

Fig. 2.S4 shows total particle volume enhancements as quantified by both the AMS and the SMPS for the OFR185 method vs. photochemical age, split into daytime and nighttime, showing that the two instruments measured similar enhancements within the errors at all ages. Data in Figs. 2.S2, 2.S3,

and 2.S4 were corrected using the sampling inlet line particle transmission efficiency curve in Fig. 2.S1 as well as a correction for the transmission of the AMS aerodynamic lens, discussed in Sect. 2.5.3.

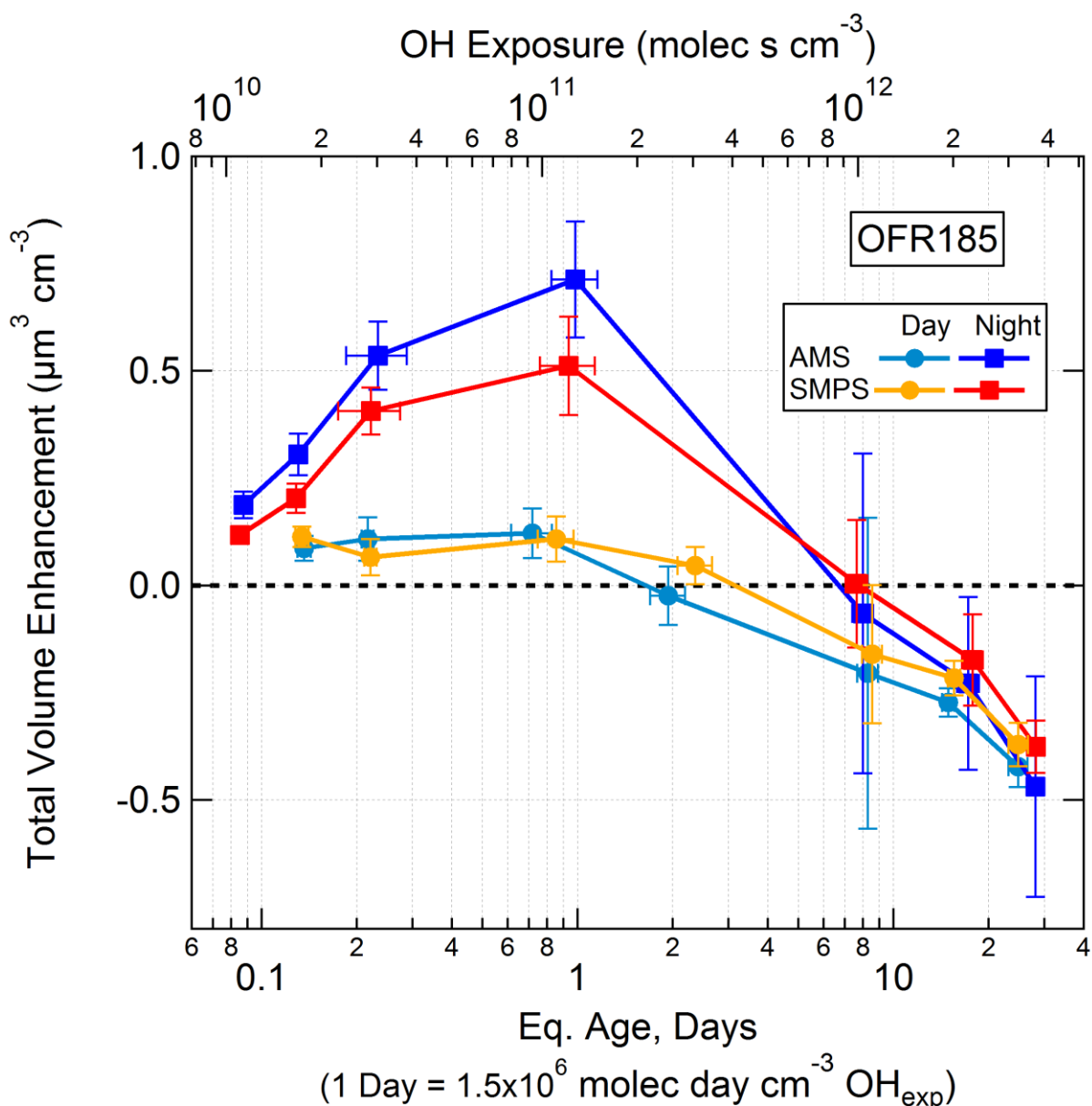


Fig. 2.S4. Total particle volume enhancement as measured by the AMS and SMPS as a function of photochemical age, split into daytime (08:00–20:00 local time) and nighttime (20:00–08:00 local time) data. AMS volume was estimated using densities of 1.52 g cm^{-3} for chloride, 1.75 g cm^{-3} for sulfate, ammonium, and nitrate (DeCarlo et al., 2004; Salcedo et al., 2006; Lide, 2013), and a parameterization using elemental composition to estimate the density of OA (Kuwata et al., 2012). All data is shown without the LVOC fate correction. Error bars represent the standard error of the mean of each quantile of data.

2.5.3 Determination of AMS aerodynamic lens transmission efficiency

As discussed in Sect. 2.3.5 and Fig. 2.9, OH oxidation of ambient air in the OFR often led to substantial new particle formation. The AMS aerodynamic lens is known to have less than 100% transmission at small sizes (Liu et al., 2007). A standard transmission curve has been suggested for correcting AMS data when lacking a determination of the transmission for the particular operating conditions of the AMS, referred to as case 0 here (Knote et al., 2011). However, it is preferable to use data from a specific experiment when available to make such a determination for specific operating conditions. The lens transmission curve was estimated for the conditions in which the AMS was operated at the BEACHON-RoMBAS campaign by empirically finding the low particle size cutoff that resulted in the highest R^2 correlation of the AMS and SMPS total volume sampled through an OFR (including all data from unperturbed to the highest OH_{exp}). We tested a range of corrections, shown in Fig. 2.S5. The results are shown in Table 2.S1. Scatterplots of total volume and change in volume for the base case (no correction) and the chosen case 2 correction are shown in Figs. 2.S6 and 2.S3, respectively. The combination of the sampling line particle loss correction and the AMS lens transmission correction added an average of 4% to the ambient OA, and an average of 12% to the total OA measured after 0.4–1.5 days of aging in the reactor (when the corrections were largest).

Table 2.S1. Slope and correlation values for a comparison of AMS vs. SMPS volume, when applying aerodynamic lens transmission correction curves 0-5 (shown in Fig. 2.S5) or no correction (base case).

<u>Total Volume</u>			<u>Change in Volume</u>		
Case	Slope	R^2	Case	Slope	R^2
0	1.056	0.85	0	1.446	0.77
1	1.036	0.85	1	1.341	0.77
2	1.017	0.86	2	1.219	0.75
3	1.001	0.85	3	1.107	0.70
4	0.989	0.84	4	1.032	0.65
5	0.983	0.82	5	0.997	0.61
base	0.981	0.81	base	0.986	0.58

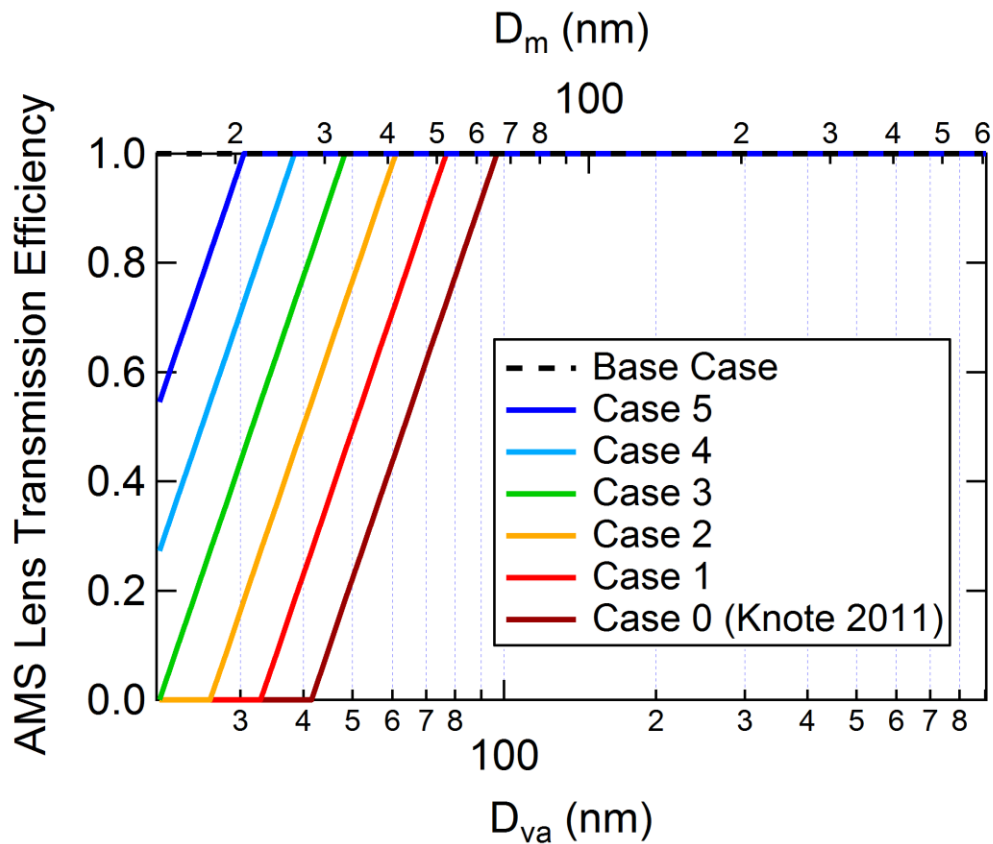


Fig. 2.S5. Potential AMS aerodynamic lens transmission efficiency curves used to evaluate small particle losses in the lens, as a function of vacuum aerodynamic diameter D_{va} and mobility diameter D_m . D_{va} was converted to D_m assuming a density of 1.45 g cm^{-3} (the campaign average). Case 0 is the recommended AMS lens transmission efficiency when no campaign-specific determination is possible (Knote et al., 2011). Case 2 was chosen as the best fit for the data under the conditions during BEACHON-RoMBAS.

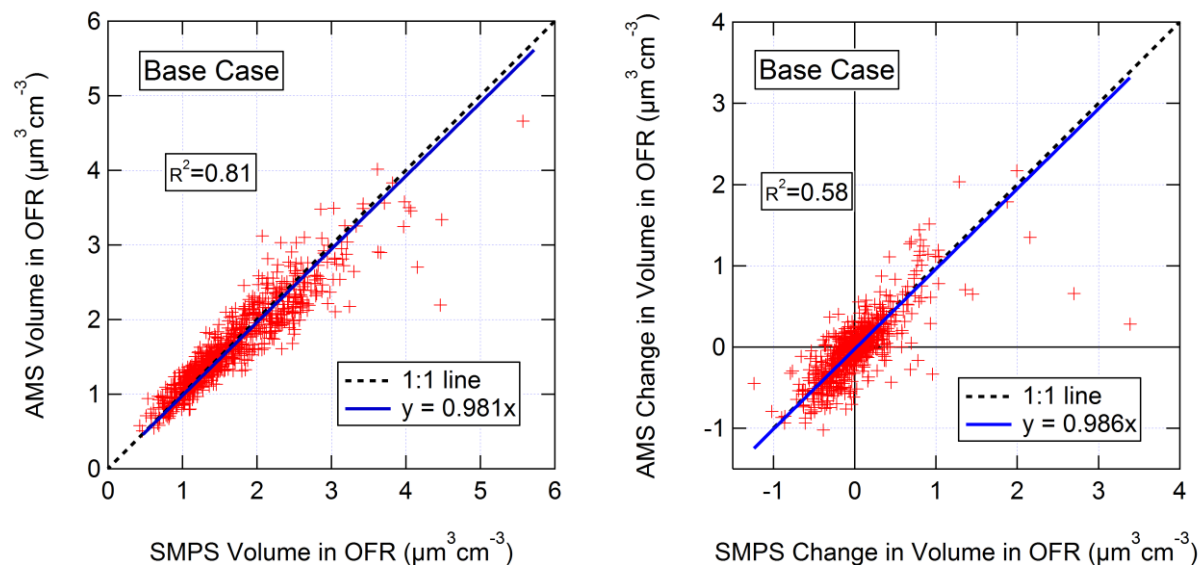


Fig. 2.S6. Scatter plot of aerosol volume and change in volume after OH aging from AMS vs. SMPS. AMS volume was estimated using densities of 1.52 g cm^{-3} for chloride, 1.75 g cm^{-3} for sulfate, ammonium, and nitrate (DeCarlo et al., 2004; Salcedo et al., 2006; Lide, 2013), and a parameterization using elemental composition to estimate the density of OA (Kuwata et al., 2012). Data is shown for base case (uncorrected) for particle transmission losses in the AMS aerodynamic lens according to Fig. 2.S5. All data is shown without the LVOC fate correction. At the highest ages, heterogeneous oxidation led to fragmentation/volatilization of preexisting OA, resulting in a net loss of OA.

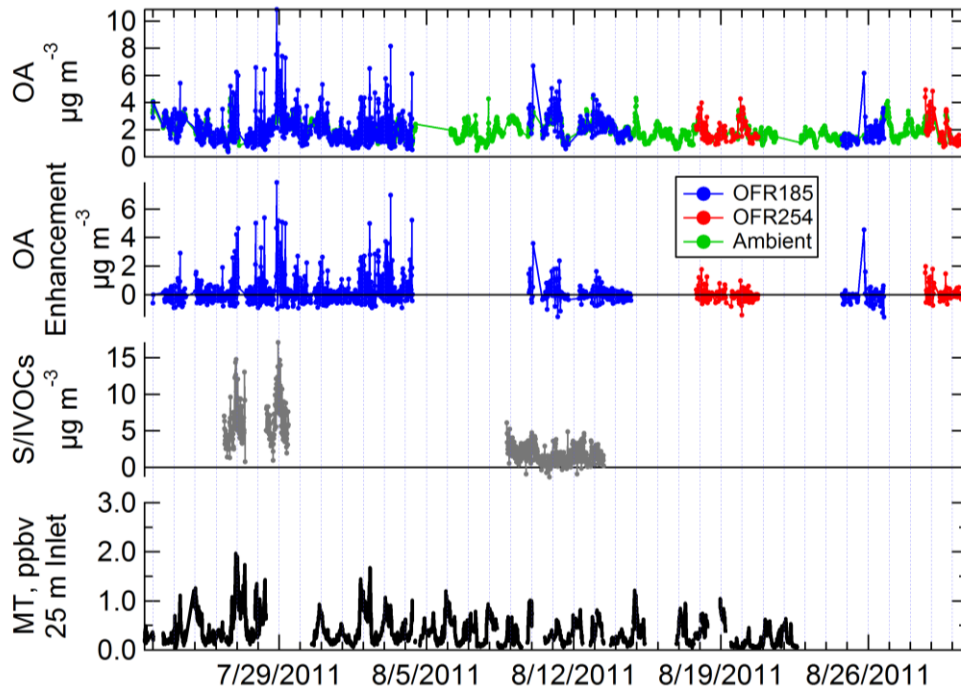


Fig. 2.S7. Time series of ambient OA, total OA, and OA enhancement for OFR185 and OFR254 methods, ambient MT (25 m inlet), and ambient S/IVOC mass concentrations measured by the TD-EIMS. The OA enhancements are not LVOC fate corrected here, and include all ages.

Finally, to account for any particle losses on the surfaces inside the OFR, the aerosol mass measured in the OFR when no oxidant was added was adjusted to be equal to the concurrent ambient aerosol data, which was interpolated from the measurements immediately before and after the OFR data. Aerosol was sampled through the OFR with no added oxidant approximately every 2 hours. The OFR data for which oxidant concentrations were increased were corrected by multiplying by the average ratio of ambient aerosol mass to aerosol mass measured through the OFR without added oxidant. This correction was small, increasing the mass of OFR data by 4%, similar in magnitude to the loss of particles in the sampling lines and aerodynamic lens.

2.5.4 In-canopy vs. 25 m height PTR-TOF-MS measurements

The primary PTR-TOF-MS dataset from BEACHON-RoMBAS was measured from an inlet located on a tower at 25 m, above the average canopy height of 16 m (Ortega et al., 2014). The OFR was located within the canopy at approximately 4 m height. Occasionally, concurrent PTR-TOF-MS measurements were available from the 25 m height and either through the OFR (1–6 and 8–10 August) or from a 1 m high inlet (19–21 August). Scatterplots of in-canopy (OFR or 1 m) vs. 25 m inlet MT, SQT, MBO+isoprene, and toluene+*p*-cymene concentrations are shown in Fig. 2.58. In-canopy concentrations were observed to be 1.9, 5.9, 1.4, and 1.2 times higher than at 25 m for those four compounds, respectively, and these ratios were used to estimate a campaign-long time series of in-canopy concentrations using the 25 m measurements. The correlations are high for MT, toluene, and MBO+isoprene ($R^2=0.80-0.82$), but the correlation for SQT is $R^2=0.12$. This low correlation adds uncertainty to the estimation of in-canopy SQT concentrations. However, this will have only a minor effect on the predicted SOA formation from VOCs (Sect. 2.3.6.1) since on average only 5% of the predicted SOA formation came from SQT.

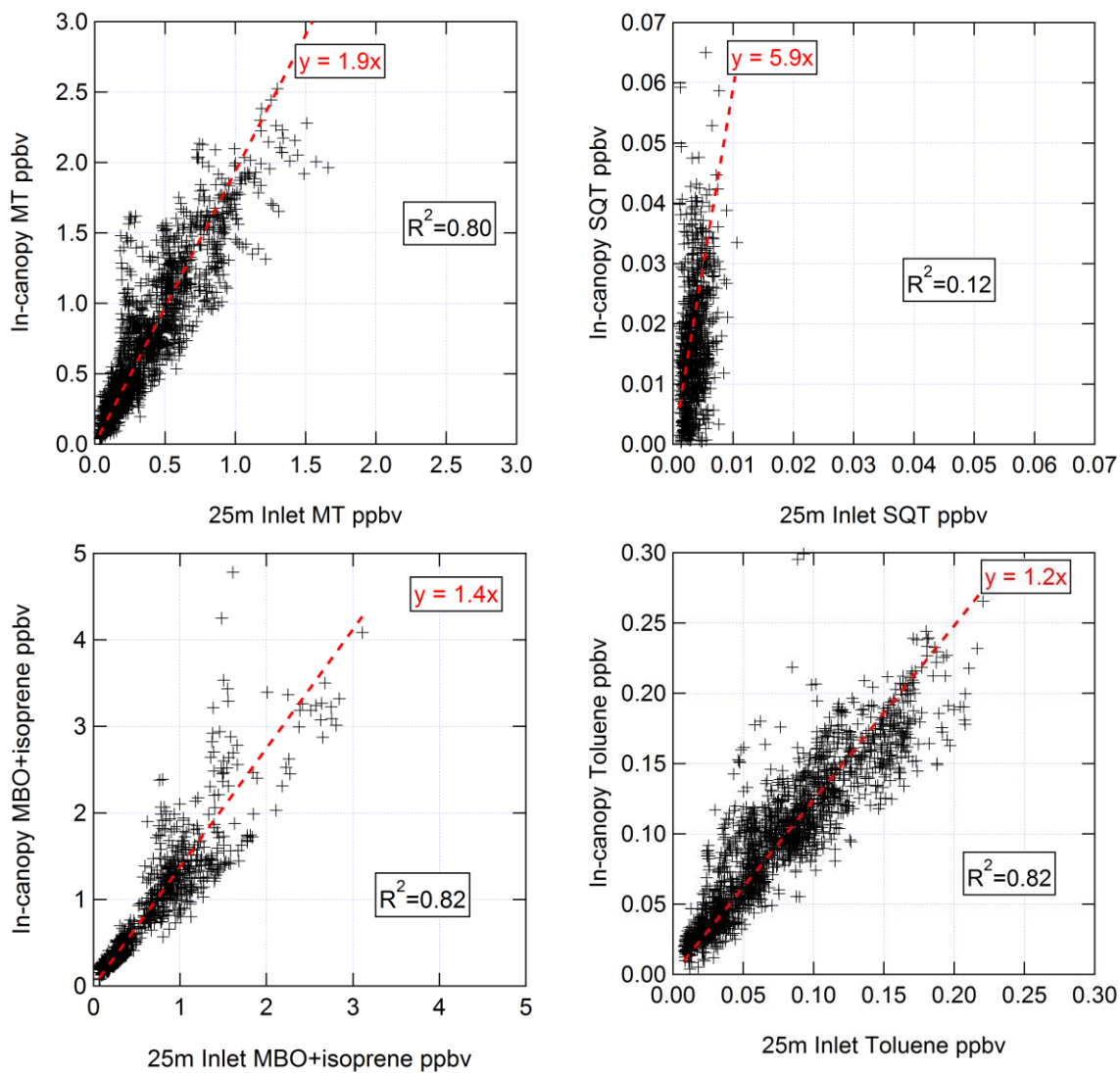


Fig. 2.S8. Scatterplots of in-canopy (through OFR or 1 m inlet) vs. 25 m inlet for PTR-TOF-MS measurements of MT, SQT, MBO+isoprene, and toluene. In-canopy concentrations were 1.9, 5.9, 1.4, and 1.2 times higher than at 25 m, respectively.

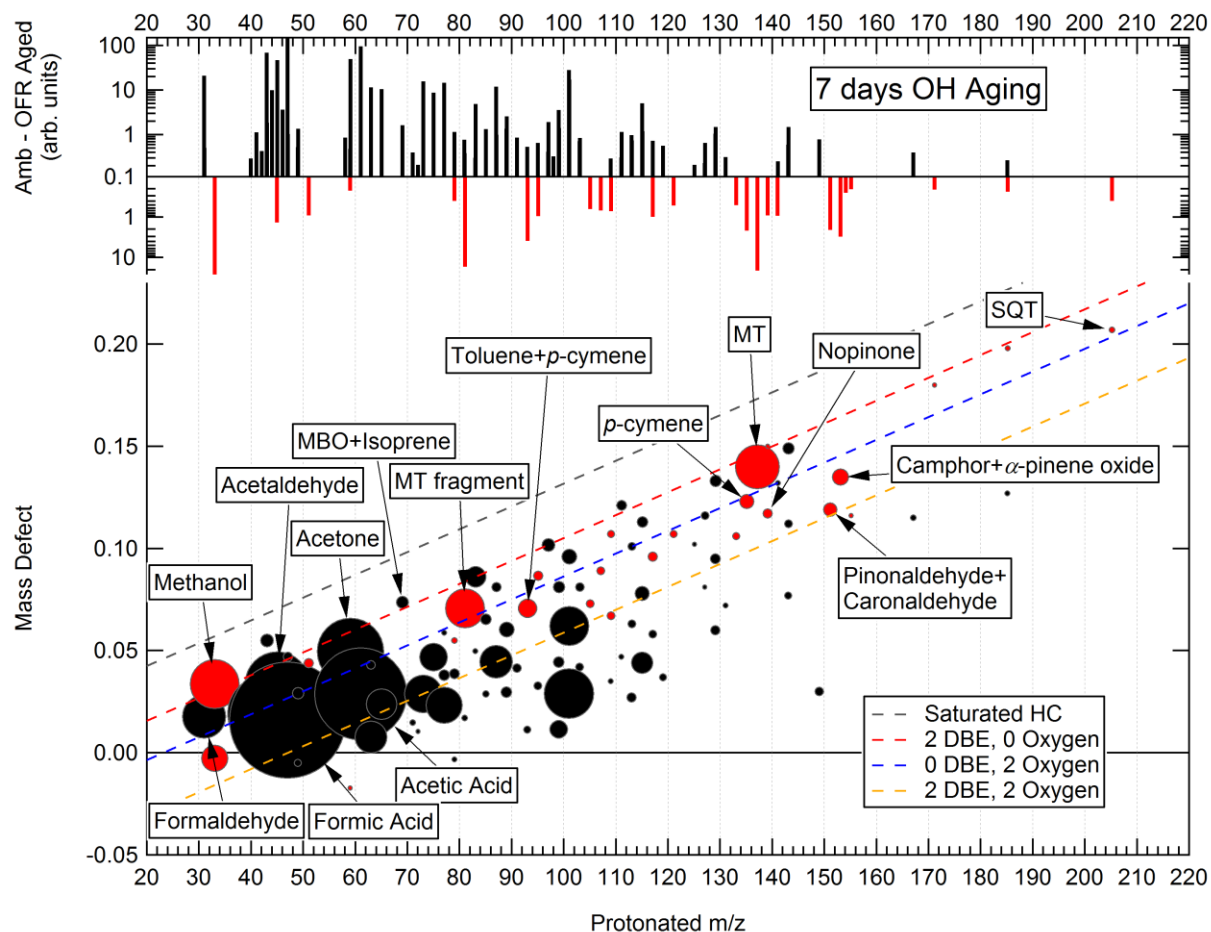


Fig. 2.S9. The absolute changes of ions (signal after OH oxidation in the reactor minus ambient signal) measured by the PTR-TOF-MS after 7 days of aging using the OFR185 method, shown as a difference mass spectrum and in a mass defect diagram. The mass spectra are 10-min averages (5 min from each of the two sample cycles used). The background-subtracted signals are shown in arbitrary units, not corrected for differences in sensitivity of each compound due to the large number of compounds and the inability to positively identify all of them. Prominent ions are labeled by name or elemental formula assignments. Dashed lines representing molecules with varying double bond equivalents (DBE) or number of oxygen atoms are shown for reference. A red marker signifies that the signal decreased due to oxidation, while a black marker indicates where signal was greater after oxidation. The markers are sized by the square root of the absolute change in signal at each peak after oxidation (i.e., marker area is proportional to signal). Minor signals with absolute change of <0.2 arb. units or change of $<20\%$ of total ambient signal are removed.

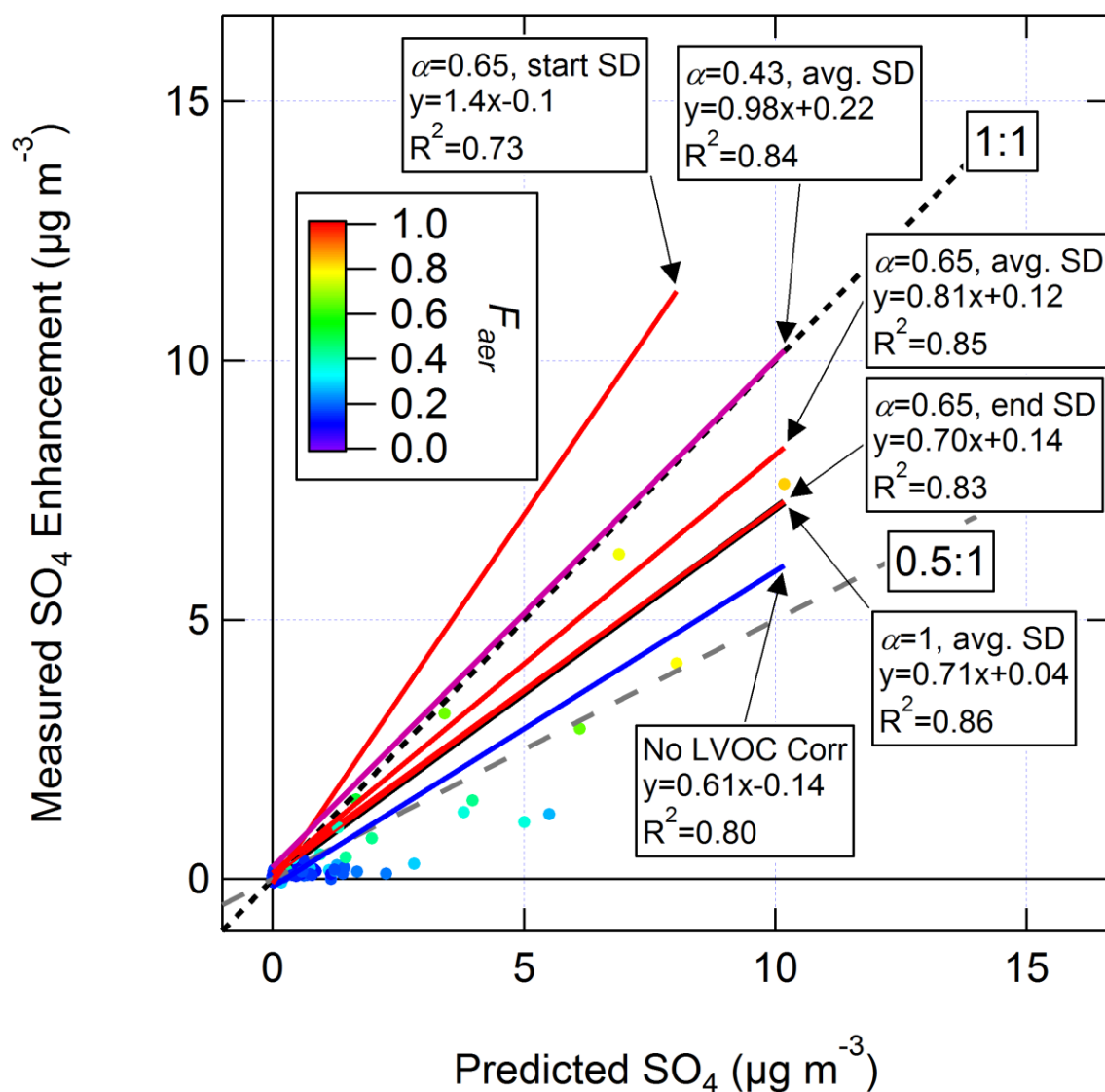


Fig. 2.S10. Sensitivity study of the measured vs. predicted SO_4 formation after OH oxidation in the OFR vs. key uncertain parameters. The data points are colored by the fraction of H_2SO_4 predicted to condense on aerosols, calculated using $\alpha = 0.65$ and the average of the SMPS size distributions (SD) measured before and after oxidation. Data are shown without applying the LVOC fate correction, along with linear fits that result from applying various sets of corrections including $\alpha = 0.43-1$ and using the ambient (start), post-oxidation (end), or average SD to calculate the CS. Ambient SO_2 concentrations <0.2 ppb have been excluded from this analysis.

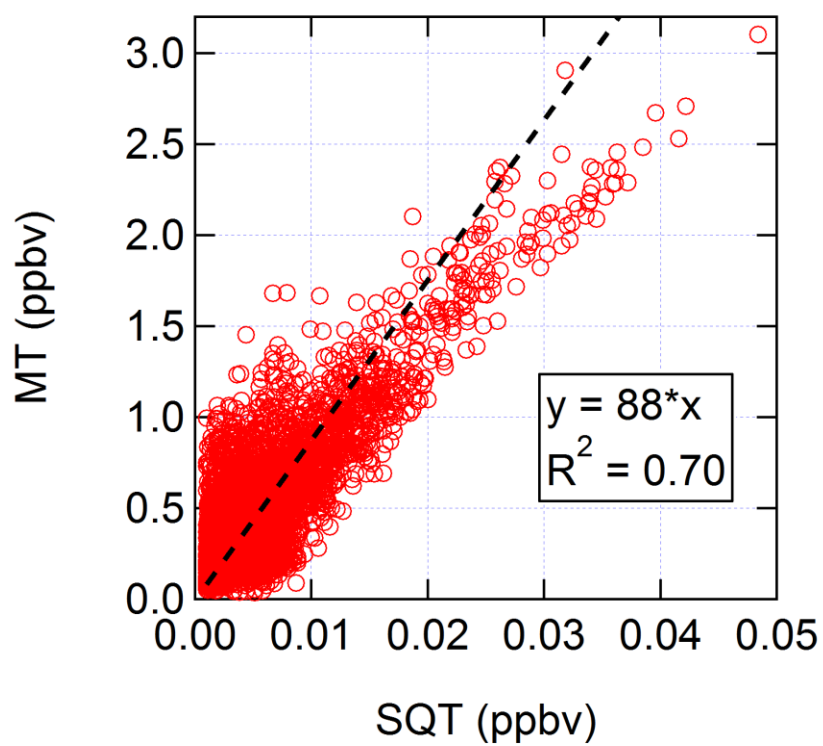


Fig. 2.S11. Scatterplot of ambient MT vs. SQT concentrations measured by the PTR-TOF-MS at the 25 m inlet above the canopy.

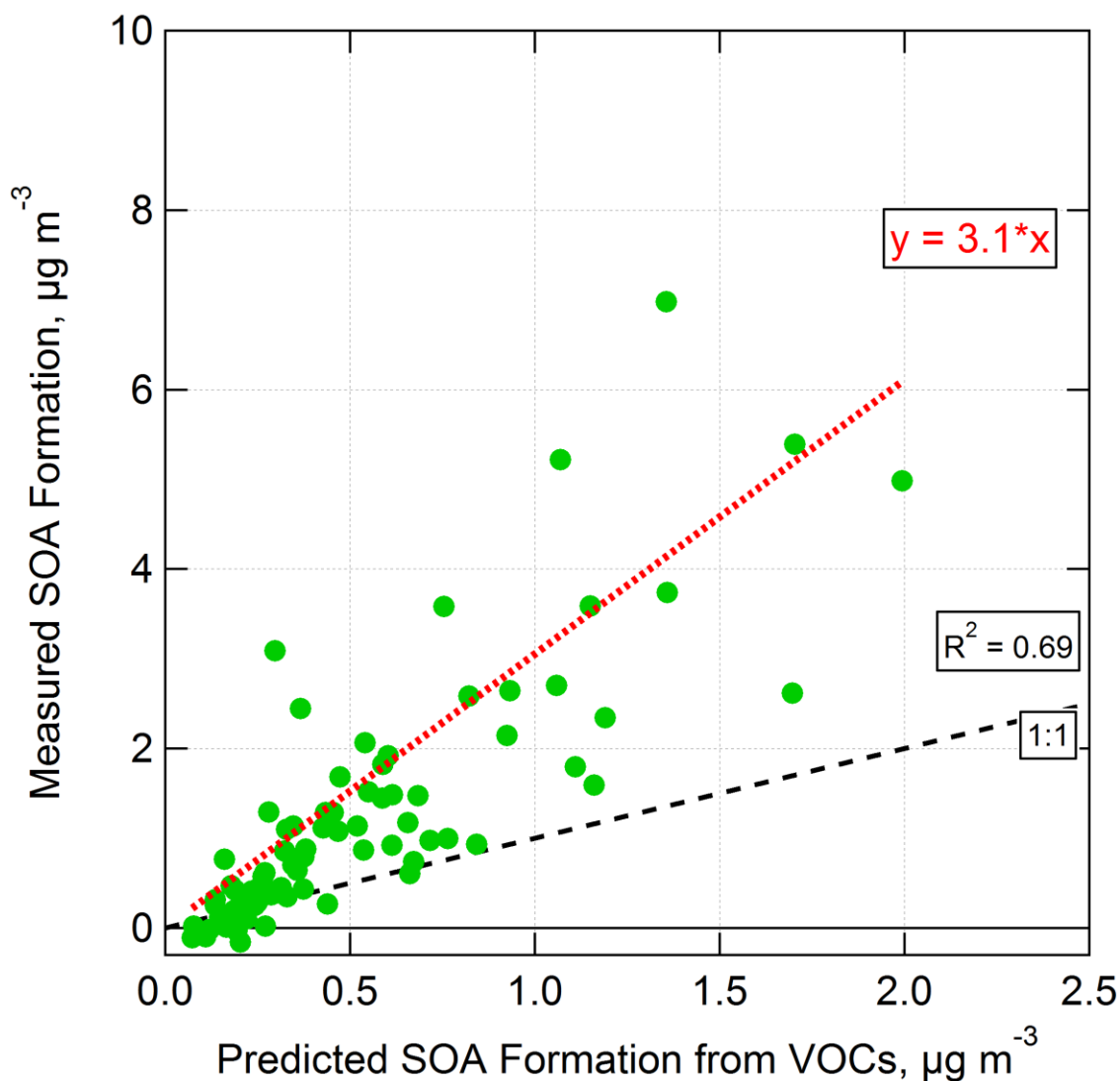


Fig. 2.S12. Measured vs. predicted SOA formation from OH oxidation of ambient air in an OFR using the OFR185 method. Only the range of photochemical ages with the highest SOA formation (0.4-1.5 eq. days) was used. The LVOC fate correction was not applied. Predicted SOA formation was calculated by applying OA concentration-dependent yields (average of 10.9%, 11.1%, 11.5%, and 2.9% for MT, SQT, toluene, and isoprene, respectively, with average OA concentration of $2.9 \mu\text{g m}^{-3}$) to VOCs reacted in the OFR (Tsimpidi et al., 2010). The amount of reacted VOCs was estimated using OH_{exp} and ambient VOC concentrations. If a non-zero y-intercept is allowed, the regression line becomes $y = 4.0x - 0.8$.

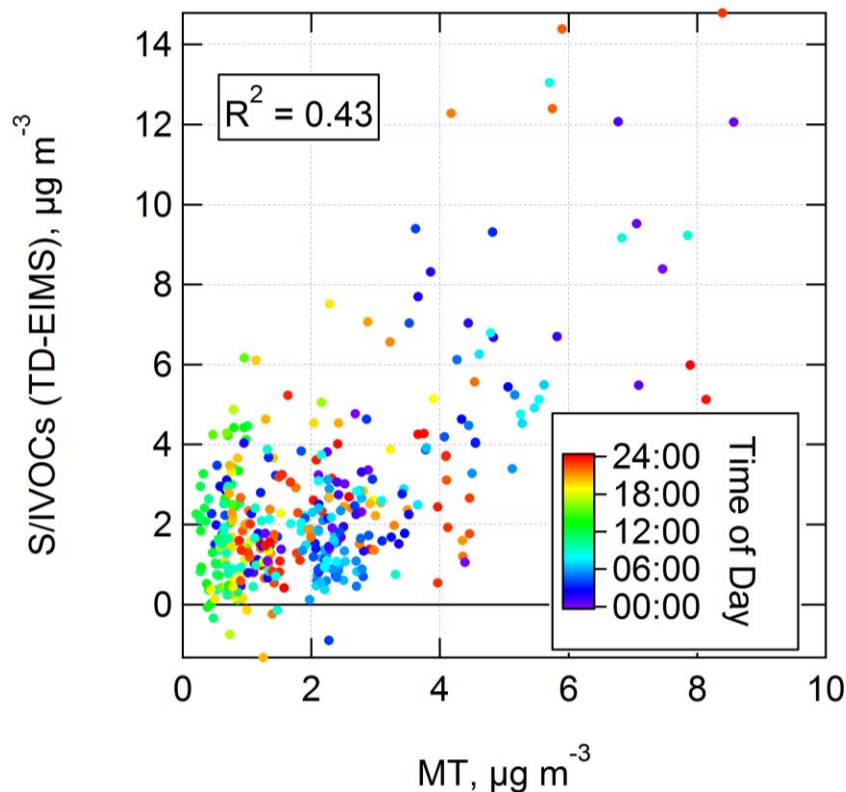


Fig. 2.S13. Scatterplot of mass concentration of ambient S/IVOCs (lower limit measured by TD-EIMS) vs. ambient MT measured by PTR-TOF-MS. Data are shown colored by local time of day.

Acknowledgements

We thank US NSF grants AGS-1243354 and AGS-1360834, NOAA grants NA13OAR4310063 and NA10OAR4310106, U.S. DOE ASR Program (Office of Science, BER, DE-SC0011105), Austrian Science Fund (FWF) project number L518-N20, and the US EPA (STAR 83587701-0) for partial support for this research. BBP acknowledges support from a CIRES Graduate Student Research Fellowship and a US EPA STAR Graduate Fellowship (FP-91761701-0). LK acknowledges support from DOC-fFORTE-fellowship of the Austrian Academy of Science. This work has not been formally reviewed by the US EPA. The views expressed are solely those of the authors, and the US EPA does not endorse any products or commercial services mentioned in this work. AMO acknowledges a fellowship from the DOE SCGP Fellowship Program (ORAU, ORISE). We are grateful to Alex Guenther and Jim Smith of NCAR for co-organizing the BEACHON-RoMBAS field campaign, to Andrew Turnipseed for SO₂ measurements, and to the USFS Manitou Experimental Forest Observatory for site support.

CHAPTER 3

Secondary organic aerosol formation from in situ OH, O₃, and NO₃ oxidation of ambient forest air in an oxidation flow reactor

Adapted from B.B. Palm, P. Campuzano-Jost, D.A. Day, A.M. Ortega, J.L. Fry, S.S. Brown, K.J. Zarzana, W. Dube, N.L. Wagner, D.C. Draper, L. Kaser, W. Jud, T. Karl, A. Hansel, C. Gutiérrez-Montes, and J.L. Jimenez. *Atmos. Chem. Phys.*, submitted. 2017.

Abstract

Ambient pine forest air was oxidized by OH, O₃, or NO₃ radicals using an oxidation flow reactor (OFR) during the BEACHON-RoMBAS (Bio-hydro-atmosphere interactions of Energy, Aerosols, Carbon, H₂O, Organics & Nitrogen–Rocky Mountain Biogenic Aerosol Study) campaign to study biogenic secondary organic aerosol (SOA) formation and organic aerosol (OA) aging. A wide range of equivalent atmospheric photochemical ages was sampled, from hours up to days (for O₃ and NO₃) or weeks (for OH). Ambient air processed by the OFR was typically sampled every 20-30 min, in order to determine how the availability of SOA precursor gases in ambient air changed with diurnal and synoptic conditions, for each of the three oxidants. More SOA was formed during nighttime than daytime for all three oxidants, indicating that SOA precursor concentrations were higher at night. At all times of day, OH oxidation led to approximately 4 times more SOA formation than either O₃ or NO₃ oxidation. This is likely because O₃ and NO₃ will only react with gases containing C=C bonds (e.g., terpenes) to form SOA, but won't react appreciably with many of their oxidation products or any species in the gas phase that lacks a C=C bond (e.g., pinonic acid, alkanes). In contrast, OH can continue to react with compounds that lack C=C bonds to produce SOA. Closure was achieved between the amount of SOA formed from O₃ and NO₃ oxidation in the OFR and the SOA predicted to form from measured concentrations of ambient monoterpenes and sesquiterpenes using published chamber yields. This is in contrast to previous work at this site (Palm et al., 2016), which has shown that a source of SOA from semi- and intermediate-

volatility organic compounds (S/IVOCs) 3.4 times larger than the source from measured VOCs is needed to explain the measured SOA formation from OH oxidation. This work suggests that those S/IVOCs typically do not contain C=C bonds. O₃ and NO₃ oxidation produced SOA with elemental O:C and H:C similar to the least oxidized OA observed in local ambient air, and neither oxidant led to net mass loss at the highest exposures, in contrast with OH oxidation. An OH exposure in the OFR equivalent to several hours of atmospheric aging also produced SOA with O:C and H:C values similar to ambient OA, while higher aging (days–weeks) led to formation of SOA with progressively higher O:C and lower H:C (and net mass loss at the highest exposures). NO₃ oxidation led to the production of particulate organic nitrates (pRONO₂), while OH and O₃ oxidation (under low NO) did not, as expected. These measurements of SOA formation provide the first direct comparison of SOA formation potential and chemical evolution from OH, O₃ and NO₃ oxidation in the real atmosphere, and help to clarify the oxidation processes that lead to SOA formation from biogenic hydrocarbons.

3.1 Introduction

Submicron atmospheric aerosols have important impacts on radiative climate forcing (Myhre et al., 2013) and human health (Pope and Dockery, 2006). A large fraction of submicron particulate mass is composed of organic aerosols (OA), and is produced from a variety of sources (Zhang et al., 2007). Primary OA (POA) is directly emitted as particles (e.g., via fossil fuel combustion, biomass burning), while secondary OA (SOA) can be formed through gas-phase oxidation and gas-to-particle conversion of directly emitted organic gases, or via aqueous pathways. Globally, SOA comprises the majority of OA, particularly in rural locations away from primary sources (Zhang et al., 2007; Jimenez et al., 2009). However, the processes of formation, chemical transformation, and removal of SOA remain uncertain (Hallquist et al., 2009; Shrivastava et al., 2016).

Hydroxyl radicals (OH), ozone (O₃), and nitrate radicals (NO₃) are the three major oxidants in the atmosphere that react with organic gases to form SOA. The initial steps of oxidation for each oxidant are summarized here according to Atkinson and Arey (2003):

- OH can react via H-abstraction or addition to a C=C double bond, depending on the structure of the organic molecule;
- O₃ generally reacts only with alkenes, adding to a C=C bond to produce a primary ozonide which then decomposes to form a carbonyl plus a Criegee intermediate;
- NO₃ radicals also react by addition to a C=C bond, producing an organic peroxy radical with an adjacent organic nitrate group that will react further. The nitrate functional group formed during the initial NO₃ addition can either remain in the product molecule or decompose to produce NO₂ (g).

Nearly all oxidation pathways in the atmosphere will lead to the production of a peroxy radical (RO₂), which can proceed to react with HO₂, NO₂, NO, another RO₂, or undergo autooxidation (Atkinson, 1997; Orlando and Tyndall, 2012; Crouse et al., 2013). Reaction rate constants and more detailed reaction mechanisms can be found elsewhere (e.g., Atkinson et al., 1982; Atkinson, 1997; Chew et al., 1998; Calvert et al., 2002).

SOA yields from the oxidation of a wide variety of precursor gases by each of these three oxidants have been reported. SOA yields are typically measured from oxidation experiments in large environmental chambers. These yields are evaluated through implementation in regional or global models, which can be compared to ambient measurements (e.g., Volkamer et al., 2006; Hayes et al., 2015). However, large chamber experiments have been shown to be affected by large losses of semivolatile and low volatility gases (Matsunaga and Ziemann, 2010; Zhang et al., 2014; Krechmer et al., 2015; La et al., 2016; Nah et al., 2016) and particles (Crump and Seinfeld, 1981; McMurry and Rader, 1985; Pierce et al., 2008) to the chamber walls. These artifacts affect the ability to accurately measure

SOA yields, and also limit the amount of oxidation that can be achieved in chambers. Large variability in OA concentrations exists between various global OA models, which typically achieve poor agreement and correlation with ambient surface and vertical profile OA concentration measurements (Tsigaridis et al., 2014).

In addition to bulk concentrations, the chemical composition of OA also determines its atmospheric properties. The elemental O:C and H:C ratios of OA can be measured using aerosol mass spectrometry (Aiken et al., 2008; Canagaratna et al., 2015). The O:C and H:C ratios can provide information about the sources and evolution of OA in the atmosphere (Aiken et al., 2008; Heald et al., 2010; Kroll et al., 2011; Ng et al., 2011b), and also often correlate with key OA properties such as hygroscopicity, material density, and phase separation (Jimenez et al., 2009; Bertram et al., 2011; Kuwata et al., 2012). Laboratory studies have typically struggled to reproduce the O:C and H:C values found in ambient OA, particularly for the highest O:C values found in remote areas (Aiken et al., 2008; Chen et al., 2015b).

While large chambers have been the standard method for studying SOA yields and composition, and are the basis for parameterized yields and oxidation in most models, oxidation flow reactors (OFRs) have recently become a popular alternative approach. OFRs typically have shorter residence times than chambers, which reduces wall contact. Also, ambient air can easily be oxidized in an OFR, while it is difficult and slow to perform such experiments in a large chamber (Tanaka et al., 2003). SOA yields from OH oxidation in OFRs for a variety of individual and mixed precursors have been reported, and generally show that yields in OFRs are similar to chamber yields (Kang et al., 2007, 2011, Lambe et al., 2011b, 2015; Li et al., 2013; Bruns et al., 2015). Properties related to SOA elemental composition have also been investigated in OFRs (Massoli et al., 2010; Lambe et al., 2011b, 2012, 2014; Saukko et al., 2012; Ortega et al., 2013, 2016). However, these studies were limited to laboratory-produced SOA from one or several precursor gases, often at very high concentrations. Several studies have reported on SOA

formation from the OH oxidation of ambient air (Ortega et al., 2016; Palm et al., 2016) or emission sources (Cubison et al., 2011; Keller and Burtscher, 2012; Ortega et al., 2013; Tkacik et al., 2014; Bruns et al., 2015; Karjalainen et al., 2016; Timonen et al., 2016), but SOA from O₃ and NO₃ oxidation of ambient air or direct source emissions has not been studied using an OFR, to our knowledge.

In this study, we oxidized ambient pine forest air with either OH, O₃, or NO₃ in an OFR to investigate how much SOA can be formed from real ambient mixtures of largely biogenic SOA precursor gases, how the SOA precursor concentrations varied with time, and the properties of the SOA formed. The amount of SOA formed from each oxidant was compared to the amount predicted to form from oxidation of the measured ambient VOCs that entered the OFR. We investigated the elemental composition of the SOA that was formed as a function of the amount of oxidant exposure (oxidant concentration multiplied by residence time) in the OFR. The contribution of organic nitrate to SOA formation was also explored and compared to the results with ambient and chamber studies.

3.2 Experimental methods

3.2.1 BEACHON-RoMBAS field campaign

The OFR measurements presented here were conducted during July–August 2011 as part of the BEACHON-RoMBAS field campaign (Bio-hydro-atmosphere interactions of Energy, Aerosols, Carbon, H₂O, Organics & Nitrogen – Rocky Mountain Biogenic Aerosol Study; <http://cires.colorado.edu/jimenez-group/wiki/index.php/BEACHON-RoMBAS>). The research site was located in a ponderosa pine forest in a mountain valley at the Manitou Experimental Forest Observatory, near Woodland Park, Colorado (39.10° N, 105.10° W; 2370 m elevation). An overview of previous research at this site, including BEACHON-RoMBAS and prior campaigns, has been presented in detail by Ortega et al. (2014). Here we present a brief summary of research site details that are relevant to this analysis.

VOC concentrations at the site (quantified using proton-transfer-reaction time-of-flight mass spectrometry; PTR-TOF-MS) varied on a diurnal cycle, dominated by 2-methyl-3-buten-2-ol (MBO)

during daytime and monoterpenes (MT) during nighttime. Fry et al. (2013) and Palm et al. (2016) show diurnal cycles of select biogenic and anthropogenic VOCs. VOC measurements from a July–September 2008 campaign at the same site have also been described in Kim et al. (2010). During BEACHON-RoMBAS, the concentration of MBO+isoprene in the forest canopy ranged from about 2 ppb during daytime to 0.4 ppb at nighttime (details can be found in Palm et al., 2016). The ratio of isoprene to MBO at this pine forest site was determined using NO^+ reagent ion chemical ionization mass spectrometry (Karl et al., 2012) and using GC-MS (Kaser et al., 2013a) to be about 21%, indicating the concentration of isoprene at this site was low (<0.3 ppb). MT concentrations in the canopy spanned from 0.4 ppb during the day to 1.1 ppb at night, on average. The Manitou Experimental Forest Observatory site is mainly influenced by biogenic emissions, but occasionally receives airflow from nearby urban areas (Denver metropolitan area and Colorado Springs, 75 and 35 km away from the site respectively), leading to moderate increases in NO_x (up to 3 ppbv), CO (up to 140 ppbv), and anthropogenic VOCs (e.g., aromatics) during late afternoon and evening (Fry et al., 2013; Ortega et al., 2014).

3.2.2 OFR methods

The OFR used in this study was the Potential Aerosol Mass (PAM) flow reactor (Kang et al., 2007, 2011). The PAM reactor is a cylindrical tube 45.7 cm long and 19.7 cm ID with a volume of approximately 13 liters. This type of OFR has been used to study SOA formation and chemistry in a number of previous studies (e.g., Kang et al., 2007, 2011; Massoli et al., 2010; Lambe et al., 2012, 2015; Li et al., 2013; Ortega et al., 2013, 2016; Tkacik et al., 2014; Palm et al., 2016). During BEACHON-RoMBAS, ambient air was sampled through a 14 cm diameter opening on one end of the OFR (with the inlet plate removed to prevent loss of gases/particles on inlet surfaces) through a coarse-grid mesh screen coated with an inert silicon coating (Sulfinert by Silcotek, Bellefonte, PA). The OFR was located on top of the measurement trailer in order to sample ambient air directly without using an inlet. Therefore the temperature and RH inside the OFR were the same as ambient conditions, with the exception of minor heating from the UV

lamps mounted inside the OFR (up to $\sim 2^\circ\text{C}$ heating at the highest lamp settings; Li et al., 2015). The OFR was operated with a residence time in the range of 2–4 min. The residence time distribution in the OFR, modeled using FLUENT for the configuration used in this study (inlet plate removed), is shown in Fig.

3.S1. The modeled residence time distribution is much more homogeneous than has been measured for OFRs operated with an inlet plate (Lambe et al., 2011; Ortega et al., 2016). However, local winds can result in some variations that are not captured by the FLUENT model. Two OFRs were used simultaneously, with one dedicated to NO_3 oxidation while the other was used for either OH or O_3 oxidation. OH radicals were produced in situ inside the OFR using two different methods, referred to as OFR185 and OFR254 (named according to the wavelength of the highest energy UV light used to generate oxidants within the reactor). These methods have been described in detail previously and showed consistent results (Palm et al., 2016). All results of OH oxidation presented in this paper used the OFR185 method. The gas-phase HO_x/O_x chemistry and possible non-OH chemistry inside the OFR was investigated with kinetic modeling (Li et al., 2015; Peng et al., 2015, 2016b). For the wide variety of compounds investigated in Peng et al. (2016b), reactions with OH dominated over other possible reactions, including $\text{O}(^1\text{D})$, $\text{O}(^3\text{P})$, O_3 , and photolysis at 185 nm or 254 nm, under the conditions of OH oxidation in the OFR during this campaign.

NO_3 radicals were generated by thermal decomposition of N_2O_5 ($\text{N}_2\text{O}_5 \rightarrow \text{NO}_2 + \text{NO}_3$), which was injected into the OFR from a cold trap held in a dry ice + isopropyl alcohol bath. The cold trap was held near -60°C using a temperature controlled copper sleeve immersed in the -78°C bath. A 10–100 sccm flow of zero air eluted N_2O_5 from the trap. This N_2O_5 +zero air mixture was injected through an approximately 14 cm diameter ring of 1/8" Teflon tubing with pinholes around the ring mounted just inside the OFR entrance inside the mesh screen. N_2O_5 concentrations were adjusted by changing this flow rate from the N_2O_5 dry ice reservoir. The concentrations of N_2O_5 and NO_3 in both the injection flow and in the output of the OFR were measured using diode laser-based cavity ring-down spectroscopy

(CRDS; Wagner et al., 2011). The concentration of NO_2 was measured in the output of the OFR using laser-induced fluorescence (Thornton et al., 2000). The experimental setup for the NO_3 -OFR system is illustrated in Fig. 3.S2 and discussed in Sect. 3.5.1.

To estimate NO_3 concentrations and exposure in the OFR, the relevant chemistry was modeled using a chemical-kinetic plug-flow model, implemented in the KinSim chemical-kinetic integrator (version 3.10) using Igor Pro 6 (<http://www.igorexchange.com/node/1333>; Wavemetrics, Lake Oswego, OR, USA). A key output of this model was the integrated NO_3 exposure experienced by MT-containing air during the OFR residence time, calculated as the integral of NO_3 concentration over the OFR residence time (in units of molecules cm^{-3} s), and multiplied by the fraction of MT that was estimated to have been mixed with the N_2O_5 flow at each residence time, due to lack of mixing from the small flow rate (see Sect. 3.5.1 for more details of the unmixed fraction estimation and parameterization). NO_3 exposure was converted to an equivalent (eq.) atmospheric age by dividing by a typical site-specific nighttime ambient NO_3 concentration, which has been estimated to be on the order of 1 ppt (Fry et al., 2013). This eq. age represents the amount of time the air would have to spend in the atmosphere with 1 ppt NO_3 to experience the same amount of NO_3 exposure as in the OFR. The unit of eq. age is a unit of exposure. When given in units of eq. days, it represents the number of 24 h periods that air would need to spend in an atmosphere containing the stated oxidant concentration in order to achieve the equivalent amount of exposure as in the OFR (which applies for OH and O_3 eq. ages as well). More details about the model can be found in Sect. 3.5.1.

The exposure metric for the NO_3 -OFR is specific to the site in which it is measured. Fry et al. (2013) estimated the average nighttime NO_3 concentration at this site (approximately 1 pptv) from an average NO_3 production rate and lifetime of approximately 0.03 pptv s^{-1} and 25 s, respectively. Other sites can have considerably different production rates for NO_3 and thus very different nighttime exposures. Remote forests, with nighttime NO_x below 50 pptv, could experience NO_3 production rates

more than 10 times slower, while forests immediately downwind of urban areas could have NO₃ production rates more than 10 times faster (e.g., outflow from Houston, TX; Brown et al., 2013). Variability in NO₃ production rates and observed NO₃ levels is a common feature of recent field observations (Brown and Stutz, 2012). Estimated eq. NO₃ ages from this study are therefore shown simply for a common point of comparison for all of the data during this study, interpretable in terms of the average chemistry occurring at the BEACHON site only. Interpretations of specific nights would need to consider night-to-night NO₃ variability, and interpretation of measurements at other sites would also need to be adjusted to local NO₃ concentrations.

To investigate SOA formation from O₃ oxidation, O₃ was produced external to the OFR by flowing pure dry O₂ gas across two low-pressure mercury UV lamps (BHK, Inc., model no. 82-9304-03). The O₂ was photolyzed by 185 nm light to produce O(³P), which further reacted with O₂ to produce O₃. This O₂+O₃ mixture was injected at 0.5 lpm into the front of the OFR through four ports distributed evenly around and just inside the 14 cm opening. O₃ concentrations were cycled by adjusting the UV lamp intensity (i.e., photon flux) in the O₃ generation setup. O₃ was measured in the output of the OFR using a 2B Technologies Model 205 Monitor. O₃ exposure was calculated by multiplying the measured O₃ concentration in the OFR output by the residence time of the OFR. Loss of injected O₃ to internal OFR walls was not investigated, so the exposure may be slightly underestimated by this method. O₃ exposure was converted to an eq. atmospheric age by dividing by a typical, site-specific, 24 h average, ambient O₃ concentration of 50 ppb. A schematic of the O₃-OFR system is also shown in Fig. 3.S2.

3.2.3 Particle and gas measurements

Ambient and OFR-oxidized particles were measured with an Aerodyne High-Resolution Time-of-Flight Aerosol Mass Spectrometer (HR-ToF-AMS, referred to here as AMS; DeCarlo et al., 2006; Canagaratna et al., 2007) and a TSI 3936 Scanning Mobility Particle Sizer (SMPS). Details of these measurements have been described previously (Palm et al., 2016). Ambient VOC concentrations were

quantified using a PTR-TOF-MS (Kaser et al., 2013a). The OFR output was sampled by the PTR-TOF-MS during selected periods only (Aug 4–6, 9–10, and 22–23 for NO₃ oxidation, and Aug. 7–9 and 23–24 for O₃ oxidation; see Palm et al. (2016) for details of sampling VOCs during OH oxidation). The particle mass measurements were corrected for particle losses to sampling line walls and at the small particle transmission limit of the AMS aerodynamic lens (combined 2% correction; details of these corrections are the same as in Palm et al., 2016). To account for particle losses to internal OFR surfaces, the particle mass was corrected by the average ratio of ambient particle mass to the particle mass measured through each OFR in the absence of oxidant (1% correction for the O₃ OFR, and 14% for the NO₃ OFR due to a different sampling port with a higher wall surface-area-to-volume ratio).

A correction was also applied to account for any condensable oxidation products (referred to as low-volatility organic compounds; LVOCs) that were formed from gas-phase oxidation in the OFR but condensed on OFR or sampling line walls instead of condensing to form SOA. This is non-atmospheric behavior, due to the short residence time in the OFR and the relatively small aerosol condensational sink in this study. A correction is needed because the dominant fate of such gases in the atmosphere will be condensation to form SOA (lifetime of ~minutes) rather than being lost to any environmental surfaces via dry or wet deposition (lifetime of ~hours to a day; Farmer and Cohen, 2008; Knote et al., 2015; Nguyen et al., 2015). This correction, referred to as the “LVOC fate correction”, was first represented in a model developed in Palm et al. (2016); the full details of the model can be found there. Briefly, the model takes several inputs, including particle condensational sink, OFR residence time, and oxidant concentration. It produces the fractional fates of LVOCs with respect to condensation onto particles, condensation onto OFR walls, further oxidation to give non-condensable molecular fragmentation products, and condensation onto sampling line walls after exiting the back of the OFR. In Palm et al. (2016), the model was verified by quantitatively explaining SO₄ aerosol formation from OH oxidation of ambient SO₂.

The results of the LVOC fate model for the O₃-PAM and NO₃-PAM conditions in this study are shown in Fig. 3.S3. The SOA formation values given in the subsequent analysis are corrected for LVOC fate by dividing the measured SOA formation by the fraction of LVOCs predicted to have condensed to form SOA in the OFR (an average correction of 0.4 μg m⁻³ for both O₃-PAM and NO₃-PAM). These corrected values refer to the amount of SOA that would form from any ambient precursors in the absence of OFR walls and the limited time for condensation within the OFR. LVOCs are assumed not to be lost to fragmentation from excessive O₃ or NO₃ reactions in the gas-phase prior to condensation due to lack of C=C bonds (which is different from the parameterization for OH reactions used in Palm et al., 2016). This assumption is reinforced by the fact that for the highest O₃ and NO₃ eq. ages achieved in this work, SOA formation was always observed when SOA-forming gases were present (see Sect. 3.3.2.1). If fragmentation reactions in the gas phase (or from heterogeneous oxidation) were important, observations would show a lack of SOA formation (or net loss of OA) at the highest ages when SOA-forming gases (e.g., MT) were present.

3.2.4 Modeling of SOA formation

In the analysis in Sect. 3.3.2.2, the amount of SOA formed by oxidation of ambient air by O₃ or NO₃ in the OFR is compared to the amount predicted to form. This predicted amount was estimated by applying SOA yields to the fraction of measured ambient MT and sesquiterpenes (SQT) concentrations that were predicted to react. Since the ambient VOC measurements were taken above the canopy at a height of 25 m, the concentrations were corrected to reflect in-canopy values that were ingested into the OFR, a technique which has been used previously (Kim et al., 2013; Wolfe et al., 2014; Palm et al., 2016). During this campaign, speciated MT and SQT measurements were not available. When predicting SOA formation in this analysis, we use previous measurements at the same site to approximate that MT consisted of an equal mix of *α*-pinene, *β*-pinene, and 3-carene and that SQT was solely isolongifolene (Kim et al., 2010). Numerous chamber studies have reported SOA yields of individual MT from O₃

oxidation (e.g., Ng et al., 2006; Pathak et al., 2007, 2008; Shilling et al., 2008; Zhao et al., 2015) and from NO₃ oxidation (Hallquist et al., 1999; Moldanova and Ljungström, 2000; Spittler et al., 2006; Fry et al., 2009, 2011, 2014; Boyd et al., 2015; Ng et al., 2016). SOA yields from SQT have also been reported for O₃ oxidation (Jaoui et al., 2003, 2013; Ng et al., 2006; Winterhalter et al., 2009; Chen et al., 2012; Tasoglou and Pandis, 2015) and NO₃ oxidation (Fry et al., 2014). In this analysis, the OA concentrations measured after O₃ or NO₃ oxidation ranged from 1–3 µg m⁻³, with few exceptions. For simplicity with this relatively narrow range, the dependence of SOA yields on OA concentrations was not included. Instead, we applied representative SOA yields of 15% for ozonolysis of α -pinene, β -pinene, and 3-carene, and 30% for ozonolysis of isolongifolene. For reaction with NO₃, SOA yields of 4%, 33%, 38%, and 86% were used for α -pinene, β -pinene, 3-carene, and isolongifolene (using β -caryophyllene as a proxy for all SQT; Fry et al., 2014; Kang et al., 2016; Ng et al., 2016). The rate constants used for reaction of α -pinene, β -pinene, 3-carene, and isolongifolene with O₃ and NO₃ were $k_{O_3} = 8.6 \times 10^{-17}$, 1.5×10^{-17} , 3.6×10^{-17} , and 1.1×10^{-17} cm³ molec⁻¹ s⁻¹, and $k_{NO_3} = 6.1 \times 10^{-12}$, 2.5×10^{-12} , 9.5×10^{-12} , and 3.9×10^{-12} cm³ molec⁻¹ s⁻¹, respectively (Canosa-Mas et al., 1999; Atkinson and Arey, 2003; Richters et al., 2015).

3.3 Results and discussion

3.3.1 Modeled vs. measured NO₃ and O₃ exposures

One of the features of the OFR technique is the short residence time required for conducting high time resolution ambient measurements. Combined with the ability to rapidly change the amount of oxidant injected or produced in the OFR, this allows for a wide range of oxidation levels to be studied in a short amount of time (and thus with limited variation of ambient conditions). In this work, the oxidant concentration was changed every 20–30 min, covering a range from no added oxidant to maximum oxidation repeatedly in 2–3 h cycles. In order to interpret the results over the wide range of oxidant exposure, the amount of exposure must be quantified. In Palm et al. (2016), OH exposure was estimated using a model-derived equation (Li et al., 2015; Peng et al., 2015) and calibrated using PTR-TOF-MS

measurements of VOC decay in the OFR. In this work, a simple box model was developed and compared with VOC decay measurements to estimate NO_3 and O_3 exposures in the OFR.

The set of reactions and rate constant parameters included in the modeling of NO_3 exposure are shown in Table 3.S1. Figure 3.1 illustrates the most important mixing ratios and reactive fluxes in the OFR with injected N_2O_5 under typical conditions. Interconversion between N_2O_5 and $\text{NO}_2 + \text{NO}_3$ was relatively rapid, which maintained the system near equilibrium at all times. Wall loss of N_2O_5 was estimated to be the main loss of the injected nitrogen-containing species (84%), while reaction of NO_3 with biogenic gases (2%), NO_3 wall losses (14%), and hydrolysis of N_2O_5 on particle surfaces (0.2%) were minor loss pathways. Figure 3.2a–c compares the N_2O_5 , NO_2 , and NO_3 mixing ratios measured in the OFR output with those predicted by the model. The model is generally consistent with the measurements. The scatter in the measurements is thought to be due mainly to incomplete and/or variable mixing of the injected N_2O_5 flow into the sampled ambient air (see Sect. 3.5.1 for more details), with some contribution from measurement variability at low ambient MT concentrations. The critical output of this model for our application is the prediction of the fraction of MT reacted. Figure 3.2d shows that the model can reproduce the measured MT decay with an error (average absolute value of modeled minus measured fraction MT remaining) of 11%, providing confirmation that using the model output NO_3 exposure in the subsequent analysis of aerosol mass yields from the OFR is justified. A similar analysis of SQT decay was not possible, because ambient SQT concentrations were too small to accurately measure fractional decays. Also, MBO did not react substantially with NO_3 in the OFR, consistent with the lifetime for reaction of NO_3 with MBO that is approximately 3 orders of magnitude slower than for reaction with MT (Atkinson and Arey, 2003). This is also representative of the atmosphere, where MBO will overwhelmingly react with OH or O_3 and not NO_3 (Atkinson and Arey, 2003).

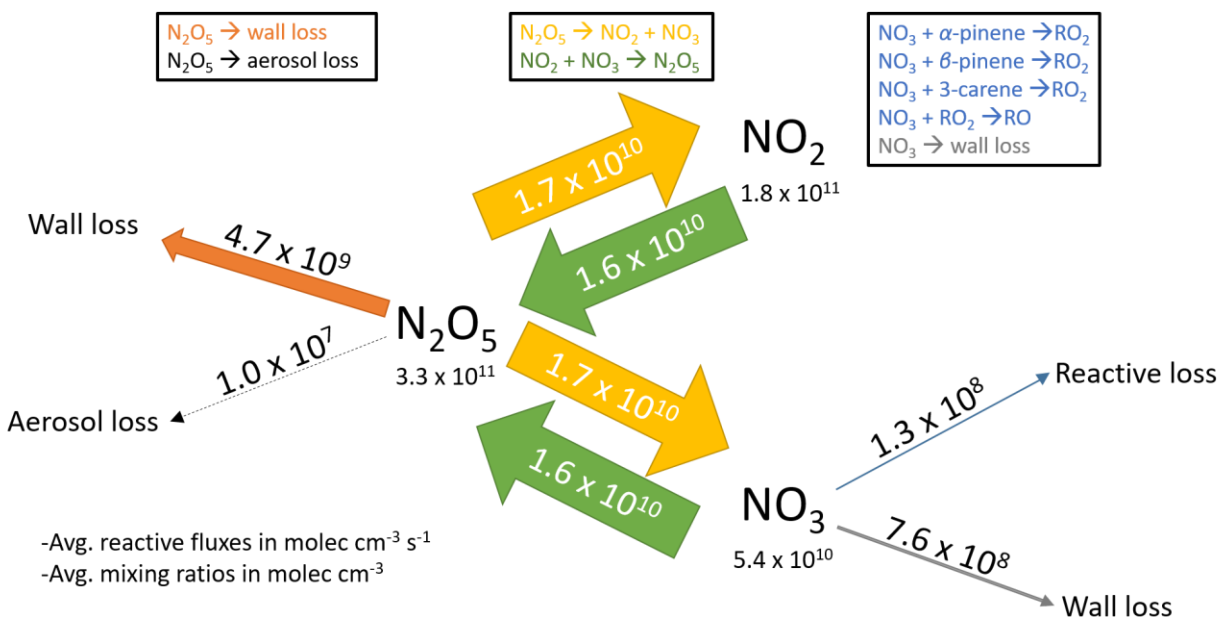


Fig. 3.1. Typical average mixing ratios and reactive fluxes for the major reactions in the NO_3 -OFR when injecting N_2O_5 to investigate SOA formation from NO_3 oxidation. These reactive fluxes resulted from running the model with inputs of 25°C, 50% RH, 50 ppb O_3 , 2 ppb NO_2 , 1.5 ppb NO_3 , 50 ppb N_2O_5 , 0.75 ppb total MT, and a rate constant for N_2O_5 uptake to aerosol surfaces of $3 \times 10^{-5} \text{ s}^{-1}$. Reaction arrow widths are sized relative to their average reactive fluxes. Reactions that were included in the model (shown in Table 3.S1) but with smaller average rates are not shown here.

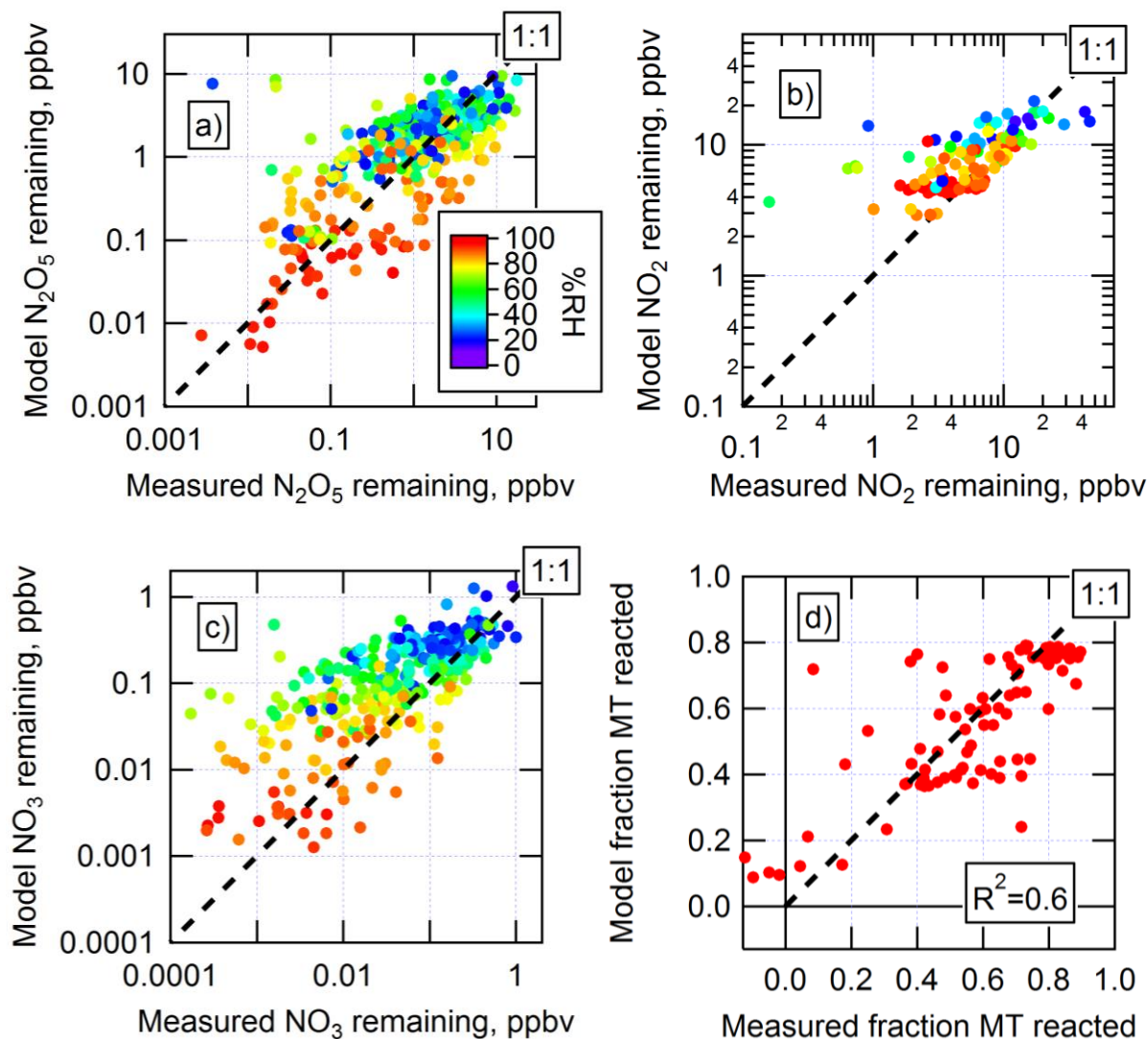


Fig. 3.2. Modeled vs. measured a) N_2O_5 , b) NO_2 , c) NO_3 , and d) fraction of ambient MT reacted with NO_3 in the output of the NO_3 -OFR.

Unlike NO_3 exposure, the estimation of O_3 exposure did not require a detailed chemical model since the O_3 system had no reservoir species analogous to N_2O_5 . O_3 exposure was simply estimated as the measured O_3 concentration in the OFR output multiplied by residence time. To verify this estimate, the measured fraction of MT that reacted in the OFR was compared in Fig. 3.3 to a model prediction calculated using a simple set of reactions of ozone with the three major MT species (Table 3.S2). The model is consistent with measurements within an error of 9%, and shows that a parameterization for mixing of the O_3 flow into ambient air was not needed. In contrast to the slower 10–100 sccm flow of

N_2O_5 , the 0.5 lpm flow of O_2+O_3 appears to have been large enough relative to the total OFR flowrate to result in sufficiently complete mixing. This result suggests that a faster flow of N_2O_5 could be used in future NO_3 oxidation experiments to facilitate better mixing.

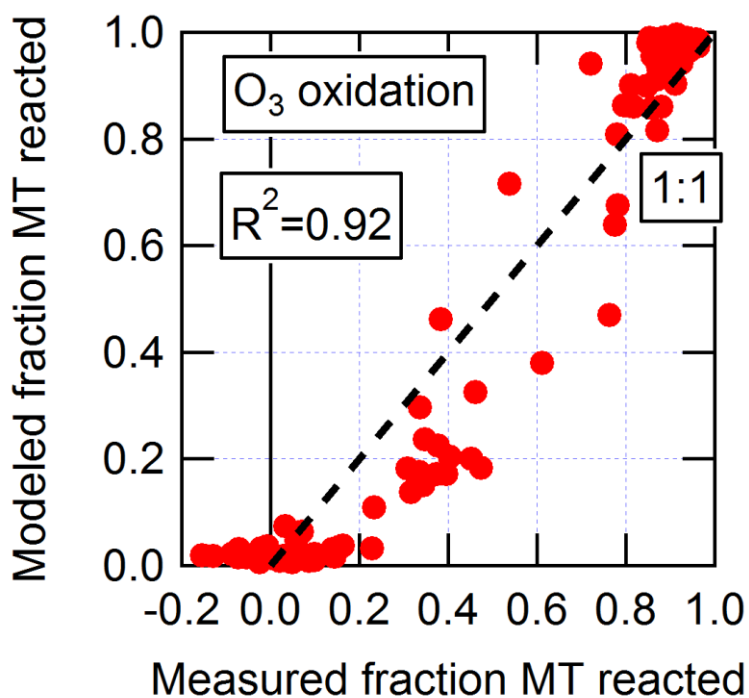


Fig. 3.3. Modeled vs. measured fraction MT reacted by O_3 oxidation in the O_3 -OFR.

Time series examples of measured and modeled MT remaining after OFR oxidation are compared to ambient MT concentrations for both NO_3 and O_3 oxidation in Fig. 3.4. These examples illustrate the dynamic range from no MT reacted (i.e., when no oxidants were added to the ambient air) to nearly all MT reacted within the 2–3 h cycles for both oxidants. Further examples are shown for NO_3 oxidation in Fig. 3.S6 and for O_3 oxidation in Fig. 3.S7.

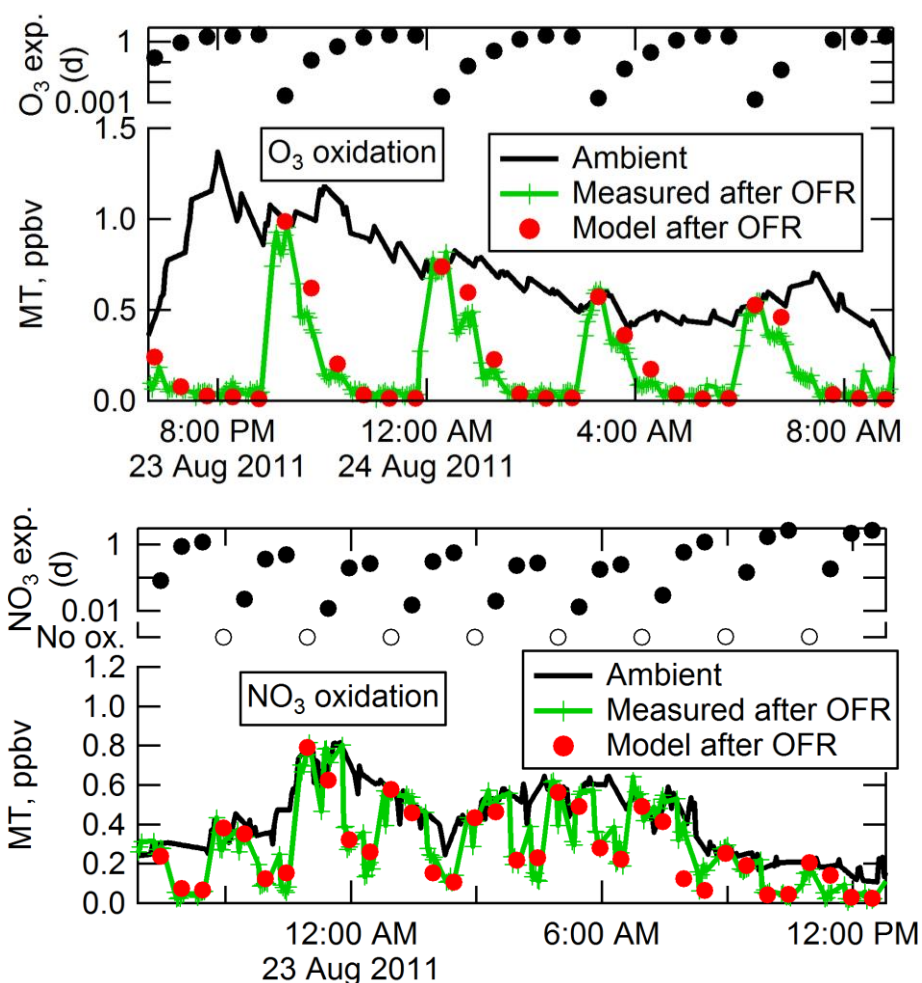


Fig. 3.4. Ambient, measured remaining, and modeled remaining MT from O₃ oxidation on Aug. 23–24 (top) and NO₃ oxidation on Aug. 22–23 (bottom) in the OFR. Modeled O₃ and NO₃ exposures are also shown. The amount of oxidation was cycled from no added oxidant (no MT reacted) to maximum oxidation (most or all MT reacted) in repeated 2–3 h cycles.

3.3.2 SOA formed from oxidation of ambient air

3.3.2.1 OA enhancement vs. photochemical age

During BEACHON-RoMBAS, ambient air was oxidized by either OH, O₃, or NO₃ in order to study the amount and properties of SOA that could be formed from ambient precursors. In situ SOA formation from OH oxidation was the subject of a previous manuscript (Palm et al., 2016). Select results are reproduced here as a comparison to SOA formation from O₃ and NO₃ oxidation. Additional new analyses of the chemical composition of SOA formed from OH oxidation is also included along with O₃ and NO₃ oxidation in Sects. 3.3.3–3.3.4.

In Palm et al. (2016), SOA formation from OH oxidation in the OFR correlated with ambient MT concentrations (and implicitly with any other gases that correlated with MT, such as SQT and possibly terpene oxidation products). Here, Fig. 3.5 shows the OA enhancement observed after O_3 and NO_3 oxidation as a function of eq. age in the OFR. Similar to OH oxidation, little SOA formation was observed from O_3 or NO_3 oxidation when ambient MT concentrations were low, regardless of the amount of exposure. When MT concentrations were higher, increasing amounts of SOA were formed with increasing exposure. As seen in Fig. 3.5 (and in Fig. 3.6 below), lower eq. NO_3 ages were achieved when MT concentrations were higher, and higher eq. NO_3 ages were achieved when MT concentrations were lower. This was because the higher MT concentrations occurred during nighttime, when lower ambient temperatures shifted the equilibrium towards N_2O_5 and away from NO_2+NO_3 , meaning lower NO_3 exposures were realized in the OFR.

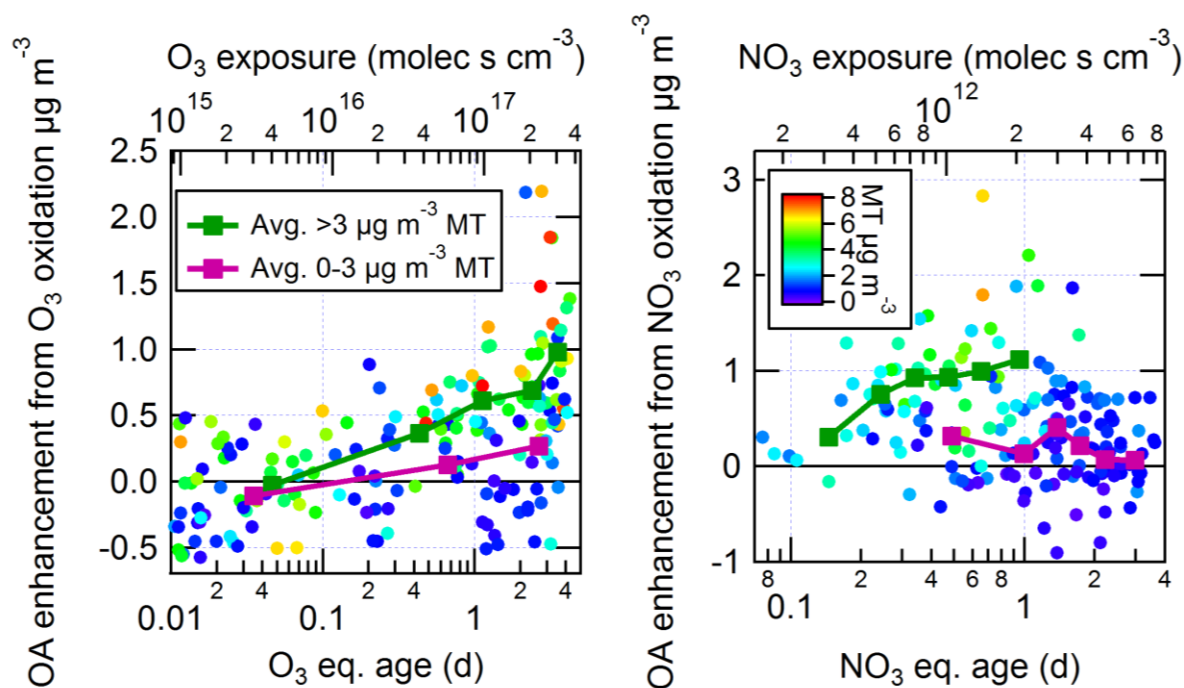
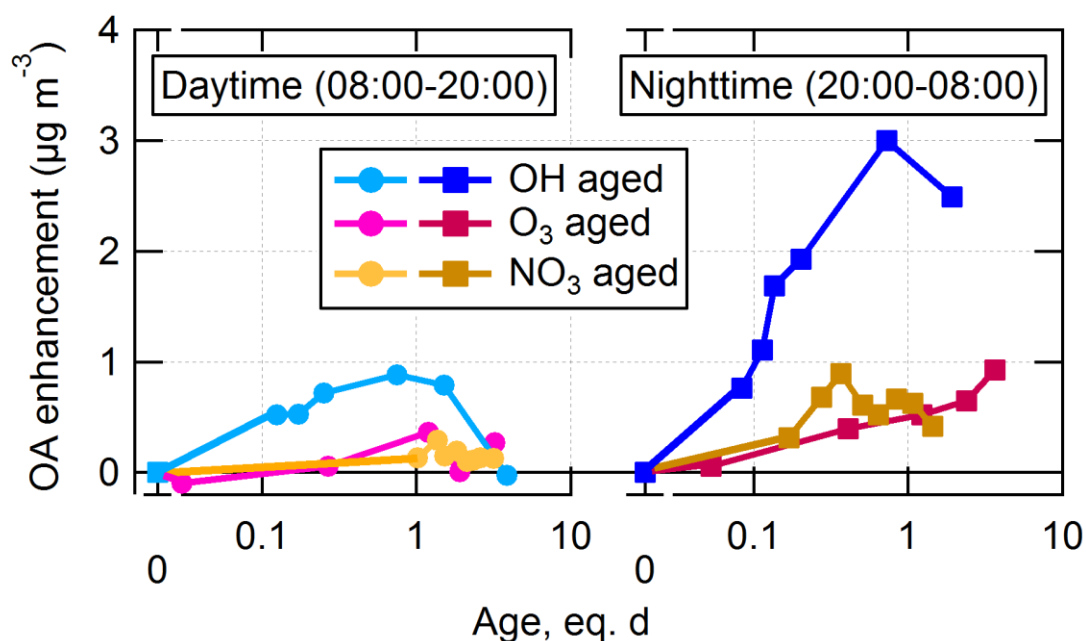


Fig. 3.5. OA enhancement from oxidation of ambient air by O_3 (left) and NO_3 (right) as a function of oxidant exposure. Data are colored by ambient in-canopy MT concentrations and include the LVOC fate correction. Binned averages for times when ambient MT concentrations were either below or above $3 \mu\text{g m}^{-3}$ (0.66 ppb) are also shown, illustrating the positive relationship between OA enhancement and MT concentrations at the higher oxidant concentrations.

Another way to examine the trends in OA enhancement is by separating the results into daytime and nighttime. Due to diurnal cycles in the emission rates (that are strong functions of temperature, and also light for some species), vertical mixing in the boundary layer, and changing rates of ambient oxidation, the concentration of MT (and other SOA precursors) in ambient air showed substantial diurnal cycles (Kim et al., 2010; Fry et al., 2013; Kaser et al., 2013a). Ambient air was characterized by higher MBO+isoprene (with ambient OH and O₃ chemistry) during the day and higher MT+SQT (with ambient O₃ and NO₃ chemistry) during the night (Fry et al., 2013). Due to these changes, it might be expected that SOA formation in the OFR would also change diurnally.

OA enhancements vs. eq. age for OH, O₃, and NO₃ oxidation are shown together in Fig. 3.6, split between daytime (08:00-20:00 LT) and nighttime (20:00-08:00 LT). For all oxidants, more SOA formation was observed during nighttime. This is consistent with the general increase in MT+SQT (average of 1.1 and 0.04 ppbv in the canopy during nighttime, and 0.4 and 0.03 ppbv during daytime, respectively) and related precursor concentrations in the shallower nighttime boundary layer. This higher SOA formation during nighttime was not a result of larger temperature-dependent partitioning to the particle phase at lower nighttime temperatures, as evidenced by stable values of measured OA enhancement per unit ambient MT (the dominant measured SOA precursor) across the whole range of ambient temperatures (shown in Fig. 3.S8). An exploration of the correlation between maximum SOA formation from each oxidant and all available ambient VOC concentrations is shown in Fig. 3.S9, illustrating that MT are the best tracer of SOA production at this forest site. The maximum amount of SOA formed from OH oxidation was approximately 4 times more than from O₃ or NO₃ oxidation for both daytime and nighttime over the eq. ages covered in this work. If the gases that formed SOA from each oxidant were the same, then this would require the SOA yields from OH oxidation to be more than 4 times larger than from O₃ or NO₃ oxidation. The references for SOA yields from O₃ and NO₃ oxidation presented herein and for OH oxidation presented in Palm et al. (2016) show this is likely not the case. Instead, one

possible explanation for this result could be that a large fraction of SOA-forming gases found in ambient air do not have C=C bonds (e.g., MT oxidation products such as pinonic acid). Such molecules would typically not react appreciably with O₃ or NO₃ over the range of eq. ages achieved in this work, but will still react with OH and may lead to SOA formation. Future O₃ and NO₃ oxidation studies could include higher eq. age ranges in order to investigate if additional SOA could be formed from ambient precursors at higher ages. This concept will be discussed further in Sect. 3.3.2.2.



(1 eq. d = 1.5×10^6 molec d cm⁻³ OH, 50 ppbv d O₃, or 1 pptv d NO₃ exposure)

Fig. 3.6. OA enhancement vs. age in eq. d for OH, O₃, and NO₃ oxidation, separated into daytime (08:00–20:00 LT) and nighttime (20:00–08:00 LT) data. All data is LVOC fate corrected. OH oxidation produced several-fold more OA enhancement than O₃ and NO₃ oxidation. OH-aged OA enhancement data is taken from Palm et al. (2016), and shows data only for <5 eq. d aging where the LVOC fate correction could be applied.

Whereas a net loss of OA was observed at >10 eq. days of OH aging due to heterogeneous oxidation (shown in Fig. 7 of Palm et al., 2016), a similar net loss of OA at the highest eq. ages of O₃ and NO₃ oxidation was not observed. Since the highest eq. ages for both O₃ and NO₃ oxidation were approximately 5 days, it is unclear if O₃ or NO₃ heterogeneous oxidation would lead to net loss of

ambient OA at substantially higher ages. Future experiments could be designed to achieve higher ages in order to investigate this effect.

3.3.2.2 Measured vs. predicted OA enhancement

When ambient air is sampled into an OFR, any gases or particles present in that air are subject to oxidation. Measurement of the resultant SOA formation is a top-down measure of the total SOA formation potential of that air as a function of eq. age of oxidation. In other words, an OFR can be used to determine the relative concentrations of SOA-forming gases present in ambient air at any given time. To provide context to the measurements in the OFR, a bottom-up analysis can be carried out by applying laboratory SOA yields to the measured ambient SOA-forming gases that are entering the OFR.

The measured SOA formation after oxidation by O_3 and NO_3 is shown vs. the SOA predicted to form from measured precursor gases in Fig. 3.7. The measured SOA formation includes all ages greater than 0.7 eq. d for O_3 -PAM and greater than 0.3 eq. d for NO_3 -PAM, where most or all of the VOCs have reacted. For both oxidants, the data are scattered along the 1:1 line of equal measured and predicted SOA formation. This is in contrast to the analysis for OH oxidation in Palm et al. (2016), where a factor of 4.4 more SOA was formed from OH oxidation than could be explained by measured VOC precursors. As shown in that analysis, the additional SOA-forming gases in ambient air were likely S/IVOCs, where the SOA formation from S/IVOCs was 3.4 times larger than the source from VOCs. This conclusion was supported by unspiciated measurements of total S/IVOC concentrations (classified by volatility). SOA yields from S/IVOCs or any other sources are not required to explain SOA formation from O_3 or NO_3 . This suggests that the majority of S/IVOCs in this ambient forest air generally did not contain C=C bonds, and therefore did not typically react with O_3 or NO_3 to produce SOA on atmospherically relevant time scales. This is consistent with expectations based on laboratory and ambient studies of MT and SQT oxidation products. Typical oxidation products include compounds such as pinic acid, pinonic acid, pinonaldehyde, caronaldehyde, and nopinone, none of which contain C=C double bonds (e.g., Calogirou et al., 1999b; Yu

et al., 1999; Lee et al., 2006). As an example, the reaction rates of pinonaldehyde with OH, O₃, and NO₃ are 3.9×10^{-11} , $<2 \times 10^{-20}$, and 2.0×10^{-14} cm³ molec⁻¹ s⁻¹, respectively (Atkinson et al., 2006). These rates correspond to eq. lifetimes of 4.7 h, >579 d, and 29 d, respectively, showing that pinonaldehyde will typically only react with OH in the atmosphere or in the OFR under the conditions in this study.

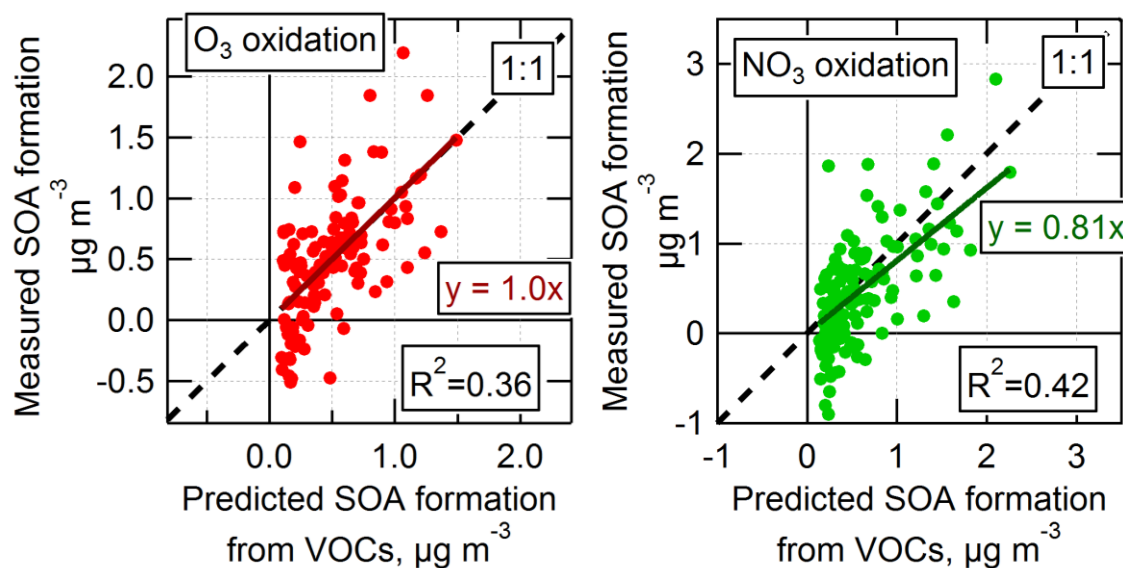


Fig. 3.7. Measured vs. predicted SOA formation for O₃ and NO₃ oxidation in an OFR. The measured SOA formation includes the LVOC fate correction, and includes all ages greater than 0.7 eq. d for O₃-PAM and greater than 0.3 eq. d for NO₃-PAM. Predicted SOA formation was estimated by applying published chamber SOA yields to the mass of VOCs predicted by the model to be oxidized in the OFR (see Sect. 3.2.3 for details).

While the measured and predicted SOA formation shown in Fig. 3.7 are consistent with each other, two main caveats limit the strength of the conclusions that can be drawn from this particular study. First, the amount and dynamic range of SOA formed from O₃ and NO₃ oxidation were relatively small, as were the total ambient aerosol concentrations. This caused the SMPS+AMS measurement noise and variability to be larger relative to the total aerosol measurements than they would be for higher aerosol concentrations. Also, as only a small amount of new SOA was formed, the aerosol condensational sink remained relatively low for all measurements. According to the LVOC fate model, on average only 31% and 36% of LVOCs condensed to form SOA during O₃ and NO₃ oxidation, respectively

(see Fig. 3.S3). This required a correction of approximately a factor of 3 to correct measured SOA formation to what would occur in normal atmospheric conditions.

3.3.3 H:C and O:C ratios of SOA formed from oxidation of ambient air

Analysis of ambient high-resolution AMS spectra can be used to estimate the elemental composition of OA (Aiken et al., 2008; Canagaratna et al., 2015). When SOA is formed in the OFR, the OA that is sampled in the OFR output is a sum of preexisting ambient OA and any SOA produced from oxidation. At sufficiently high eq. ages, the sampled OA will also include the effects of heterogeneous oxidation. The amount of O, C, and H atoms added by oxidation can be calculated by subtracting the ambient elemental concentrations from those measured after aging. The amounts of each element added by oxidation can be used to determine the O:C and H:C elemental ratios of the SOA that is formed in the OFR.

The amounts of O and H vs. C added from OH oxidation are shown in Fig. 3.8. Slopes were fit to the data with positive net addition of C in order to determine the O:C and H:C of the SOA formed for the eq. photochemical age ranges of 0.1–0.4 (avg.=0.18) d, 0.4–1.5 (avg.=0.9) d, 1.5–5 (avg.=2.7) d, and 5–15 (avg.=10) d. The elemental O:C (H:C) ratios of the SOA mass formed in those ranges were 0.55 (1.60), 0.84 (1.44), 1.13 (1.36), and 1.55 (1.22). For data with ages of longer than several eq. days, O was added coincident with loss of C (i.e., negative x-intercept), which is likely due to heterogeneous oxidation leading to fragmentation/evaporation of preexisting OA. This conclusion is reinforced by the evidence that for eq. OH ages greater than several days, heterogeneous oxidation resulted in a net loss of C when ambient MT concentrations were low (Fig. 3.S10), but not for lower eq. ages. Similarly, George and Abbatt (2010) suggested that the lifetime of ambient OA with respect to heterogeneous OH oxidation is approximately two to three days. Therefore, the change in amounts of O, C, and H after several eq. days of oxidation will be a mix of heterogeneous change to preexisting OA and addition of new SOA. These effects of heterogeneous oxidation (i.e., x- and y-intercepts) are likely to be approximately the same for

all data within each given age range, meaning the slopes fitted above are independent of the heterogeneous processes and contain information about the elemental changes associated with the formation of varying amounts of SOA within each age range.

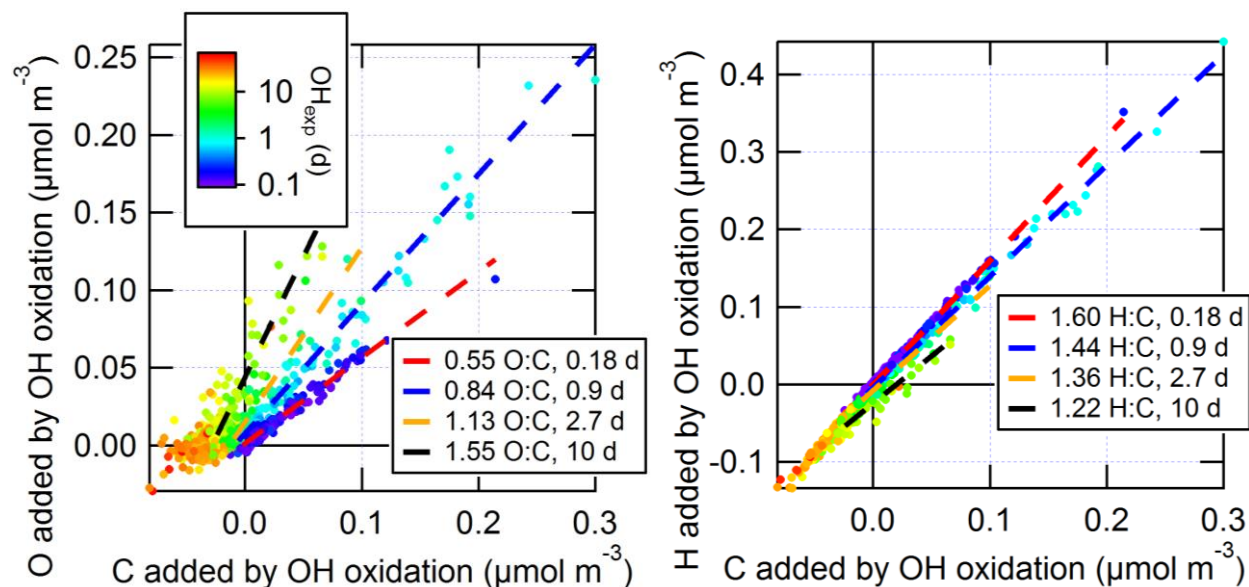


Fig. 3.8. Scatter plots of $\mu\text{mol m}^{-3}$ O and $\mu\text{mol m}^{-3}$ H added per $\mu\text{mol m}^{-3}$ C added from OH oxidation of ambient air in the OFR. Slopes are fit to the photochemical age ranges of 0.1–0.4 (avg.=0.18) d, 0.4–1.5 (avg.=0.9) d, 1.5–5 (avg.=2.7) d, and 5–15 (avg.=10) d, showing that the atomic O:C(H:C) ratios of the SOA mass formed in those ranges were 0.55 (1.60), 0.84 (1.44), 1.13 (1.36), and 1.55 (1.22), respectively. At higher ages, heterogeneous oxidation led to loss of C and H and little to no loss of O.

Analogous to Fig. 3.8, the amount of O and H vs. C added from O_3 and NO_3 oxidation are shown in Figs. 3.9–3.10. The SOA added from O_3 oxidation had O:C and H:C ratios of 0.50 and 1.61. The SOA added from NO_3 oxidation had O:C and H:C ratios of 0.39 and 1.60. This O:C value of 0.39 for NO_3 oxidation includes only the O atoms that were bound to the C backbone of the organic molecules, and excludes the two O atoms that are bound only to N in the $-\text{ONO}_2$ (nitrate) functional group (Farmer et al., 2010). If all O atoms in the nitrate functional group are included, the O:C of this added SOA mass was 0.44. Inclusion of only the carbon-bound oxygen of the nitrate functional group is more reflective of the carbon oxidation state, and is also what is typically reported for AMS O/C measurements (since the organic $-\text{NO}_2$ moiety is measured in the AMS as total nitrate and typically not separated from inorganic nitrate).

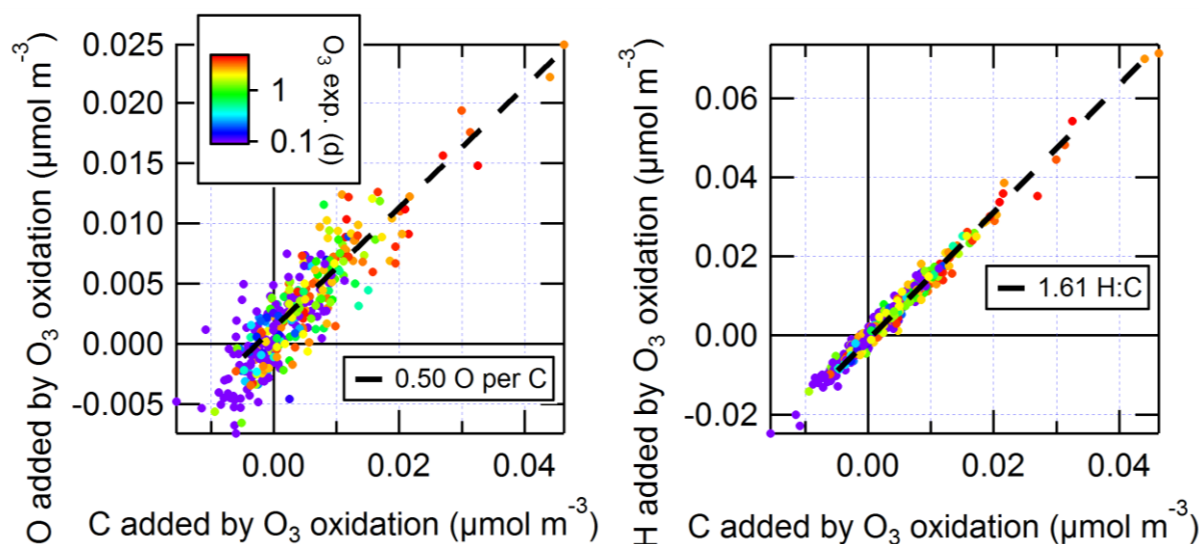


Fig. 3.9. Scatter plots of $\mu\text{mol m}^{-3}$ O and $\mu\text{mol m}^{-3}$ H added per $\mu\text{mol m}^{-3}$ C added from O_3 oxidation of ambient air in the OFR. Data are colored by eq. d of O_3 exposure. The slopes show that the atomic O:C (H:C) ratio of the SOA mass formed was 0.50 (1.61). The slopes did not change with increasing photochemical age.

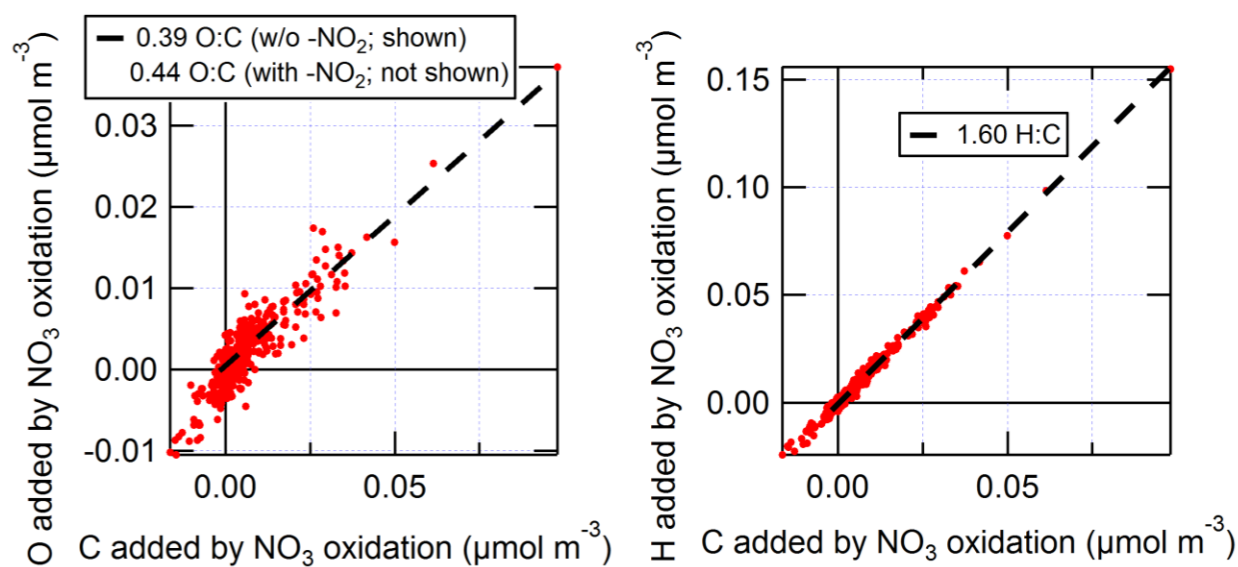


Fig. 3.10. Scatter plots of $\mu\text{mol m}^{-3}$ O and $\mu\text{mol m}^{-3}$ H added per $\mu\text{mol m}^{-3}$ C added from NO_3 oxidation of ambient air in the OFR. The amount of O added is shown without including the O from the $-\text{NO}_2$ group, since those O atoms do not affect the oxidation state of C. The slopes show that the atomic O:C(H:C) ratio of the SOA mass formed was 0.39 (1.60). The slopes did not change with increasing NO_3 exposure. Contrary to Figs. 3.8–3.9, data are not colored by NO_3 exposure. The ranges of NO_3 exposure achieved during daytime vs. nighttime were unequal (Figs. 3.5-3.6, 3.S12), obscuring any trend of OA enhancement vs. eq. age.

Heterogeneous oxidation was not expected to be a factor for the O₃ and NO₃ ages used in this work. This assumption was reinforced by the fact that no net loss of C was observed for these amounts of oxidation, even when ambient MT concentrations (and OA enhancement) were low, as shown in Figs. 3.S11–3.S12. This assumption is also consistent with previous research on lifetimes of OA components with respect to O₃ and NO₃ heterogeneous oxidation. For instance, several aldehydes were found to have a relatively long lifetime equivalent to approximately 2–8 days for NO₃ heterogeneous oxidation when calculated using 1 pptv ambient NO₃ (Iannone et al., 2011). Ng et al. (2016) summarized that reactive uptake of NO₃ into particles is slow for most molecules, with the exception of unsaturated or aromatic molecules, which were unlikely to be major components of the ambient OA in this remote forest (Chan et al., 2016). Although the lifetime of pure oleic acid (which contains a C=C bond) particles with respect to heterogeneous O₃ oxidation can be as short as tens of minutes (Morris et al., 2002), lifetimes for oleic acid in atmospheric particle organic matrices can be tens of hours to days (Rogge et al., 1991; Ziemann, 2005). Furthermore, the uptake coefficients for O₃ to react with saturated molecules are typically 1–2 orders of magnitude slower than for unsaturated molecules (de Gouw and Lovejoy, 1998). In summary, this previous research suggests that heterogeneous oxidation by O₃ or NO₃ may be important at higher eq. ages, but not for those achieved in the present work.

To put the O:C and H:C values of the SOA formed in the OFR in perspective, Van Krevelen diagrams of H:C vs O:C ratios for OA measured after OH, O₃, and NO₃ oxidation are shown compared to concurrent measurements of ambient OA in Fig. 3.11a–c, and summarized together in Fig. 3.11d. The effect of heterogeneous OH oxidation on preexisting aerosol is also shown as a line with a slope of -0.58. This line was fitted to the H:C vs. O:C of all OH-aged data where a net loss of C was observed (i.e., SOA formation was not observed and heterogeneous oxidation dominated). Generally speaking, less oxidized (“fresh”) OA will lie in the upper left portion of a Van Krevelen plot, with higher H:C values and lower O:C values. Conversely, more oxidized (“aged”) OA will move towards the lower right, with lower H:C

values and higher O:C values (Heald et al., 2010; Ng et al., 2011b). Shown in Fig. 3.11, the SOA formed from O_3 , NO_3 , and the lowest amount of OH aging (0.1–0.4 eq. days) was found at the upper left of the range occupied by ambient OA. As OH aging increased to higher ranges, the values of H:C decreased and the values of O:C increased, already moving beyond the local ambient range after 0.9 eq. days. At the higher ages, the H:C of the SOA formed lies at higher H:C values than those of the total OA measured after OH aging, which are closer to the trend of heterogeneous oxidation in the Van Krevelen space. This shows that SOA formed via gas-phase OH oxidation processes in an OFR has a higher H:C than the OA that results from heterogeneous oxidation, while both processes lead to similar increases in O:C. The net movement in the Van Krevelen space can be considered as starting at the ambient H:C and O:C and moving along two vectors: one vector along the heterogeneous oxidation line and another towards the H:C and O:C values of the new SOA formed in the gas phase, where the length of those two vectors are weighted by the amount of OA resulting from each process. When little SOA is formed, the H:C and O:C measured after oxidation lie along the heterogeneous oxidation line. When high amounts of SOA are formed, the H:C and O:C after oxidation shift to higher H:C values, lying closer to the curve defined by the H:C and O:C of SOA mass added in the OFR at the different age ranges (see Fig. 3.S13). While these two vectors describe the possible oxidation processes in the OFR, there may be other vectors (e.g., from condensed phase chemistry or reactive uptake) occurring in the atmosphere. As documented in Hu et al. (2016), SOA formation processes that require reactive uptake (such as uptake of isoprene epoxydiols to form IEPOX-SOA) and/or occur on time scales longer than the several minute residence time in the OFR are not captured with the OFR method used in this work. This is because the rate of reactive uptake does not scale with increased OH. Another process that would not be captured in the OFR is uptake of MBO oxidation products to form particulate organosulfates, which was shown to occur at the BEACHON-RoMBAS site (Zhang et al., 2012).

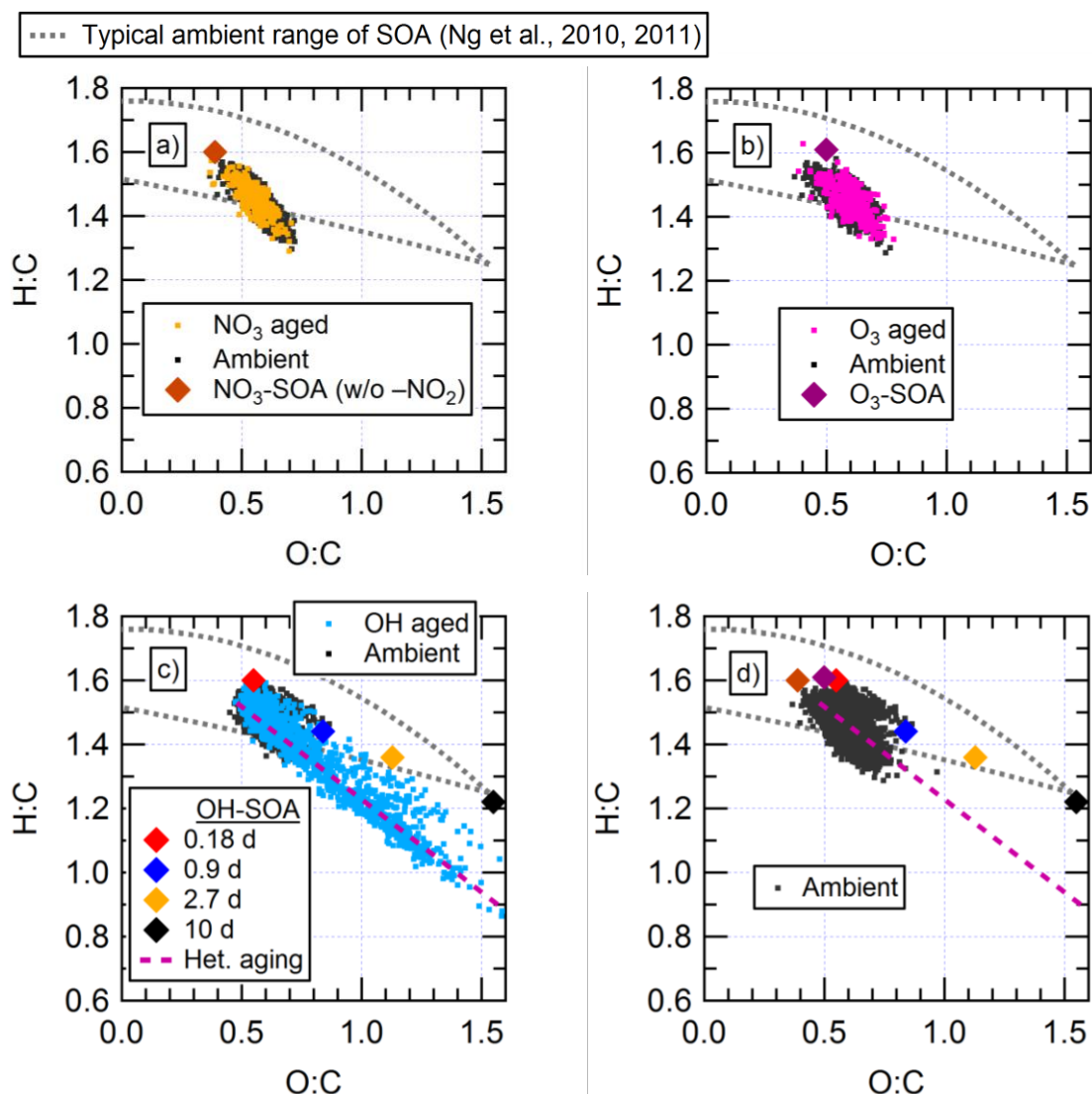


Fig. 3.11. Van Krevelen diagrams of H:C vs. O:C ratios of OA after oxidation by a) NO_3 , b) O_3 , and c) OH along with concurrent ambient ratios. The H:C and O:C ratios of the new SOA mass formed in the OFR (i.e., the slopes from Figs. 3.8–3.10) are shown for each oxidant (diamonds), and are summarized in d) compared with all ambient measurements. For data where no net C addition was observed after OH oxidation, the slope along which heterogeneous OH oxidation transforms the ambient OA is shown (purple dashed line).

The H:C of the least oxidized SOA formed in the OFR from all oxidants was near 1.6. As discussed in Palm et al. (2016), SOA formation from OH oxidation in the OFR correlated with MT, and the *S*/IVOC sources of SOA may have been MT oxidation products or other related biogenic gases. Biogenic terpenes are composed of isoprene units, meaning they all have H:C of 1.6. Therefore, the SOA formed from the lowest eq. ages in the OFR was consistent with oxidation processes that add roughly 4–6 O atoms

without removing net H atoms. Addition of –OH or –OOH functional groups after –H abstraction by OH radicals results in addition of O without loss of H, and are consistent with the $\text{RO}_2 + \text{HO}_2$ reaction conditions that are expected during OH oxidation in the OFR (Kroll and Seinfeld, 2008; Ortega et al., 2016). OH can also add to a C=C bond, which could lead to addition of H atoms after oxidation. O_3 and NO_3 are expected to react with MT almost exclusively by addition to a C=C bond, which leads to addition of O without initial removal of H atoms (Atkinson and Arey, 2003). However, previous research has shown that many precursor gases, including aromatic molecules with initial H:C close to 1, can form SOA with H:C close to 1.6 (Chen et al., 2011; Chhabra et al., 2011; Canagaratna et al., 2015; Hildebrandt Ruiz et al., 2015). Therefore, H:C alone cannot provide direct evidence about the specific identities of precursor gases in ambient air. The SOA from O_3 , NO_3 , and 0.1–0.4 eq. days OH aging had H:C values similar to typical semi-volatile oxidized organic aerosol (SV-OOA), while the H:C of SOA from 0.4–1.5 eq. days or longer OH aging resembled low volatility oxidized organic aerosol (LV-OOA); these two types of SOA have been identified in ambient air at many locations (Jimenez et al., 2009; Canagaratna et al., 2015).

The relative time scales of oxidation and condensation in the OFR also need to be considered in order to properly interpret the H:C and O:C of the SOA mass formed in the OFR. In the atmosphere, once a molecule is oxidized to an LVOC that is able to condense onto a particle, lifetimes for condensation onto aerosols are on the order of several minutes (Farmer and Cohen, 2008; Knote et al., 2015; Nguyen et al., 2015). This is typically much shorter than the lifetimes for subsequent reaction with OH, O_3 , or NO_3 of tens of minutes to several hours or longer, so condensation will likely occur prior to further oxidation. In OFR oxidation experiments, the lifetime for subsequent oxidation of LVOCs is shortened proportional to the increase in oxidant concentration. However, the condensation lifetime does not scale with oxidant concentration, and remains roughly constant. At sufficiently high oxidant concentrations, LVOCs can be subjected to further oxidation steps that they would not be subjected to

in the atmosphere prior to having a chance to condense to form SOA. To compare SOA formation in the OFR vs. ambient air, these relative time scales are considered here as a function of both oxidant type and amount of oxidant exposure.

The lowest range of OH aging for which O:C and H:C values were measured was 0.1–0.4 (avg. 0.18) eq. d, which is 2.4–9.6 (avg. 4.3) eq. h of oxidation. Typical terpenes have lifetimes for reaction with OH on the order of tens of minutes to several hours in the atmosphere (Atkinson and Arey, 2003), which is similar to this lowest eq. age range in the OFR. Typical terpene oxidation products have lifetimes ranging from 3.9 h (caronaldehyde; Alvarado et al., 1998) to 4.7 h (pinonaldehyde; Atkinson et al., 2006) to 11–13 h (nopinone; Atkinson and Aschmann, 1993; Calogirou et al., 1999a) to a computationally estimated 18–21 h (pinic and pinonic acid; Vereecken and Peeters, 2002). As a rough approximation, this suggests that the SOA formed in the OFR is likely a result of approximately one or at most a few oxidation steps occurring to the molecules that enter the OFR (which may have already experienced one or more oxidation steps in the atmosphere prior to entering the OFR). The aging in this range strikes a balance between achieving enough oxidation to react all incoming precursors at least once while not reacting them an unrealistic number of times in the gas phase before allowing sufficient time for condensation. In the next age range of 0.4–1.5 (avg. 0.9) eq. d of OH aging, in which the maximum OA enhancement occurred, some primary precursors are likely starting to be oxidized multiple times inside the OFR prior to condensation, while some oxidation products will still be oxidized only ~1–2 times. The SOA formed in this range may represent SOA formed from multiple generations of chemistry. At higher ages in the OFR, the aerosol is likely mainly modified by heterogeneous oxidation, with a small contribution from condensation of highly oxidized products. This OA at the highest ages resembles ambient OA found in remote locations (Jimenez et al., 2009; Chen et al., 2015b). Indeed, OFRs have previously been used to study heterogeneous oxidation processes (George et al., 2008; Smith et al., 2009).

For O_3 and NO_3 oxidation, the oxidants will react only with C=C double-bond-containing gases. The major MT and SQT species at this field site all contain only a single C=C bond (isoprene and minor MT and SQT species contain two). Subsequent reaction lifetimes of oxidation products with these oxidants will likely be longer than the lifetime for condensation onto particles. For example, the lifetimes for pinonaldehyde with respect to O_3 and NO_3 oxidation are >579 d, and 29 d, respectively (Atkinson et al., 2006). Therefore, we can approximate that multiple generations of oxidation are not dominant for SOA formation when investigating O_3 or NO_3 oxidation in the OFR at this site. This is consistent with previous chamber SOA formation experiments that suggested that first-generation oxidation products dominate SOA formation from O_3 oxidation of a variety of biogenic compounds with a single C=C bond, rather than products of later generations of oxidation (Ng et al., 2006). The SOA formed via O_3 or NO_3 oxidation in the OFR is likely formed from reaction with primary VOCs and a small subset of their reaction products that still contain C=C bonds, such as the α -pinene oxidation product campholenic aldehyde (Kahnt et al., 2014). This SOA should be representative of typical atmospheric SOA formation processes.

3.3.4 Particulate organic nitrate (pRONO₂) formation from NO₃ oxidation of ambient air

In addition to estimating the elemental composition of OA, the AMS can also be used to estimate the amount of inorganic vs. organic nitrate in submicron aerosols (Farmer et al., 2010; Fry et al., 2013). The ratio of NO_2^+ to NO^+ fragment ions produced by thermal decomposition on the AMS vaporizer and electron impact ionization depends on the type of nitrate. NH_4NO_3 typically produces a ratio of approximately 0.3-1, while particulate organic nitrate (pRONO₂), in which the $-ONO_2$ functional group is covalently bonded to the carbon backbone (R) through an oxygen atom, typically produces a ratio ~2-3 times lower (Fry et al., 2009; Bruns et al., 2010; Farmer et al., 2010; Liu et al., 2012; Day et al., 2017). The measured NO_2^+ to NO^+ ratio is a linear combination of these two chemical components. Using this principle, the NO_3 measured by the AMS was split into the estimated fractions of NH_4NO_3 and

pRONO₂ according to the method described in Fry et al. (2013). For the instrument in this work, ratios of 0.3 and 0.13 were used for the NO₂⁺ to NO⁺ ratios of NH₄NO₃ and pRONO₂, respectively (Fry et al., 2013).

A two-night example of both ambient and NO₃-radical aged aerosol on Aug. 20–22 is shown in Fig. 3.12. In ambient air, the majority of NO₃ aerosol was organic. After oxidation in the OFR, different behavior was seen on the two nights shown. On the first night, mainly inorganic nitrate was produced, as evidenced by the higher NO₂⁺ to NO⁺ ratio, the formation of NH₄ aerosol, and the relatively small amount of SOA formed. On the second night, pRONO₂ was produced, as evidenced by the lower NO₂⁺/NO⁺ ratio, a lack of NH₄ aerosol formation, and substantial SOA formation. The organic nitrate formation and SOA formation also roughly tracked the ambient MT concentrations.

These two distinct behaviors in the NO₃-OFR were likely controlled by ambient RH. There was a competition between thermal dissociation of injected N₂O₅ to produce NO₃+NO₂ (favored at high temperatures and low RH) and the hydrolysis of N₂O₅ on wetted OFR walls to produce HNO₃ (favored at low temperatures and high RH). When hydrolysis occurred rapidly, then there was a sharp decrease in N₂O₅ concentrations. The NO₃ radical concentrations were also greatly reduced, and thus fewer NO₃ radicals were available to react with ambient gases (e.g., MT) to produce pRONO₂. HNO₃ reacted with NH₃ in ambient air or evaporating from OFR surfaces to produce NH₄NO₃. The results shown in Fig. 3.12 illustrate this behavior, with NO₃ radical exposure being reduced while NH₄NO₃ was produced during the first night. Despite the presence of similar MT concentrations on both nights, little SOA was produced on the first night. Future applications could include heating of the OFR slightly above ambient temperatures in order to prevent hydrolysis of N₂O₅ on the OFR walls. Inhibiting NH₄NO₃ formation artifacts would be especially critical for data interpretation if measuring aerosol enhancements with only non-chemical instruments such as an SMPS.

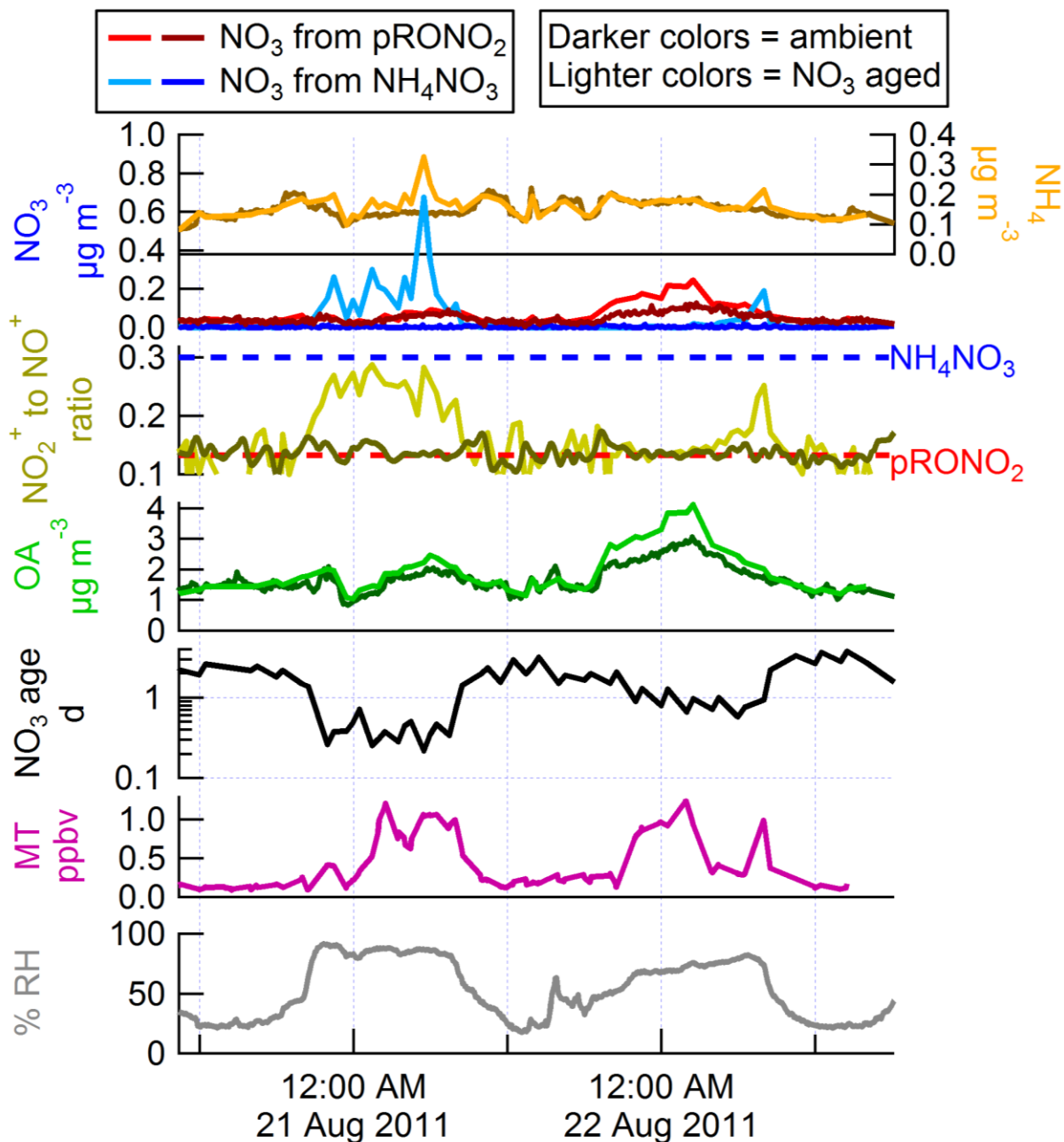


Fig. 3.12. Example time series of OA, NH_4 , and NO_3 (split into pRONO_2 and NH_4NO_3) aerosol measurements after NO_3 oxidation in the OFR, compared to ambient aerosol, NO_2^+ to NO^+ ratio, model-derived eq. age of NO_3 oxidation, MT concentration, and RH measurements. Production of both NH_4NO_3 and pRONO_2 was observed at different times, which appears to depend on changes in experimental conditions.

Despite this complex chemistry, information about the chemical composition of pRONO_2 formed from real atmospheric precursors can still be derived from times when conditions favored pRONO_2 formation. Shown in Fig. 3.13 is the mass of organic $-\text{ONO}_2$ added vs. SOA added from oxidation by each

of the three oxidants. Substantial formation of pRONO₂ was observed only for NO₃ radical oxidation, and not for O₃ or OH oxidation. This was expected, since ambient NO_x concentrations were generally low (0.5–4 ppb; Ortega et al., 2014), and the NO₃ oxidation experiment was the only one with an added source of reactive nitrogen. The slopes of Fig. 3.13 represent the ratio of –ONO₂ to the rest of the organic molecules in pRONO₂. In this study, the slope after NO₃ radical oxidation was 0.10, which is similar to the range of 0.1–0.18 found in previous chamber studies of NO₃ oxidation of terpenes (Fry et al., 2009, 2011; Boyd et al., 2015). To put this in context, if every SOA molecule formed in the OFR contained a single –ONO₂ group (with its mass of 62 g mol⁻¹), then the molecular mass of the full pRONO₂ molecules would be an average of 620 g mol⁻¹ (giving the slope of 62 g mol⁻¹ / 620 g mol⁻¹ = 0.10 in Fig. 3.13). Alternatively, if all molecules are assumed to have a mass of 200 or 300 g mol⁻¹, then 32% or 48% of the molecules, respectively, would contain a –ONO₂ functional group (assuming no molecules contain more than one –ONO₂ group). Again, this result is roughly consistent with previous research. For the fraction of OA composed of pRONO₂ in NO₃+β-pinene SOA, Fry et al. (2009) estimated 32–41% (assuming an average molecular weight of 215–231 g mol⁻¹), Fry et al. (2014) estimated 56% (assuming 214 g mol⁻¹), and Boyd et al. (2015) estimated 45–68% (assuming 200–300 g mol⁻¹).

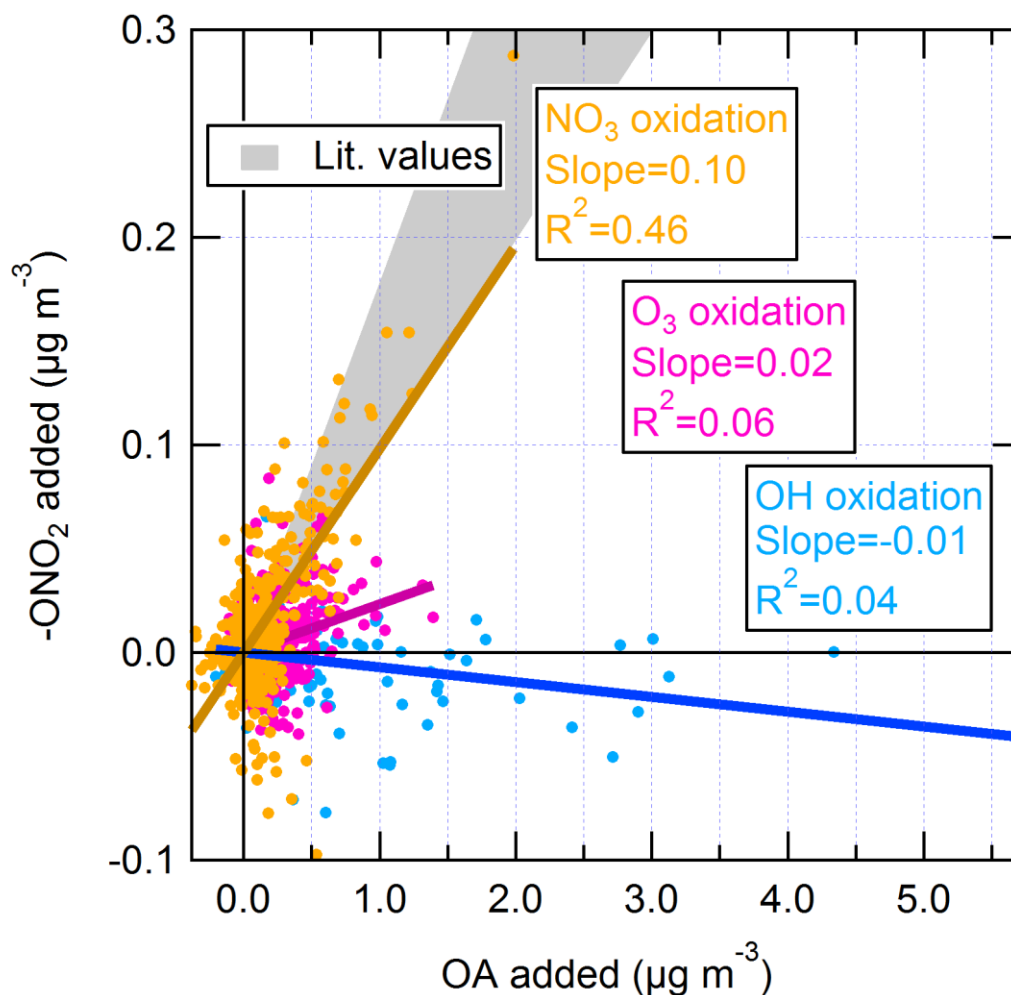


Fig. 3.13. Organic $-\text{ONO}_2$ mass added vs. OA added from OH, O_3 , and NO_3 oxidation in an OFR. No pRONO_2 formation was observed (or expected) from OH or O_3 oxidation under the experimental conditions. The slope of 0.10 from NO_3 oxidation is consistent with previous chamber measurements (shown in grey), which range from approximately 0.1–0.18 (Fry et al., 2009, 2011; Boyd et al., 2015).

3.4 Conclusions

In situ SOA formation from ambient pine forest air after oxidation by OH, O_3 , or NO_3 radicals was measured using an OFR for the first time. SOA formation from these real ambient mixes of aerosol and SOA precursors was measured semi-continuously, capturing diurnal and daily changes in the relative ambient concentrations of SOA precursor gases. In general, more SOA was formed from the precursors present in nighttime air than in daytime air for all three oxidants. At all times of day, OH oxidation produced approximately 4 times more SOA than O_3 or NO_3 oxidation. The O:C and H:C ratios of the SOA

formed by O_3 , NO_3 , and several eq. hours of OH oxidation was similar to the oxidation levels of ambient OA.

The OFR is a tool that can be used to measure the total SOA formation potential of ambient air at any given time, and how that potential changes with time, whether or not the SOA precursor gases are measured and/or speciated. As discussed in Palm et al. (2016), ambient VOC concentrations alone could not explain the amount of SOA formed in the OFR by OH oxidation. Instead, SOA was likely being formed from S/IVOCs that entered the OFR. In contrast, the quantity of measured VOCs was sufficient to explain the amount of SOA formed from O_3 and NO_3 oxidation; closure between measured and predicted SOA formation in an OFR was achieved. In other words, O_3 and NO_3 oxidation of the ambient S/IVOCs do not appear to produce appreciable amounts of SOA. This suggests that the ambient S/IVOCs tend not to have double bonds.

While this work does not investigate the source of the S/IVOCs, one possibility is that they are oxidation products of primary VOCs (e.g., MT or SQT). The primary VOCs could be emitted upwind of the site, and by the time the molecule enters the OFR, the double bond(s) will have reacted, leaving an oxidation product that reacts further with OH but not O_3 or NO_3 . If the lifetime for further reaction of these oxidation products is slower than the lifetime for the double-bond-containing primary emissions, then the oxidation products will build up in the atmosphere. Under this hypothesis, such S/IVOC compounds are not new or unexpected sources of SOA. In most regional and global models, they would already be implicitly accounted for, by tracking the emissions of the primary VOCs which have corresponding overall SOA yields. In this work, we consider only the primary VOCs that are measured to be entering the OFR, not the integrated sum of upwind emissions that were emitted into the air that eventually entering the OFR after some degree of ambient photochemical processing. SOA formation in the OFR takes a snapshot of the atmosphere, which consists of a mix of primary emissions and their oxidation products at various stages of oxidative progress. For this study, those snapshots demonstrate

that for OH oxidation, only approximately a quarter of the SOA-forming gases are in the form of primary VOC, while for O₃ and NO₃ oxidation almost all are in the form of primary VOC. It also suggests that for these precursor mixtures, multi-generational chemistry plays a major role in the overall amount of SOA formed from OH oxidation (and much less so for O₃ and NO₃).

If these SOA-forming S/IVOCs do not react with ambient O₃ or NO₃, they will build up in the atmosphere during the night when OH is absent. When the sun rises and OH is produced, a sudden burst of SOA formation might be expected. However, this coincides with dilution of gases and particles due to convective vertical mixing, potentially offsetting such new SOA formation and making it difficult to observe it without detailed chemical and boundary layer dynamics measurements and/or modeling. These OFR measurements and analysis elucidate the presence and properties of S/IVOCs in the atmosphere, and highlight the need for more measurements and modeling of such gases in order to better understand ambient SOA formation. This work also demonstrates the utility of the OFR as a tool for studying SOA formation from all three major atmospheric oxidants.

3.5 Supplementary information

3.5.1 NO₃ oxidant modeling

To estimate NO₃ exposure in the OFR when injecting N₂O₅, the KinSim chemical-kinetic integrator (version 3.10) was used. Table 3.S1 contains the reactions and rate constant parameters implemented in the model. The model was run with a residence time calculated from the total measured flow in the OFR (between 150 and 240 s). The model was run using this research site's ambient pressure of 770 mbar, and was initialized with measurements of ambient temperature, RH, O₃ concentrations, monoterpene (MT) concentrations, a constant 0.15 ppb NO, and injected NO₂, NO₃, and N₂O₅ concentrations for each data point. The N₂O₅ wall loss rate constant k_{wall} , shown in Fig. 3.S4a, was empirically determined to have a base value of 0.014 s⁻¹ (lifetime of 71 s) using the measured N₂O₅ difference between the injection flow and OFR output concentrations while injecting N₂O₅ into dry zero

air in the reactor. Using measurements when injecting into ambient air, an empirical increase in this wall loss rate was required when RH was greater than 80% in order to reproduce the concentrations of N_2O_5 injected and remaining in the OFR output (see Fig. 3.2a). Figure 3.S4b shows the modeled vs. measured N_2O_5 remaining, illustrating the need for the increasing wall loss rate at high RH. The base wall loss rate of 0.014 s^{-1} is several times faster than the wall loss rate of 0.0025 s^{-1} estimated in Palm et al. (2016) for condensable organic gases (LVOCs) produced by oxidation in the OFR. This empirical result may be a consequence of the N_2O_5 flow being injected through a Teflon ring that was mounted close to the OFR wall, increasing the effective surface-area-to-volume ratio experienced by the injected N_2O_5 . Injection near the wall may also have been the cause for the relatively large increase in wall loss rate at high RH. The N_2O_5 wall loss rate also implicitly includes any losses on the sampling line walls after the OFR, which also had higher surface-area-to-volume ratios that would likely lead to larger apparent loss rates. The NO_3 wall loss rate was assumed to be equal to the N_2O_5 wall loss rate (and has little effect on the key model outputs). The rate constant for reactive uptake of N_2O_5 onto particulate water surfaces, k_{aer} , is shown as a function of RH in Fig. 3.S5. It was calculated using the measured ambient aerosol condensational sink using the same method described for condensation of LVOCs onto aerosols in Palm et al (2016), except using an organic-mass-fraction-corrected uptake efficiency $\gamma(\text{N}_2\text{O}_5)$ from Gaston et al. (2014). This heterogeneous uptake was typically several orders of magnitude slower than the wall loss rate, and was therefore a minor loss pathway for N_2O_5 .

Table 3.S1. List of reactions and parameters used in modeling of the oxidant chemistry in the OFR when performing NO₃ oxidation. The rate constants are calculated using the modified Arrhenius equation $k = A \cdot \left(\frac{T(K)}{300}\right)^{-n} \cdot e^{-\frac{E}{RT(K)}}$ with pressure dependence as described in Sect. 2 of JPL (Sander et al., 2011). Parameter values are from JPL, with exceptions noted.

Reactant 1	Reactant 2	Product 1	Product 2	Product 3	A _∞	E _∞ /R	n _∞	A ₀	E ₀ /R	n ₀
NO	O ₃	NO ₂	O ₂		3e-12	1500	0	0	0	0
NO ₂	O ₃	NO ₃	O ₂		1.2e-13	2450	0	0	0	0
N ₂ O ₅		NO ₂	NO ₃		9.7e+14 ¹	11080	-0.1	0.0013	11000	3.5
N ₂ O ₅		Wall loss			k_{wall}^2	0	0	0	0	0
NO ₃		Wall loss			k_{wall}^2	0	0	0	0	0
NO ₃	α-pinene	RO ₂			1.2e-12 ¹	-490	0	0	0	0
NO ₃	3-carene	RO ₂			9.1e-12 ¹	0	0	0	0	0
NO ₃	β-pinene	RO ₂			2.5e-12 ¹	0	0	0	0	0
N ₂ O ₅	H ₂ O(g)	HNO ₃	HNO ₃		1e-22	0	0	0	0	0
N ₂ O ₅	H ₂ O(aerosol)	HNO ₃	HNO ₃		k_{aer}^2	0	0	0	0	0
NO	NO ₃	NO ₂	NO ₂		1.8e-11	-110	0	0	0	0
NO ₂	NO ₃	NO	NO ₂	O ₂	4.5e-14	1260	0	0	0	0
NO ₃	NO ₃	NO ₂	NO ₂	O ₂	8.5e-13	2450	0	0	0	0
NO ₂	NO ₃	N ₂ O ₅			1.9e-12 ¹	0	-0.2	3.6e-30	0	4.1
NO ₃	RO ₂	RO			1.5e-12	0	0	0	0	0
MT mixing source		α-pinene	3-carene	β-pinene	0.01 ²	0	0	0	0	0

¹Parameter values taken from IUPAC (Atkinson et al., 2004, 2006)

²See Sect. 3.5.1 for parameter details

Table 3.S2. List of reactions and parameters used in modeling of the oxidant chemistry in the OFR when performing O₃ oxidation. The rate constants are calculated using the modified Arrhenius equation $k = A \cdot \left(\frac{T(K)}{300}\right)^{-n} \cdot e^{-\frac{E}{T(K)}}$. Parameter values are from IUPAC (Atkinson et al., 2006).

Reactant 1	Reactant 2	Product 1	A	E	n
O ₃	α-pinene	Products	8.05×10^{-16}	640	0
O ₃	β-pinene	Products	1.35×10^{-15}	1270	0
O ₃	3-carene	Products	4.8×10^{-17}	0	0

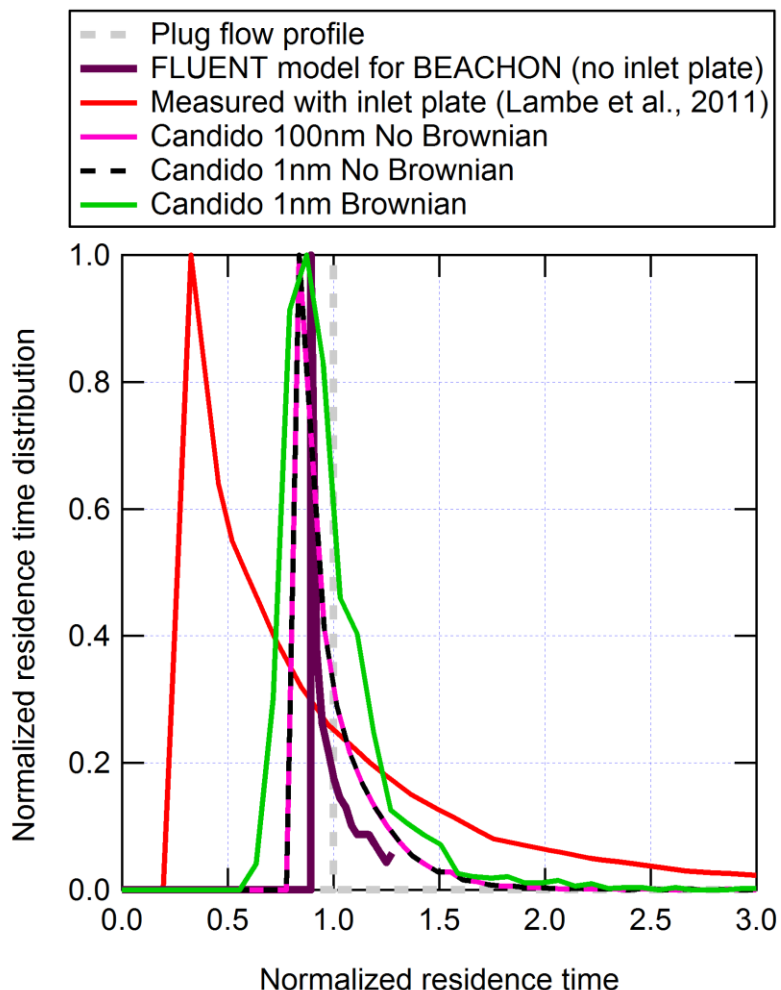


Fig. 3.S1. Normalized residence time distributions in the OFR as a function of normalized residence time (1 = avg. residence time of each distribution). The FLUENT model was used to calculate the residence time for the OFR configuration without the inlet plate used during BEACHON-RoMBAS. This distribution is compared to the bis(2-ethylhexyl) sebacate (BES) particle residence time distribution measured with the inlet plate on in Lambe et al. (2011a) and to the ideal plug flow distribution (where all particles have equal residence time calculated as the OFR volume divided by the total flow rate through the OFR). The residence time distribution without the inlet plate is much narrower than with the plate and is close to plug flow, though local winds will create a broader distribution than the model shows.

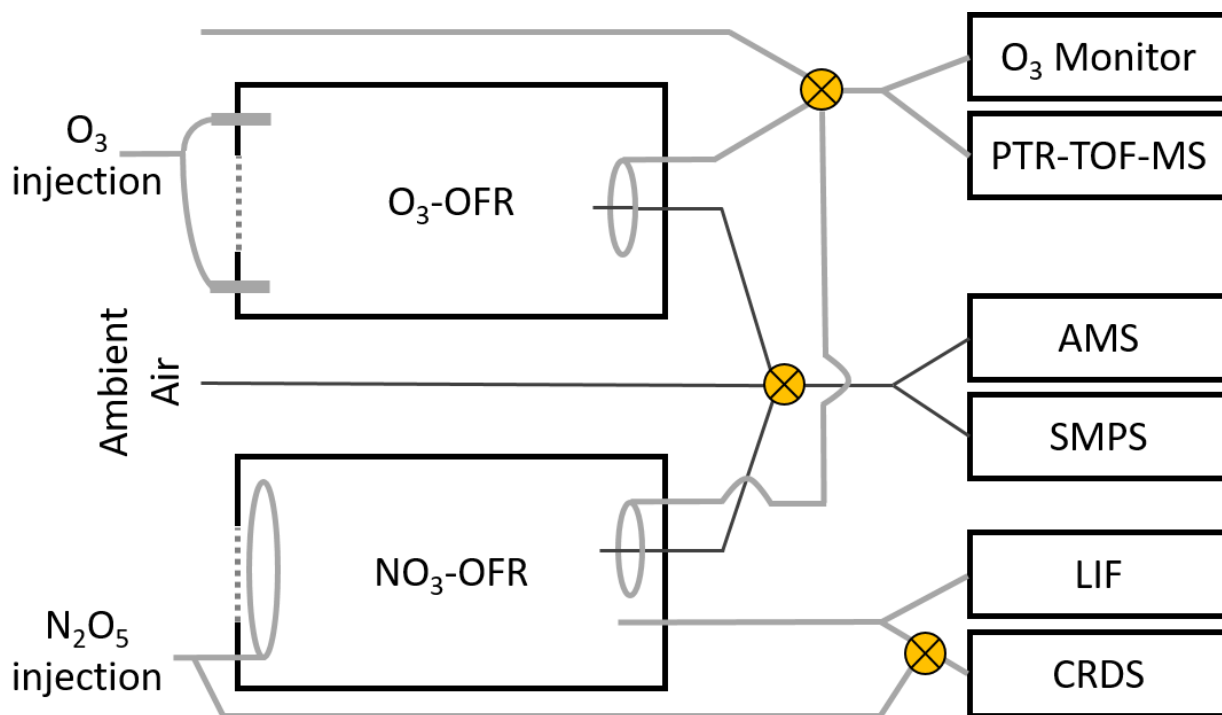


Fig. 3.S2. Schematic of experimental setup of NO_3 -OFR and O_3 -OFR experiments.

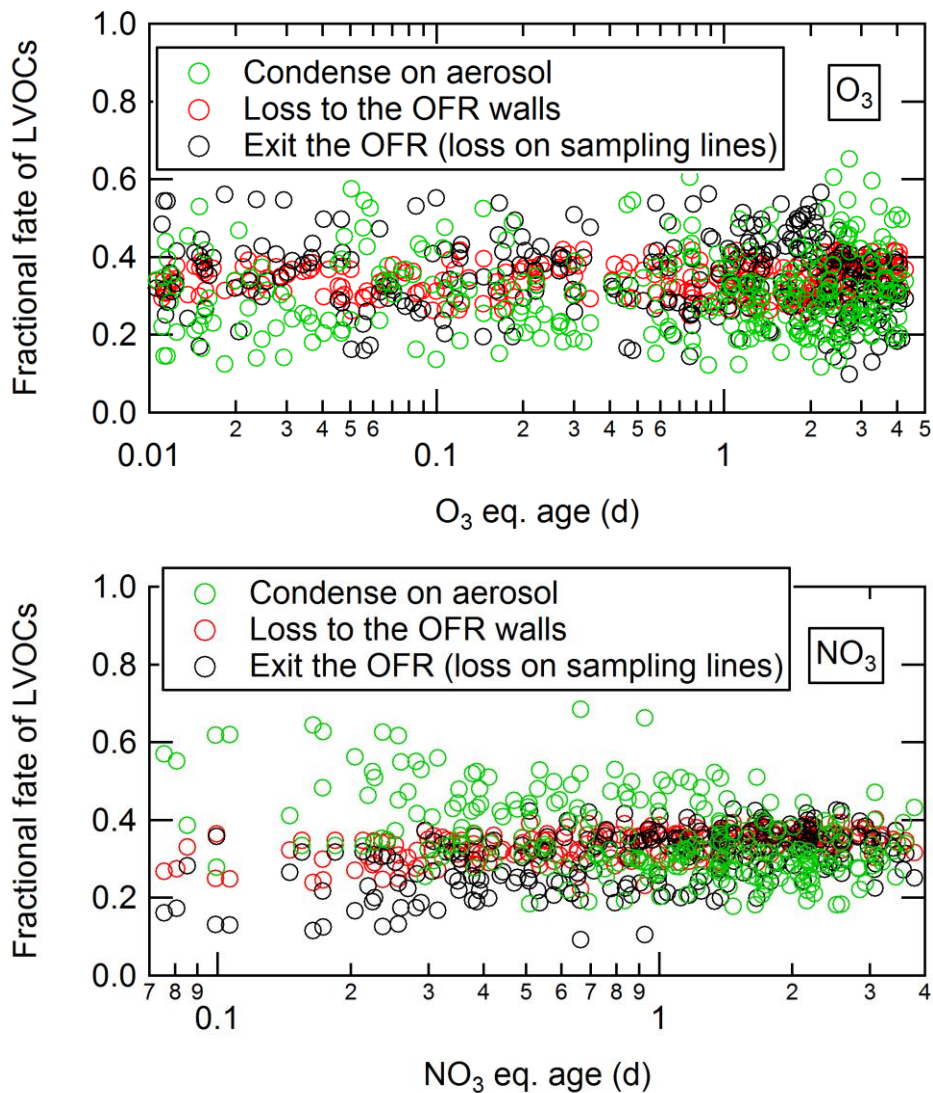


Fig. 3.S3. Modeled fractional fates of condensable low-volatility organic compounds (LVOCs) produced in the OFR, as a function of eq. age for O_3 oxidation (top) and NO_3 oxidation (bottom). For O_3 oxidation, on average 31% of LVOCs condensed onto particles, 34% condensed on OFR walls, and 35% exited the OFR to condense on sampling line walls. For NO_3 oxidation, on average 36% of LVOCs condensed onto particles, 34% condensed on OFR walls, and 30% exited the OFR to condense on sampling line walls.

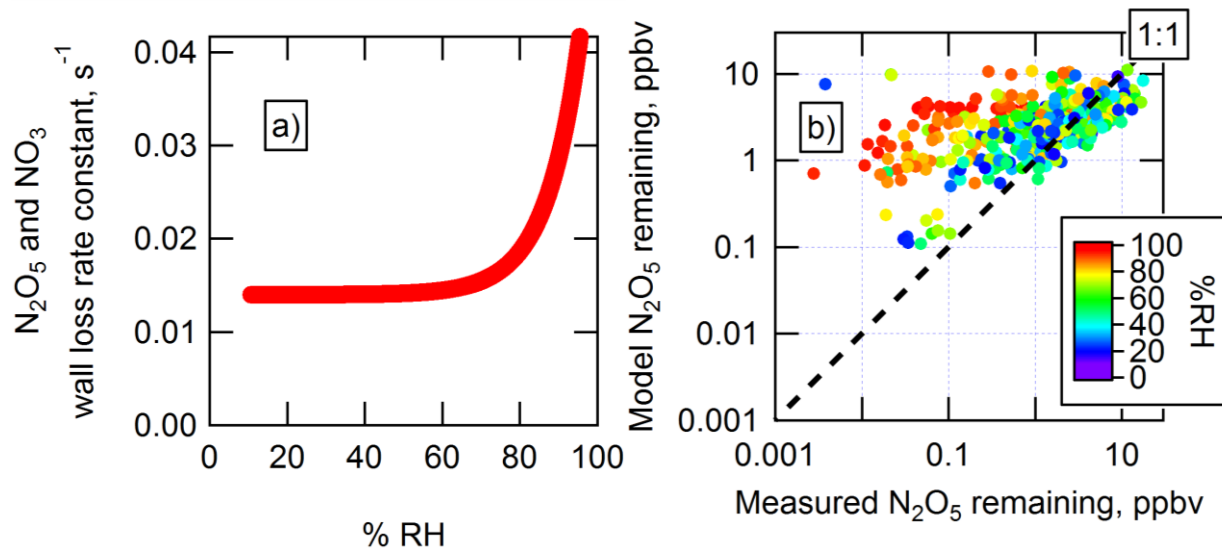


Fig. 3.S4. a) The wall loss rate constant of N_2O_5 and NO_3 vs. %RH, determined empirically in order to achieve agreement between modeled and measured N_2O_5 concentrations (Fig. 3.2a). b) Modeled vs. measured N_2O_5 remaining (analogous to Fig. 3.2a), shown if the N_2O_5 and NO_3 wall loss rate was assumed to be a constant 0.014 s^{-1} at all %RH.

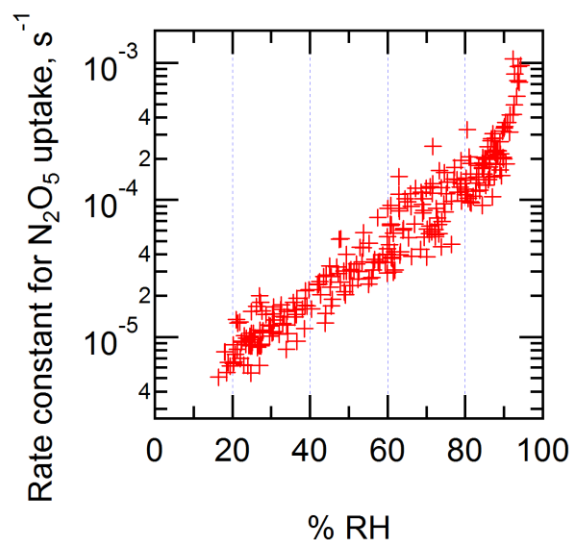


Fig. 3.S5. Calculated rate constant for reactive uptake of N_2O_5 onto particles, as a function of RH. The rate constant was calculated using the same method for condensation of gases onto aerosols described in Palm et al (2016), using the measured ambient aerosol condensational sink and using an organic-mass-fraction-corrected uptake efficiency $\gamma(\text{N}_2\text{O}_5)$ from Gaston et al. (2014).

Time constraints prevented the full characterization of the flow characteristics of the experimental setup during the field measurements. Instead, PTR-TOF-MS measurements of the decay of ambient MT in the OFR were used to parameterize the mixing process. With relatively robust constraints provided by measurements of N_2O_5 , NO_2 , and NO_3 , the model results make it clear that a well-mixed OFR would contain more than enough NO_3 to react virtually all ambient biogenic gases, if gases were immediately well-mixed. However, the PTR-TOF-MS measurements verified that substantial amounts of MT often remained in the OFR output. Incomplete mixing of the injected N_2O_5 was the most likely explanation for this observation. A parameterization for the time constant needed for mixing of the injected N_2O_5 flow with ambient air at the entrance of the OFR was added to the model to provide an effective empirical mixing time scale of 100 s. This parameterization for mixing has the same effect as the high wall loss rates of N_2O_5 , which is to decrease the concentrations of oxidant experienced by MT inside the reactor. The true time scale of mixing and wall loss rate may be somewhat different, but the model results presented herein suggest the values used in this work capture the net behavior satisfactorily. The time series of measured and modeled MT decay are shown in Fig. 3.S6–3.S7, which are in addition to the example given in Fig. 3.4.

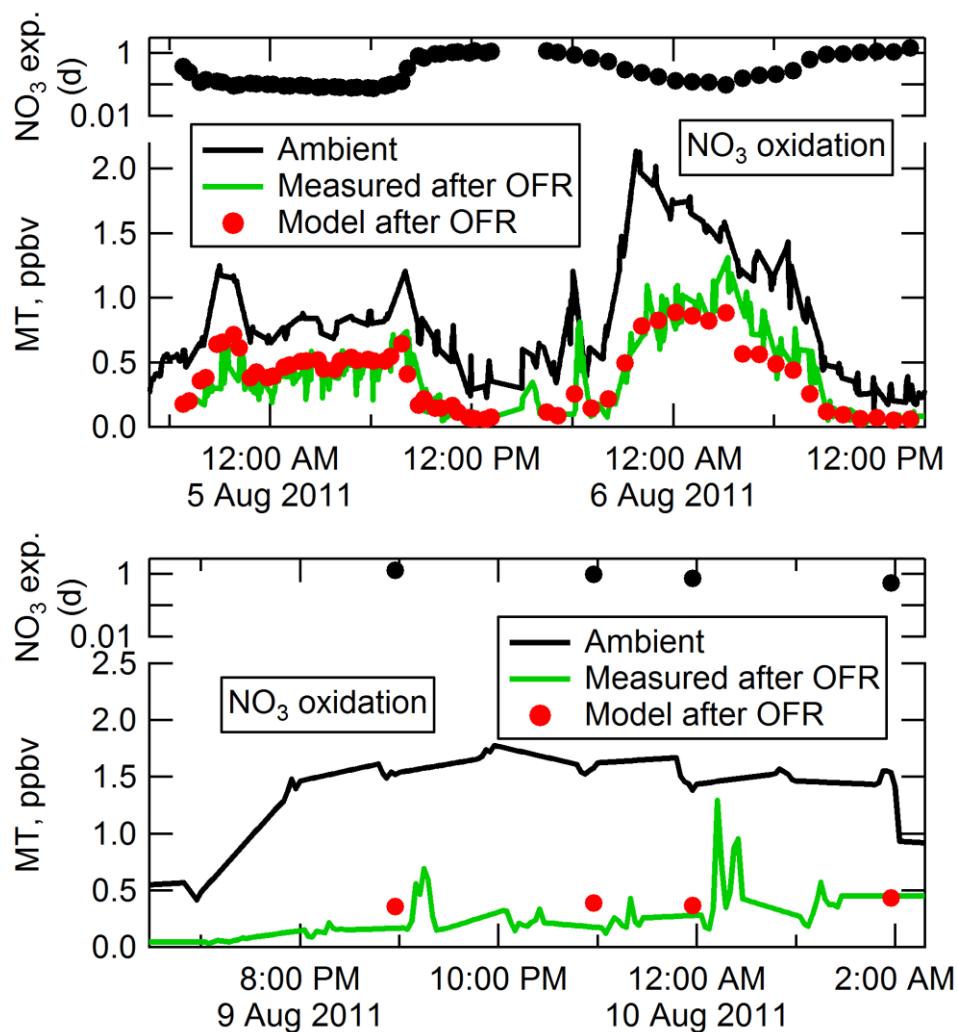


Fig. 3.S6. Ambient, measured remaining, and modeled remaining MT from NO₃ oxidation in the OFR on Aug. 4–6 and Aug. 9–10, along with modeled NO₃ exposure (d). For these examples, the amount of injected N₂O₅ was held roughly constant (with a higher constant value injected on Aug. 9–10).

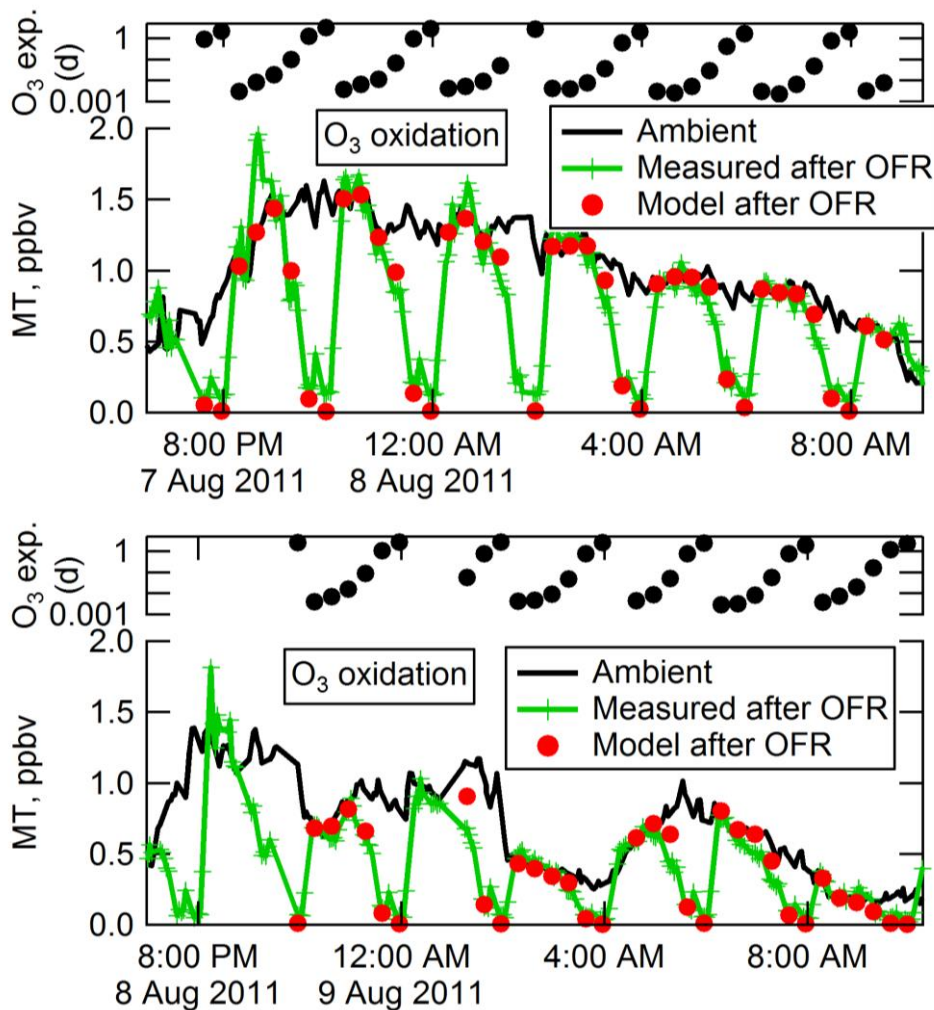


Fig. 3.S7. Ambient, measured remaining, and modeled remaining MT from O_3 oxidation in the OFR on Aug. 7–8 and Aug. 8–9, along with modeled O_3 exposure (d). The amount of oxidation was cycled from no added oxidant (no MT reacted) to maximum oxidation (most or all MT reacted) in repeated 2–3 h cycles. Note that the ambient MT were sampled through a separate inlet within the canopy, several meters from the OFR. Short periods of higher MT concentrations measured through the OFR (at low O_3 exposures) may be due to brief spatial heterogeneity in ambient MT concentrations within the canopy.

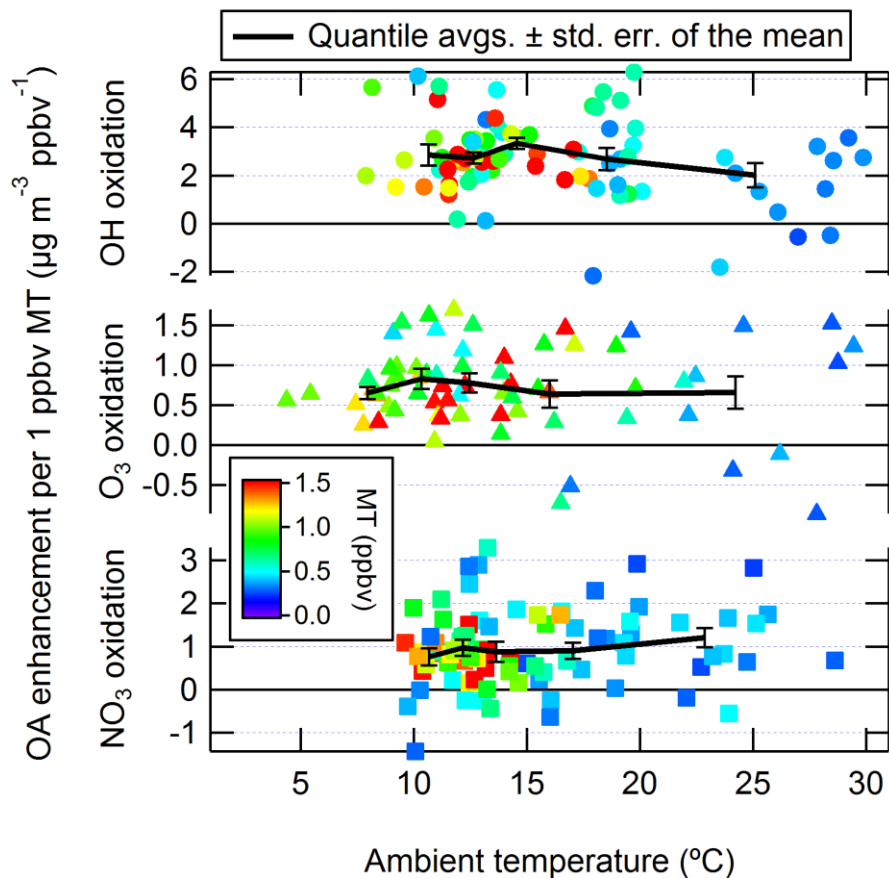


Fig. 3.S8. OA enhancement per ppbv ambient MT for OH, O₃ and NO₃ oxidation in the OFR as a function of ambient temperature. Enhancement is defined as the difference between the concentrations measured after oxidation and in ambient air, where positive enhancements signify formation in the OFR. Data are colored by ambient in-canopy MT concentrations, and include the LVOC fate correction. Quantile averages of OA enhancement per ppbv MT are shown for each oxidant, with error bars corresponding to the standard error of the mean of each quantile.

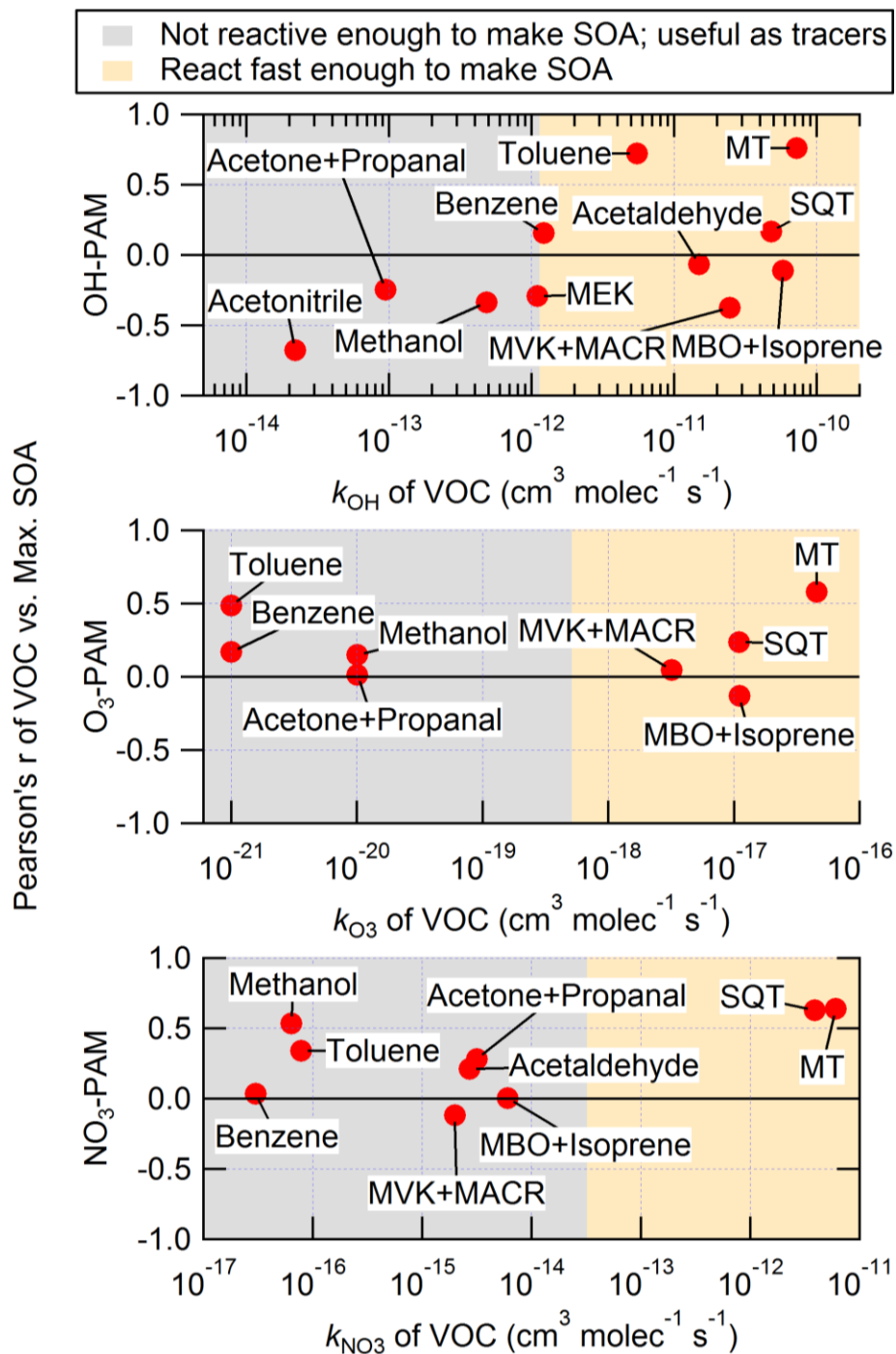


Fig. 3.S9. Pearson's r for the correlation between maximum SOA formation for each oxidant and the available ambient VOC concentrations. Maximum SOA formation is defined as the ranges of 0.4–1.5 eq. d for OH-PAM, 0.7–5 eq. d for O₃-PAM, 0.3–4 eq. d for NO₃-PAM. Reaction rate constants are taken from Atkinson and Arey (2003) and the IUPAC database (Atkinson et al., 2006). The orange colored background denotes rate constants that are fast enough so that $\geq 20\%$ of the VOC can react to form SOA under the conditions of maximum SOA formation in the OFR for each oxidant. In contrast, the grey background shows rate constants where the molecules do not react in the OFR and cannot contribute to SOA formation, but could be useful as tracers.

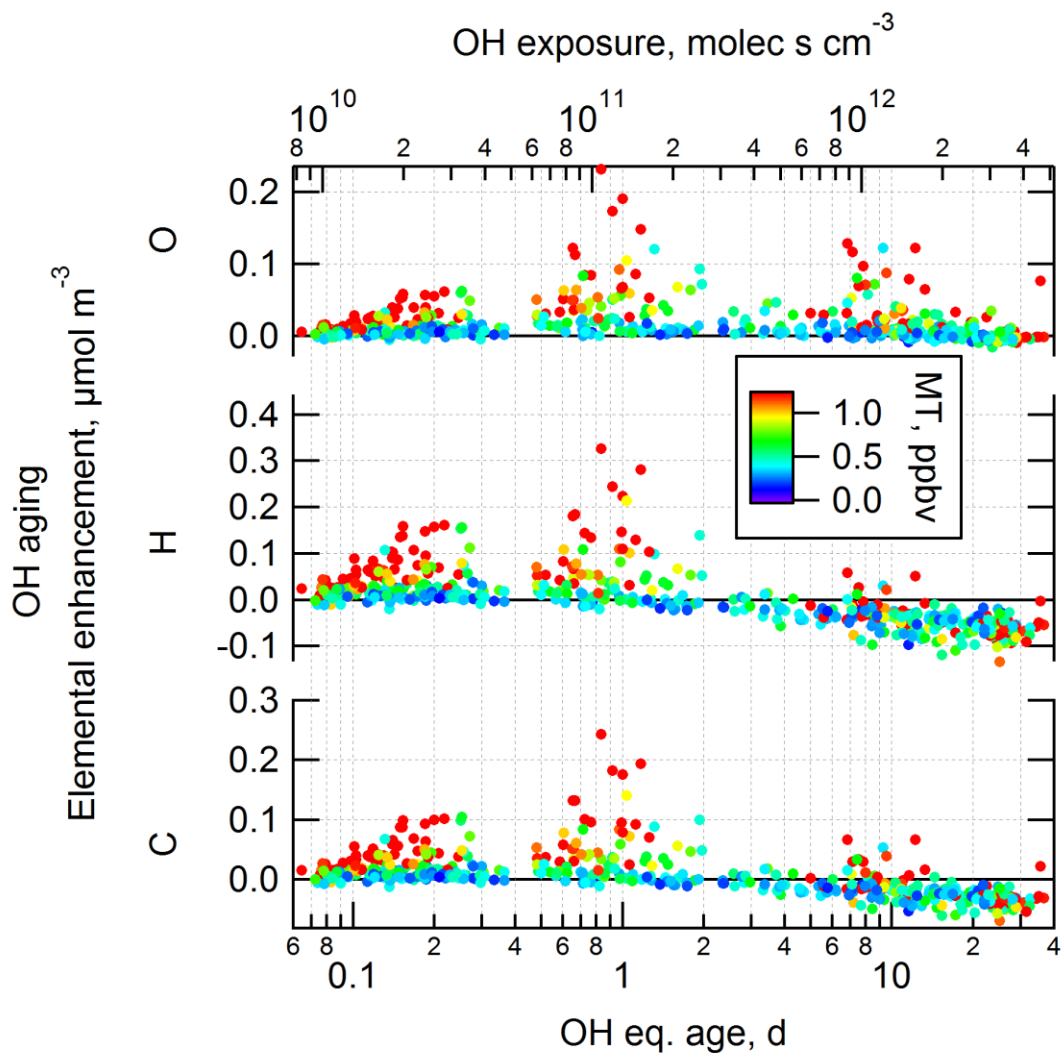


Fig. 3.S10. Elemental C, H, and O enhancements due to OH aging in the OFR, as a function of eq. OH age and exposure. Enhancement is defined as the difference between the concentrations measured after oxidation and in ambient air, where positive enhancements signify formation in the OFR. Data are colored by ambient in-canopy MT concentrations, and do not include the LVOC fate correction.

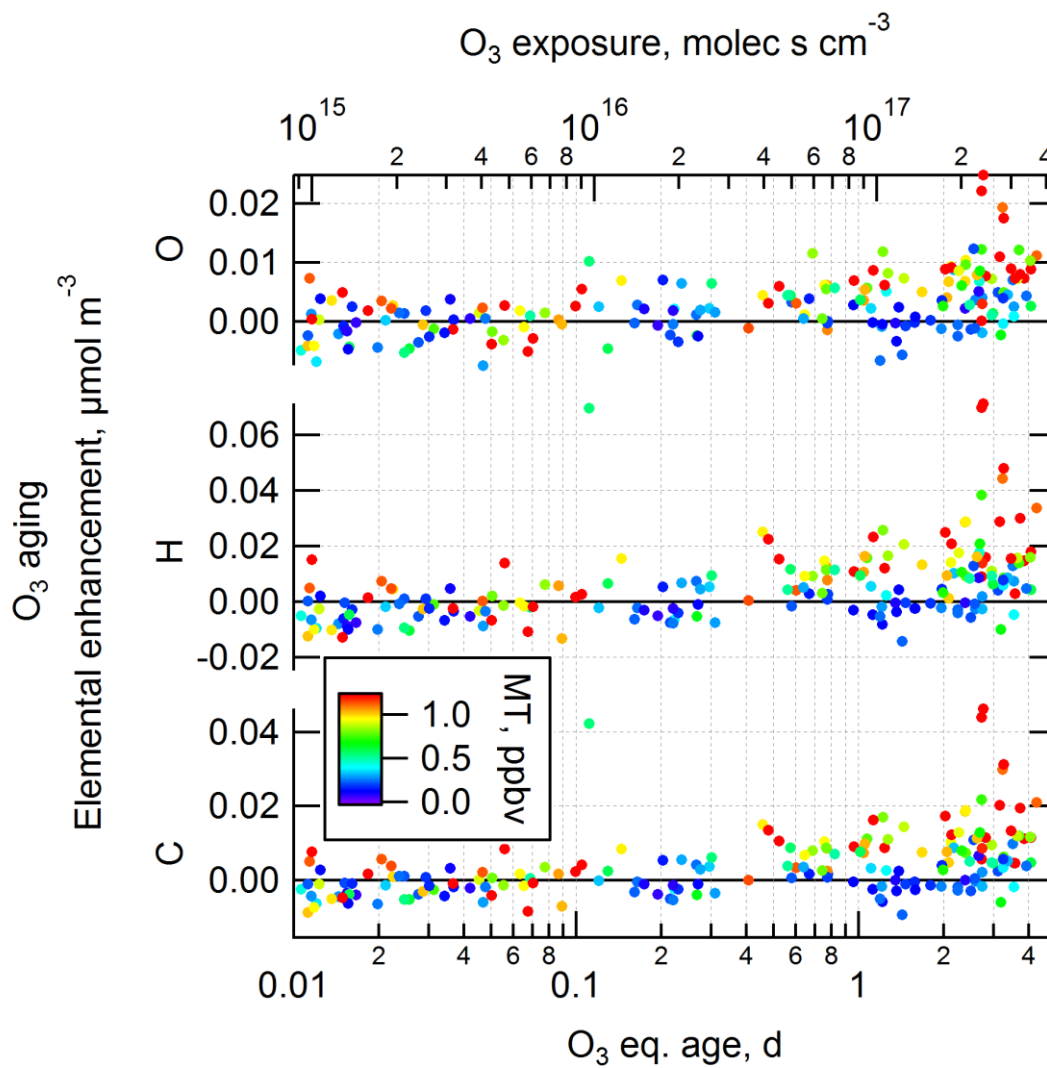


Fig. 3.S11. Elemental C, H, and O enhancements due to O_3 aging in the OFR, as a function of eq. O_3 age and exposure. Enhancement is defined as the difference between the concentrations measured after oxidation and in ambient air, where positive enhancements signify formation in the OFR. Data are colored by ambient in-canopy MT concentrations, and do not include the LVOC fate correction.

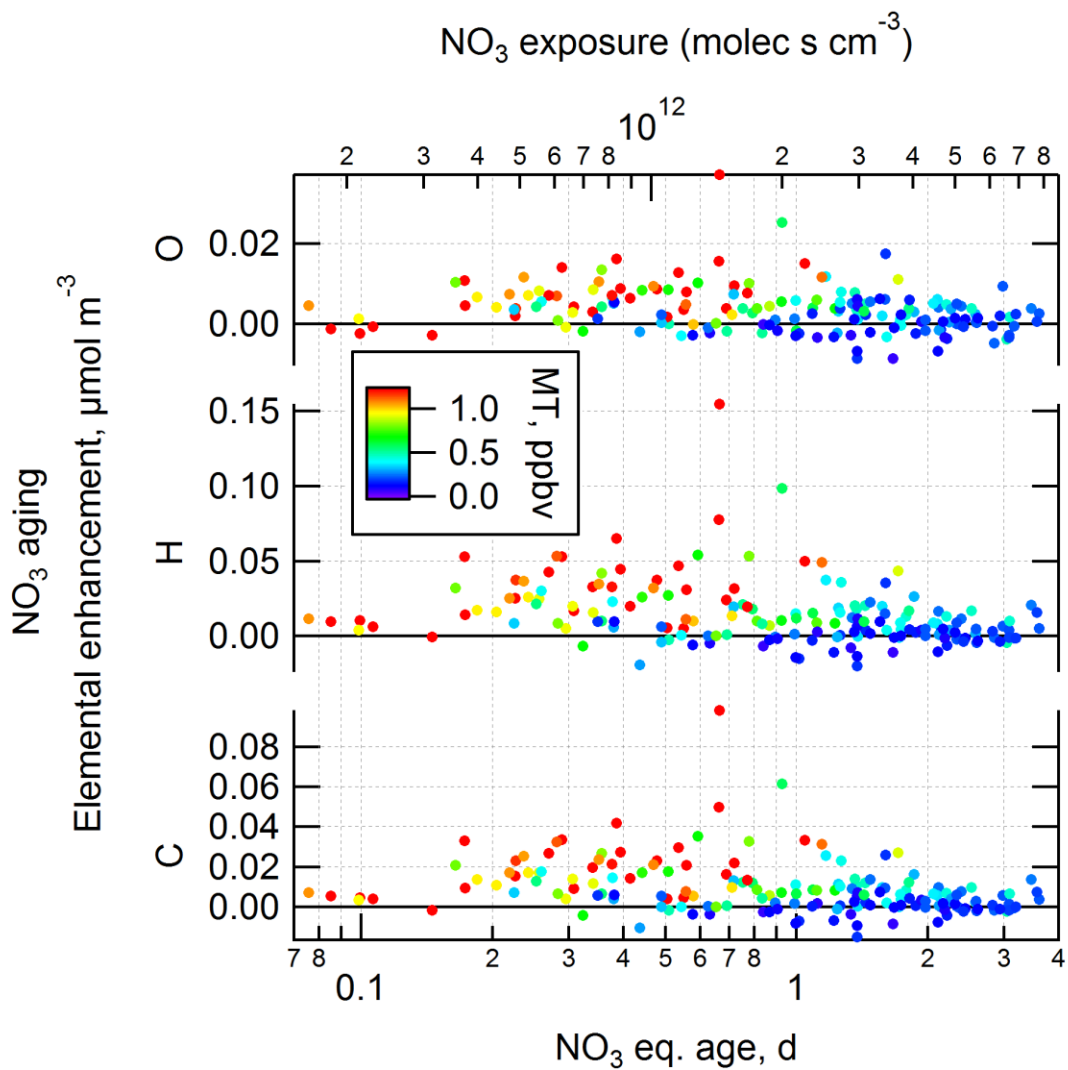


Fig. 3.S12. Elemental C, H, and O enhancements due to NO_3 aging in the OFR, as a function of eq. NO_3 age and exposure. Enhancement is defined as the difference between the concentrations measured after oxidation and in ambient air, where positive enhancements signify formation in the OFR. Data are colored by ambient in-canopy MT concentrations, and do not include the LVOC fate correction.

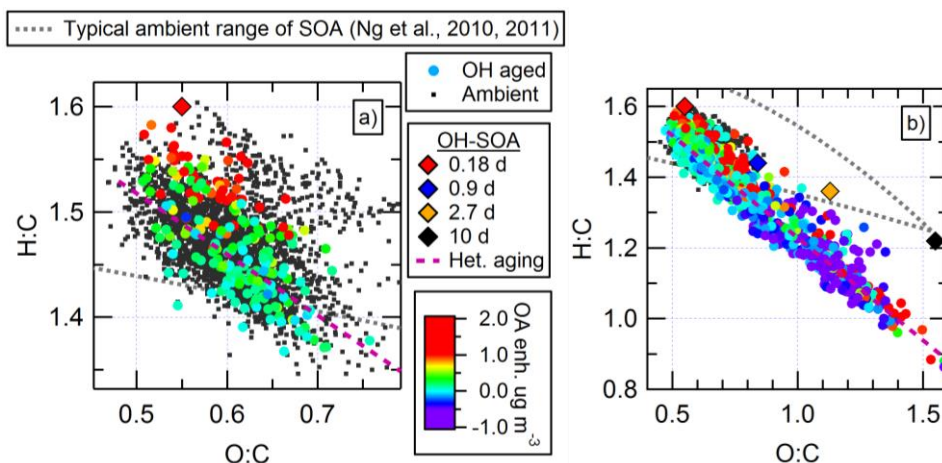


Fig. 3.S13. Van Krevelen diagrams of H:C vs. O:C ratios of OA after OH oxidation of ambient air in an OFR, along with values for ambient OA. OH aged data are colored by the amount of OA enhancement observed after oxidation. The H:C and O:C ratios of the new SOA mass formed in the OFR (i.e., the slopes from Fig. 3.8) are shown (diamonds; see Fig. 3.11). For data where no net C addition was observed after OH oxidation, the slope along which heterogeneous OH oxidation transforms the ambient OA is shown (purple dashed line). Panel a) shows only data in the eq. range of 0.1–0.4 (avg.=0.18) d, while panel b) shows all data.

Acknowledgements

We thank William H. Brune for discussions and contributions including the initial development of the PAM OFR. We thank US NSF grants AGS-1243354 and AGS-1360834, NOAA grant NA13OAR4310063, U.S. DOE ASR Program (Office of Science, BER, DE-SC0011105 & DE-SC0016559), Austrian Science Fund (FWF) project number L518-N20, and the US EPA (STAR 83587701-0) for partial support for this research. BBP acknowledges support from a CIRES Graduate Student Research Fellowship and a US EPA STAR Graduate Fellowship (FP-91761701-0). This work has not been formally reviewed by the US EPA. The views expressed are solely those of the authors, and the US EPA does not endorse any products or commercial services mentioned in this work. LK acknowledges support from DOC-fORTE-fellowship of the Austrian Academy of Science. The National Center for Atmospheric Research (NCAR) is sponsored by the National Science Foundation. AMO acknowledges a fellowship from the DOE SCGP Fellowship Program (ORAU, ORISE). KJZ was supported by NASA grant NNX09AE12G. We are grateful to Alex Guenther and Jim Smith of NCAR for co-organizing the BEACHON-RoMBAS field campaign, and to the USFS Manitou Experimental Forest Observatory for site support.

CHAPTER 4

Secondary organic aerosol formation from ambient air in an oxidation flow reactor during GoAmazon2014/5

Adapted from B.B. Palm, S.S. de Sá, D.A. Day, P. Campuzano-Jost, W.W. Hu, R. Seco, S.J. Sjostedt, J.-H. Park, A.B. Guenther, S. Kim, J. Brito, F. Wurm, P. Artaxo, L.D. Yee, G. Isaacman-VanWertz, A.H. Goldstein, Y. Liu, S.R. Springston, R. Souza, M.K. Newburn, M.L. Alexander, S.T. Martin, and J.L. Jimenez. *Atmos. Chem. Phys.*, in preparation, 2017.

Abstract

Secondary organic aerosol (SOA) formation from ambient air was studied using an oxidation flow reactor (OFR) during both the wet and dry seasons at the Observations and Modeling of the Green Ocean Amazon (GoAmazon2014/5) field campaign. Measurements were made at two sites downwind of the city of Manaus, Brazil. Ambient air was oxidized in the OFR using variable concentrations of either OH or O₃, over ranges from hours to days (O₃) or to weeks (OH) of equivalent atmospheric aging. The amount of SOA formed in the OFR ranged from 0 to greater than 10 μg m⁻³, depending on the amount of SOA precursor gases in ambient air. Typically, more SOA was formed during nighttime than daytime, and more from OH than from O₃ oxidation. SOA yields of individual organic precursors under OFR conditions were measured by standard addition into ambient air, and confirmed to be consistent with published environmental chamber-derived SOA yields. The measured SOA formation was compared to the amount predicted from the concentrations of measured ambient SOA precursors and their SOA yields. While measured ambient precursors were sufficient to explain the amount of SOA formed from O₃, they could only explain 10–50% of the SOA formed from OH. Previous OFR studies have shown that typically unmeasured semivolatile and intermediate volatility gases are present in ambient air and can explain such additional SOA formation. To investigate the sources of the unmeasured SOA-forming gases during this campaign, multilinear regression analysis was performed between measured SOA formation and

gas-phase tracers representing different precursor sources. The observed potential for SOA formation was attributed 65% (61%), 33% (17%), and 6% (17%) to biogenic, anthropogenic, and biomass burning emissions during the wet (dry) season. The majority of SOA-forming gases present during both seasons were biogenic, while biomass burning sources were more important during the dry season.

4.1 Introduction

Atmospheric submicron aerosols have impacts on radiative climate forcing, air quality, and human health (Pope and Dockery, 2006; IPCC, 2013). Organic aerosol (OA), in particular secondary OA (SOA) formed through various gas-to-particle processes, comprises the majority of ambient submicron particulate mass (Zhang et al., 2007; Jimenez et al., 2009). SOA can be produced from gases emitted from biogenic, anthropogenic, and biomass burning sources, upon oxidation by OH, O₃, and NO₃ (Ziemann and Atkinson, 2012). In order to mitigate aerosol impacts, the sources, formation, properties, and loss processes of SOA need to be understood. Modeling of OA remains extremely uncertain due to uncertainties in these underlying processes (Tsigaridis et al., 2014).

These uncertainties are due in part to limitations in our ability to speciate and quantify the majority of organic compounds in the atmosphere (Goldstein and Galbally, 2007). These organic compounds range over greater than ten orders of magnitude in volatility, a property which is vital in determining a compound's phase state, lifetime, and fate in the atmosphere (e.g., Donahue et al., 2013). The most volatile organics are called volatile organic compounds (VOCs). VOCs reside in the gas-phase until they deposit or are chemically transformed, and they are relatively easier to speciate and quantify. The lowest volatility compounds are found almost entirely in the particle phase (i.e. as OA), and under most conditions they can also be quantified (online, e.g., using AMS or SMPS) and at least partially speciate (offline, e.g., GC-MS, CIMS, electrospray mass spectrometry). The compounds with volatilities between VOCs and OA include semi- and intermediate volatility organic compounds (SVOCs and IVOCs, or S/IVOCs; Robinson et al., 2007). There have been recent attempts to quantify bulk S/IVOCs (Cross et

al., 2013; Hunter et al., 2016), to speciate subsets of S/IVOCs (e.g., Zhao et al., 2014; Chan et al., 2016), and to model SOA formation from such gases (Robinson et al., 2007; Dzepina et al., 2009; Hodzic et al., 2010; Jathar et al., 2011; Miracolo et al., 2011; Woody et al., 2015). However, much remains to be learned about these compounds in order to adequately understand SOA formation.

SOA parameterizations in atmospheric models have been developed by measuring SOA yields after the oxidation of VOC precursors in large environmental chambers. However, the interpretation and quantification of chamber experiments can be impaired as the result of substantial losses of S/IVOC gases (Matsunaga and Ziemann, 2010; Zhang et al., 2014; Krechmer et al., 2015; La et al., 2016; Nah et al., 2016) and particles (Crump and Seinfeld, 1981; McMurry and Rader, 1985; Pierce et al., 2008) to the chamber walls.

Due to the frequently poor performance of SOA models for field studies (Tsigaridis et al., 2014), it is of high interest to study SOA formation from ambient air. Portable large Teflon chambers have been built, but to our knowledge they have mainly been used to age exhaust from various emission sources (Presto et al., 2011; Platt et al., 2013). It is difficult to use large chambers to age ambient air, due to their size and complexity, as well as the low time resolution of the results (~1 experiment per day). To our knowledge only a few studies have studied ozone formation from ambient air using such chambers (Tanaka et al., 2003), and only one study has used a large chamber to process ambient air for aerosol aging research (Peng et al., 2016a), with no published studies on SOA formation from ambient air with that technique.

Recently, an alternative method of studying SOA formation, namely oxidation flow reactors (OFRs), has been developed. OFRs are relatively small (on the order of 10 L volume) vessels that employ high oxidant concentrations (OH, O₃, or NO₃) with a short residence time of several minutes (Kang et al., 2007; Lambe et al., 2011a). This allows anywhere between hours and months of equivalent atmospheric oxidation to be achieved in an experimental setup that is small and portable, allowing ambient air to be

directly sampled and oxidized in the OFR in near real-time, allowing rapid tracking of changes in ambient SOA precursor gases. Oxidation of ambient forest air (Palm et al., 2016) and urban air (Ortega et al., 2016) has shown that ambient S/IVOCs are likely important precursors for ambient SOA formation from OH oxidation, and not for O₃ oxidation (Palm et al., 2017).

In this work, we use an OFR to investigate SOA formation from the oxidation of ambient air at a tropical rainforest site with varying degrees of urban/anthropogenic and biomass burning influence during the GoAmazon2014/5 field campaign. Ambient air was oxidized by either OH or O₃, and the subsequent SOA formation was used to investigate the types, amounts, and diurnal/seasonal changes in the amounts of ambient SOA precursor gases. SOA yields in the OFR under standard OFR experimental conditions were investigated by injecting and oxidizing known amounts of individual precursor gases in ambient air in the OFR. These results are discussed in the context of improving our understanding of atmospheric SOA formation and sources.

4.2 Experimental methods

4.2.1 GoAmazon2014/5 field campaign

The Observations and Modeling of the Green Ocean Amazon (GoAmazon2014/5) field campaign took place near the city of Manaus in the state of Amazonas, Brazil, during 2014 and 2015 (Martin et al., 2016a, 2016b). The majority of the measurements presented in this work were conducted at the “T3” supersite, located approximately 70 km west (downwind) of Manaus, a city of 2 million people. The site was located in a large clearing (2.5 km by 2 km) and surrounded by rainforest, 10 km NE of the city of Manacapuru. These measurements were taken during the two intensive operating periods, referred to as IOP1 (Feb. 1–Mar. 31, 2014) and IOP2 (Aug. 15–Oct. 15, 2014). IOP1 took place during the wet season, while IOP2 was during the dry season. Measurements were also conducted at the “T2” site, located approximately 10 km west of Manaus on the opposite bank of the Rio Negro, between Mar. 30–

May 9, 2014 (wet season) and August 3–September 2, 2014 (dry season). Further details about the GoAmazon2014/5 field campaign can be found in Martin et al. (2016a, 2016b).

4.2.2 Oxidation flow reactor

The specific OFR used in this work was a Potential Aerosol Mass (PAM) reactor (Kang et al., 2007; Lambe et al., 2011a). The PAM reactor is a cylindrical aluminium tube with a volume of approximately 13 L. Ambient air was sampled through an approximately 2-cm-diameter hole in the inlet plate on one end of the OFR, followed immediately by passing through a coarse mesh grid (1.2 mm spacing) that was coated by an inert silicon coating (Sulfinert by SilcoTek, Bellefonte, PA) in order to minimize gas and particle losses. Two identical OFRs were located on the roof of a trailer where the instrumentation was located with a residence time between 2.5–3.9 min. To investigate OH oxidation in the OFR, OH radicals were produced in situ using the “OFR185” method described elsewhere (Li et al., 2015; Peng et al., 2015). OH exposure was estimated using a kinetic model-derived equation, which uses inputs of ambient water vapor concentration, temperature, O_3 produced in the OFR (measured in the output flow), and external OH reactivity (OHR_{ext}) as input parameters (Li et al., 2015; Peng et al., 2015). OHR_{ext} is the OHR from ambient gases such as VOCs. Since there were no direct OHR_{ext} measurements at the T3 site during this campaign, OHR_{ext} was assumed to be equal to the average diurnal profile of the measurements in Williams et al. (2016), ranging from 27–74 s^{-1} (shown in Fig. 4.S1). The OH exposure estimation equation is discussed in Peng et al. (2015) can be downloaded from the PAM Wiki (<https://sites.google.com/site/pamwiki/>). The model-estimated OH exposure (OH_{exp}) was verified by comparing it with measured decay of ambient VOCs and CO (which was injected into the OFR), as shown in Sect. 4.3.1. OH_{exp} was converted to equivalent (eq.) days of atmospheric aging by dividing by a typical 24 h average atmospheric concentration of 1.5×10^6 molec cm^{-3} OH (Mao et al., 2009).

To study O_3 oxidation, O_3 was injected into the OFR using a technique previously described in Palm et al. (2017). Elevated O_3 concentrations from hundreds of ppb up to 150 ppm were achieved in

the OFR by flowing 0.5 lpm of ultra-high purity O₂ (g) over UV lamps (externally to the reactor). The O₂ was photolyzed by 185 nm light, which produced O(³P) that further reacted with O₂ to produce an O₂+O₃ mixture. The oxidant flow was then injected through four ports located around the inlet plate inside the OFR. O₃ concentrations in the OFR were cycled by adjusting the UV lamp intensity used for O₃ production. O₃ exposure was calculated by multiplying the O₃ concentration by the average residence time in the OFR. This O₃ exposure was converted to eq. atmospheric days of oxidation by dividing by a typical 24 h average ambient O₃ concentration of 30 ppb.

Measurements of O₃ in the outflow of each OFR were made using a 2B Technologies Model 205 Ozone Monitor and a Thermo Scientific Model 49i Ozone Analyzer at a time resolution of 10 seconds.

4.2.3 Gas and particle measurements

For the measurements at the T3 site, particles in ambient air and after OFR oxidation were sampled using an Aerodyne high-resolution time-of-flight aerosol mass spectrometer (HR-ToF-AMS, hereafter referred to as AMS; DeCarlo et al., 2006; Canagaratna et al., 2007) and a TSI 3936 Scanning Mobility Particle Sampler (SMPS). Ambient and OFR-oxidized VOC concentrations were sampled during the entire campaign using an IONICON proton-transfer-reaction time-of-flight mass spectrometer (PTR-TOF-MS), which sampled using H₃O⁺ as the reagent ion during IOP1 and NO⁺ as the reagent ion during IOP2. At the T2 site, the gases and particles in ambient air and after the OFR were sampled using an Aerodyne Aerosol Chemical Speciation Monitor (ACSM; Ng et al., 2011a) and a unit-resolution quadrupole PTR-MS (IONICON).

At both sites, a system of automated valves (Aerodyne AutoValve) cycled by custom LabView (National Instruments, Inc.) software was used to alternate sampling between ambient and oxidized air. The flowrate through all sampling lines and the OFRs was kept constant at all times by pulling a bypass flow when not actively sampling with a given instrument. Ambient temperature and humidity were recorded using Vaisala HM70 probes. All aerosol samples were dried to below approximately 30% RH

prior to or at the same time as being sampled into the measurement trailer, to prevent condensation in the sampling lines when sampling into air conditioned trailers. The decay of injected CO (~2 ppm in reactor) was used to help estimate OH exposures in the OFR. CO was measured in ambient air and after oxidation using a Picarro G2401 CO/CO₂/CH₄/H₂O Cavity Ringdown Spectrometer.

OH and O₃ oxidation was typically performed in one of two ways. The majority of the time, the oxidant concentration was cycled through ~20 min steps (16–24 min in practice) covering a range of concentrations from no added oxidant to maximum added oxidant over the course of a 2–3 h full cycle. The OFR aerosol was sampled for the last 4 min of every step, allowing time for the OFR conditions to stabilize before measurement. An alternative method was also used, where the oxidant concentrations were held constant. In this manner, the OA enhancement from a constant amount of oxidation could be sampled every 16–24 min or faster rather than once every 2–3 h. For example, the concentration that typically produces the maximum amount of SOA formation could be sampled, or the UV lights could be set to achieve the highest oxidant concentrations in order to investigate heterogeneous oxidation.

The aerosol data at the T3 site was corrected for diffusive particle losses in the sampling line, estimated using the Max Planck Particle Loss Calculator (von der Weiden et al., 2009). To account for particle losses to the internal surfaces of the OFR, the OFR data was corrected by the ratio of ambient OA to the OA measured through the OFR in the absence of added oxidant (an average correction of +6%). A key data product in this work is OA enhancement, which is defined as the OA concentration measured after oxidation minus the ambient OA concentration (measured immediately before and after OFR sampling). The maximum OA enhancement (or maximum SOA formation) observed in this study was typically between 0.5 and 2 eq. days of OH aging, or above 1 eq. day of O₃ aging. Unless otherwise specified, the OA enhancements were corrected for low-volatility organic compound (LVOC) fate to account for losses of condensable gases on OFR surfaces, excessive gas-phase oxidation leading to fragmentation prior to condensation, and limited timescales for condensation in the OFR that are not

expected in the atmosphere, as explained in Palm et al. (2016). The AMS data at T3 was calculated using a collection efficiency (CE) of 1 for IOP1 and a composition-dependent CE (mostly 0.5; Middlebrook et al., 2012) for IOP2. These values were verified based on comparison with the SMPS data, which is shown in Fig. 4.S2. The CE of 1 during the wet season, while unusual, corresponds to the value determined during a previous campaign in the wet season in central Amazonia, which is dominated by liquid biogenic SOA under high humidity conditions (Chen et al., 2009; Pöschl et al., 2010).

4.2.4 Predicting SOA formation in the OFR

In Sect. 4.3.5 below, the measured SOA formation in the OFR is compared with the amount predicted to form in order to investigate which ambient gases are contributing to SOA formation. In order to predict the amount of SOA that will form, SOA yields are applied to the mass concentrations of all known SOA precursor gases measured in ambient air.

For OH oxidation, these gases include isoprene, monoterpenes (MT), sesquiterpenes (SQT), benzene, toluene, xylenes, trimethylbenzenes, and the sum of four biomass burning tracers (vanillin, vanillic acid, syringol, and guaiacol). The SQT and biomass burning tracers were measured using the semi-volatile thermal desorption aerosol gas chromatograph (SV-TAG), and the rest were measured by one of two PTR-TOF-MS instruments sampling at the T3 site (Martin et al., 2016a). First, the fraction of the ambient gas predicted to react in the OFR for a given oxidant exposure was calculated. Then, the OA concentration-dependent SOA yield parameterizations from Tsimpidi et al. (2010) were used to calculate the amount of SOA predicted to form (except for isoprene, where the yield parameterization from Henze and Seinfeld (2006) was used). The average yields used in these calculations for IOP1(IOP2) were 3%(5%) for isoprene, 10%(18%) for MT (also used for the biomass burning tracers), 10%(23%) for SQT, 11(22%) for benzene and toluene, and 12%(26%) for xylenes and trimethylbenzenes.

For O₃ oxidation, ambient MT and SQT were used to predict SOA formation. As for previous O₃ oxidation experiments in an OFR, representative SOA yields of 15% for MT and 30% for SQT were used

(Palm et al., 2017). Due to the lack of certainty of SOA yields for these gases from O₃ oxidation, and also due to the lack of speciation of MT and SQT at the T3 site, these values were chosen to be generally representative of the yield values that have been published (e.g., Jaoui et al., 2003, 2013; Ng et al., 2006; Pathak et al., 2007, 2008; Shilling et al., 2008; Winterhalter et al., 2009; Chen et al., 2012; Tasoglou and Pandis, 2015; Zhao et al., 2015).

4.3 Results and Discussion

4.3.1 Using VOC decay to determine OH and O₃ exposure

One of the benefits of the OFR system over environmental chambers is the ability to rapidly change the amount of oxidant in the OFR over a wide range of concentrations. As described above, OH exposure in the OFR was estimated using a model-derived equation, while O₃ exposure was estimated as the measured O₃ concentration after the OFR multiplied by the average residence time. Because there are uncertainties related to these estimates (e.g., uncertain OH reactivity, residence time distribution, intrinsic uncertainties of the model), it is important to use in situ measurements to verify the exposures achieved in the OFR. This can be done by measuring the decay of various gases, including gases present in ambient air or gases that are injected into the OFR. Previous experiments have injected deuterated compounds, which prevent contamination of the signal with ambient gases and allow the reaction rate constant of the injected compound to be known precisely (Bruns et al., 2015). In this work, decay of ambient toluene and MT and injected CO was used to verify the OH and O₃ exposures. Any changes in the ambient concentrations of these gases between the times of the surrounding ambient measurements and the time of the decay in the OFR (approximately 5 min apart) translates into noise in the measurement of the fraction reacted. The speciation of MT in ambient air was also unknown. In this analysis, the fraction remaining was predicted using α -pinene (an important MT in the Amazon; e.g., Rinne et al., 2002; Jardine et al., 2015) with rate constants $k_{OH} = 5.3 \times 10^{-11}$ and $k_{O_3} = 8.6 \times 10^{-17}$ cm³ molec⁻¹ s⁻¹ (Atkinson and Arey, 2003).

The decay of ambient MT, ambient toluene, and injected CO in the OH-OFR is shown in Fig. 4.1, along with the theoretical decay curves predicted assuming either plug flow (i.e., a single residence time) or using the residence time distribution (RTD) for particles from Lambe et al (2011a), which is likely to be more skewed than the RTD in this work (due to our use of a larger inlet). In general, the OH exposure predicted from the model-derived equation matches the OH exposure estimated from the decay of gases within a factor of approximately 2-3, consistent with expectations (Li et al., 2015). The model equation appears to over-predict OH exposure at the lowest achieved exposures for MT (but not for toluene or CO), while under-predicting at the highest exposures for CO while over-predicting for toluene. When taking the results for all species, the average errors are relatively small. Interferences in the PTRMS detector for MT from MT products may mask the decay of these species a low remaining fraction. Also, it is likely that the true RTD has some differences from the one used in the calculation, and perhaps some variability in time. If even small plumes of ambient air transit through the OFR without being exposed to as much oxidant due to variability in the internal air flow fields, this can lead to increases in the measured fraction remaining, particularly for lower exposures. At high exposures, the model assumes that the OH reactivity of the ambient air decays at the same rate as SO₂ (Peng et al., 2015). If this estimated decay is too slow (e.g. due to faster decay of isoprene-related reactivity), it could lead to an under-prediction of OH exposure at high exposures.

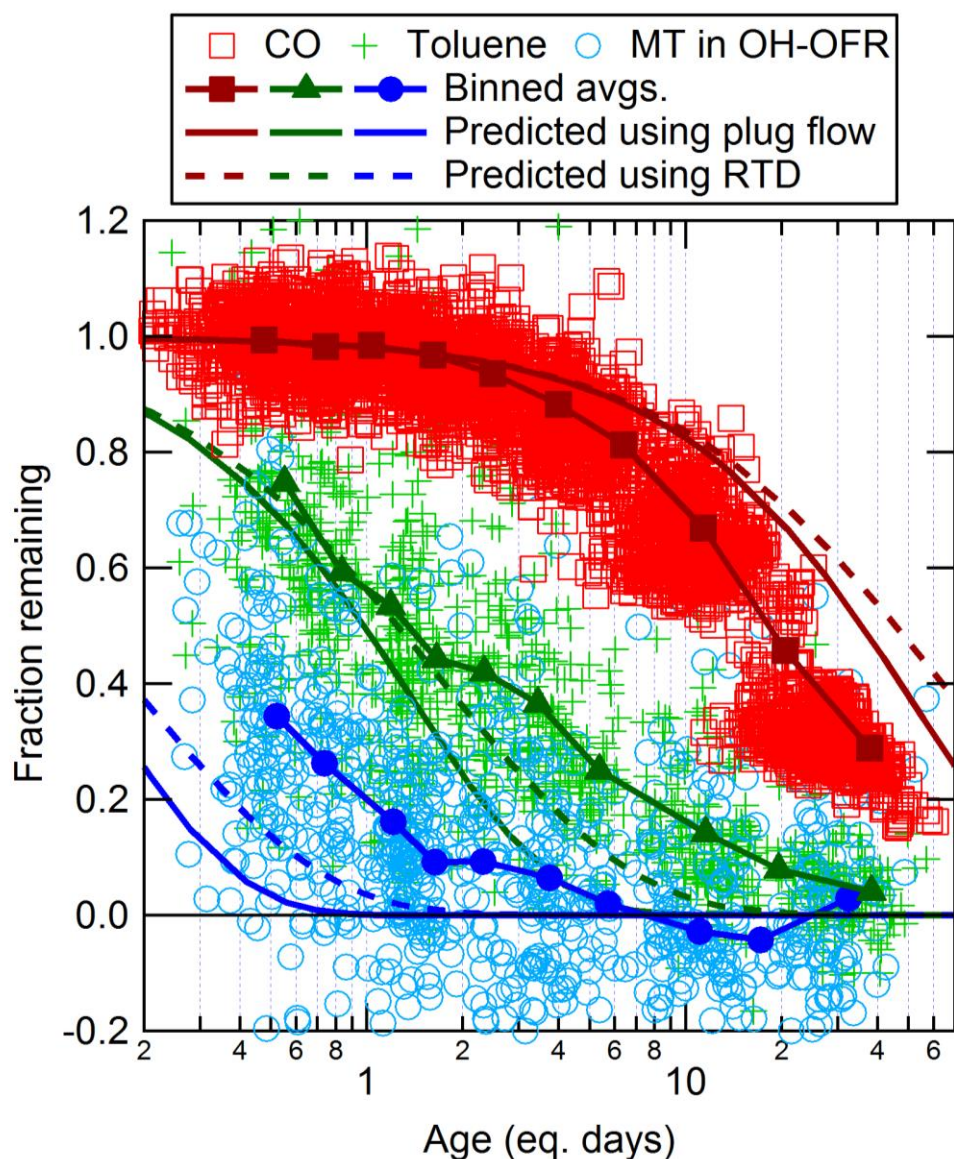


Fig. 4.1. Fraction of ambient toluene, ambient MT, and injected CO remaining after OH oxidation in the OFR, as a function of equation-estimated photochemical age (Peng et al., 2015). Binned averages of the fraction remaining are also shown, compared to the amount predicted to remain assuming either plug flow or using the residence time distribution (RTD) for particles from Lambe et al. (2011a).

The decay of MT in the O_3 -OFR is shown in Fig. 4.2, along with predictions for the plug flow and Lambe et al. (2011a) residence times. Again, the O_3 exposures estimated from the model and from MT decay match within a factor of approximately 2-3. All MT were reacted after an exposure of 1 eq. day.

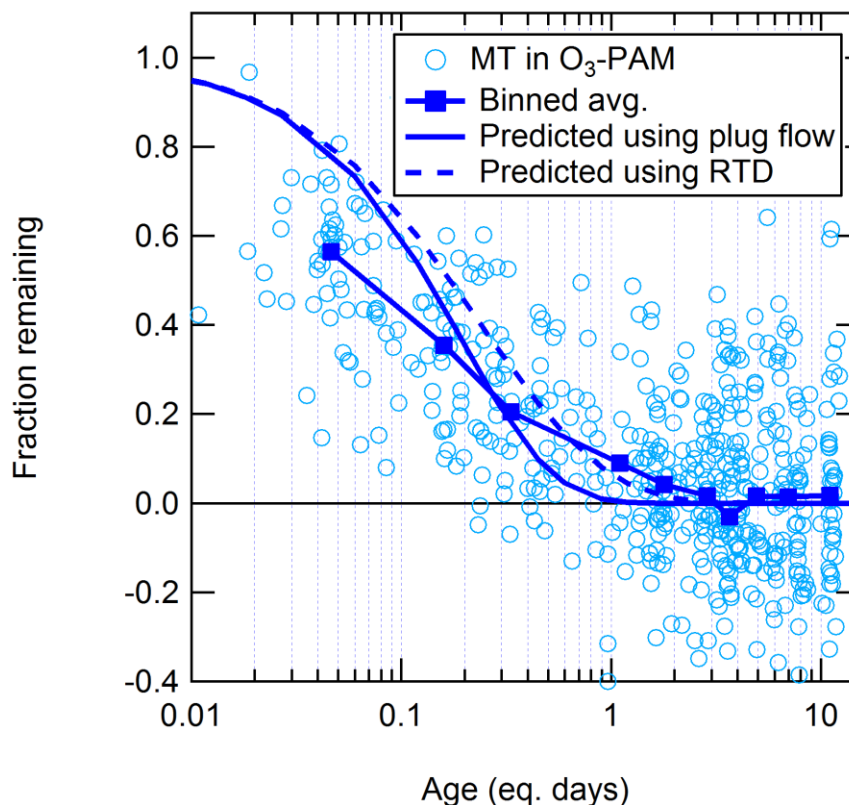


Fig. 4.2. Fraction of ambient MT remaining after O_3 oxidation in the OFR, as a function of photochemical age. Binned averages of the fraction remaining are also shown, compared to the amount predicted to remain assuming either plug flow or using the RTD of particles from Lambe et al. (2011a).

4.3.2 SOA formation from ambient biogenic and anthropogenic gases in OFR

A basic premise of the OFR technique (as used in this work) is that SOA precursor gases entering the OFR can be oxidized to form SOA. A simple way to investigate and illustrate this concept for ambient experiments is to compare SOA formation with ambient VOCs over a period of time. Figure 4.3 shows a two-night example of OA measured in ambient air compared to OA measured after OH oxidation at the T3 site, along with ambient total MT and copaene (a SQT). In this example, the OH exposure was kept nearly constant for the entire time at approximately 3 eq. days, near the range where maximum SOA formation was expected. Using this method, maximum SOA formation was sampled every 24 min rather than every 2–3 h as with the standard cycling of OH exposure. Note that in theory, ambient and OFR measurements could be alternated at much faster frequencies (as fast as ~ 10 s). In practice during this time period, the instrumentation was alternating between measurements of ambient air, two OFRs, and

a thermodenuder, and longer averages of the data (1–2 min) were preferred to reduce noise and data volume, limiting the frequency with which the OFR measurements were taken. In Fig. 4.3, the times when SOA was formed in the OFR clearly coincide with the spikes in ambient MT and SQT concentrations, illustrating an example of likely biogenic-dominated SOA formation. This is evidence that the SOA being formed in the OFR was derived from gases that were entering the OFR. Importantly, this example illustrates that the ambient precursor concentrations at the site can change rapidly, even faster than the typical 2–3 h cycles.

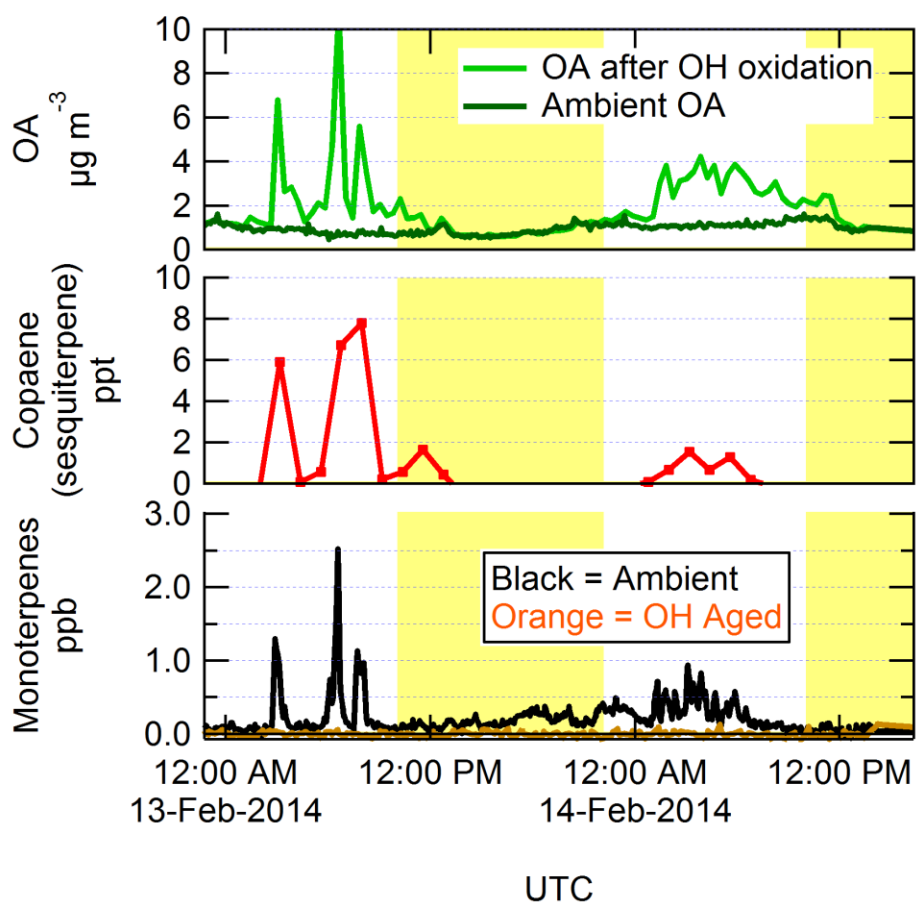


Fig. 4.3. An example of the time series of OA concentrations measured in ambient air and after OH oxidation of ambient air in the OFR, shown together with ambient copaene (a sesquiterpene, measured by SV-TAG) and monoterpenes (measured by PTR-TOF-MS before and after the OFR). Daytime hours are indicated with the yellow background. OH exposure in the OFR was held constant throughout this time at approximately 3 eq. days. The SOA formed in the OFR is shown as measured, without the LVOC fate correction. In this example, the SOA formation from OH oxidation closely follows the availability of ambient biogenic gases, though the amount of SOA formed was substantially larger than could be formed from the measured ambient gases.

Another example of SOA formation from ambient precursors, this time from the T2 site (close to Manaus), is shown in Fig. 4.4. In this example, the OH exposure was cycled through the whole range of eq. ages, including one step each cycle with no OH. In the OFR, SOA was formed at three distinct times, labeled Periods 1, 2, and 3 in Fig. 4.4. During Period 1, ambient MT concentrations were near zero, and elevated concentrations of xylenes and TMB strongly suggest the presence of an anthropogenic plume affecting the T2 site. The SOA formed during this cycle was likely formed from predominantly anthropogenic precursors. In contrast, the SOA formed during Period 3 was produced in the presence of MT but not the anthropogenic tracers, suggesting the SOA was predominantly biogenic. The SOA formed during Period 2 was produced in the presence of both anthropogenic and biogenic gases, and likely was formed from a mix of both types of gases. These two examples clearly illustrate the usefulness of the OFR technique for measuring potential SOA formation from ambient air.

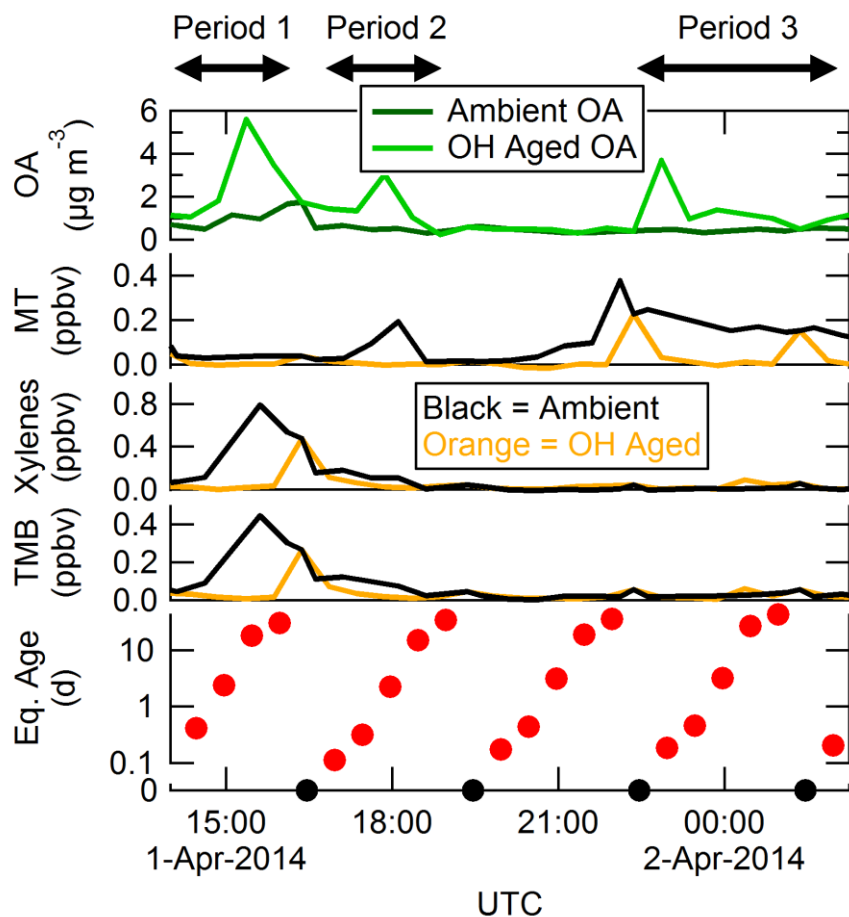


Fig. 4.4. An example of OA concentrations in ambient air and after OH oxidation of ambient air in the OFR at the T2 site, shown together with MT, xylenes, and trimethylbenzene (TMB) measured in ambient air and after OH oxidation. The OH exposure is also shown (in eq. days). OH age was cycled through a range of exposures, including no added exposure (black circles) where none of the VOCs were reacted in the OFR. This example illustrates how SOA formation in the OFR can come from anthropogenic (Period 1), biogenic (Period 3), or mixed (Period 2) precursors, depending on ambient conditions.

4.3.3 OA enhancement vs. photochemical age

As part of the GoAmazon2014/5 campaign, the formation of aerosol from the oxidation of ambient air was sampled over a wide range of conditions. This includes the changes of ambient air composition between the wet and dry seasons, and the diurnal, synoptic, and other changes during each season. OH oxidation of ambient air was performed at both the T2 and T3 sites, and O_3 oxidation was performed at the T3 site. A basic way to view the differences across these conditions is by comparing the OA enhancement from each subset as a function of photochemical age. This is shown for OH

oxidation in Fig. 4.5 and O_3 oxidation in Fig. 4.6, split into daytime (06:00–18:00 LT) and nighttime (18:00–06:00 LT) for each season and location. The data here are shown without the LVOC fate correction, in order to illustrate the measurements over the entire age range. The LVOC fate correction is nontrivial to apply at ages above approximately 5 eq. days when heterogeneous oxidation becomes important, and here we want to show the effects of high ages.

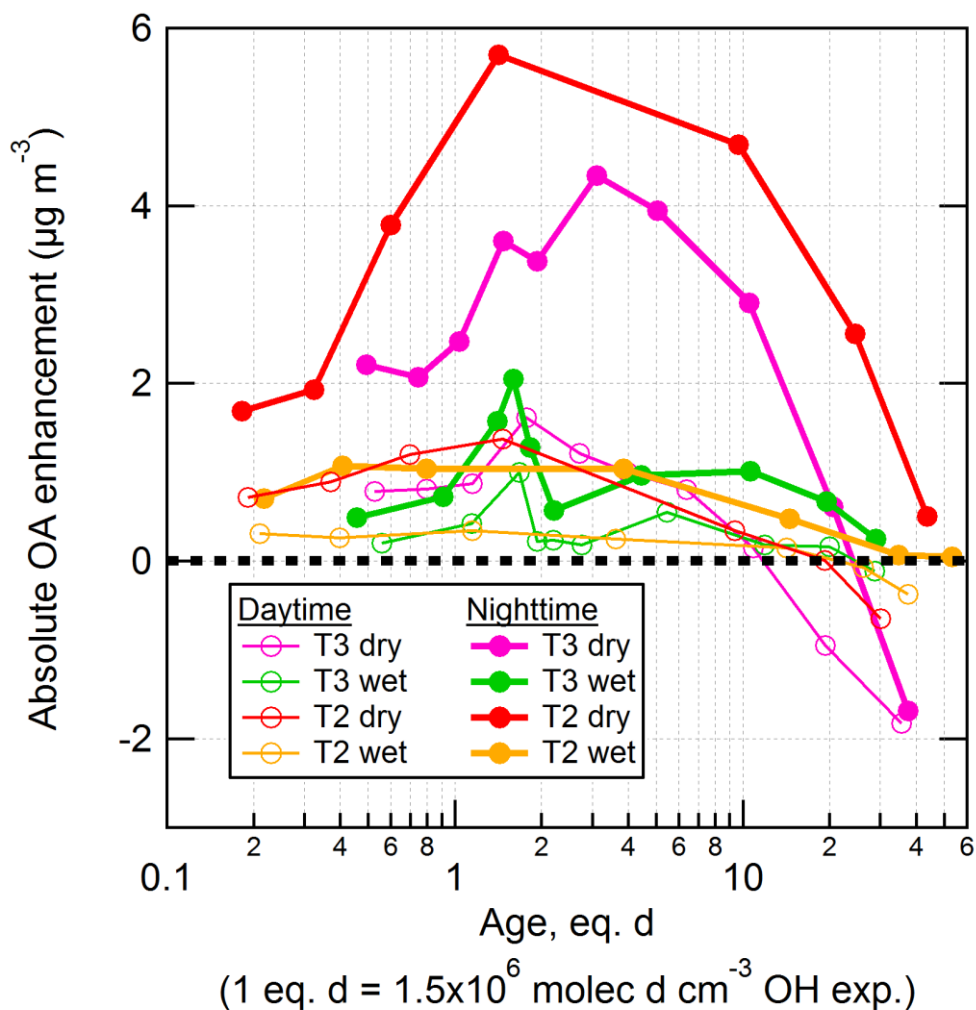


Fig. 4.5. Absolute OA enhancement after OH oxidation in the OFR as a function of photochemical age, shown as binned averages for the wet and dry seasons at both the T2 and T3 measurement sites, and split into daytime (06:00–18:00 LT) and nighttime (18:00–06:00 LT) data. This data is not corrected for LVOC fate, in order to show measurement behavior at the highest OH_{exp} .

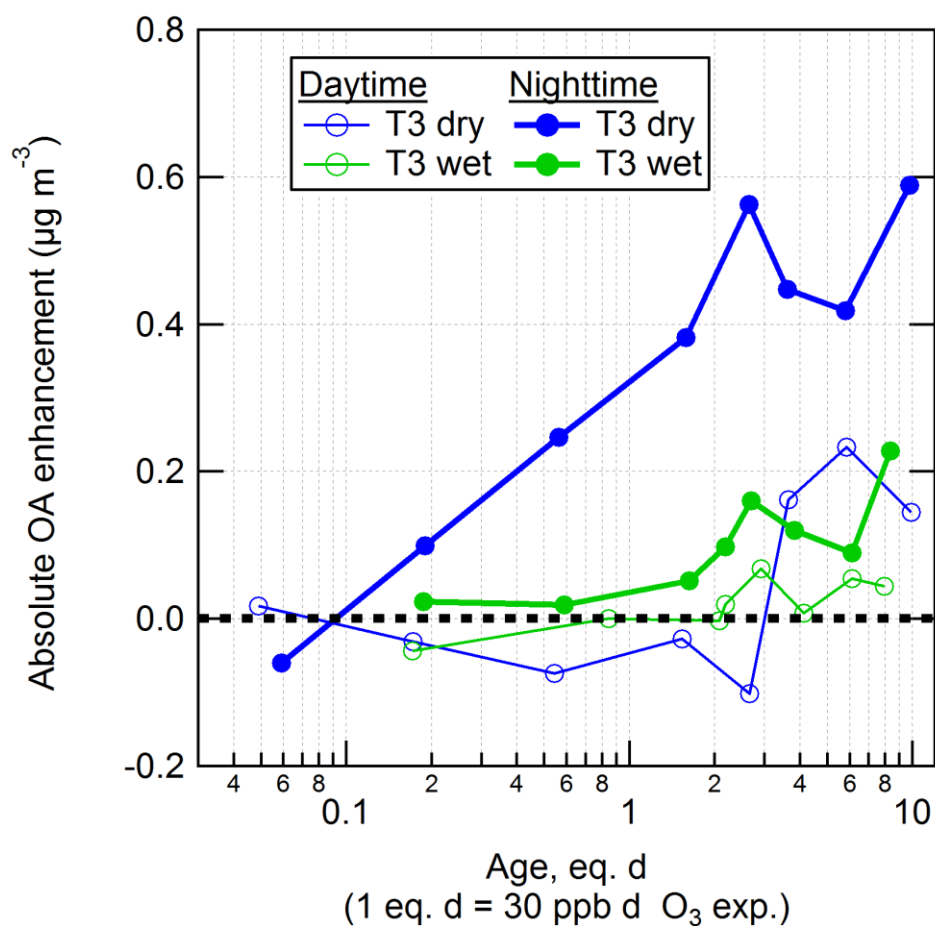


Fig 4.6. Absolute OA enhancement after O_3 oxidation in the OFR as a function of photochemical age, shown as binned averages for the wet and dry seasons at the T3 measurement site, and split into daytime (06:00–18:00 LT) and nighttime (18:00–06:00 LT) data. The data is not corrected for LVOC fate.

For OH oxidation at each site and season, an increasing amount of SOA formation was observed for increasing ages, up to a maximum amount of SOA formed in the range of approximately 1–4 eq. days of OH oxidation. At higher ages, the net amount of SOA formed became less or even negative (net loss of OA compared to ambient air). This result is due to a combination of two effects (which have also been observed previously): rapid oxidation of condensable gases prior to those gases having time to condense on particles, leading to fragmentation that produces volatile oxidation products; and heterogeneous oxidation of preexisting (and newly formed) particle mass, leading to fragmentation and evaporation of the particles (George and Abbatt, 2010; Lambe et al., 2012; Ortega et al., 2016; Palm et al., 2016).

The amount of SOA formed at the T2 and T3 sites was roughly the same within each season. At both sites, approximately 4 times more SOA was formed during the dry season than the wet season. While there may have been specific instances when plumes of SOA precursor gases affected the T2 site more strongly due to its closer proximity to Manaus than the T3 site, these measurements suggest that the seasonal changes in SOA precursor gases are more important than the proximity to Manaus. One possibility is that a substantial fraction of the anthropogenic SOA had already formed by the time the air passed over the T2 site, so formation in the OFR of the remaining potential SOA did not lead to a very large difference between the sites sources.

As shown in Fig. 4.6, approximately 4 times more SOA was formed from O_3 oxidation during the dry season than the wet season as well, with higher formation during nighttime than daytime hours. The amount of SOA formation increased with O_3 eq. age, with maximum values above approximately 1 eq. day of O_3 oxidation. This is consistent with the age at which the ambient MT (and likely other compounds) were all reacted, as shown in Fig. 4.2. As observed before, O_3 oxidation only produced $\sim 1/6^{\text{th}}$ of the SOA that was formed from OH (Palm et al., 2017).

4.3.4 Investigating SOA yields in an OFR using standard addition

One of the original intents of the PAM OFR was to oxidize air containing aerosol precursors and measure the “potential” amount of aerosol that can be formed. Since the initial development of the PAM reactor (Kang et al., 2007), subsequent research has shown that there are many factors related to exactly how the PAM reactor is operated that can affect the amount of aerosol that is formed (Peng et al., 2015, 2016b; Hu et al., 2016; Palm et al., 2016). For OH oxidation, the amount of SOA formed increases as OH exposure increases, up to a maximum amount of SOA formed in the range of OH exposures between the exposure where most of the reactive precursor gases have reacted and approximately 5 eq. days of exposure. At higher exposures, the high amounts of OH radicals start reacting many times with gases faster than condensation can occur, which fragments them to form

volatile oxidation products that can no longer condense. Also, these high OH exposures start heterogeneously oxidizing any preexisting (or newly formed) aerosol, leading to fragmentation and evaporation (Lambe et al., 2012; Ortega et al., 2016; Palm et al., 2016). So, in order to measure the maximum “potential” aerosol formation, the experiment needs to be operated over the range of exposures below approximately 5 eq. days.

Achieving the proper range of OH exposures, however, is also non-trivial. OH exposure in the OFR has been shown to be sensitive to many factors, including UV photon fluxes, , sample air composition (water vapor content, external OH reactivity, and OFR residence time and distribution (Li et al., 2015; Peng et al., 2015). All of these factors need to be considered when estimating OH exposure. Special care must be taken to avoid operating the OFR at conditions that lead to significant influence on the chemistry from non-OH reactions (e.g., photolysis; Peng et al., 2016b). Also, Palm et al. (2016) showed that some fraction of the condensable gases will condense on OFR walls, sampling lines, or react further with OH and fragment instead of condensing to form SOA. This behavior is sensitive to the condensational sink (i.e., surface area of seed aerosol) available in the OFR. These alternate fates are artifacts of the OFR experiment, and must be corrected using the measured condensational sink in order to determine the true potential aerosol mass that would form in the atmosphere.

All of these effects can matter for OFR experiments that attempt to compare measured vs. predicted SOA formation, and they have been considered in, e.g., the SOA formation from oxidation of ambient air in Palm et al. (2016, 2017) and in the subsequent analysis in this work. In these analyses, this carefully-quantified maximum amount of SOA formation was compared to the amount predicted to form from the oxidation of the speciated precursor gases measured in ambient air. The amount of predicted SOA was estimated by applying typical chamber-derived SOA yields to the measured amount of ambient gas. One important aspect of this analysis that has not been as carefully examined in the literature is whether (or how well) these typical chamber SOA yields apply to the SOA formation in the

OFR, particularly under ambient operating conditions. Several previous results have suggested that SOA yields in the OFR were similar to published chamber yields (Kang et al., 2007; Bruns et al., 2015; Lambe et al., 2015). However, these conclusions were drawn from experiments that likely suffered from one or more of the following issues: (1) not considering factors such as high VOC concentrations (high external OH reactivity, leading to OH suppression) when determining OH exposure (Peng et al., 2015); (2) not considering the alternate fates of condensable gases, particularly for short OFR residence times or when using no seed aerosol (Palm et al., 2016); (3) not considering possible non-OH reactions, particularly under “high risk conditions” such as high external OH reactivity (Peng et al., 2016b); (4) not considering possible effects of the water vapor concentration of the sample air on both OH exposure and aerosol liquid water content (Peng et al., 2015; Palm et al., 2016); (5) not performing the SOA yield experiments at atmospherically relevant OA concentrations.

Due to these limitations of prior OFR SOA yield studies, during the GoAmazon2014/5 field campaign we endeavored to investigate whether SOA yields in the OFR are indeed consistent with published chamber yields, while avoiding or at least considering all of the above-mentioned potential pitfalls. SOA yields were quantified by injecting several pure VOCs (individually) into the ambient air at the entrance to the OFR, exposing them to varying concentrations of either OH or O₃, and measuring the resultant SOA formation as well as VOC decay. By injecting the VOCs into ambient air, we were able to measure the yields at ambient temperature, humidity (and aerosol liquid water content), and seed OA concentrations. The injected VOC concentrations were also kept low in order to minimize the undesired effects of added external OH reactivity (with the exception of isoprene, as discussed below). Both constant and stepped oxidant concentrations were used in these experiments. The amounts of OH aging used for these yield calculations were all below approximately 5 eq. days of aging, in order to minimize the influence of heterogeneous oxidation and excessive oxidation reactions in the gas phase. O₃ ages above 1 eq. day were used.

The measured SOA yields are shown in Fig. 4.7, along with relevant chamber yield parameterizations (low-NO_x yields corresponding to the conditions in the OFR; Li et al., 2015). The SOA yields were measured to be 52% for β -caryophyllene+OH, 51% for longifolene+OH, 27% for β -caryophyllene+O₃, 30% for limonene+OH, 18% for β -pinene+OH, 11% for α -pinene+OH, 17% for limonene+O₃, 21% for α -pinene +O₃, 11% for toluene+OH, and 6% for isoprene+OH. These yield values are generally consistent with the values that have been determined in large chambers, with the averages of each type of species being all within a factor of 2 of the chamber yields. Importantly, there is no indication that the OFR is more efficient at forming SOA than the chamber yields would indicate. This confirms that the OFR can be used to quantitatively determine the amount of SOA that would form upon oxidation of an ambient mix of precursor gases. Furthermore, it supports the analyses presented in Palm et al. (2016, 2017) that ambient VOCs alone could explain the amount of SOA formed from O₃ oxidation but not OH oxidation, where unspciated S/IVOCs contributed a majority of the SOA formation in the OFR.

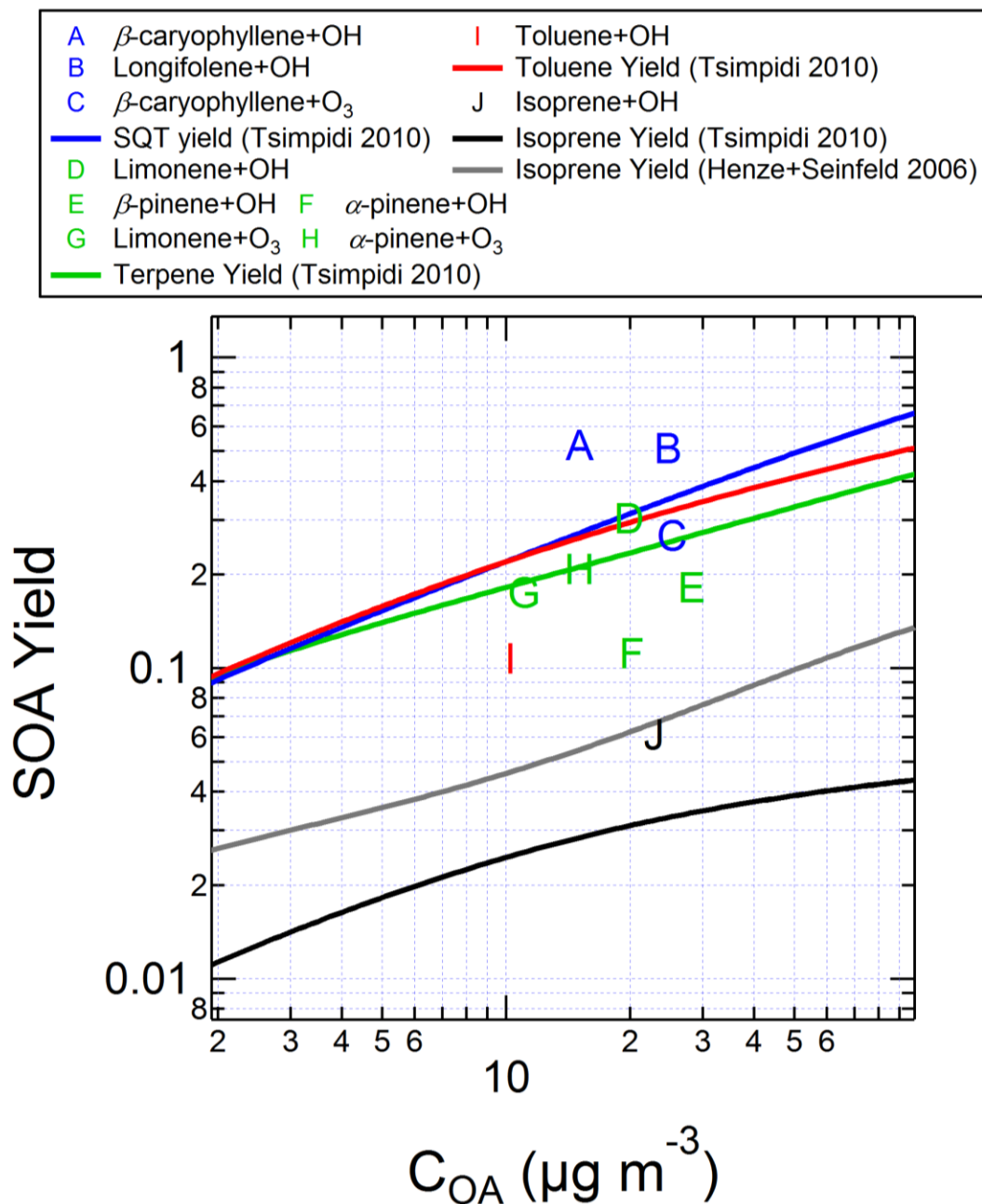


Fig. 4.7. SOA yields measured for individual VOCs in the OFR by standard addition into ambient air, as a function of OA concentration. Typical SOA yield parameterizations from environmental chamber experiments are also shown. The VOCs were injected into ambient air at the entrance to the OFR, and aged between 0–5 eq. days. Data are corrected for LVOC fate.

The SOA yields were calculated as the mass concentration of SOA formed divided by the mass concentration of the injected VOC that reacted in the OFR. This assumes that the only gas that formed SOA was the injected VOC, i.e., that there were no SOA precursor gases present in the ambient air (or

that they formed an insignificant amount of SOA). The standard addition experiments were performed during daytime hours, when this assumption was valid, with few exceptions. The toluene injection experiment was performed during the evening hours. Concurrently and immediately adjacent to the OFR with toluene injection, a second OFR was operated using OH oxidation of ambient air. In this OFR, approximately $3 \mu\text{g m}^{-3}$ of SOA was formed from ambient precursors during the time of the toluene injection, so this amount was subtracted from the amount formed in the toluene-injected reactor to determine the SOA yield from toluene. The OH oxidation of limonene was performed overnight. However, the adjacent OFR was not sampling in a manner that could be used to determine the SOA forming potential of ambient air. Instead, an average value of $5 \mu\text{g m}^{-3}$ of SOA (a typical value during the dry season) was assumed to form from ambient precursors and was subtracted when calculating the SOA yield. Therefore, the measured SOA yield for limonene+OH is more uncertain than the other measured yields. If the ambient air was assumed to have no SOA precursor gases (very unlikely), then the SOA yield for limonene+OH would be 59% as an upper limit, a value still too low to change the conclusions of these measured vs. predicted SOA analyses.

The isoprene+OH experiment has the caveat that in order to achieve a measurable amount of SOA formation from isoprene oxidation, approximately 85 ppb of isoprene was injected. This amounted to an added external OH reactivity of approximately 212 s^{-1} , which could have resulted in lower OH_{exp} and thus non-OH reactions becoming more important. Regardless, the isoprene injection experiments (including at lower isoprene concentrations) showed that the SOA yield from isoprene+OH could not be larger than several percent (but was larger than zero). The SOA yields of the SQT species were also more uncertain because the sensitivity of SQT in the PTR-TOF-MS was not calibrated during the campaign. Instead, the PTR-TOF-MS signal was calibrated by comparing the SQT measured in ambient air with the PTR-TOF-MS with the sum of SQT measured by the SV-TAG. Furthermore, variance in the sensitivities of different species of MT and SQT was not accounted for, and will add a small amount of uncertainty.

4.3.5 Measured vs. predicted SOA formation

When SOA precursor gases enter the OFR, either in ambient or injected air as illustrated above, SOA can be produced by oxidizing the gases in the sampled air. As shown in Sect. 4.3.4, when a known concentration of VOCs is added to the OFR, the amount of SOA formed upon oxidation by either OH or O₃ is consistent with what would be expected from published chamber experiments. Therefore, when oxidizing ambient air and comparing the SOA formation to the amount predicted to form from measured ambient gases, we can determine if all of the SOA formation is accounted for, or if there are other SOA-forming gases present in ambient air that are not being measured and quantified. Previous studies of OFR oxidation of urban or pine forest ambient air has shown that poorly characterized S/IVOCs are likely an important source of SOA from OH oxidation (Ortega et al., 2016; Palm et al., 2016). In contrast, SOA formed from O₃ and NO₃ oxidation in a biogenic environment can be accounted for from ambient VOCs alone, presumably indicating that S/IVOC precursors do not have C=C double bonds (Palm et al., 2017).

The measured SOA formation (at the eq. ages of maximum SOA production, as discussed above) from ambient air in the OFR during GoAmazon2014/5 is shown in Fig. 4.8, for both wet (IOP1) and dry (IOP2) seasons and both OH and O₃ oxidation. The measured SOA formation is corrected for LVOC fate. The predicted SOA formation was estimated by applying typical chamber SOA yield values to measured ambient VOC concentrations, as described in Sect. 4.2.4.

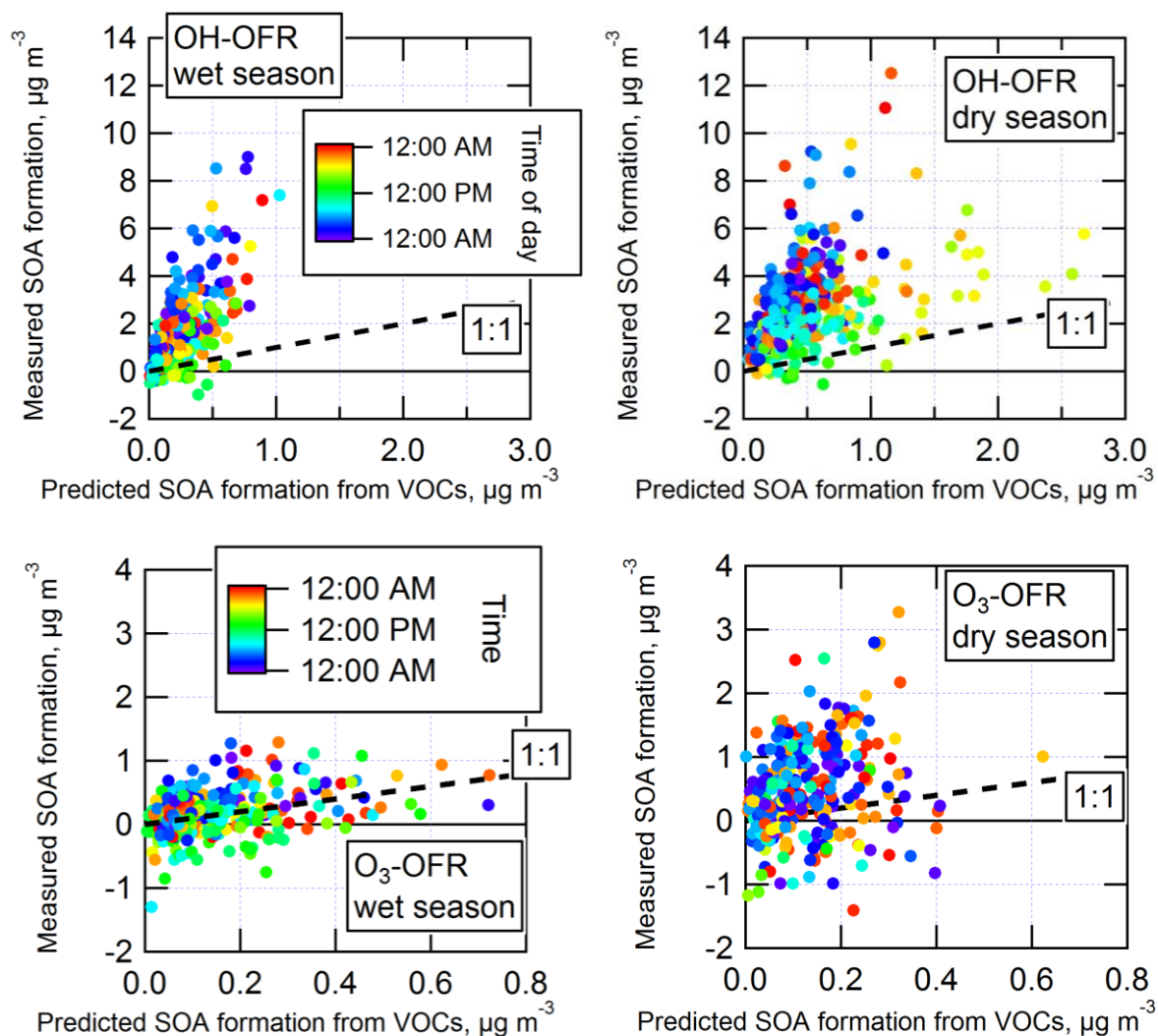


Fig. 4.8. Measured SOA formation vs. the concentration of SOA predicted to form from the oxidation of ambient VOCs, shown for OH and O₃ oxidation during both wet and dry seasons. Data are colored by local time of day. Measured SOA formation is corrected for LVOC fate.

OH oxidation of ambient air produced up to 10 times more SOA than could be accounted for from ambient VOCs. In contrast, the amount of SOA formed from O₃ oxidation generally could be explained from ambient VOCs. Both of these conclusions are consistent with previous OFR measurements, suggesting that typically unmeasured ambient gases play a substantial role in ambient SOA formation from OH oxidation, but not from O₃ oxidation. These gases may be the typically unmeasured/unspecified class of lower volatility S/IVOCs. Unfortunately there were no instruments dedicated to quantifying the total concentration of these gases during GoAmazon2014/5. The

measurement of such gases remains a critical gap in our understanding of the lifecycle of carbon in the atmosphere. However, the SOA formed in the OFR that cannot be accounted for by VOCs is effectively an integrated measure of these S/IVOC gases (multiplied by their SOA yield). They are measured by first converting them into SOA, which is much more readily measureable and quantifiable than S/IVOCs with current instrumentation.

Whereas the slope of the measured vs. predicted SOA formation from pine forest air in Palm et al. (2016) was roughly constant at approximately 4, the slope of the measured vs. predicted SOA formation from OH oxidation in the Amazon varied as a function of time of day. The diurnal cycles of measured and predicted SOA formation are shown for both seasons in Fig. 4.9. The predicted SOA was on average slightly lower during nighttime than during daytime. The cycle of measured SOA formation was the opposite, leading to slopes (in Fig. 4.8) that were lowest during daytime and highest in the hours before sunrise. The reasons for the observed trends are unclear, but likely result from the confluence of several processes, e.g., diurnal changes in emission and concentration profiles (of VOCs and/or S/IVOCs), boundary layer dynamics, and varying ambient oxidant concentrations.

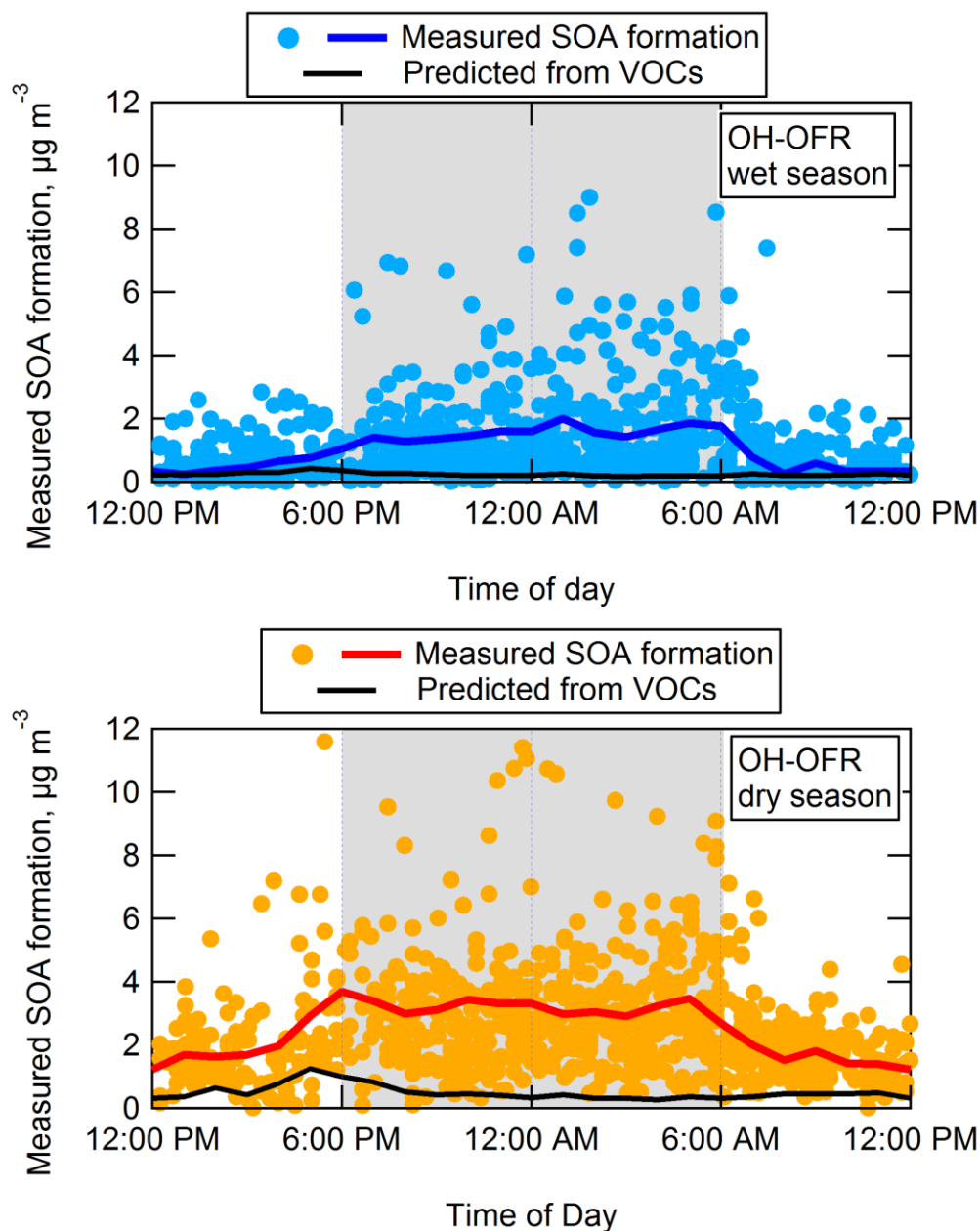


Fig. 4.9. Measured SOA formation vs. local time of day and diurnal cycles of measured and predicted SOA formation, shown for OH oxidation during both wet and dry seasons.

In addition to showing the diurnal average SOA formation, Fig. 4.9 also illustrates that a wide range of potential SOA formation is possible at any given time of day. There were some nights when as little as $1 \mu\text{g m}^{-3}$ of SOA was formed, and other nights when nearly $10 \mu\text{g m}^{-3}$ was formed. During the nights when little SOA was formed, Fig. 4.8 also shows that these nights also had the lowest predicted amounts of SOA formation. This shows that, while the amount of SOA formation correlated with

measured ambient SOA precursor VOCs, they could not quantitatively explain the total amount of SOA formed. Other SOA-forming gases were apparently present at the same times as VOCs, though in varying ratios to those VOCs.

4.3.6 Positive Matrix Factorization (PMF) of SOA after OH oxidation

PMF is a common technique for source apportionment of ambient aerosol (e.g., Ulbrich et al., 2009; Zhang et al., 2011). It can be used to split the full mass spectrum into the sum of several statistical factors, where each factor is the mass spectrum that is produced from a group of related molecules in the ambient aerosol that vary together in time. Here, we present results of PMF analysis of OA after OH oxidation in an OFR, as an investigation into what types of SOA were formed and how heterogeneous oxidation affected the types of pre-existing OA that entered the reactor in ambient air. To the best of our knowledge, these results are the first report of PMF analysis of OA after oxidation in an OFR.

The factors identified in OA sampled through the OFR with no added oxidant were the same as the factors identified in ambient air. When oxidant was added, the concentration of the factors measured after the OFR were expected to change relative the concentrations measured when no oxidant is added. Therefore, the factors in ambient OA were first identified by running the PMF analysis on just the unoxidized measurements through the OFR (and comparing with PMF of ambient OA). Several factors were identified during both wet and dry seasons that are common in PMF literature, including hydrocarbon-like OA (HOA), biomass burning OA (BBOA), isoprene epoxydiols-derived SOA (IEPOX-SOA), and several oxidized OA (OOA) factors that represent SOA (e.g., Aiken et al., 2009; Ulbrich et al., 2009; Zhang et al., 2011; Hu et al., 2015). A factor with a characteristic signal at m/z 91, referred to here as the “91fac” factor was also identified during the wet season. The factor profiles for both wet and dry season are shown in Fig. 4.S3–4.S4. The HOA and BBOA factors are typically dominated by primary OA (POA, i.e., direct particle emissions), and are not expected to be produced from the chemistry in the OFR. IEPOX-SOA, while representing a type of SOA, was also not expected to be

produced in the OFR. As detailed in Hu et al. (2016), IEPOX can be formed in the gas phase in the OFR, but the rate of reactive uptake in the OFR does not increase with the increased OH concentrations, resulting in negligible formation of IEPOX-SOA in the OFR.

For the wet season, PMF of the OH-aged aerosol was performed with a total of 6 factors, using the Source Finder analysis software (SoFi, version 6.2; Canonaco et al., 2013) to constrain the HOA, BBOA, 91fac, and IEPOX-SOA factors to be exactly the same as the factor profiles found in ambient air, and allowing for two free-spectra SOA-related factors. These two factors are referred to as less-oxidized OOA (LO-OOA) and more-oxidized OOA (MO-OOA) based on their relative O:C. For the dry season, the HOA, BBOA, and IEPOX-SOA factors were constrained and the two OOA factors were allowed, for a total of 5 factors.

The changes in the mass concentrations associated with each factor are shown in Fig. 4.10, for the changes compared to unoxidized OA sampled through the OFR during both seasons. The factors associated with POA or with SOA from reactive uptake processes were not enhanced by the OFR oxidation, as expected, and were depleted as the eq. age of OH oxidation increased. The 91fac also fell into this category. Notably, the factor concentrations decayed at different rates, with HOA (and 91fac) decaying at faster relative rates than IEPOX-SOA and BBOA. This is particularly clear in the dry season. The decay of these factors at higher eq. ages is likely due to heterogeneous oxidation leading to fragmentation and evaporation of the preexisting aerosol.

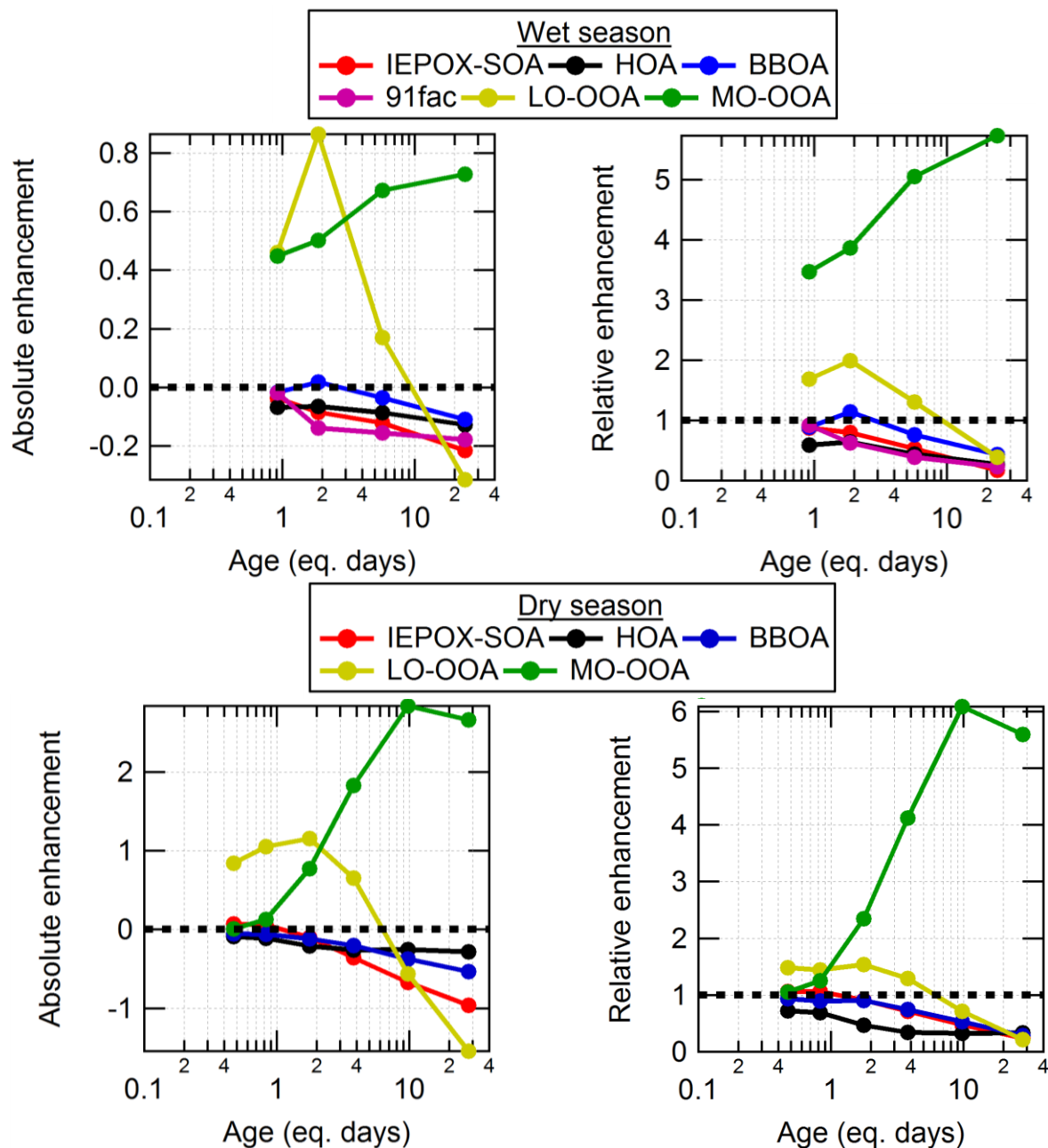


Fig. 4.10. Absolute and relative changes in PMF factors as a function of eq. days of OH aging in the OH-OFR, for the wet season (top panels) and the dry season (bottom panels).

In contrast, the OOA factors were produced in the OFR at concentrations that varied as a function of eq. age. SOA associated with the LO-OOA factor was produced at the lower ages, peaking around approximately 1 eq. day of aging. As the age increased, a plateauing of LO-OOA was observed, followed by a decay. Eventually at ages larger than 6-9 equivalent days a decrease of LO-OOA below the preexisting amount in ambient air was observed, indicating that the pre-existing ambient LO-OOA was

being heterogeneously oxidized, and that no new LO-OOA was surviving the OFR (either it was not formed, or it was formed but then converted into MO-OOA or heterogeneously oxidized to gas-phase species). The MO-OOA factor concentration increased as a function of age, peaking and then plateauing around 10 eq. days of aging, where heterogeneous oxidation was a dominant process affecting the OA sampled out of the OFR.

This PMF analysis shows that the SOA formed in the OFR from hours up to several days of eq. OH aging produces a mass spectrum in the AMS that resembles the spectra of ambient OOA. Importantly, this suggests that SOA formed in an OFR is not likely to be a result of any processes that are substantially different from what happens in the atmosphere. The decay of HOA, BBOA, and IEPOX-SOA factors suggest that heterogeneous oxidation is indeed minor at the low eq. ages, though it may have a stronger impact on HOA. For OH oxidation of urban air in an OFR, this should be considered. At the highest ages, this analysis suggests that all of the factors (except MO-OOA) decay to near zero relative to their initial concentration, and that the remaining aerosol is all associated with the MO-OOA factor. This suggests that heterogeneous oxidation can be a source of MO-OOA in the atmosphere. This also indicates that the diffusion in the ambient OA is fast enough, so that most ambient OA is not shielded from oxidation by slow diffusion.

This analysis describes how these characteristic factors changes as a function of OH aging in an OFR. The results should be interpreted in the context of how OFR oxidation affects the concentration of these types of factors, which are commonly found in PMF analyses of ambient OA. The interpretation of these factors in the ambient OA is outside of the scope of this analysis, and will be the subject of a separate manuscript (de Sá et al., 2017).

4.3.7 Hygroscopicity of the organic component of CCN after OH oxidation

In addition to characterizing the OA mass as a function of eq. age of oxidation in an OFR, we can also investigate the properties of the OA as a function of aging in the OFR. During Oct. 7–15 in the dry

season, the OFR output was size-selected by a DMA and the output was analyzed with a CCN counter. Using that measurement, the hygroscopicity (κ) of the CCN was determined. When coupled with the chemical speciation measurements provided by the AMS and using the relatively well known values of κ for the inorganic aerosol components, the κ of the organic component of CCN (κ_{OA}) can be determined (Petters and Kreidenweis, 2007). This analysis for ambient OA during GoAmazon2014/5 has been presented elsewhere (Thalman et al., 2017). Here, we present an analysis of how κ_{OA} changed upon oxidation in the OFR.

Due to the sampling time requirements of the CCN counter, these experiments were performed while keeping the amount of oxidation in the OFR constant. As previous research of OH oxidation in an OFR has illustrated, the OFR can be operated under conditions dominated by SOA formation with very limited heterogeneous oxidation (at ages below approximately one to a few eq. days), conditions dominated by heterogeneous oxidation with minimal new SOA formation (the highest ages above approximately 10 eq. days), or conditions where both processes are occurring (the intermediate age range). When sampling the OFR with the CCN counter during GoAmazon2014/5, the OFR was operated to investigate both the SOA formation and heterogeneous oxidation regimes, at separate times. During nighttime hours, when SOA-forming gases were expected to be present in ambient air, the OFR was operated at a constant age in the range of 1–3 eq. days. During daytime hours, when SOA-forming gases were present in lower concentrations, the OFR was operated at a constant age in the range of 12–44 eq. days of OH aging. The evolution of bulk O:C vs. eq. days of OH aging is shown in Fig. 4.S5. To increase confidence that the measurements at the very high eq. ages were a result of heterogeneous oxidation of preexisting aerosol and not influenced by new SOA formation of highly oxidized gases, a parallel-plate carbon filter denuder (Sunset Laboratory Inc.) was mounted on the inlet of the OFR during these high-age measurements in order to remove SOA-forming gases from ambient air.

Figure 4.11 shows κ_{org} as a function of bulk O:C in both ambient and oxidized air. The κ_{OA} of ambient OA was in the range of 0.05–0.2. When operating in the 1–3 eq. day range (corresponding to OFR data with O:C less than ~ 1.2), measurements of κ_{OA} for both 100 nm and 160 nm mobility diameter particles show that κ_{OA} increased slightly to as high as 0.23 with increasing O:C, up to an O:C of approximately 1.1. This is consistent with previous measurements that showed a monotonic increase of κ_{OA} with increasing O:C (or f_{44} , the fraction of signal found at m/z 44) for the heterogeneous oxidation of POA surrogate particles (Petters et al., 2006a; George et al., 2009; Cappa et al., 2011; Lambe et al., 2011a) and measurements of SOA formed in an OFR in laboratory experiments (Massoli et al., 2010; Lambe et al., 2011a, 2011b).

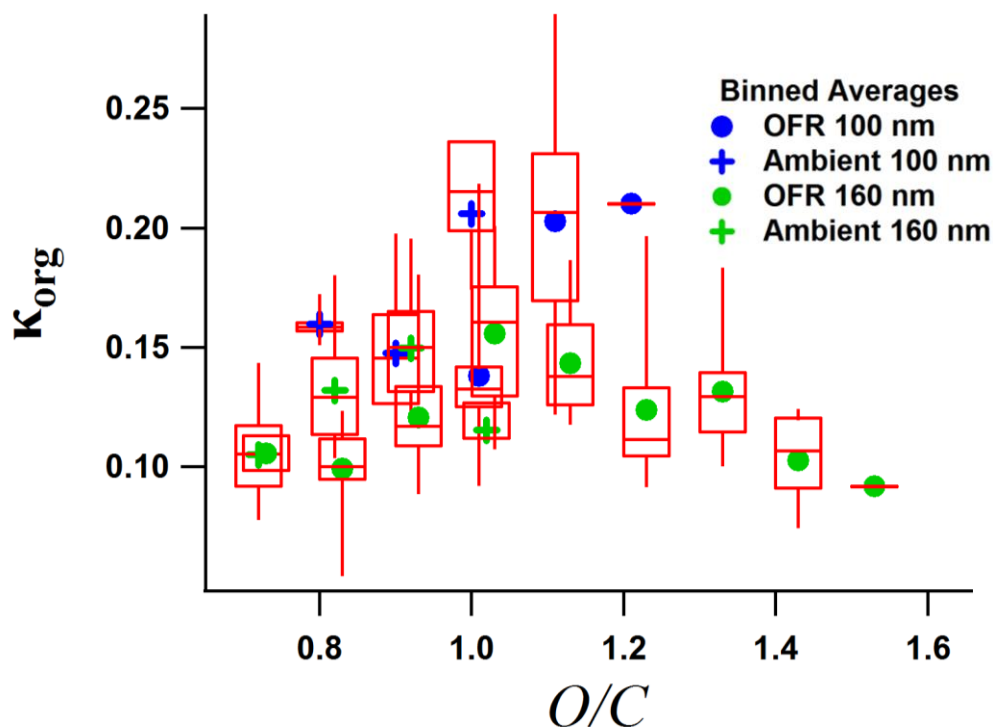


Fig. 4.11. Binned averages of hygroscopicity of OA (κ_{OA}) as a function of bulk O:C of the OA. The data includes ambient data, measurements after 1–3 eq. days OH aging (at both 100 and 160 nm) to sample maximum SOA formation, and measurements after 12–44 eq. days aging (at only 160 nm) sampled through a gas denuder in order to sample the result of heterogeneous oxidation of pre-existing OA.

The measurements made at high eq. OH ages (corresponding to O:C greater than ~ 1.2) showed unexpected results. Instead of continuing to increase at very high O:C values, κ_{OA} decreased to below 0.1 with increasing O:C above 1.2, even as O:C increased to higher than 1.4. While this decrease in κ_{OA} with

increasing O:C was unexpected, it is not necessarily inconsistent with the previous measurements. Those experiments of heterogeneous oxidation of POA did not achieve O:C values or eq. ages as high as the maximum values achieved in this study (~ 0.25). At their highest amounts of oxidation, a plateau in κ_{OA} of approximately 0.1 or lower was observed, which matched the lower values achieved at the highest ages in this study. OFR measurements of CCN activity of SOA formed in the OFR in Massoli et al. (2010) and Lambe et al. (2011a, 2011b) did achieve O:C levels and eq. ages closer to the levels in this study, and reported continued monotonic increases in κ_{OA} with increasing O:C. However in those experiments, SOA was formed in the reactor by homogeneous nucleation of injected gas-phase precursors, and no organic seed aerosol was used. Therefore, the OA measured from the OFR was likely dominated by SOA formed via condensation of highly oxidized gases (with limited time for heterogeneous oxidation to occur after condensation). The gases that condense to form SOA after being oxidized in the gas phase at such high ages (up to 13–20 eq. days in those studies) may not be representative of the molecules in typical atmospheric particles. This is in strong contrast to the processing of the OA sampled from the OFR during GoAmazon2014/5. The OA in this study started as real ambient OA, and was affected dominantly by heterogeneous (or condensed phase) reactions with OH, with minimal influence from condensation of gases due to the use of a denuder on the OFR inlet. These results suggest that heterogeneous or particle phase reactions of OA with OH can lead to a decrease in κ_{OA} .

The specific processes that lead to the observed decrease in κ_{OA} are uncertain. One possible process that can lead to a decrease in CCN activity is oligomerization, causing an increase in the molecular weight and decrease in polarity of the particulate organic molecules (VanReken et al., 2005; Petters et al., 2006b; Xu et al., 2014). Oligomerization was suspected in a previous study where heating of OA in a thermodenuder led to a decrease in κ_{OA} (Kuwata et al., 2011). Other studies have shown that OH oxidation in the condensed phase can lead to oligomerization (e.g., Altieri et al., 2008; Lim et al., 2010; Sun et al., 2010; Tan et al., 2010, 2012). Similar processes may have occurred in this study. These

measurements warrant future OFR studies to investigate the effects of heterogeneous oxidation on particle phase composition and properties.

4.3.8 Estimating source contributions to potential SOA using multi-linear regression analysis

The results in Sects. 4.3.4–4.3.5 led to the conclusion that a dominant fraction of the SOA formation potential from oxidation of ambient air by OH, particularly during nighttime hours, was derived from gases that were not speciated or quantified during this campaign. Also, these gases could form SOA upon OH oxidation, but little or no SOA after O₃ oxidation, suggesting they tended not to contain C=C bonds. These conclusions are consistent with previous measurements of the oxidation of ambient pine forest air in the US Rocky Mountains an OFR (Palm et al., 2016, 2017). In the analyses of those pine forest measurements, it was found that the unmeasured SOA-forming gases were likely to be S/IVOCs. Because the measured SOA formation correlated well with ambient MT, it was likely that the S/IVOCs were biogenic oxidation products (or were at least co-emitted with MT). With respect to ambient SOA-forming gases, the rural pine forest air system was relatively simple and was generally dominated by biogenic, terpene-related gases.

Unfortunately, a measurement of the total concentration of S/IVOCs during GoAmazon2014/5 was not available (as is typical for most large field campaigns at present). However, we can still extract information about the main sources contributing to the SOA formation potential from S/IVOCs present in ambient air by comparing with available VOC and/or tracer measurements. In this analysis, we make the assumption that the conclusion from the pine forest measurements, specifically that VOCs and S/IVOCs from a given emission type correlate well with tracers from that same source, will also apply to all of the emission types at the T3 site.

The T3 site of GoAmazon2014/5 was chosen because it was expected to be impacted by multiple types of emissions. These include regional biogenic emissions (isoprene, MT, SQT, etc.), anthropogenic emissions from the city of Manaus and other towns and roads closer to the site, and local

and regional biomass burning emissions. The scatterplots of maximum SOA formation vs. precursors or tracers from each of these three emission types (MT, SQT, the sum of available biomass burning tracers, and NO_y) are shown in Figs. 4.12 and 4.13 for IOP1 and IOP2, respectively. Scatterplots with several other available SOA precursor gases or tracers (including isoprene) are shown in Figs. 4.S6-4.S7 for comparison. Unlike the previous results at the pine forest or the Los Angeles area, the maximum amount of SOA formation in the OFR did not correlate well with any single SOA precursor gas, indicating the variable impacts of multiple sources.

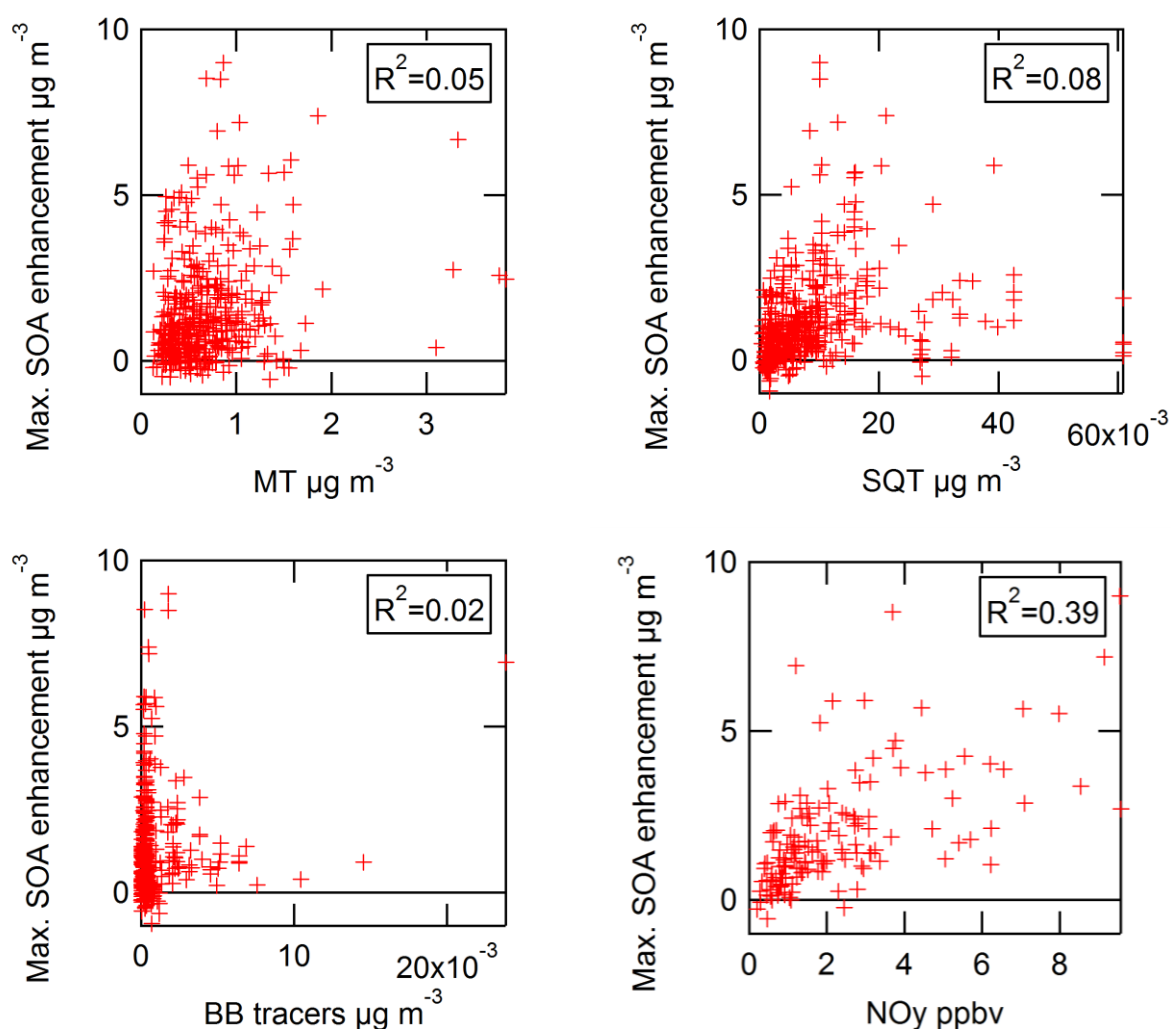


Fig. 4.12. Scatterplots of maximum measured SOA enhancement from OH oxidation at the T3 site during IOP1, vs. several ambient SOA precursor tracer gases. Correlation coefficients (R^2) are shown for each scatterplot.

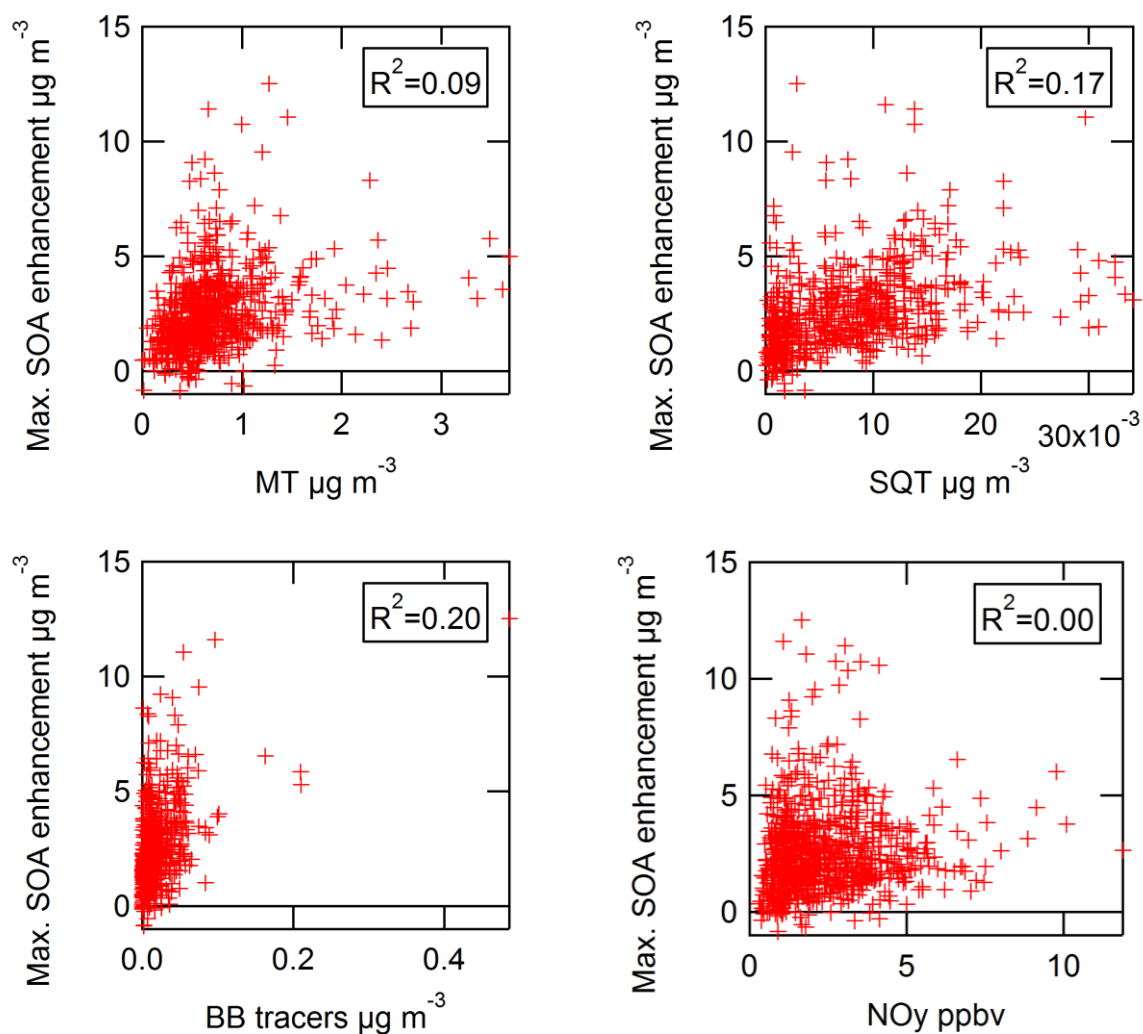


Fig. 4.13. Scatterplots of maximum measured SOA enhancement from OH oxidation at the T3 site during IOP2, vs. several ambient SOA precursor tracer gases. Correlation coefficients (R^2) are shown for each scatterplot.

If the assumption holds that VOCs and S/IVOCs from a given emission type correlate well, then a multivariate relationship should exist, where the measured SOA formation should correlate well with the sum of measured concentration of VOCs/tracers of each source, multiplied by coefficients. The coefficients would quantify the relative contributions to potential SOA from VOCs + S/IVOCs from each source, relative to the tracer. For this analysis, we used tracer gases that were likely to be dominated by a single type of source, including MT, SQT, and isoprene for biogenic emissions, NO_y for anthropogenic emissions, and the sum of the measured BB tracers (vanillin, vanillic acid, syringol, and guaiacol) for

biomass burning emissions. The background concentrations of the biogenic and BB tracers in air that did not contain emissions from those sources were near zero and they all react on roughly the same time scale on which SOA formation occurred (on the order of a day or less). This makes these chosen tracers better suited for this type of analysis, since they were found only in the relatively fresh emissions that contain SOA forming gases, and were not measured in air after long range transport when the potential SOA would have already been formed. NO_y is not itself an SOA-forming gas, but enhancements above the background were indicative of the total exposure of the air to anthropogenic sources, and it also accounted for dilution of the air in transport to the T3 site. For this analysis, a background of 0.7 ppb NO_y was subtracted before performing the multilinear regression (MLR). Longer-lived tracers such as acetonitrile and benzene, were not suitable for this analysis, because their concentrations depended more on the long term history of the air. Also, gases such as benzene, toluene, and xylene can be emitted from anthropogenic, biomass burning, and even biogenic sources, which makes them less distinct tracers of a given source type (e.g., Misztal et al., 2015).

Figures 4.14 and 4.15 (wet and dry seasons, respectively) illustrate the scatterplots of measured SOA formation vs. the amounts predicted by the MLR approach. The R^2 values increased substantially compared to the correlations with any individual precursors, up to 0.46 (0.32) for the wet (dry) season. Also shown are the estimated contributions to potential SOA from each source type. The coefficients found for each precursor from the multivariate regression were 0.13, 85, 0, 0.52, and 65 for IOP1 and 1.1, 108, 0, 0.16, and 22 for IOP2, for MT, SQT, isoprene, NO_y , and BB tracers, respectively, in units of $(\mu\text{g m}^{-3})/(\mu\text{g m}^{-3})$ except for NO_y which is $(\mu\text{g m}^{-3})/(\text{ppbv})$. These coefficients can be interpreted as SOA “yields” compared to the mass of the tracer. For example, the coefficient for MT for IOP2 was 1.1, meaning, that 110% as much mass as the ambient MT mass became SOA in the OFR from MT-related gases. As illustrated in Sect. 4.3.4, the real SOA yields from MT are smaller, and therefore this analysis indicates that there are other gases correlated with MT that are forming SOA. The coefficient for NO_y

cannot be interpreted in this way, since NO_y itself does not form SOA, however the logic of its relationship to unmeasured SOA-forming gases is equivalent. The BB tracer coefficients were relatively large because the four tracers available for use in this analysis were a small subset of the total BB-related gases.

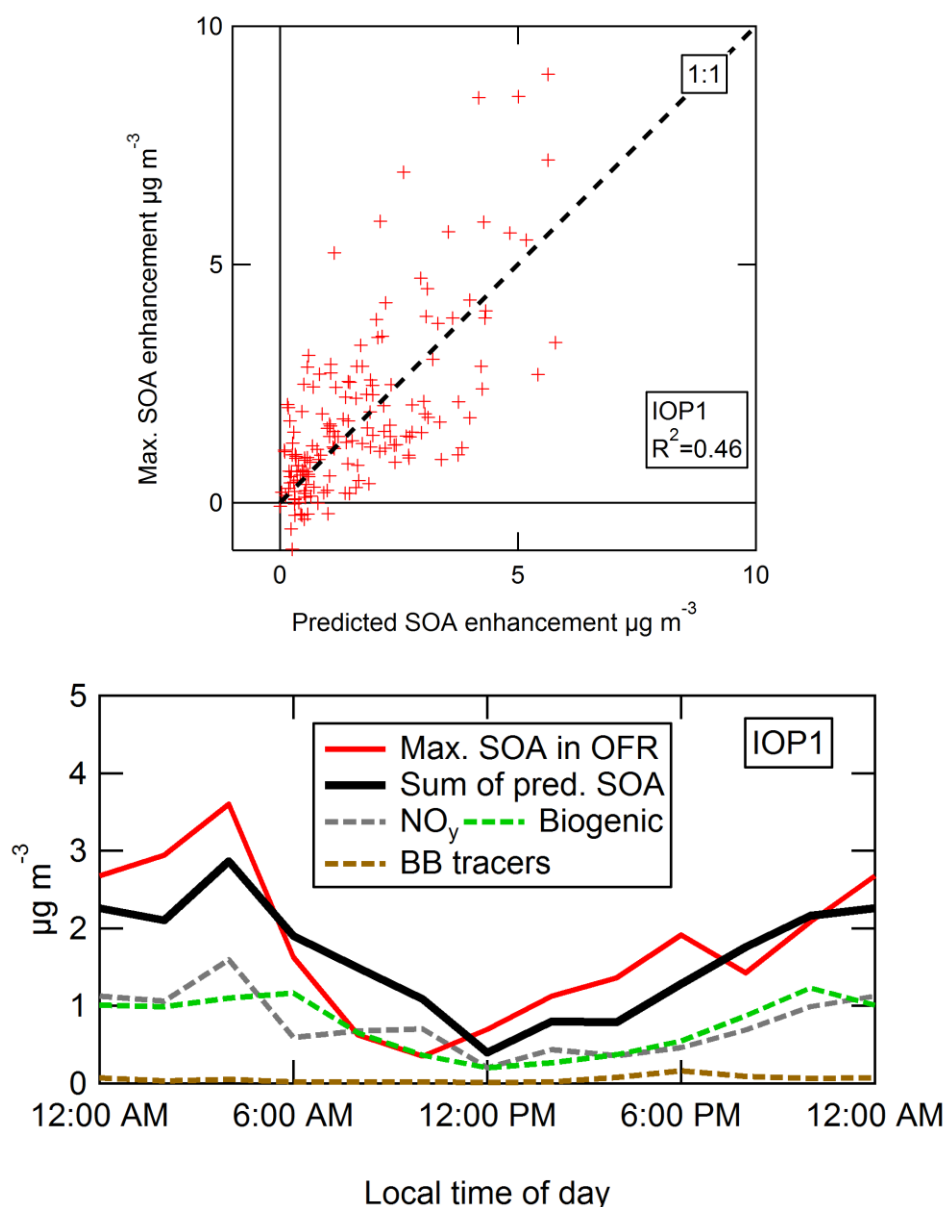


Fig. 4.14. Top: Maximum measured SOA enhancement from OH oxidation in the OFR during the wet season (IOP1), vs. the total amount predicted from multilinear regression analysis. Bottom: Diurnal average values of the maximum measured SOA formation from OH oxidation during the wet season, the amount attributed to each emission source, and the total amount predicted from all source.

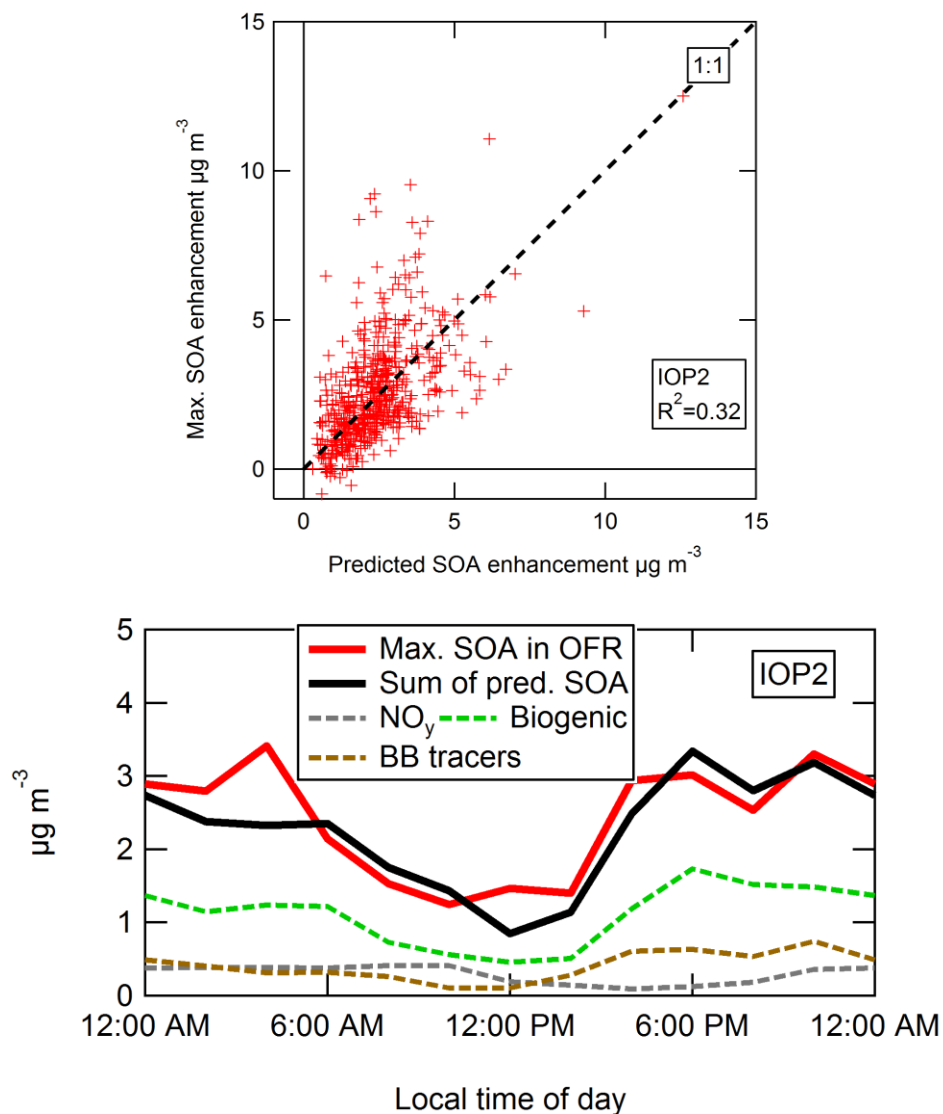


Fig. 4.15. Top: Maximum measured SOA enhancement from OH oxidation in the OFR at the T3 site during the dry season (IOP2), vs. the total amount predicted from multilinear regression analysis. Bottom: Diurnal average values of the maximum measured SOA formation from OH oxidation at the T3 site during the dry season, the amount attributed to each emission source, and the total amount predicted from all sources.

In both seasons, an optimal coefficient of 0 suggested that a negligible amount of SOA was formed from isoprene and related precursors. However in Sect. 4.3.4, the oxidation of injected isoprene in the OFR indeed resulted in SOA formation. For a typical daytime mass concentration of isoprene of approximately $10 \mu\text{g m}^{-3}$ at this site, an SOA yield of several percent would predict that several tenths of a $\mu\text{g m}^{-3}$ would be produced. We believe that this result simply illustrates the limitations of this type of MLR analysis. When the independent variables correlate with each other, the regression cannot

distinguish between the variables. In this case, the R^2 between isoprene and MT were 0.18 and 0.39 in IOP1 and IOP2, which were the largest values between the variables used. The SOA mass produced from isoprene-related gases was likely assigned to MT due to this correlation. If the analysis is done without MT, as shown in Fig. 4.S8, then coefficients of 0.03 and 0.11 are found for isoprene. The R^2 values between measured and total predicted SOA formation remain essentially unchanged at 0.45 (0.31) for the wet (dry) season. This accounted for the daytime biogenic SOA formation, and the coefficients for SQT also increased slightly to account for the nighttime biogenic SOA formation that had been assigned to MT-related gases. The amounts predicted from anthropogenic and BB sources remain roughly unchanged. This analysis shows that the biogenic precursors are all correlated enough that we can only confidently determine the summed potential SOA from all biogenic sources. The coefficients of individual tracers are less meaningful than the total amount predicted to form from the oxidation of all biogenic gases.

This analysis was carried out by allowing a single, fixed coefficient value for each tracer, i.e. implicitly assuming that the ratio of total SOA forming gases to the tracer was constant at all times of day and throughout each season. Given the natural variability of the atmosphere, this ratio is unlikely to be constant at all times (e.g., due to changing emission type compositions or degree of ambient photochemical aging). Ideally, the multilinear regression analysis could be performed as a function of time of day, which would allow the coefficient fits to vary with time of day. However, when performing the analysis this way, the correlation between independent variables rises to values sufficiently high that the multilinear fit can no longer distinguish between independent sources, and the analysis is no longer conclusive.

The average amounts and fractions of total SOA formation estimated from each of the biogenic, anthropogenic, and BB sources during each IOP are shown in Fig. 4.16. An average of 1.8 and 2.4 $\mu\text{g m}^{-3}$ were formed from ambient air during the wet and dry seasons. Of these amounts, 0.81 (50%), 0.74

(46%), and 0.06 (3%) $\mu\text{g m}^{-3}$ during the wet season and 1.65 (69%), 0.31 (13%), and 0.43 (18%) $\mu\text{g m}^{-3}$ during the dry season were attributed to biogenic, anthropogenic, and BB sources, respectively. These results indicate that biogenic SOA forming-gases were the most important contributors during both seasons. Anthropogenic sources contributed double the mass and triple the fraction during the wet season compared to the dry season. BB sources of SOA-forming gases were almost an order-of-magnitude larger during the dry season compared to the wet season.

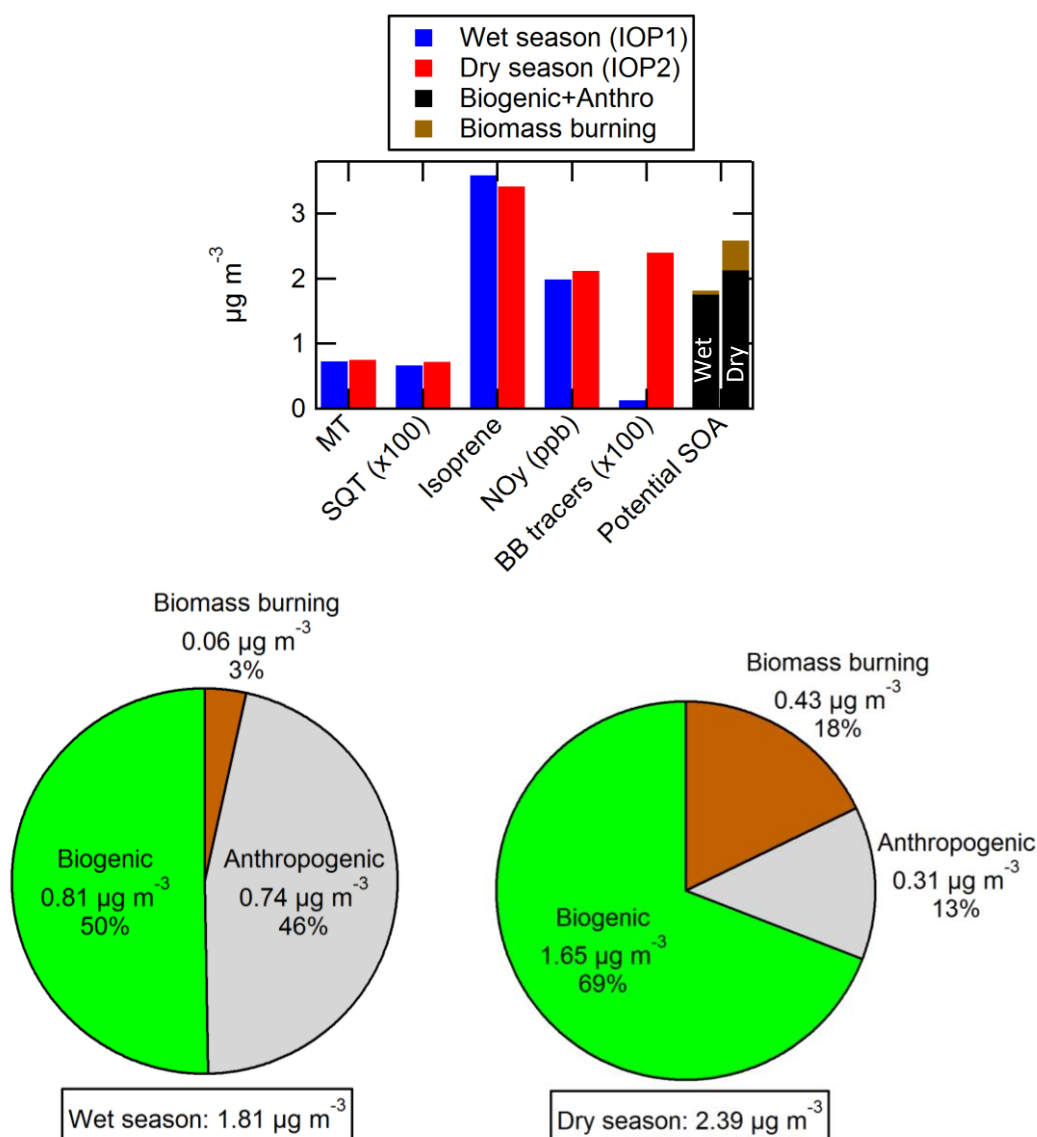


Fig. 4.16. Top: comparison of the average tracer concentrations and potential SOA formation during wet and dry seasons. Bottom: the amounts and fraction of the total SOA formation from OH oxidation in the OFR at the T3 site that were attributed to biogenic, anthropogenic, and biomass burning emission types using multilinear regression analysis.

One way to help interpret these results is by comparing the average concentrations of the tracers in each season, along with the average potential SOA formation in the OFR, as shown in Fig. 4.16. As expected (Martin et al., 2016a), the BB tracers were found in much larger concentrations (~20x) during the dry season, which gives confidence in the much larger contribution (x7) of those gases to potential SOA. The biogenic and anthropogenic tracers were found in roughly equal concentrations in each season. This contrasts with the twice larger total contribution of anthropogenic SOA-forming gases during the wet season, vs. twice larger for biogenic sources during the dry season. One hypothesis is that during the wet season, ambient photochemistry was slower, so that more SOA precursor gases survived the transport from Manaus and more SOA could be formed in the OFR. In the dry season, these gases may have already been oxidized in the atmosphere to form SOA, entered the OFR as OA, and did not contribute to potential SOA formation. The stronger oxidation during the dry season should increase the biogenic S/IVOC to primary VOC ratio. Since the primary VOCs were very similar in both seasons, the higher biogenic SIVOCs in the dry season could explain the larger potential SOA from that source. The very different spatial footprints of anthropogenic and biogenic emissions would then result in these different effects on potential SOA from each source at the T3 sites. These hypotheses should be tested with future modeling studies.

This analysis estimates the contributions from each of these three emission types to the SOA forming gases (measured and unmeasured) at the T3 site. This provides information about what types of SOA could form upon further oxidation of this air at or downwind of the T3 site. Importantly, this analysis does not provide information about what amounts or fractions of the pre-existing (i.e. ambient) OA measured at the T3 site came from each of these sources. To investigate the sources of OA that impact the site, positive matrix factorization (PMF) analysis or other tracer analysis can be done, but is outside the scope of this work and will be presented in future manuscripts. However, it would seem likely that the biogenic and biomass burning potential SOA sources observed here would also be

important in formation the OA on a regional scale, whereas the anthropogenic source type may be more intense in the Manaus plume (within approximately the first day of transport) and less important on a regional scale.

It would be of interest to perform this multilinear analysis on the measurements from the T2 site closer to the city of Manaus. However, that analysis was not included as part of this work. The measurements at the T2 site were limited to a shorter period of time, and the available tracer measurements were less extensive. Multilinear analysis was also not performed or needed for the SOA formation from O_3 oxidation at the T3 site, since Sect. 4.3.4 showed that all of the SOA formation can be roughly accounted for using the measured VOCs. In addition, the signal-to-noise of SOA formation from O_3 was low, which would limit this type of analysis.

4.4 Conclusions

During GoAmazon2014/5, ambient air was oxidized by OH or O_3 in an OFR in order to quantify (with high time resolution) the amount of potential SOA that could form from any precursors in ambient air. Essentially, this was a measure of the relative concentrations of SOA-forming gases (multiplied by their SOA yields) in the atmosphere, where the gases were measured by first converting them into more easily measurable particles. The potential to form SOA from ambient air changed with time of day, from one day to the next, and between the wet and dry seasons. As has been reported for previous field campaigns in a variety of locations, there were typically more SOA precursor gases found in ambient air during nighttime than during daytime. The amount of SOA from O_3 oxidation was consistent with the amount expected from the measured ambient precursors, but the amount formed from OH oxidation was up to several times larger than could be accounted for with available measured gases. This provided further evidence that the unmeasured SOA-forming gases tended to not contain C=C bonds. These results suggest that during the day the high ambient OH is already converting most SOA precursors to SOA rapidly, while at night the lack of OH allows precursors to accumulate, especially those that do not

have C=C bonds and do not react with O₃ or NO₃. A multilinear regression analysis indicated that approximately two thirds of the particle mass formed was biogenic in origin, while the remainder was mostly anthropogenic during the wet season and an equal mix of anthropogenic and biomass burning emissions during the dry season.

For the first time, SOA yields in the OFR were measured under ambient RH and temperature conditions, ambient external OHR levels, and using ambient aerosol as seeds for condensation. With careful consideration to many factors that can affect the quantification of SOA yields in OFR experiments, the measurements presented herein increase the confidence of the conclusion that SOA yields in the OFR (particularly when performing measurements of the oxidation of ambient air) are similar to yields measured in large environmental chambers.

This work adds to the growing body of literature that employs an OFR to investigate SOA formation from ambient air. Such experiments are consistently suggesting that gases other than the commonly measured VOCs are ubiquitous in the atmosphere, possibly having low volatilities and/or concentrations that make them difficult to measure, but with relatively high total potential to form SOA. In order to fully understand gas-to-particle SOA formation, we need to know more about these gases, including their identity, lifetime, reaction rates, SOA yields, deposition rates, etc., in order to be able to sufficiently model aerosol concentrations on regional and global scales.

Acknowledgements

This research was supported by the U.S. Department of Energy's (DOE) Atmospheric Science Program (Office of Science, BER, Grants No. DE-SC0016559 and DE-SC0011105), and the DOE SBIR program (DE-SC0011218), as well as NSF AGS-1360834 and EPA STAR 83587701-0. BBP is grateful for an EPA STAR graduate fellowship (FP-91761701-0). This manuscript has not been reviewed by EPA and not endorsement should be inferred. A portion of this research was performed using EMSL, a DOE Office of Science User Facility sponsored by the office of Biological and Environmental Research and located at

Pacific Northwest National Laboratory. We thank Dr. Francesco Canonaco for providing the SoFi software.

4.5 Supplementary information

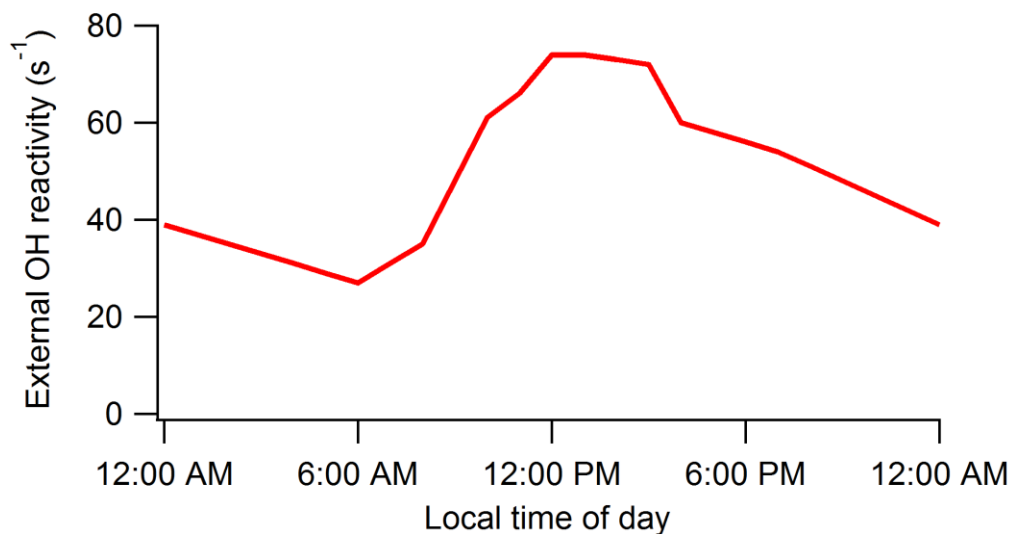


Fig. 4.S1. Mean ambient OH reactivity used as a parameter in the equation to estimate OH exposure in the OFR, shown as a function of local time of day. This diurnal cycle of OH reactivity was adapted and smoothed from Williams et al. (2016).

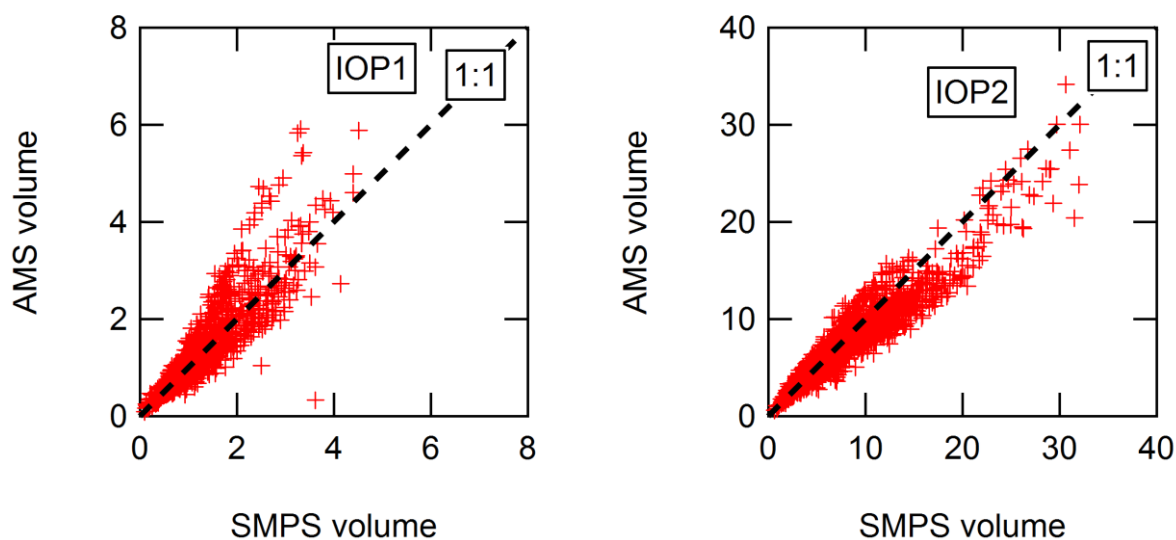


Fig. 4.S2. Aerosol volume measured in the AMS vs. in the SMPS for IOP1 and IOP2. The AMS mass was converted to volume using species densities of 1.75 g cm^{-3} for SO_4 , NO_3 , and NH_4 , 1.52 g cm^{-3} for Chl (DeCarlo et al., 2004; Salcedo et al., 2006; Lide, 2013), and the parameterization for OA density using elemental ratios described in Kuwata et al. (2012). AMS data was calculated using $\text{CE}=1$ during IOP1 and a composition-dependent CE (mostly $\text{CE}=0.5$; Middlebrook et al., 2012) during IOP2.

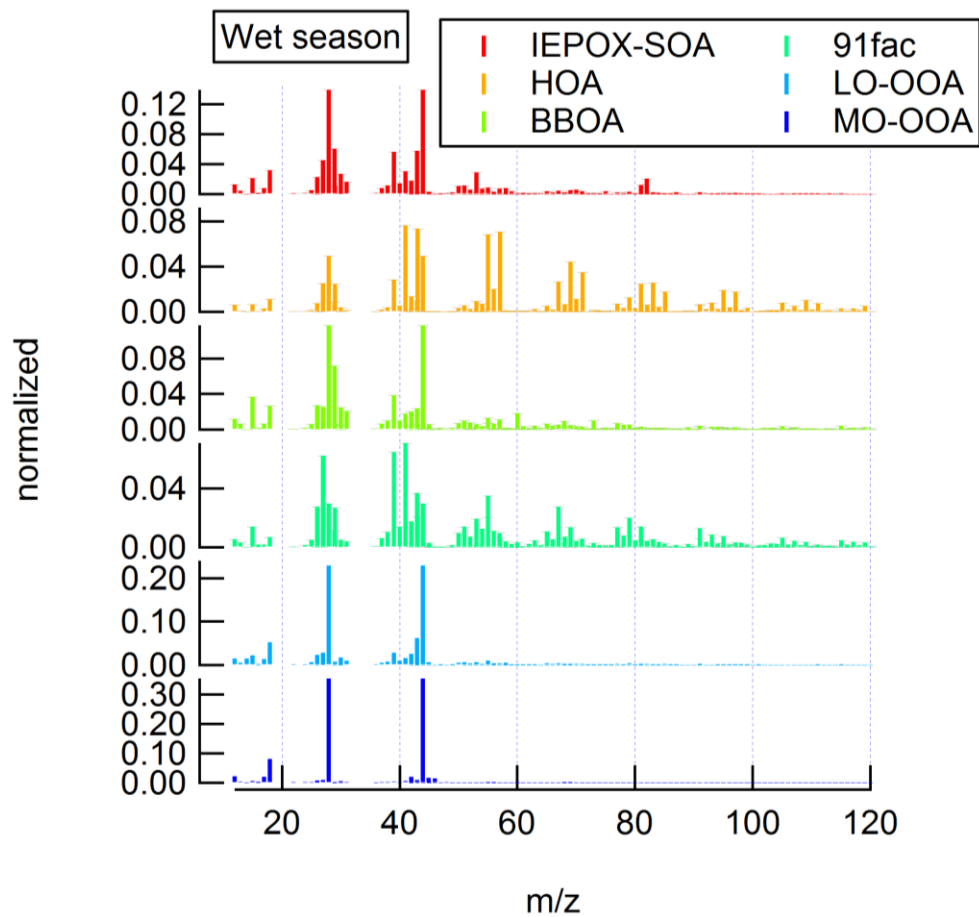


Fig. 4.S3. High-resolution factor profiles for the PMF analysis of the wet season, normalized to a total sum of 1.

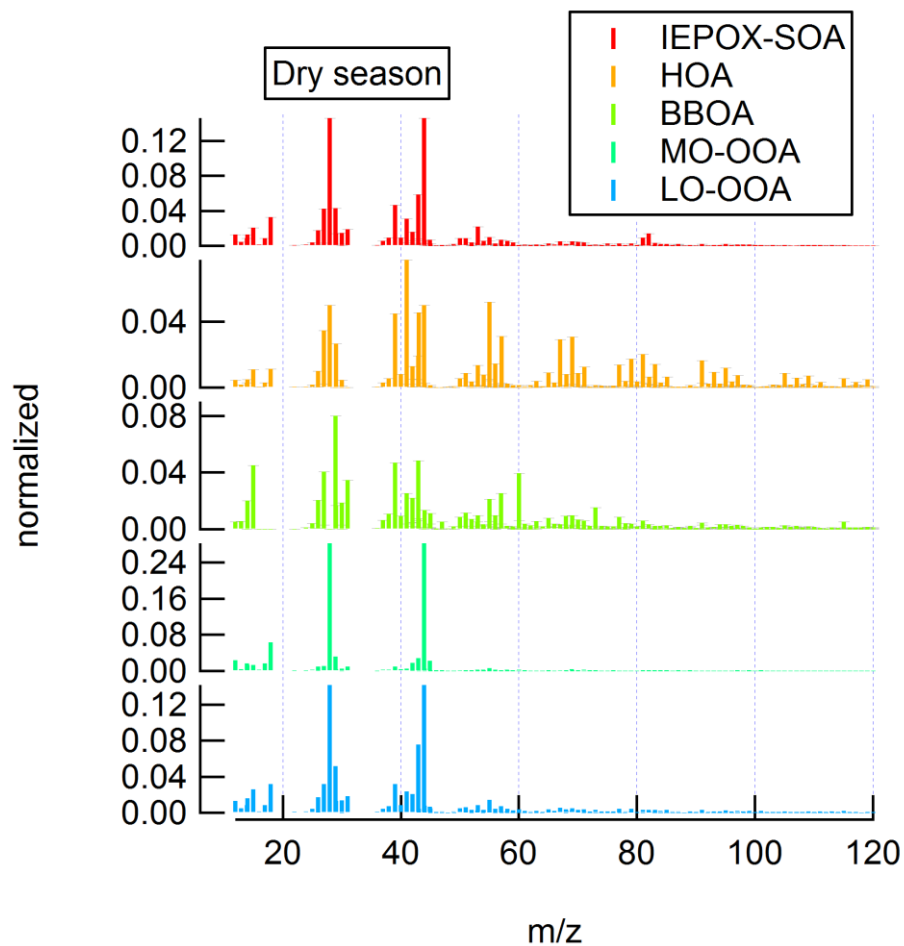


Fig. 4.S4. High-resolution factor profiles for the PMF analysis of the dry season, normalized to a total sum of 1.

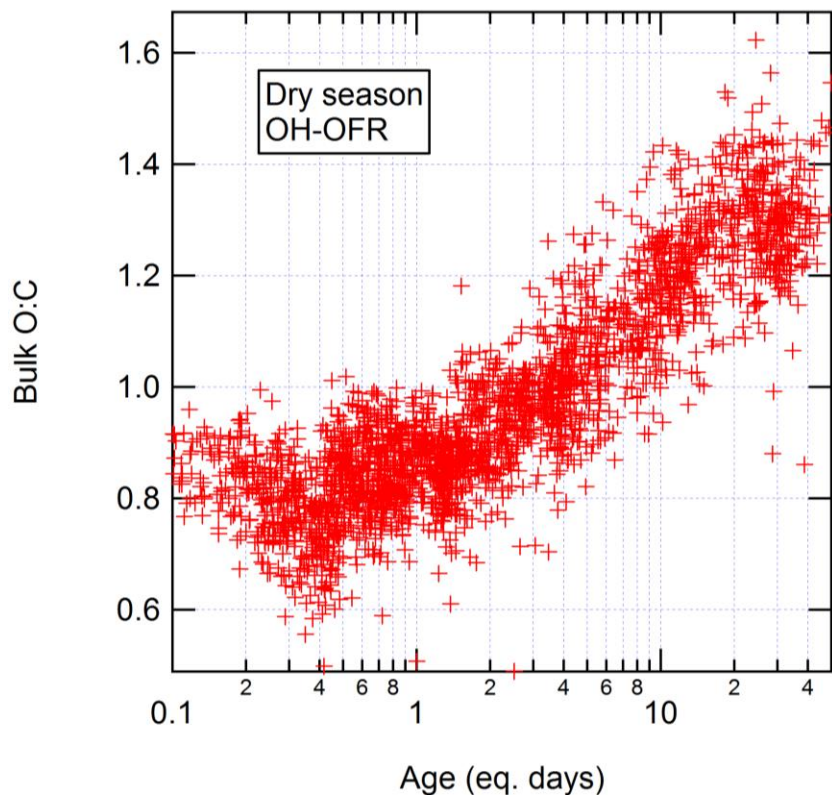


Fig. 4.S5. Elemental O:C ratio of the bulk OA measured after OH oxidation in the OFR, as a function of eq. age of OH aging during the dry season.

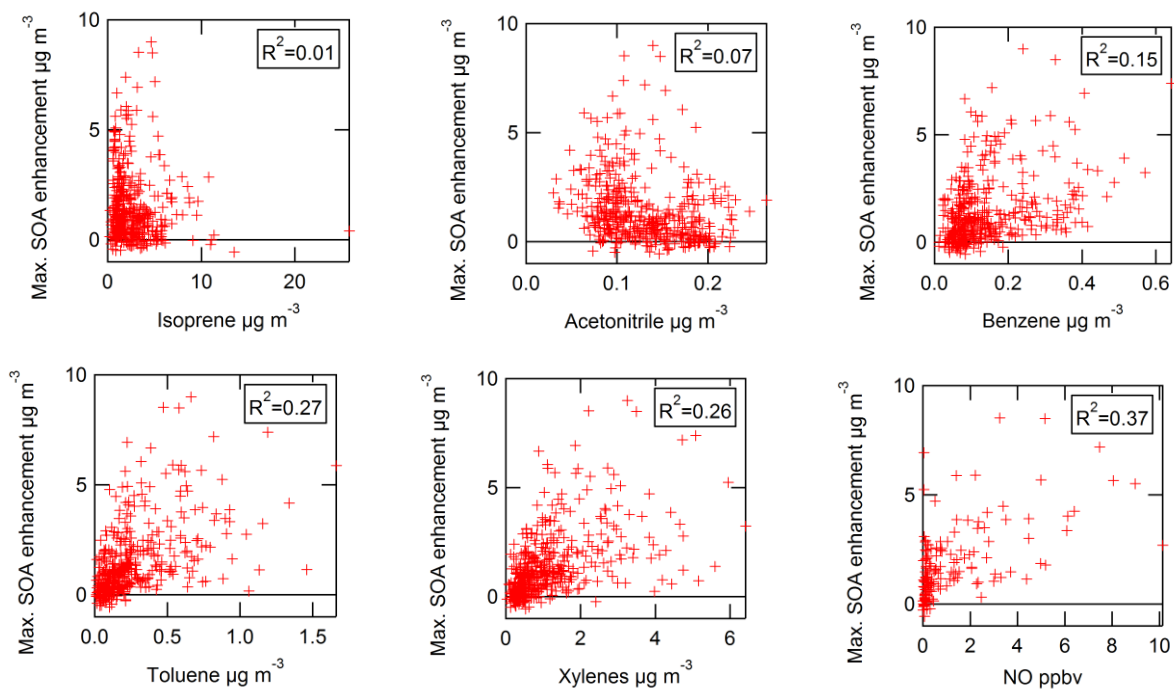


Fig. 4.S6. Scatterplots of maximum measured SOA enhancement from OH oxidation at the T3 site during IOP1, vs. several ambient SOA precursor tracer gases. Correlation coefficients (R^2) are shown for each scatterplot.

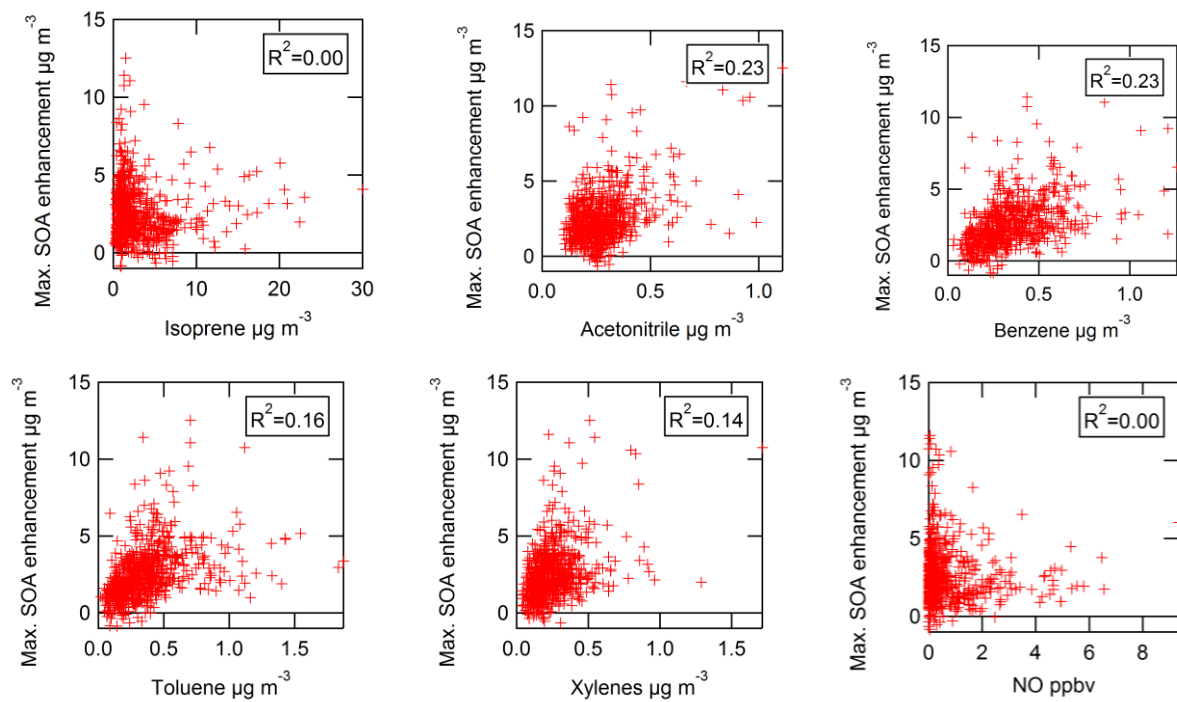


Fig. 4.S7. Scatterplots of maximum measured SOA enhancement from OH oxidation at the T3 site during IOP2, vs. several ambient SOA precursor tracer gases. Correlation coefficients (R^2) are shown for each scatterplot.

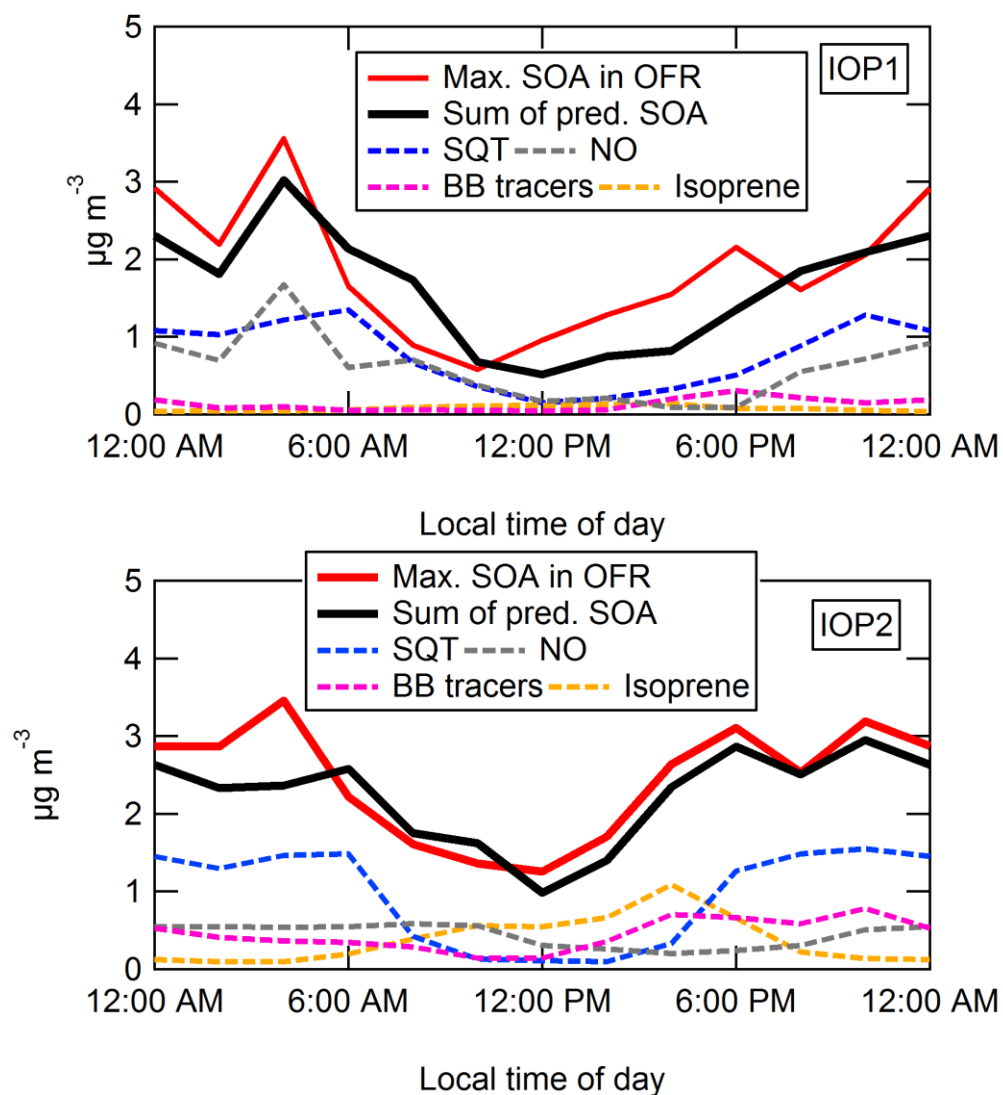


Fig. 4.S8. Diurnal average values of the maximum measured SOA formation from OH oxidation during IOP1 (top) and IOP2 (bottom), along with the amount attributed to each tracer, and the total amount predicted from all tracers. These results were calculated without including MT as a tracer, for comparison with the bottom panels in Figs. 4.12–4.13.

Chapter 5

Conclusions and Future Work

5.1 Conclusions

In this dissertation, I have presented the development and application of an OFR for the purpose of studying SOA formation from the oxidation of ambient air. The OFR was first used to investigate SOA formation from OH, O₃, and NO₃ oxidation of montane pine forest air during the BEACHON-RoMBAS 2011 field campaign. The OFR was also used to study SOA formation from OH and O₃ oxidation from a mix of biogenic, anthropogenic, and biomass burning sources in the Amazon forest during the GoAmazon2014/5 campaign. In the course of these campaigns, I developed new operation and calibration protocols that substantially improved the scope, reproducibility and fidelity of using the OFR to sample ambient air. I showed that this technique can be used to quantitatively determine the amount of SOA that could be formed. Through the analysis of the data, I advanced our understanding of the interpretation of the technique, including how the results can inform us about SOA formation processes in the atmosphere.

The analysis and interpretation of the deployment of the OFR at the BEACHON-RoMBAS campaign, presented in Chapters 2–3, represented the majority of my thesis work. These results laid the foundation for future OFR research. The main scientific result was that approximately three quarters of the SOA that could be formed from OH oxidation of ambient air was formed from S/IVOCs, with only a quarter of the potential SOA coming from the VOCs that are conventionally assumed to be the main precursors. This was an important result because these S/IVOCs are very difficult to speciate and quantify, and relatively little is known about their presence and impact in the atmosphere. My measurements also showed that the S/IVOCs did not react with O₃ or NO₃ to produce SOA in the OFR, suggesting they tend to not contain C=C bonds (i.e., any C=C bonds in the emitted precursor molecules had already reacted) in this forest atmosphere. Finally, the chemical properties of SOA produced from

the oxidation of ambient air during BEACHON-RoMBAS was investigated in novel ways. This included an elemental analysis of the SOA formed (O:C and H:C values), and analysis of the formation of particulate organic nitrates.

Many “firsts” were accomplished with the BEACHON-RoMBAS measurements. New methods were developed to perform O₃ and NO₃ oxidation of ambient air in the OFR. The NO₃ oxidation technique (via injection of N₂O₅) was particularly novel, as was my modeling of the oxidant chemistry inside the NO₃-OFR. I showed for the first time that the two methods of OH radical production (OFR185 and OFR254) produce similar SOA formation results. I pioneered the methods of sampling VOCs through the OFR (and ambient air, using an automated valve system) with a PTR-TOF-MS in order to measure VOC decay after oxidation and verify oxidant exposures in the reactor. Perhaps the most important technical innovation from the BEACHON-RoMBAS analysis was modeling the fate of low volatility organic compounds (LVOCs), which are the gases formed by oxidation in the OFR that can condense to form SOA. Through this modeling we started for the first time to fully understand the competing time scales of oxidation and condensation in the OFR, and how these details can be used to design experiments to isolate the process of either SOA formation or heterogeneous oxidation. The analysis in Chapter 2 (Palm et al., 2016) set the standard for quantitative analysis of OFR measurements in future studies.

Building on everything learned from the BEACHON-RoMBAS measurements, Chapter 4 presented my measurements of OH and O₃ oxidation during the GoAmazon2014/5 campaign. Improvements in the experimental setup (hardware and software) and in pre-campaign planning led to greatly improved coverage of measurements and the ability to target specific hypotheses. I carefully designed an experiment to measure SOA yields from individual VOCs under the conditions found in ambient OFR experiments, the first such OFR “calibrations” designed specifically to consider the important details learned from the BEACHON-RoMBAS analysis. These measurements verified that SOA yields in the OFR were not substantially different from typical chamber yields. This also increased

confidence that S/IVOCs were present and account for the majority of potential SOA formation from OH oxidation.

Since there was a general lack of S/IVOC measurements during GoAmazon2014/5 (which is typical for most field campaigns), I made other attempts to determine the sources of these elusive SOA-forming gases. PMF analysis of SOA after OFR oxidation yielded interesting results, but also reinforced the fact that source apportionment of SOA using AMS measurements is difficult. This is particularly true after high degrees of oxidation, since individual source profiles (mass spectra) tend to become very similar after aging. A multilinear regression analysis between the SOA formation and tracers for biogenic, anthropogenic, and biomass burning sources showed some promise in identifying the sources of the unmeasured gases that contribute to SOA formation. However, a major conclusion from this analysis is that our knowledge of S/IVOCs remains limited.

5.2 Future Work

The OFR technique is becoming more popular every year. It is a versatile, relatively inexpensive technique, and it has recently been commercialized. There are many possibilities for it to advance our knowledge of many aspects of atmospheric science. Here, I present my thoughts about the possibilities for further improvement of the OFR technique, and about scientific questions that could be answered.

5.2.1 OFR technique improvements

The type of OFR used in this dissertation was the Potential Aerosol Mass (PAM) reactor, designed by Prof. William Brune at Penn State University and now sold commercially by Aerodyne Research, Inc. However, there are many custom-built OFRs in use by other researchers (e.g., George et al., 2008; Smith et al., 2009; Keller and Burtscher, 2012). As with large environmental chambers, there is no “perfect” OFR design. Different designs can be optimized to study different processes, and the designs can be improved through trial and error, characterization experiments, modeling, and careful attention to detail. The PAM reactor benefits from having a large user group, and from the years of work

in this thesis and elsewhere (though the PAM reactor used here is a slightly different design than the commercially available option). However, through the experiences I gained in this dissertation, I believe there are ways to improve upon the PAM design for the purpose of measuring SOA formation from ambient air. Specifically, I have identified several limitations of the current technique that could be remedied.

The first limitation of the current method is that we often operated under conditions where a relatively small fraction (~30%) of the LVOCs formed in the OFR would condense to form SOA. This was particularly an issue when oxidizing ambient air in locations with a low ambient aerosol condensational sink, such as during BEACHON-RoMBAS, where large correction factors (e.g., up to a factor of 3) were required at times (especially during periods when little SOA was formed from ambient air). A second limitation is that the residence time distribution in the PAM is not as narrow as it could be (in relation to other OFR designs; Lambe et al., 2011a; Huang et al., 2017), particularly when sampling with the front plate installed on the PAM (which was often required due to windy conditions in the field). Finally, a limitation with all OFR designs (to the best of my knowledge) is that sampling several data points over the whole range of possible exposures from hours to weeks/months requires several hours to accomplish. In this thesis work, we typically operated on a repeating cycle of 2–3 h for the whole range of exposures. This length is required by the waiting time between setting the oxidant level (either UV lamps or injected oxidant) and when the reactor conditions have stabilized at that oxidant level, which is typically several residence times (16–24 min used in this work). During this 2–3 h cycle, the concentrations of gases and particles in ambient air are likely to have changed. Although this effect can be mitigated by averaging multiple cycles, it adds uncertainty to the technique.

In Fig. 5.1, I propose a possible OFR design that I believe could improve upon these limitations. To give a narrower distribution of residence times, I would propose a narrower cylinder, perhaps ~10–15 cm inner diameter, with cones on the inlet and outlet to eliminate the “dead volume” around the inlet

plate of the PAM. With the higher surface-area-to-volume ratio, this new design would be more susceptible to wall losses, particularly for LVOC gases. To counteract that, I would include a port inside the inlet where a seed aerosol (perhaps ammonium sulfate) would be injected, to provide a large condensational sink on which the LVOCs could condense. Particle-phase losses to the walls would be much easier to correct for than gas-phase losses. The most innovative part of the design would be a moveable sampling port (with separate gas and particle sampling lines). With this design, the UV lights (or injected oxidant) could be held constant at all times, and increasing ages are sampled by moving the sampling ports to a further distance into the reactor. As long as the sampling flow remains several times smaller than the exhaust flow, the effects on the flow profile in the OFR should be small. If the sampling instruments have high time resolution (e.g., 1 Hz), the sampling port could be moved along the entire length of the reactor in just several minutes and sample a wide range of exposures in a very short amount of time. This would greatly increase the chances that the concentrations of gases and particles entering the reactor have not changed during the measurement. In the scenario where each measurement requires several minutes (e.g., an SMPS scan), then the sampling ports could be held in place at a handful of reaction distances, spanning the range of concentrations in as little as 10 min or so. Many details remain to be worked out to optimize this design (e.g., perhaps the complexity of a moveable sampling port could be replaced with several permanent sampling ports along the length of the reactor body), but a design based on the one in Fig. 5.1 would have the potential to address many of the limitations of reactors such as the PAM design.

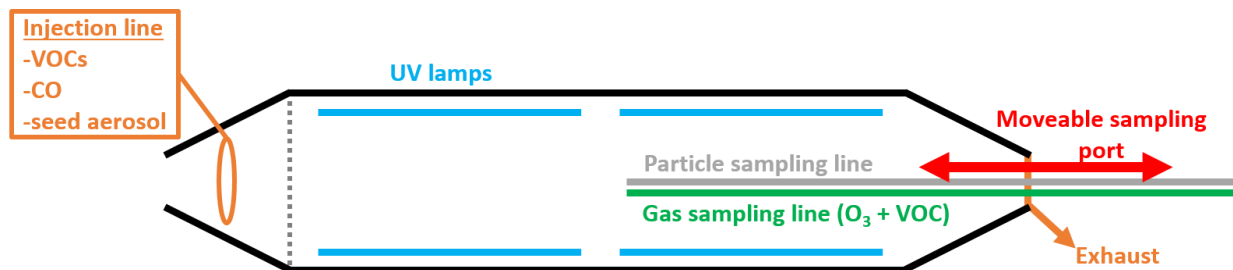


Fig. 5.1. Possible design improvements for a future OFR. Condensational sink could be increased by injecting a seed aerosol through a permanent injection line designed to optimize mixing with ambient air before passing through a mesh grid. A narrower and longer reactor could help to decrease the distribution of residence times. Finally, the particle and gas sampling lines could be moved along the length of the OFR in order to sample different ages (with oxidant concentration held roughly constant).

5.2.2 Measurement possibilities

With regard to the possibilities for future research that could build upon this dissertation, there are two main avenues. First, how can we learn more about the elusive SOA-forming *S/IVOCs* that appear to be present in a wide variety of locations? The answer to this question doesn't necessarily require an OFR (though one could be used, see below). Recently, numerous instruments have been developed to speciate and/or quantify subsets of *S/IVOCs* (e.g., Lopez-Hilfiker et al., 2013; Zhao et al., 2013; Krechmer et al., 2016), or quantify the bulk or volatility-separated concentrations of such gases (e.g., Cross et al., 2013). Such measurement techniques will continue to develop and provide new information. As models continue to evolve and explicitly track the composition and volatility of organic molecules through many oxidation steps, they will also likely provide more insight into the chemistry of lower volatility gases.

The second avenue for future research asks: what is the future for using OFRs to study the atmosphere? OFRs will certainly continue to be used in cutting-edge experiments. Here are a few ideas that could be investigated:

- 1) *S/IVOCs*- OFRs could be sampled by the novel instruments mentioned above, or the *S/IVOCs* could continue to be inferred by oxidizing them to form SOA. More OFR measurements of the oxidation of ambient air or synthetic mixtures in the laboratory could answer a variety of questions. Where else are *S/IVOCs* located? Are they primary or secondary? What are

their lifetimes and fates in the atmosphere? How big of a role do they play in ambient SOA formation?

- 2) *OFRs as predictive tools*- An OFR could be used to measure potential SOA formation as a function of distance downwind of a point source or urban area in a Lagrangian experiment. This could be done by deploying the OFR in a mobile lab or airplane, and would be most easily accomplished if the OFR design improvements suggested above were implemented to increase the sampling rate. One could also imagine regional networks of OFRs to measure long-term or seasonal potential SOA formation, which could help to inform regional and global SOA models.
- 3) *Investigating specific mechanisms or processes*- As mentioned above, OFRs have been used by a growing number of research groups to investigate specific processes, such as heterogeneous oxidation, SOA yields from a variety of gases, properties of OA (CCN activity, phase state, elemental composition, etc). As OFRs become better characterized and more widespread, these types of experiments will become as popular as typical large chamber studies. With the dramatically lower cost and short time required for measurements, the future of OFR research is vast.

In conclusion, OFRs are versatile tools that can be used in conjunction with a variety of instruments and sampling strategies to investigate a range of research questions. My dissertation contributed significantly to the development of OFRs, particularly demonstrating the viability of quantifying SOA formation from the oxidation of ambient air, and it will serve as a foundation for future research in atmospheric chemistry.

References

- Aiken, A. C., DeCarlo, P. F., Kroll, J. H., Worsnop, D. R., Huffman, J. A., Docherty, K. S., Ulbrich, I. M., Mohr, C., Kimmel, J. R., Sueper, D., Sun, Y., Zhang, Q., Trimborn, A., Northway, M., Ziemann, P. J., Canagaratna, M. R., Onasch, T. B., Alfarra, M. R., Prevot, A. S. H., Dommen, J., Duplissy, J., Metzger, A., Baltensperger, U. and Jimenez, J. L.: O/C and OM/OC Ratios of Primary, Secondary, and Ambient Organic Aerosols with High-Resolution Time-of-Flight Aerosol Mass Spectrometry, *Environ. Sci. Technol.*, **42**, 4478–4485, doi:10.1021/es703009q, 2008.
- Aiken, A. C., Salcedo, D., Cubison, M. J., Huffman, J. a., DeCarlo, P. F., Ulbrich, I. M., Docherty, K. S., Sueper, D., Kimmel, J. R., Worsnop, D. R., Trimborn, A., Northway, M., Stone, E. a., Schauer, J. J., Volkamer, R. M., Fortner, E., de Foy, B., Wang, J., Laskin, A., Shutthanandan, V., Zheng, J., Zhang, R., Gaffney, J., Marley, N. a., Paredes-Miranda, G., Arnott, W. P., Molina, L. T., Sosa, G. and Jimenez, J. L.: Mexico City aerosol analysis during MILAGRO using high resolution aerosol mass spectrometry at the urban supersite (T0) - Part 1: Fine particle composition and organic source apportionment, *Atmos. Chem. Phys.*, **9**, 8377–8427, doi:10.5194/acpd-9-8377-2009, 2009.
- Alarcón, P., Bohn, B., Zetzsch, C., Rayez, M.-T. and Rayez, J.-C.: Reversible addition of the OH radical to *p*-cymene in the gas phase: multiple adduct formation. Part 2., *Phys. Chem. Chem. Phys.*, **16**, 17315–26, doi:10.1039/c4cp02073a, 2014.
- Altieri, K. E., Seitzinger, S. P., Carlton, a. G., Turpin, B. J., Klein, G. C. and Marshall, a. G.: Oligomers formed through in-cloud methylglyoxal reactions: Chemical composition, properties, and mechanisms investigated by ultra-high resolution FT-ICR mass spectrometry, *Atmos. Environ.*, **42**, 1476–1490, doi:10.1016/j.atmosenv.2007.11.015, 2008.
- Alvarado, A., Arey, J. and Atkinson, R.: Kinetics of the Gas-Phase Reactions of OH and NO₃ Radicals and O₃ with the Monoterpene Reaction Products Pinonaldehyde, Caronaldehyde, and Sabinaketone, *J. Atmos. Chem.*, **31**, 281–297, doi:10.1023/A:1006010915971, 1998.
- Atkinson, R.: Gas-Phase Tropospheric Chemistry of Volatile Organic Compounds: 1. Alkanes and Alkenes, *J. Phys. Chem. Ref. Data*, **26**, 215–290, doi:10.1063/1.556012, 1997.
- Atkinson, R. and Arey, J.: Gas-phase tropospheric chemistry of biogenic volatile organic compounds: a review, *Atmos. Environ.*, **37**, 197–219, doi:10.1016/S1352-2310(03)00391-1, 2003.
- Atkinson, R. and Aschmann, S. M.: Atmospheric chemistry of the monoterpene reaction products nopinone, camphenilone, and 4-acetyl-1-methylcyclohexene, *J. Atmos. Chem.*, **16**, 337–348, doi:10.1007/BF01032629, 1993.
- Atkinson, R., Winer, A. M. and Pitts Jr., J.: Rate constants for the gas-phase reactions of O₃ with the natural hydrocarbons isoprene and α and β -pinene, *Atmos. Environ.*, **16**, 1017–1020, 1982.
- Atkinson, R., Baulch, D. L., Cox, R. A., Crowley, J. N., Hampson, R. F., Hynes, R. G., Jenkin, M. E., Rossi, M. J. and Troe, J.: Evaluated kinetic and photochemical data for atmospheric chemistry: Volume I - gas phase reactions of O_x, HO_x, NO_x and SO_x species, *Atmos. Chem. Phys.*, **4**, 1461–1738, doi:10.5194/acp-4-1461-2004, 2004.
- Atkinson, R., Baulch, D. L., Cox, R. A., Crowley, J. N., Hampson, R. F., Hynes, R. G., Jenkin, M. E., Rossi, M. J., Troe, J. and IUPAC Subcommittee: Evaluated kinetic and photochemical data for atmospheric chemistry: Volume II - gas phase reactions of organic species, *Atmos. Chem. Phys.*, **6**, 3625–4055, doi:10.5194/acp-6-3625-2006, 2006.

- Bertram, A. K., Martin, S. T., Hanna, S. J., Smith, M. L., Bodsworth, A., Chen, Q., Kuwata, M., Liu, A., You, Y. and Zorn, S. R.: Predicting the relative humidities of liquid-liquid phase separation, efflorescence, and deliquescence of mixed particles of ammonium sulfate, organic material, and water using the organic-to-sulfate mass ratio of the particle and the oxygen-to-carbon ele, *Atmos. Chem. Phys.*, **11**, 10995–11006, doi:10.5194/acp-11-10995-2011, 2011.
- Boyd, C. M., Sanchez, J., Xu, L., Eugene, A. J., Nah, T., Tuet, W. Y., Guzman, M. I. and Ng, N. L.: Secondary organic aerosol formation from the β -pinene+NO₃ system: effect of humidity and peroxy radical fate, *Atmos. Chem. Phys.*, **15**, 7497–7522, doi:10.5194/acp-15-7497-2015, 2015.
- Brito, J., Rizzo, L. V., Morgan, W. T., Coe, H., Johnson, B., Haywood, J., Longo, K., Freitas, S., Andreae, M. O. and Artaxo, P.: Ground-based aerosol characterization during the South American Biomass Burning Analysis (SAMBBA) field experiment, *Atmos. Chem. Phys.*, **14**, 12069–12083, doi:10.5194/acp-14-12069-2014, 2014.
- Brown, S. S. and Stutz, J.: Nighttime radical observations and chemistry, *Chem. Soc. Rev.*, **41**, 6405, doi:10.1039/c2cs35181a, 2012.
- Brown, S. S., Dubé, W. P., Bahreini, R., Middlebrook, A. M., Brock, C. A., Warneke, C., de Gouw, J. A., Washenfelder, R. A., Atlas, E., Peischl, J., Ryerson, T. B., Holloway, J. S., Schwarz, J. P., Spackman, R., Trainer, M., Parrish, D. D., Fehsenfeld, F. C. and Ravishankara, A. R.: Biogenic VOC oxidation and organic aerosol formation in an urban nocturnal boundary layer: aircraft vertical profiles in Houston, TX, *Atmos. Chem. Phys.*, **13**, 11317–11337, doi:10.5194/acp-13-11317-2013, 2013.
- Bruns, E. A., Perraud, V., Zelenyuk, A., Ezell, M. J., Johnson, S. N., Yu, Y., Imre, D., Finlayson-Pitts, B. J., Alexander, M. L., Bruns, A. E., Perraud, V., Zelenyuk, A., Ezell, M. J., Johnson, S. N., Yu, Y., Imre, D., Finlayson-Pitts, B. J. and Alexander, M. L.: Comparison of FTIR and particle mass spectrometry for the measurement of particulate organic nitrates, *Environ. Sci. Technol.*, **44**, 1056–61, doi:10.1021/es9029864, 2010.
- Bruns, E. A., El Haddad, I., Keller, A., Klein, F., Kumar, N. K., Pieber, S. M., Corbin, J. C., Slowik, J. G., Brune, W. H., Baltensperger, U. and Prévôt, A. S. H.: Inter-comparison of laboratory smog chamber and flow reactor systems on organic aerosol yield and composition, *Atmos. Meas. Tech.*, **8**, 2315–2332, doi:10.5194/amt-8-2315-2015, 2015.
- Calogirou, A., Jensen, N. R., Nielsen, C. J., Kotzias, D. and Hjorth, J.: Gas-Phase Reactions of Nopinone, 3-Isopropenyl-6-oxo-heptanal, and 5-Methyl-5-vinyltetrahydrofuran-2-ol with OH, NO₃, and Ozone, *Environ. Sci. Technol.*, **33**, 453–460, doi:10.1021/es980530j, 1999a.
- Calogirou, A., Larsen, B. R. and Kotzias, D.: Gas-phase terpene oxidation products: a review, *Atmos. Environ.*, **33**, 1423–1439, doi:10.1016/S1352-2310(98)00277-5, 1999b.
- Calvert, J. G., Atkinson, R., Becker, K. H., Kamens, R. M., Seinfeld, J. H., Wallington, T. H. and Yarwood, G.: *The Mechanisms of Atmospheric Oxidation of the Aromatic Hydrocarbons*, Oxford University Press, New York, USA, 2002.
- Canagaratna, M. R., Jayne, J. T., Jimenez, J. L., Allan, J. D., Alfarra, M. R., Zhang, Q., Onasch, T. B., Drewnick, F., Coe, H., Middlebrook, A., Delia, A., Williams, L. R., Trimborn, A. M., Northway, M. J., DeCarlo, P. F., Kolb, C. E., Davidovits, P. and Worsnop, D. R.: Chemical and microphysical characterization of ambient aerosols with the aerodyne aerosol mass spectrometer, *Mass Spectrom. Rev.*, **26**, 185–222, doi:10.1002/mas.20115, 2007.

- Canagaratna, M. R., Jimenez, J. L., Kroll, J. H., Chen, Q., Kessler, S. H., Massoli, P., Hildebrandt Ruiz, L., Fortner, E., Williams, L. R., Wilson, K. R., Surratt, J. D., Donahue, N. M., Jayne, J. T. and Worsnop, D. R.: Elemental ratio measurements of organic compounds using aerosol mass spectrometry: characterization, improved calibration, and implications, *Atmos. Chem. Phys.*, **15**, 253–272, doi:10.5194/acp-15-253-2015, 2015.
- Canonaco, F., Crippa, M., Slowik, J. G., Baltensperger, U. and Prévôt, a. S. H.: SoFi, an IGOR-based interface for the efficient use of the generalized multilinear engine (ME-2) for the source apportionment: ME-2 application to aerosol mass spectrometer data, *Atmos. Meas. Tech.*, **6**, 3649–3661, doi:10.5194/amt-6-3649-2013, 2013.
- Canosa-Mas, C. E., King, M. D., Scarr, P. J., Thompson, K. C. and Wayne, R. P.: An experimental study of the gas-phase reactions of the NO₃ radical with three sesquiterpenes: isolongifolene, alloisolongifolene, and α -neoclovene, *Phys. Chem. Chem. Phys.*, **1**, 2929–2933, doi:10.1039/a902034i, 1999.
- Cappa, C. D. and Jimenez, J. L.: Quantitative estimates of the volatility of ambient organic aerosol, *Atmos. Chem. Phys.*, **10**, 5409–5424, doi:10.5194/acp-10-5409-2010, 2010.
- Cappa, C. D., Che, D. L., Kessler, S. H., Kroll, J. H. and Wilson, K. R.: Variations in organic aerosol optical and hygroscopic properties upon heterogeneous OH oxidation, *J. Geophys. Res.*, **116**, D15204, doi:10.1029/2011JD015918, 2011.
- Chan, A. W. H., Kautzman, K. E., Chhabra, P. S., Surratt, J. D., Chan, M. N., Crouse, J. D., Kürten, A., Wennberg, P. O., Flagan, R. C. and Seinfeld, J. H.: Secondary organic aerosol formation from photooxidation of naphthalene and alkyl naphthalenes: implications for oxidation of intermediate volatility organic compounds (IVOCs), *Atmos. Chem. Phys.*, **9**, 3049–3060, doi:10.5194/acp-9-3049-2009, 2009.
- Chan, A. W. H., Kreisberg, N. M., Hohaus, T., Campuzano-Jost, P., Zhao, Y., Day, D. A., Kaser, L., Karl, T., Hansel, A., Teng, A. P., Ruehl, C. R., Sueper, D. T., Jayne, J. T., Worsnop, D. R., Jimenez, J. L., Hering, S. V. and Goldstein, A. H.: Speciated measurements of semivolatile and intermediate volatility organic compounds (S/IVOCs) in a pine forest during BEACHON-RoMBAS 2011, *Atmos. Chem. Phys.*, **16**, 1187–1205, doi:10.5194/acp-16-1187-2016, 2016.
- Chen, H., Ezell, M. J., Arquero, K. D., Varner, M. E., Dawson, M. L., Gerber, R. B. and Finlayson-Pitts, B. J.: New particle formation and growth from methanesulfonic acid, trimethylamine and water, *Phys. Chem. Chem. Phys.*, **17**, 13699–13709, doi:10.1039/C5CP00838G, 2015a.
- Chen, Q., Farmer, D. K., Schneider, J., Zorn, S. R., Heald, C. L., Karl, T. G., Guenther, A., Allan, J. D., Robinson, N., Coe, H., Kimmel, J. R., Pauliquevis, T., Borrmann, S., Pöschl, U., Andreae, M. O., Artaxo, P., Jimenez, J. L. and Martin, S. T.: Mass spectral characterization of submicron biogenic organic particles in the Amazon Basin, *Geophys. Res. Lett.*, **36**, L20806, doi:10.1029/2009GL039880, 2009.
- Chen, Q., Liu, Y., Donahue, N. M., Shilling, J. E. and Martin, S. T.: Particle-phase chemistry of secondary organic material: modeled compared to measured O:C and H:C elemental ratios provide constraints., *Environ. Sci. Technol.*, **45**, 4763–70, doi:10.1021/es104398s, 2011.
- Chen, Q., Li, Y. L., McKinney, K. A., Kuwata, M. and Martin, S. T.: Particle mass yield from β -caryophyllene ozonolysis, *Atmos. Chem. Phys.*, **12**, 3165–3179, doi:10.5194/acp-12-3165-2012, 2012.
- Chen, Q., Heald, C. L., Jimenez, J. L., Canagaratna, M. R., Zhang, Q., He, L., Huang, X.-F., Campuzano-Jost, P., Palm, B. B., Poulain, L., Kuwata, M., Martin, S. T., Abbatt, J. P. D., Lee, A. K. Y. and Liggi, J.: Elemental

composition of organic aerosol: The gap between ambient and laboratory measurements, *Geophys. Res. Lett.*, 42, 4182–4189, doi:10.1002/2015GL063693, 2015b.

Chen, Q., Farmer, D. K., Rizzo, L. V., Pauliquevis, T., Kuwata, M., Karl, T. G., Guenther, A., Allan, J. D., Coe, H., Andreae, M. O., Pöschl, U., Jimenez, J. L., Artaxo, P. and Martin, S. T.: Submicron particle mass concentrations and sources in the Amazonian wet season (AMAZE-08), *Atmos. Chem. Phys.*, 15, 3687–3701, doi:10.5194/acp-15-3687-2015, 2015c.

Chew, A. A., Atkinson, R. and Aschmann, S. M.: Kinetics of the gas-phase reactions of NO₃ radicals with a series of alcohols, glycol ethers, ethers and chloroalkenes, *J. Chem. Soc. Trans.*, 94, 1083–1089, 1998.

Chhabra, P. S., Ng, N. L., Canagaratna, M. R., Corrigan, A. L., Russell, L. M., Worsnop, D. R., Flagan, R. C. and Seinfeld, J. H.: Elemental composition and oxidation of chamber organic aerosol, *Atmos. Chem. Phys.*, 11, 8827–8845, doi:10.5194/acp-11-8827-2011, 2011.

Cross, E. S., Hunter, J. F., Carrasquillo, A. J., Franklin, J. P., Herndon, S. C., Jayne, J. T., Worsnop, D. R., Miake-Lye, R. C. and Kroll, J. H.: Online measurements of the emissions of intermediate-volatility and semi-volatile organic compounds from aircraft, *Atmos. Chem. Phys.*, 13, 7845–7858, doi:10.5194/acp-13-7845-2013, 2013.

Crouse, J. D., Nielsen, L. B., Jørgensen, S., Kjaergaard, H. G. and Wennberg, P. O.: Autoxidation of Organic Compounds in the Atmosphere, *J. Phys. Chem. Lett.*, 4, 3513–3520, doi:10.1021/jz4019207, 2013.

Crump, J. G. and Seinfeld, J. H.: Turbulent deposition and gravitational sedimentation of an aerosol in a vessel of arbitrary shape, *J. Aerosol Sci.*, 12, 405–415, doi:10.1016/0021-8502(81)90036-7, 1981.

Cubison, M. J., Ortega, A. M., Hayes, P. L., Farmer, D. K., Day, D., Lechner, M. J., Brune, W. H., Apel, E., Diskin, G. S., Fisher, J. A., Fuelberg, H. E., Hecobian, A., Knapp, D. J., Mikoviny, T., Riemer, D., Sachse, G. W., Sessions, W., Weber, R. J., Weinheimer, A. J., Wisthaler, A. and Jimenez, J. L.: Effects of aging on organic aerosol from open biomass burning smoke in aircraft and laboratory studies, *Atmos. Chem. Phys.*, 11, 12049–12064, doi:10.5194/acp-11-12049-2011, 2011.

Day, D. A., Campuzano-Jost, P., Palm, B. B., Hu, W. W., Nault, B. A., Wooldridge, P. J., Cohen, R. C., Docherty, K. S., Huffman, J. A. and Jimenez, J. L.: Evaluation of methods for quantification of bulk particle-phase organic nitrates using real-time aerosol mass spectrometry, *In prep.*, 2017.

DeCarlo, P. F., Slowik, J. G., Worsnop, D. R., Davidovits, P. and Jimenez, J. L.: Particle Morphology and Density Characterization by Combined Mobility and Aerodynamic Diameter Measurements. Part 1: Theory, *Aerosol Sci. Technol.*, 38, 1185–1205, doi:10.1080/027868290903907, 2004.

DeCarlo, P. F., Kimmel, J. R., Trimborn, A., Northway, M. J., Jayne, J. T., Aiken, A. C., Gonin, M., Fuhrer, K., Horvath, T., Docherty, K. S., Worsnop, D. R. and Jimenez, J. L.: Field-Deployable, High-Resolution, Time-of-Flight Aerosol Mass Spectrometer, *Anal. Chem.*, 78, 8281–8289, doi:10.1021/ac061249n, 2006.

DeCarlo, P. F., Dunlea, E. J., Kimmel, J. R., Aiken, A. C., Sueper, D., Crouse, J., Wennberg, P. O., Emmons, L., Shinozuka, Y., Clarke, A., Zhou, J., Tomlinson, J., Collins, D. R., Knapp, D., Weinheimer, A. J., Montzka, D. D., Campos, T. and Jimenez, J. L.: Fast airborne aerosol size and chemistry measurements above Mexico City and Central Mexico during the MILAGRO campaign, *Atmos. Chem. Phys.*, 8, 4027–4048, doi:10.5194/acp-8-4027-2008, 2008.

Donahue, N. M., Robinson, A. L., Stanier, C. O. and Pandis, S. N.: Coupled Partitioning, Dilution, and Chemical Aging of Semivolatile Organics, *Environ. Sci. Technol.*, 40, 2635–2643, doi:10.1021/es052297c,

2006.

Donahue, N. M., Chuang, W., Epstein, S. A., Kroll, J. H., Worsnop, D. R., Robinson, A. L., Adams, P. J. and Pandis, S. N.: Why do organic aerosols exist? Understanding aerosol lifetimes using the two-dimensional volatility basis set, *Environ. Chem.*, **10**, 151, doi:10.1071/EN13022, 2013.

Dzepina, K., Volkamer, R. M. R., Madronich, S., Tulet, P., Ulbrich, I. M., Zhang, Q., Cappa, C. D., Ziemann, P. J. and Jimenez, J. L.: Evaluation of recently-proposed secondary organic aerosol models for a case study in Mexico City, *Atmos. Chem. Phys.*, **9**, 5681–5709, doi:10.5194/acp-9-5681-2009, 2009.

Ehn, M., Thornton, J. A., Kleist, E., Sipilä, M., Junninen, H., Pullinen, I., Springer, M., Rubach, F., Tillmann, R., Lee, B., Lopez-Hilfiker, F., Andres, S., Acir, I.-H., Rissanen, M., Jokinen, T., Schobesberger, S., Kangasluoma, J., Kontkanen, J., Nieminen, T., Kurtén, T., Nielsen, L. B., Jørgensen, S., Kjaergaard, H. G., Canagaratna, M., Maso, M. D., Berndt, T., Petäjä, T., Wahner, A., Kerminen, V.-M., Kulmala, M., Worsnop, D. R., Wildt, J. and Mentel, T. F.: A large source of low-volatility secondary organic aerosol, *Nature*, **506**, 476–479, doi:10.1038/nature13032, 2014.

Ervens, B.: Modeling the Processing of Aerosol and Trace Gases in Clouds and Fogs, *Chem. Rev.*, **115**, 4157–4198, doi:10.1021/cr5005887, 2015.

Ervens, B., Turpin, B. J. and Weber, R. J.: Secondary organic aerosol formation in cloud droplets and aqueous particles (aqSOA): a review of laboratory, field and model studies, *Atmos. Chem. Phys.*, **11**, 11069–11102, doi:10.5194/acp-11-11069-2011, 2011.

Ezell, M. J., Chen, H., Arquero, K. D. and Finlayson-Pitts, B. J.: Aerosol fast flow reactor for laboratory studies of new particle formation, *J. Aerosol Sci.*, **78**, 30–40, doi:10.1016/j.jaerosci.2014.08.009, 2014.

Farmer, D. K. and Cohen, R. C.: Observations of HNO₃, ΣAN, ΣPN and NO₂ fluxes: evidence for rapid HO_x chemistry within a pine forest canopy, *Atmos. Chem. Phys.*, **8**, 3899–3917, doi:10.5194/acp-8-3899-2008, 2008.

Farmer, D. K., Matsunaga, A., Docherty, K. S., Surratt, J. D., Seinfeld, J. H., Ziemann, P. J. and Jimenez, J. L.: Response of an aerosol mass spectrometer to organonitrates and organosulfates and implications for atmospheric chemistry, *P. Natl. Acad. Sci. USA*, **107**, 6670–6675, doi:10.1073/pnas.0912340107, 2010.

Fry, J. L., Kiendler-Scharr, A., Rollins, A. W., Wooldridge, P. J., Brown, S. S., Fuchs, H., Dubé, W., Mensah, A., dal Maso, M., Tillmann, R., Dorn, H.-P., Brauers, T. and Cohen, R. C.: Organic nitrate and secondary organic aerosol yield from NO₃ oxidation of β-pinene evaluated using a gas-phase kinetics/aerosol partitioning model, *Atmos. Chem. Phys.*, **9**, 1431–1449, doi:10.5194/acp-9-1431-2009, 2009.

Fry, J. L., Kiendler-Scharr, A., Rollins, A. W., Brauers, T., Brown, S. S., Dorn, H.-P., Dubé, W. P., Fuchs, H., Mensah, A., Rohrer, F., Tillmann, R., Wahner, A., Wooldridge, P. J., Cohen, R. C. and Dube, W.: SOA from limonene: role of NO₃ in its generation and degradation, *Atmos. Chem. Phys.*, **11**, 3879–3894, doi:doi:10.5194/acp-11-3879-2011, 2011.

Fry, J. L., Draper, D. C., Zarzana, K. J., Campuzano-Jost, P., Day, D. A., Jimenez, J. L., Brown, S. S., Cohen, R. C., Kaser, L., Hansel, A., Cappellin, L., Karl, T., Hodzic Roux, A., Turnipseed, A., Cantrell, C., Lefer, B. L. and Grossberg, N.: Observations of gas- and aerosol-phase organic nitrates at BEACHON-RoMBAS 2011, *Atmos. Chem. Phys.*, **13**, 8585–8605, doi:10.5194/acp-13-8585-2013, 2013.

Fry, J. L., Draper, D. C., Barsanti, K. C., Smith, J. N., Ortega, J., Winkler, P. M., Lawler, M. J., Brown, S. S., Edwards, P. M., Cohen, R. C. and Lee, L.: Secondary Organic Aerosol Formation and Organic Nitrate Yield from NO₃ Oxidation of Biogenic Hydrocarbons, *Environ. Sci. Technol.*, **48**, 11944–11953,

doi:10.1021/es502204x, 2014.

Gaston, C. J., Thornton, J. A. and Ng, N. L.: Reactive uptake of N_2O_5 to internally mixed inorganic and organic particles: the role of organic carbon oxidation state and inferred organic phase separations, *Atmos. Chem. Phys.*, 14, 5693–5707, doi:10.5194/acp-14-5693-2014, 2014.

George, I. J. and Abbatt, J. P. D.: Heterogeneous oxidation of atmospheric aerosol particles by gas-phase radicals., *Nat. Chem.*, 2, 713–22, doi:10.1038/nchem.806, 2010.

George, I. J., Slowik, J. and Abbatt, J. P. D.: Chemical aging of ambient organic aerosol from heterogeneous reaction with hydroxyl radicals, *Geophys. Res. Lett.*, 35, L13811, doi:10.1029/2008GL033884, 2008.

George, I. J., Chang, R. Y.-W., Danov, V., Vlasenko, A. and Abbatt, J. P. D.: Modification of cloud condensation nucleus activity of organic aerosols by hydroxyl radical heterogeneous oxidation, *Atmos. Environ.*, 43, 5038–5045, doi:10.1016/j.atmosenv.2009.06.043, 2009.

Godish, T., Davis, W. T. and Fu, J. S.: *Air Quality*, 5th Editio, CRC Press, 2014.

Goldstein, A. H. and Galbally, I. E.: Known and Unexplored Organic Constituents in the Earth's Atmosphere, *Environ. Sci. Technol.*, 41, 1514–1521, doi:10.1021/es072476p, 2007.

de Gouw, J. A. and Lovejoy, E. R.: Reactive uptake of ozone by liquid organic compounds, *Geophys. Res. Lett.*, 25, 931–934, doi:10.1029/98GL00515, 1998.

Grieshop, A. P., Logue, J. M., Donahue, N. M. and Robinson, A. L.: Laboratory investigation of photochemical oxidation of organic aerosol from wood fires 1: measurement and simulation of organic aerosol evolution, *Atmos. Chem. Phys.*, 9, 1263–1277, doi:10.5194/acp-9-1263-2009, 2009.

Hallquist, M., Wängberg, I., Ljungström, E., Barnes, I. and Becker, K.-H.: Aerosol and product yields from NO_3 radical-initiated oxidation of selected monoterpenes, *Environ. Sci. Technol.*, 33, 553–559, doi:10.1021/es980292s, 1999.

Hallquist, M., Wenger, J. C., Baltensperger, U., Rudich, Y., Simpson, D., Claeys, M., Dommen, J., Donahue, N. M., George, C., Goldstein, A. H., Hamilton, J. F., Herrmann, H., Hoffmann, T., Iinuma, Y., Jang, M., Jenkin, M. E., Jimenez, J. L., Kiendler-Scharr, A., Maenhaut, W., McFiggans, G., Mentel, T. F., Monod, A., Prévôt, A. S. H., Seinfeld, J. H., Surratt, J. D., Szmigielski, R. and Wildt, J.: The formation, properties and impact of secondary organic aerosol: current and emerging issues, *Atmos. Chem. Phys.*, 9, 5155–5236, doi:10.5194/acp-9-5155-2009, 2009.

Hanson, D. R. and Eisele, F.: Diffusion of H_2SO_4 in Humidified Nitrogen: Hydrated H_2SO_4 , *J. Phys. Chem. A*, 104, 1715–1719, doi:10.1021/jp993622j, 2000.

Hayes, P. L., Carlton, A. G., Baker, K. R., Ahmadov, R., Washenfelder, R. A., Alvarez, S., Rappenglück, B., Gilman, J. B., Kuster, W. C., de Gouw, J. A., Zotter, P., Prévôt, A. S. H., Szidat, S., Kleindienst, T. E., Offenberg, J. H., Ma, P. K. and Jimenez, J. L.: Modeling the formation and aging of secondary organic aerosols in Los Angeles during CalNex 2010, *Atmos. Chem. Phys.*, 15, 5773–5801, doi:10.5194/acp-15-5773-2015, 2015.

Heald, C. L., Kroll, J. H., Jimenez, J. L., Docherty, K. S., DeCarlo, P. F., Aiken, A. C., Chen, Q., Martin, S. T., Farmer, D. K. and Artaxo, P.: A simplified description of the evolution of organic aerosol composition in the atmosphere, *Geophys. Res. Lett.*, 37, L08803, doi:10.1029/2010gl042737, 2010.

Henze, D. K. and Seinfeld, J. H.: Global secondary organic aerosol from isoprene oxidation, *Geophys. Res. Lett.*, **33**, L09812, doi:10.1029/2006GL025976, 2006.

Hildebrandt Ruiz, L., Paciga, A. L., Cerully, K. M., Nenes, A., Donahue, N. M. and Pandis, S. N.: Formation and aging of secondary organic aerosol from toluene: changes in chemical composition, volatility, and hygroscopicity, *Atmos. Chem. Phys.*, **15**, 8301–8313, doi:10.5194/acp-15-8301-2015, 2015.

Hodzic, A., Jimenez, J. L., Madronich, S., Aiken, A. C., Bessagnet, B., Curci, G., Fast, J., Lamarque, J. F., Onasch, T. B., Roux, G., Schauer, J. J., Stone, E. A. and Ulbrich, I. M.: Modeling organic aerosols during MILAGRO: importance of biogenic secondary organic aerosols, *Atmos. Chem. Phys.*, **9**, 6949–6981, 2009.

Hodzic, A., Jimenez, J. L., Madronich, S., Canagaratna, M. R., DeCarlo, P. F., Kleinman, L. and Fast, J.: Modeling organic aerosols in a megacity: potential contribution of semi-volatile and intermediate volatility primary organic compounds to secondary organic aerosol formation, *Atmos. Chem. Phys.*, **10**, 5491–5514, doi:doi:10.5194/acp-10-5491-2010, 2010.

Hu, W., Palm, B. B., Day, D. A., Campuzano-Jost, P., Krechmer, J. E., Peng, Z., de Sá, S. S., Martin, S. T., Alexander, M. L., Baumann, K., Hacker, L., Kiendler-Scharr, A., Koss, A. R., de Gouw, J. A., Goldstein, A. H., Seco, R., Sjostedt, S. J., Park, J.-H., Guenther, A. B., Kim, S., Canonaco, F., Prévôt, A. S. H., Brune, W. H. and Jimenez, J. L.: Volatility and lifetime against OH heterogeneous reaction of ambient isoprene-epoxydiols-derived secondary organic aerosol (IEPOX-SOA), *Atmos. Chem. Phys.*, **16**, 11563–11580, doi:10.5194/acp-16-11563-2016, 2016.

Hu, W. W., Campuzano-Jost, P., Palm, B. B., Day, D. a, Ortega, a M., Hayes, P. L., Krechmer, J. E., Chen, Q., Kuwata, M., Liu, Y. J., de Sá, S. S., Martin, S. T., Hu, M., Budisulistiorini, S. H., Riva, M., Surratt, J. D., St. Clair, J. M., Isaacman-Van Wertz, G., Yee, L. D., Goldstein, a. H., Carbone, S., Artaxo, P., de Gouw, J. a., Koss, A., Wisthaler, A., Mikoviny, T., Karl, T., Kaser, L., Jud, W., Hansel, A., Docherty, K. S., Robinson, N. H., Coe, H., Allan, J. D., Canagaratna, M. R., Paulot, F. and Jimenez, J. L.: Characterization of a real-time tracer for Isoprene Epoxydiols-derived Secondary Organic Aerosol (IEPOX-SOA) from aerosol mass spectrometer measurements, *Atmos. Chem. Phys.*, **15**, 11807–11833, doi:10.5194/acp-15-11807-2015, 2015.

Huang, Y., Coggon, M. M., Zhao, R., Lignell, H., Bauer, M. U., Flagan, R. C. and Seinfeld, J. H.: The Caltech Photooxidation Flow Tube reactor: design, fluid dynamics and characterization, *Atmos. Meas. Tech.*, **10**, 839–867, doi:10.5194/amt-10-839-2017, 2017.

Huffman, J. A., Ziemann, P. J., Jayne, J. T., Worsnop, D. R. and Jimenez, J. L.: Development and Characterization of a Fast-Stepping/Scanning Thermodenuder for Chemically-Resolved Aerosol Volatility Measurements, *Aerosol Sci. Technol.*, **42**, 395–407, doi:10.1080/02786820802104981, 2008.

Hunter, J. F., Day, D. A., Yatavelli, R. N., Chan, A., Kaser, L., Cappellin, L., Hayes, P. L., Palm, B. B., Cross, E. B., Carrasquillo, A., Campuzano-Jost, P., Stark, H., Zhao, Y., Hohaus, T., Smith, J. N., Hansel, A., Karl, T., Goldstein, A. H., Guenther, A., Worsnop, D. R., Thornton, J. A., Heald, C. L., Jimenez, J. L. and Kroll, J. H.: Comprehensive characterization of atmospheric organic carbon at a forested site, submitted, 2016.

Iannone, R., Xiao, S. and Bertram, A. K.: Potentially important nighttime heterogeneous chemistry: NO₃ with aldehydes and N₂O₅ with alcohols, *Phys. Chem. Chem. Phys.*, **13**, 10214, doi:10.1039/c1cp20294d, 2011.

IPCC: IPCC 2013: Climate Change 2013: The Physical Science Basis. Contribution of Working Group I to the Fifth Assessment Report of the Intergovernmental Panel on Climate Change, edited by Stocker, T. F., Qin, D., Plattner, G., Tignor, M., Allen, S. K., Bex, V., and Midgley, P. M., Cambridge University Press,

Cambridge, United Kingdom and New York, NY, USA, 2013.

Jaoui, M., Leungsakul, S. and Kamens, R. M.: Gas and Particle Products Distribution from the Reaction of β -Caryophyllene with Ozone, *J. Atmos. Chem.*, **45**, 261–287, doi:10.1023/A:1024263430285, 2003.

Jaoui, M., Kleindienst, T. E., Docherty, K. S., Lewandowski, M. and Offenberg, J. H.: Secondary organic aerosol formation from the oxidation of a series of sesquiterpenes: α -cedrene, β -caryophyllene, α -humulene and α -farnesene with O₃, OH and NO₃ radicals, *Environ. Chem.*, **10**, 178, doi:10.1071/EN13025, 2013.

Jardine, A. B., Jardine, K. J., Fuentes, J. D., Martin, S. T., Martins, G., Durgante, F., Carneiro, V., Higuchi, N., Manzi, A. O. and Chambers, J. Q.: Highly reactive light-dependent monoterpenes in the Amazon, *Geophys. Res. Lett.*, **42**, 1576–1583, doi:10.1002/2014GL062573, 2015.

Jathar, S. H., Farina, S. C., Robinson, A. L. and Adams, P. J.: The influence of semi-volatile and reactive primary emissions on the abundance and properties of global organic aerosol, *Atmos. Chem. Phys.*, **11**, 7727–7746, doi:10.5194/acp-11-7727-2011, 2011.

Jimenez, J. L., Canagaratna, M. R., Donahue, N. M., Prevot, A. S. H., Zhang, Q., Kroll, J. H., DeCarlo, P. F., Allan, J. D., Coe, H., Ng, N. L., Aiken, A. C., Docherty, K. S., Ulbrich, I. M., Grieshop, A. P., Robinson, A. L., Duplissy, J., Smith, J. D., Wilson, K. R., Lanz, V. A., Hueglin, C., Sun, Y. L., Tian, J., Laaksonen, A., Raatikainen, T., Rautiainen, J., Vaattovaara, P., Ehn, M., Kulmala, M., Tomlinson, J. M., Collins, D. R., Cubison, M. J., Dunlea, J., Huffman, J. A., Onasch, T. B., Alfarra, M. R., Williams, P. I., Bower, K., Kondo, Y., Schneider, J., Drewnick, F., Borrmann, S., Weimer, S., Demerjian, K., Salcedo, D., Cottrell, L., Griffin, R., Takami, A., Miyoshi, T., Hatakeyama, S., Shimono, A., Sun, J. Y., Zhang, Y. M., Dzepina, K., Kimmel, J. R., Sueper, D., Jayne, J. T., Herndon, S. C., Trimborn, A. M., Williams, L. R., Wood, E. C., Middlebrook, A. M., Kolb, C. E., Baltensperger, U. and Worsnop, D. R.: Evolution of Organic Aerosols in the Atmosphere, *Science*, **326**, 1525–1529, doi:10.1126/science.1180353, 2009.

Julin, J., Winkler, P. M. P., Donahue, N. M., Wagner, P. E. and Riipinen, I.: Near-unity mass accommodation coefficient of organic molecules of varying structure., *Environ. Sci. Technol.*, **48**, 12083–9, doi:10.1021/es501816h, 2014.

Kahnt, A., Iinuma, Y., Mutzel, A., Böge, O., Claeys, M. and Herrmann, H.: Campholenic aldehyde ozonolysis: a mechanism leading to specific biogenic secondary organic aerosol constituents, *Atmos. Chem. Phys.*, **14**, 719–736, doi:10.5194/acp-14-719-2014, 2014.

Kang, E., Root, M. J., Toohey, D. W. and Brune, W. H.: Introducing the concept of Potential Aerosol Mass (PAM), *Atmos. Chem. Phys.*, **7**, 5727–5744, doi:10.5194/acp-7-5727-2007, 2007.

Kang, E., Toohey, D. W. and Brune, W. H.: Dependence of SOA oxidation on organic aerosol mass concentration and OH exposure: experimental PAM chamber studies, *Atmos. Chem. Phys.*, **11**, 1837–1852, doi:10.5194/acp-11-1837-2011, 2011.

Kang, H., Day, D. A., Krechmer, J. E., Ayres, B. R., Keehan, N. I., Thompson, S. L., Hu, W., Campuzano-Jost, P., Schroder, J. C., Stark, H., Ranney, A. P., Ziemann, P. J., Zarzana, K. J., Wild, R. J., Dube, W. P., Brown, S. S., Fry, J. L. and Jimenez, J. L.: A33E-0280: Secondary organic aerosol mass yields from the dark NO₃ oxidation of α -pinene and Δ -carene: effect of RO₂ radical fate, in American Geophysical Union Fall Meeting, 2016.

Karjalainen, P., Timonen, H., Saukko, E., Kuuluvainen, H., Saarikoski, S., Aakko-Saksa, P., Murtonen, T., Bloss, M., Dal Maso, M., Simonen, P., Ahlberg, E., Svenningsson, B., Brune, W. H., Hillamo, R., Keskinen,

J. and Rönkkö, T.: Time-resolved characterization of primary particle emissions and secondary particle formation from a modern gasoline passenger car, *Atmos. Chem. Phys.*, **16**, 8559–8570, doi:10.5194/acp-16-8559-2016, 2016.

Karl, T., Hansel, A., Cappellin, L., Kaser, L., Herdlinger-Blatt, I. and Jud, W.: Selective measurements of isoprene and 2-methyl-3-buten-2-ol based on NO^+ ionization mass spectrometry, *Atmos. Chem. Phys.*, **12**, 11877–11884, doi:10.5194/acp-12-11877-2012, 2012.

Kaser, L., Karl, T., Schnitzhofer, R., Graus, M., Herdlinger-Blatt, I. S., DiGangi, J. P., Sive, B., Turnipseed, A., Hornbrook, R. S., Zheng, W., Flocke, F. M., Guenther, A., Keutsch, F. N., Apel, E. and Hansel, A.: Comparison of different real time VOC measurement techniques in a ponderosa pine forest, *Atmos. Chem. Phys.*, **13**, 2893–2906, doi:10.5194/acp-13-2893-2013, 2013a.

Kaser, L., Karl, T., Guenther, A., Graus, M., Schnitzhofer, R., Turnipseed, A., Fischer, L., Harley, P., Madronich, M., Gochis, D., Keutsch, F. N. and Hansel, A.: Undisturbed and disturbed above canopy ponderosa pine emissions: PTR-TOF-MS measurements and MEGAN 2.1 model results, *Atmos. Chem. Phys.*, **13**, 11935–11947, doi:10.5194/acp-13-11935-2013, 2013b.

Keller, A. and Burtscher, H.: A continuous photo-oxidation flow reactor for a defined measurement of the SOA formation potential of wood burning emissions, *J. Aerosol Sci.*, **49**, 9–20, doi:10.1016/j.jaerosci.2012.02.007, 2012.

Kim, S., Karl, T., Guenther, A., Tyndall, G., Orlando, J., Harley, P., Rasmussen, R. and Apel, E.: Emissions and ambient distributions of Biogenic Volatile Organic Compounds (BVOC) in a ponderosa pine ecosystem: interpretation of PTR-MS mass spectra, *Atmos. Chem. Phys.*, **10**, 1759–1771, doi:10.5194/acp-10-1759-2010, 2010.

Kim, S., Wolfe, G. M., Mauldin, L., Cantrell, C., Guenther, A., Karl, T., Turnipseed, A., Greenberg, J., Hall, S. R., Ullmann, K., Apel, E., Hornbrook, R., Kajii, Y., Nakashima, Y., Keutsch, F. N., DiGangi, J. P., Henry, S. B., Kaser, L., Schnitzhofer, R., Graus, M., Hansel, A., Zheng, W. and Flocke, F. F.: Evaluation of HO_x sources and cycling using measurement-constrained model calculations in a 2-methyl-3-butene-2-ol (MBO) and monoterpene (MT) dominated ecosystem, *Atmos. Chem. Phys.*, **13**, 2031–2044, doi:10.5194/acp-13-2031-2013, 2013.

Kirkby, J., Curtius, J., Almeida, J., Dunne, E., Duplissy, J., Ehrhart, S., Franchin, A., Gagné, S., Ickes, L., Kürten, A., Kupc, A., Metzger, A., Riccobono, F., Rondo, L., Schobesberger, S., Tsagkogeorgas, G., Wimmer, D., Amorim, A., Bianchi, F., Breitenlechner, M., David, A., Dommen, J., Downard, A., Ehn, M., Flagan, R. C., Haider, S., Hansel, A., Hauser, D., Jud, W., Junninen, H., Kreissl, F., Kvashin, A., Laaksonen, A., Lehtipalo, K., Lima, J., Lovejoy, E. R., Makhmutov, V., Mathot, S., Mikkilä, J., Minginette, P., Mogo, S., Nieminen, T., Onnela, A., Pereira, P., Petäjä, T., Schnitzhofer, R., Seinfeld, J. H., Sipilä, M., Stozhkov, Y., Stratmann, F., Tomé, A., Vanhanen, J., Viisanen, Y., Vrtala, A., Wagner, P. E., Walther, H., Weingartner, E., Wex, H., Winkler, P. M., Carslaw, K. S., Worsnop, D. R., Baltensperger, U. and Kulmala, M.: Role of sulphuric acid, ammonia and galactic cosmic rays in atmospheric aerosol nucleation, *Nature*, **476**, 429–433, doi:10.1038/nature10343, 2011.

Knote, C., Brunner, D., Vogel, H., Allan, J., Asmi, A., Äijälä, M., Carbone, S., van der Gon, H. D., Jimenez, J. L., Kiendler-Scharr, A., Mohr, C., Poulain, L., Prévôt, A. S. H., Swietlicki, E. and Vogel, B.: Towards an online-coupled chemistry-climate model: evaluation of trace gases and aerosols in COSMO-ART, *Geosci. Model Dev.*, **4**, 1077–1102, doi:10.5194/gmd-4-1077-2011, 2011.

Knote, C., Hodzic, A. and Jimenez, J. L.: The effect of dry and wet deposition of condensable vapors on

secondary organic aerosols concentrations over the continental US, *Atmos. Chem. Phys.*, 15, 1–18, doi:10.5194/acp-15-1-2015, 2015.

Krechmer, J. E., Coggon, M. M., Massoli, P., Nguyen, T. B., Crouse, J. D., Hu, W., Day, D. A., Tyndall, G. S., Henze, D. K., Rivera-Rios, J. C., Nowak, J. B., Kimmel, J. R., Mauldin, R. L., Stark, H., Jayne, J. T., Sipilä, M., Junninen, H., Clair, J. M. St., Zhang, X., Feiner, P. A., Zhang, L., Miller, D. O., Brune, W. H., Keutsch, F. N., Wennberg, P. O., Seinfeld, J. H., Worsnop, D. R., Jimenez, J. L. and Canagaratna, M. R.: Formation of Low Volatility Organic Compounds and Secondary Organic Aerosol from Isoprene Hydroxyhydroperoxide Low-NO Oxidation, *Environ. Sci. Technol.*, 49, 10330–10339, doi:10.1021/acs.est.5b02031, 2015.

Krechmer, J. E., Groessl, M., Zhang, X., Junninen, H., Massoli, P., Lambe, A. T., Kimmel, J. R., Cubison, M. J., Graf, S., Lin, Y.-H., Budisulistiorini, S. H., Zhang, H., Surratt, J. D., Knochenmuss, R., Jayne, J. T., Worsnop, D. R., Jimenez, J.-L. and Canagaratna, M. R.: Ion mobility spectrometry–mass spectrometry (IMS–MS) for on- and offline analysis of atmospheric gas and aerosol species, *Atmos. Meas. Tech.*, 9, 3245–3262, doi:10.5194/amt-9-3245-2016, 2016.

Kroll, J. H. and Seinfeld, J. H.: Chemistry of secondary organic aerosol: Formation and evolution of low-volatility organics in the atmosphere, *Atmos. Environ.*, 42, 3593–3624, doi:10.1016/j.atmosenv.2008.01.003, 2008.

Kroll, J. H., Donahue, N. M., Jimenez, J. L., Kessler, S. H., Canagaratna, M. R., Wilson, K. R., Altieri, K. E., Mazzoleni, L. R., Wozniak, A. S., Bluhm, H., Mysak, E. R., Smith, J. D., Kolb, C. E. and Worsnop, D. R.: Carbon oxidation state as a metric for describing the chemistry of atmospheric organic aerosol., *Nat. Chem.*, 3, 133–9, doi:10.1038/nchem.948, 2011.

Kulmala, M. and Wagner, P. E.: Mass accommodation and uptake coefficients — a quantitative comparison, *J. Aerosol Sci.*, 32, 833–841, doi:10.1016/S0021-8502(00)00116-6, 2001.

Kuwata, M., Chen, Q. and Martin, S. T.: Cloud condensation nuclei (CCN) activity and oxygen-to-carbon elemental ratios following thermodenuder treatment of organic particles grown by α -pinene ozonolysis, *Phys. Chem. Chem. Phys.*, 13, 14571, doi:10.1039/c1cp20253g, 2011.

Kuwata, M., Zorn, S. R. and Martin, S. T.: Using elemental ratios to predict the density of organic material composed of carbon, hydrogen, and oxygen., *Environ. Sci. Technol.*, 46, 787–94, doi:10.1021/es202525q, 2012.

La, Y. S., Camredon, M., Ziemann, P. J., Valorso, R., Matsunaga, A., Lannuque, V., Lee-Taylor, J., Hodzic, A., Madronich, S. and Aumont, B.: Impact of chamber wall loss of gaseous organic compounds on secondary organic aerosol formation: explicit modeling of SOA formation from alkane and alkene oxidation, *Atmos. Chem. Phys.*, 16, 1417–1431, doi:10.5194/acp-16-1417-2016, 2016.

Lambe, A. T., Ahern, A. T., Williams, L. R., Slowik, J. G., Wong, J. P. S., Abbatt, J. P. D., Brune, W. H., Ng, N. L., Wright, J. P., Croasdale, D. R., Worsnop, D. R., Davidovits, P. and Onasch, T. B.: Characterization of aerosol photooxidation flow reactors: heterogeneous oxidation, secondary organic aerosol formation and cloud condensation nuclei activity measurements, *Atmos. Meas. Tech.*, 4, 445–461, doi:10.5194/amt-4-445-2011, 2011a.

Lambe, A. T., Onasch, T. B., Massoli, P., Croasdale, D. R., Wright, J. P., Ahern, A. T., Williams, L. R., Worsnop, D. R., Brune, W. H. and Davidovits, P.: Laboratory studies of the chemical composition and cloud condensation nuclei (CCN) activity of secondary organic aerosol (SOA) and oxidized primary organic aerosol (OPOA), *Atmos. Chem. Phys.*, 11, 8913–8928, doi:10.5194/acp-11-8913-2011, 2011b.

- Lambe, A. T., Onasch, T. B., Croasdale, D. R., Wright, J. P., Martin, A. T., Franklin, J. P., Massoli, P., Kroll, J. H., Canagaratna, M. R., Brune, W. H., Worsnop, D. R. and Davidovits, P.: Transitions from Functionalization to Fragmentation Reactions of Laboratory Secondary Organic Aerosol (SOA) Generated from the OH Oxidation of Alkane Precursors, *Environ. Sci. Technol.*, 46, 5430–5437, doi:10.1021/es300274t, 2012.
- Lambe, A. T., Ahern, A. T., Wright, J. P., Croasdale, D. R., Davidovits, P. and Onasch, T. B.: Oxidative aging and cloud condensation nuclei activation of laboratory combustion soot, *J. Aerosol Sci.*, 79, 31–39, doi:10.1016/j.jaerosci.2014.10.001, 2014.
- Lambe, A. T., Chhabra, P. S., Onasch, T. B., Brune, W. H., Hunter, J. F., Kroll, J. H., Cummings, M. J., Brogan, J. F., Parmar, Y., Worsnop, D. R., Kolb, C. E. and Davidovits, P.: Effect of oxidant concentration, exposure time, and seed particles on secondary organic aerosol chemical composition and yield, *Atmos. Chem. Phys.*, 15, 3063–3075, doi:10.5194/acp-15-3063-2015, 2015.
- Lane, T. E., Donahue, N. M. and Pandis, S. N.: Effect of NO_x on secondary organic aerosol concentrations, *Environ. Sci. Technol.*, 42, 6022–6027, doi:10.1021/Es703225a, 2008.
- Lee, A., Goldstein, A. H., Kroll, J. H., Ng, N. L., Varutbangkul, V., Flagan, R. C. and Seinfeld, J. H.: Gas-phase products and secondary aerosol yields from the photooxidation of 16 different terpenes, *J. Geophys. Res.*, 111, D17305, doi:10.1029/2006JD007050, 2006.
- Levin, E. J. T., Prenni, A. J., Palm, B. B., Day, D. A., Campuzano-Jost, P., Winkler, P. M., Kreidenweis, S. M., Demott, P. J., Jimenez, J. L. and Smith, J. N.: Size-resolved aerosol composition and its link to hygroscopicity at a forested site in Colorado, *Atmos. Chem. Phys.*, 14, 2657–2667, 2014.
- Li, R., Palm, B. B., Borbon, A., Graus, M., Warneke, C., Ortega, A. M., Day, D. A., Brune, W. H., Jimenez, J. L., de Gouw, J. A. and Brune, B.: Laboratory studies on secondary organic aerosol formation from crude oil vapors., *Environ. Sci. Technol.*, 47, 12566–74, doi:10.1021/es402265y, 2013.
- Li, R., Palm, B. B., Ortega, A. M., Hlywiak, J., Hu, W., Peng, Z., Day, D. A., Knote, C., Brune, W. H., de Gouw, J. A. and Jimenez, J. L.: Modeling the Radical Chemistry in an Oxidation Flow Reactor: Radical Formation and Recycling, Sensitivities, and the OH Exposure Estimation Equation, *J. Phys. Chem. A*, 119, 4418–4432, doi:10.1021/jp509534k, 2015.
- Lide, D. R.: *CRC Handbook of Chemistry and Physics*, 94th Edition, 2013–2014, 2013.
- Lim, Y. B. and Ziemann, P. J.: Effects of Molecular Structure on Aerosol Yields from OH Radical-Initiated Reactions of Linear, Branched, and Cyclic Alkanes in the Presence of NO_x, *Environ. Sci. Technol.*, 43, 2328–2334, doi:10.1021/es803389s, 2009.
- Lim, Y. B., Tan, Y., Perri, M. J., Seitzinger, S. P. and Turpin, B. J.: Aqueous chemistry and its role in secondary organic aerosol (SOA) formation, *Atmos. Chem. Phys.*, 10, 10521–10539, doi:10.5194/acp-10-10521-2010, 2010.
- Liu, P. S. K., Deng, R., Smith, K. a., Williams, L. R., Jayne, J. T., Canagaratna, M. R., Moore, K., Onasch, T. B., Worsnop, D. R. and Deshler, T.: Transmission Efficiency of an Aerodynamic Focusing Lens System: Comparison of Model Calculations and Laboratory Measurements for the Aerodyne Aerosol Mass Spectrometer, *Aerosol Sci. Technol.*, 41, 721–733, doi:10.1080/02786820701422278, 2007.
- Liu, S., Shilling, J. E., Song, C., Hiranuma, N., Zaveri, R. A. and Russell, L. M.: Hydrolysis of Organonitrate Functional Groups in Aerosol Particles, *Aerosol Sci. Technol.*, 46, 1359–1369, doi:10.1080/02786826.2012.716175, 2012.

Lopez-Hilfiker, F. D., Mohr, C., Ehn, M., Rubach, F., Kleist, E., Wildt, J., Mentel, T. F., Lutz, a., Hallquist, M., Worsnop, D. and Thornton, J. a.: A novel method for on-line analysis of gas and particle composition: description and evaluation of a Filter Inlet for Gases and AEROSols (FIGAERO), *Atmos. Meas. Tech.*, 6, 9347–9395, doi:10.5194/amt-7-983-2014, 2013.

Lopez-Hilfiker, F. D., Mohr, C., D'Ambro, E. L., Lutz, A., Riedel, T. P., Gaston, C. J., Iyer, S., Zhang, Z., Gold, A., Surratt, J. D., Lee, B. H., Kurten, T., Hu, W. W., Jimenez, J., Hallquist, M. and Thornton, J. A.: Molecular Composition and Volatility of Organic Aerosol in the Southeastern U.S.: Implications for IEPOX Derived SOA, *Environ. Sci. Technol.*, 50, 2200–2209, doi:10.1021/acs.est.5b04769, 2016.

Mao, J., Ren, X., Brune, W. H., Olson, J. R., Crawford, J. H., Fried, A., Huey, L. G., Cohen, R. C., Heikes, B., Singh, H. B., Blake, D. R., Sachse, G. W., Diskin, G. S., Hall, S. R. and Shetter, R. E.: Airborne measurement of OH reactivity during INTEX-B, *Atmos. Chem. Phys.*, 9, 163–173, doi:10.5194/acp-9-163-2009, 2009.

Martin, S. T., Artaxo, P., Machado, L. A. T., Manzi, A. O., Souza, R. A. F., Schumacher, C., Wang, J., Andreae, M. O., Barbosa, H. M. J., Fan, J., Fisch, G., Goldstein, A. H., Guenther, A., Jimenez, J. L., Pöschl, U., Silva Dias, M. A., Smith, J. N. and Wendisch, M.: Introduction: Observations and Modeling of the Green Ocean Amazon (GoAmazon2014/5), *Atmos. Chem. Phys.*, 16, 4785–4797, doi:10.5194/acp-16-4785-2016, 2016a.

Martin, S. T., Artaxo, P., Machado, L., Manzi, A. O., Souza, R. A. F., Schumacher, C., Wang, J., Biscaro, T., Brito, J., Calheiros, A., Jardine, K., Medeiros, A., Portela, B., de Sá, S. S., Adachi, K., Aiken, A. C., Albrecht, R., Alexander, L., Andreae, M. O., Barbosa, H. M. J., Buseck, P., Chand, D., Comstock, J. M., Day, D. A., Dubey, M., Fan, J., Fast, J., Fisch, G., Fortner, E., Giangrande, S., Gilles, M., Goldstein, A. H., Guenther, A., Hubbe, J., Jensen, M., Jimenez, J. L., Keutsch, F. N., Kim, S., Kuang, C., Laskin, A., McKinney, K., Mei, F., Miller, M., Nascimento, R., Pauliquevis, T., Pekour, M., Peres, J., Petäjä, T., Pöhlker, C., Pöschl, U., Rizzo, L., Schmid, B., Shilling, J. E., Silva Dias, M. A., Smith, J. N., Tomlinson, J. M., Tóta, J. and Wendisch, M.: The Green Ocean Amazon Experiment (GoAmazon2014/5) Observes Pollution Affecting Gases, Aerosols, Clouds, and Rainfall over the Rain Forest, *Bull. Am. Meteorol. Soc.*, BAMS-D-15-00221.1, doi:10.1175/BAMS-D-15-00221.1, 2016b.

Massoli, P., Lambe, A. T., Ahern, A. T., Williams, L. R., Ehn, M., Mikkilä, J., Canagaratna, M. R., Brune, W. H., Onasch, T. B., Jayne, J. T., Petäjä, T., Kulmala, M., Laaksonen, A., Kolb, C. E., Davidovits, P. and Worsnop, D. R.: Relationship between aerosol oxidation level and hygroscopic properties of laboratory generated secondary organic aerosol (SOA) particles, *Geophys. Res. Lett.*, 37, L24801, doi:10.1029/2010GL045258, 2010.

Matsunaga, A. and Ziemann, P. J.: Gas-Wall Partitioning of Organic Compounds in a Teflon Film Chamber and Potential Effects on Reaction Product and Aerosol Yield Measurements, *Aerosol Sci. Technol.*, 44, 881–892, doi:10.1080/02786826.2010.501044, 2010.

McMurry, P. H. and Grosjean, D.: Gas and aerosol wall losses in Teflon film smog chambers, *Environ. Sci. Technol.*, 19, 1176–82, doi:10.1021/es00142a006, 1985.

McMurry, P. H. and Rader, D. J.: Aerosol Wall Losses in Electrically Charged Chambers, *Aerosol Sci. Technol.*, 4, 249–268, doi:10.1080/02786828508959054, 1985.

Middlebrook, A. M., Bahreini, R., Jimenez, J. L. and Canagaratna, M. R.: Evaluation of Composition-Dependent Collection Efficiencies for the Aerodyne Aerosol Mass Spectrometer using Field Data, *Aerosol Sci. Technol.*, 46, 258–271, doi:10.1080/02786826.2011.620041, 2012.

Miracolo, M. A., Presto, A. A., Lambe, A. T., Hennigan, C. J., Donahue, N. M., Kroll, J. H., Worsnop, D. R.

and Robinson, A. L.: Photo-Oxidation of Low-Volatility Organics Found in Motor Vehicle Emissions: Production and Chemical Evolution of Organic Aerosol Mass, *Environ. Sci. Technol.*, **44**, 1638–1643, doi:10.1021/es902635c, 2010.

Miracolo, M. A., Hennigan, C. J., Ranjan, M., Nguyen, N. T., Gordon, T. D., Lipsky, E. M., Presto, A. A., Donahue, N. M. and Robinson, A. L.: Secondary aerosol formation from photochemical aging of aircraft exhaust in a smog chamber, *Atmos. Chem. Phys.*, **11**, 4135–4147, doi:10.5194/acp-11-4135-2011, 2011.

Misztal, P. K., Hewitt, C. N., Wildt, J., Blande, J. D., Eller, A. S. D., Fares, S., Gentner, D. R., Gilman, J. B., Graus, M., Greenberg, J., Guenther, A. B., Hansel, A., Harley, P., Huang, M., Jardine, K., Karl, T., Kaser, L., Keutsch, F. N., Kiendler-Scharr, A., Kleist, E., Lerner, B. M., Li, T., Mak, J., Nölscher, A. C., Schnitzhofer, R., Sinha, V., Thornton, B., Warneke, C., Wegener, F., Werner, C., Williams, J., Worton, D. R., Yassaa, N. and Goldstein, A. H.: Atmospheric benzenoid emissions from plants rival those from fossil fuels, *Sci. Rep.*, **5**, 12064, doi:10.1038/srep12064, 2015.

Moldanova, J. and Ljungström, E.: Modeling of particle formation from NO₃ oxidation of selected monoterpenes, *J. Aerosol Sci.*, **31**, 1317–1333, doi:10.1016/S0021-8502(00)00041-0, 2000.

Morris, J. W., Davidovits, P., Jayne, J. T., Jimenez, J. L., Shi, Q., Kolb, C. E., Worsnop, D. R., Barney, W. S. and Cass, G.: Kinetics of submicron oleic acid aerosols with ozone: A novel aerosol mass spectrometric technique, *Geophys. Res. Lett.*, **29**, 71-1-71-4, doi:10.1029/2002GL014692, 2002.

Murphy, D. M., Cziczo, D. J., Froyd, K. D., Hudson, P. K., Matthew, B. M., Middlebrook, a. M., Peltier, R. E., Sullivan, A., Thomson, D. S. and Weber, R. J.: Single-particle mass spectrometry of tropospheric aerosol particles, *J. Geophys. Res.*, **111**, D23S32, doi:10.1029/2006jd007340, 2006.

Myhre, G., Shindell, D., Bréon, F.-M., Collins, W., Fuglestedt, J., Huang, J., Koch, D., Lamarque, J.-F., Lee, D., Mendoza, B., Nakajima, T., Robock, A., Stephens, G., Takemura, T. and Zhang, H.: Anthropogenic and Natural Radiative Forcing, in *Climate Change 2013: The Physical Science Basis. Contribution of Working Group I to the Fifth Assessment Report of the Intergovernmental Panel on Climate Change*, edited by Stocker, T. F., Qin, D., Plattner, G.-K., Tignor, M., Allen, S. K., Boschung, J., Nauels, A., Xia, Y., Bex, V., and Midgley, P. M., Cambridge University Press, Cambridge, UK, New York, NY, USA, 659–740, 2013.

Nah, T., McVay, R. C., Zhang, X., Boyd, C. M., Seinfeld, J. H. and Ng, N. L.: Influence of seed aerosol surface area and oxidation rate on vapor wall deposition and SOA mass yields: a case study with α -pinene ozonolysis, *Atmos. Chem. Phys.*, **16**, 9361–9379, doi:10.5194/acp-16-9361-2016, 2016.

Nakashima, Y., Kato, S., Greenberg, J., Harley, P., Karl, T., Turnipseed, A., Apel, E., Guenther, A., Smith, J. and Kajii, Y.: Total OH reactivity measurements in ambient air in a southern Rocky mountain ponderosa pine forest during BEACHON-SRM08 summer campaign, *Atmos. Environ.*, **85**, 1–8, doi:10.1016/j.atmosenv.2013.11.042, 2014.

Ng, N. L., Kroll, J. H., Keywood, M. D., Bahreini, R., Varutbangkul, V., Flagan, R. C., Seinfeld, J. H., Lee, A. and Goldstein, A. H.: Contribution of first- versus second-generation products to secondary organic aerosols formed in the oxidation of biogenic hydrocarbons, *Environ. Sci. Technol.*, **40**, 2283–2297, doi:10.1021/es052269u, 2006.

Ng, N. L., Chhabra, P. S., Chan, A. W. H., Surratt, J. D., Kroll, J. H., Kwan, A. J., McCabe, D. C., Wennberg, P. O., Sorooshian, A., Murphy, S. M., Dalleska, N. F., Flagan, R. C. and Seinfeld, J. H.: Effect of NO_x level on secondary organic aerosol (SOA) formation from the photooxidation of terpenes, *Atmos. Chem. Phys.*, **7**, 5159–5174, doi:10.5194/acp-7-5159-2007, 2007.

Ng, N. L., Herndon, S. C., Trimborn, a., Canagaratna, M. R., Croteau, P. L., Onasch, T. B., Sueper, D., Worsnop, D. R., Zhang, Q., Sun, Y. L. and Jayne, J. T.: An Aerosol Chemical Speciation Monitor (ACSM) for Routine Monitoring of the Composition and Mass Concentrations of Ambient Aerosol, *Aerosol Sci. Technol.*, 45, 780–794, doi:10.1080/02786826.2011.560211, 2011a.

Ng, N. L., Canagaratna, M. R., Jimenez, J. L., Chhabra, P. S., Seinfeld, J. H. and Worsnop, D. R.: Changes in organic aerosol composition with aging inferred from aerosol mass spectra, *Atmos. Chem. Phys.*, 11, 6465–6474, doi:10.5194/acp-11-6465-2011, 2011b.

Ng, N. L., Brown, S. S., Archibald, A. T., Atlas, E., Cohen, R. C., Crowley, J. N., Day, D. A., Donahue, N. M., Fry, J. L., Fuchs, H., Griffin, R. J., Guzman, M. I., Hermann, H., Hodzic, A., Iinuma, Y., Jimenez, J. L., Kiendler-Scharr, A., Lee, B. H., Luecken, D. J., Mao, J., McLaren, R., Mutzel, A., Osthoff, H. D., Ouyang, B., Picquet-Varrault, B., Platt, U., Pye, H. O. T., Rudich, Y., Schwantes, R. H., Shiraiwa, M., Stutz, J., Thornton, J. A., Tilgner, A., Williams, B. J. and Zaveri, R. A.: Nitrate radicals and biogenic volatile organic compounds: oxidation, mechanisms and organic aerosol, *Atmos. Chem. Phys. Discuss.*, 1–111, doi:10.5194/acp-2016-734, 2016.

Nguyen, T. B., Crouse, J. D., Teng, A. P., St. Clair, J. M., Paulot, F., Wolfe, G. M. and Wennberg, P. O.: Rapid deposition of oxidized biogenic compounds to a temperate forest, *P. Natl. Acad. Sci. USA*, 112, E392–E401, doi:10.1073/pnas.1418702112, 2015.

Orlando, J. J. and Tyndall, G. S.: Laboratory studies of organic peroxy radical chemistry: an overview with emphasis on recent issues of atmospheric significance, *Chem. Soc. Rev.*, 41, 6294, doi:10.1039/c2cs35166h, 2012.

Ortega, A. M., Day, D. A., Cubison, M. J., Brune, W. H., Bon, D., de Gouw, J. A. and Jimenez, J. L.: Secondary organic aerosol formation and primary organic aerosol oxidation from biomass-burning smoke in a flow reactor during FLAME-3, *Atmos. Chem. Phys.*, 13, 11551–11571, doi:10.5194/acp-13-11551-2013, 2013.

Ortega, A. M., Hayes, P. L., Peng, Z., Palm, B. B., Hu, W., Day, D. A., Li, R., Cubison, M. J., Brune, W. H., Graus, M., Warneke, C., Gilman, J. B., Kuster, W. C., de Gouw, J., Gutiérrez-Montes, C. and Jimenez, J. L.: Real-time measurements of secondary organic aerosol formation and aging from ambient air in an oxidation flow reactor in the Los Angeles area, *Atmos. Chem. Phys.*, 16, 7411–7433, doi:10.5194/acp-16-7411-2016, 2016.

Ortega, J., Turnipseed, A., Guenther, A. B., Karl, T. G., Day, D. A., Gochis, D., Huffman, J. A., Prenni, A. J., Levin, E. J. T., Kreidenweis, S. M., DeMott, P. J., Tobo, Y., Patton, E. G., Hodzic, A., Cui, Y. Y., Harley, P. C., Hornbrook, R. S., Apel, E. C., Monson, R. K., Eller, A. S. D., Greenberg, J. P., Barth, M. C., Campuzano-Jost, P., Palm, B. B., Jimenez, J. L., Aiken, A. C., Dubey, M. K., Geron, C., Offenberg, J., Ryan, M. G., Fornwalt, P. J., Pryor, S. C., Keutsch, F. N., DiGangi, J. P., Chan, A. W. H., Goldstein, A. H., Wolfe, G. M., Kim, S., Kaser, L., Schnitzhofer, R., Hansel, A., Cantrell, C. A., Mauldin, R. L. and Smith, J. N.: Overview of the Manitou Experimental Forest Observatory: site description and selected science results from 2008 to 2013, *Atmos. Chem. Phys.*, 14, 6345–6367, doi:10.5194/acp-14-6345-2014, 2014.

Palm, B. B., Campuzano-Jost, P., Ortega, A. M., Day, D. A., Kaser, L., Jud, W., Karl, T., Hansel, A., Hunter, J. F., Cross, E. S., Kroll, J. H., Peng, Z., Brune, W. H. and Jimenez, J. L.: In situ secondary organic aerosol formation from ambient pine forest air using an oxidation flow reactor, *Atmos. Chem. Phys.*, 16, 2943–2970, doi:10.5194/acp-16-2943-2016, 2016.

Palm, B. B., Campuzano-Jost, P., Day, D. A., Ortega, A. M., Fry, J. L., Brown, S. S., Zarzana, K. J., Dube, W.,

- Wagner, N. L., Draper, D. C., Kaser, L., Jud, W., Karl, T., Hansel, A., Gutiérrez-Montes, C. and Jimenez, J. L.: Secondary organic aerosol formation from in situ OH, O₃, and NO₃ oxidation of ambient forest air in an oxidation flow reactor, *Atmos. Chem. Phys. Discuss.*, 1–46, doi:10.5194/acp-2016-1080, 2017.
- Pankow, J. F.: An absorption model of gas/particle partitioning of organic compounds in the atmosphere, *Atmos. Environ.*, 28, 185–188, doi:10.1016/1352-2310(94)90093-0, 1994.
- Pathak, R., Donahue, N. M. and Pandis, S. N.: Ozonolysis of β -Pinene: Temperature Dependence of Secondary Organic Aerosol Mass Fraction, *Environ. Sci. Technol.*, 42, 5081–5086, doi:10.1021/es070721z, 2008.
- Pathak, R. K., Presto, A. A., Lane, T. E., Stanier, C. O., Donahue, N. M. and Pandis, S. N.: Ozonolysis of α -pinene: parameterization of secondary organic aerosol mass fraction, *Atmos. Chem. Phys.*, 7, 3811–3821, doi:10.5194/acp-7-3811-2007, 2007.
- Paulot, F., Crouse, J. D., Kjaergaard, H. G., Kürten, A., St. Clair, J. M., Seinfeld, J. H. and Wennberg, P. O.: Unexpected Epoxide Formation in the Gas-Phase Photooxidation of Isoprene, *Science*, 325, 730–733, doi:10.1126/science.1172910, 2009.
- Peng, J., Hu, M., Guo, S., Du, Z., Zheng, J., Shang, D., Levy Zamora, M., Zeng, L., Shao, M., Wu, Y.-S., Zheng, J., Wang, Y., Glen, C. R., Collins, D. R., Molina, M. J. and Zhang, R.: Markedly enhanced absorption and direct radiative forcing of black carbon under polluted urban environments, *P. Natl. Acad. Sci. USA*, 113, 4266–4271, doi:10.1073/pnas.1602310113, 2016a.
- Peng, Z., Day, D. A., Stark, H., Li, R., Lee-Taylor, J., Palm, B. B., Brune, W. H. and Jimenez, J. L.: HO_x radical chemistry in oxidation flow reactors with low-pressure mercury lamps systematically examined by modeling, *Atmos. Meas. Tech.*, 8, 4863–4890, doi:10.5194/amt-8-4863-2015, 2015.
- Peng, Z., Day, D. A., Ortega, A. M., Palm, B. B., Hu, W., Stark, H., Li, R., Tsigaridis, K., Brune, W. H. and Jimenez, J. L.: Non-OH chemistry in oxidation flow reactors for the study of atmospheric chemistry systematically examined by modeling, *Atmos. Chem. Phys.*, 16, 4283–4305, doi:10.5194/acp-16-4283-2016, 2016b.
- Petters, M. D. and Kreidenweis, S. M.: A single parameter representation of hygroscopic growth and cloud condensation nucleus activity, *Atmos. Chem. Phys.*, 7, 1961–1971, doi:10.5194/acp-7-1961-2007, 2007.
- Petters, M. D., Prenni, A. J., Kreidenweis, S. M., DeMott, P. J., Matsunaga, A., Lim, Y. B. and Ziemann, P. J.: Chemical aging and the hydrophobic-to-hydrophilic conversion of carbonaceous aerosol, *Geophys. Res. Lett.*, 33, doi:Artn L24806Doi 10.1029/2006gl027249, 2006a.
- Petters, M. D., Kreidenweis, S. M., Snider, J. R., Koehler, K. A., Wang, Q., Prenni, A. J. and Demott, P. J.: Cloud droplet activation of polymerized organic aerosol, *Tellus B Chem. Phys. Meteorol.*, 58, 196–205, doi:10.1111/j.1600-0889.2006.00181.x, 2006b.
- Pierce, J. R., Engelhart, G. J., Hildebrandt, L., Weitkamp, E. A., Pathak, R. K., Donahue, N. M., Robinson, A. L., Adams, P. J. and Pandis, S. N.: Constraining Particle Evolution from Wall Losses, Coagulation, and Condensation-Evaporation in Smog-Chamber Experiments: Optimal Estimation Based on Size Distribution Measurements, *Aerosol Sci. Technol.*, 42, 1001–1015, doi:10.1080/02786820802389251, 2008.
- Pirjola, L., Kulmala, M., Wilck, M., Bischoff, A., Stratmann, F. and Otto, E.: Formation Of Sulphuric Acid Aerosols And Cloud Condensation Nuclei: An Expression For Significant Nucleation And Model

Comparison, *J. Aerosol Sci.*, 30, 1079–1094, doi:10.1016/S0021-8502(98)00776-9, 1999.

Platt, S. M., El Haddad, I., Zardini, a. a., Clairotte, M., Astorga, C., Wolf, R., Slowik, J. G., Temime-Roussel, B., Marchand, N., Ježek, I., Drinovec, L., Močnik, G., Möhler, O., Richter, R., Barmet, P., Bianchi, F., Baltensperger, U. and Prévôt, a. S. H.: Secondary organic aerosol formation from gasoline vehicle emissions in a new mobile environmental reaction chamber, *Atmos. Chem. Phys.*, 13, 9141–9158, doi:10.5194/acp-13-9141-2013, 2013.

Pope, C. A. and Dockery, D. W.: Health Effects of Fine Particulate Air Pollution: Lines that Connect, *J. Air Waste Manage. Assoc.*, 56, 709–742, doi:10.1080/10473289.2006.10464485, 2006.

Pöschl, U., Canagaratna, M., Jayne, J. T., Molina, L. T., Worsnop, D. R., Kolb, C. E. and Molina, M. J.: Mass Accommodation Coefficient of H₂SO₄ Vapor on Aqueous Sulfuric Acid Surfaces and Gaseous Diffusion Coefficient of H₂SO₄ in N₂/H₂O, *J. Phys. Chem. A*, 102, 10082–10089, doi:10.1021/jp982809s, 1998.

Pöschl, U., Martin, S. T., Sinha, B., Chen, Q., Gunthe, S. S., Huffman, J. a, Borrmann, S., Farmer, D. K., Garland, R. M., Helas, G., Jimenez, J. L., King, S. M., Manzi, A., Mikhailov, E., Pauliquevis, T., Petters, M. D., Prenni, A. J., Roldin, P., Rose, D., Schneider, J., Su, H., Zorn, S. R., Artaxo, P. and Andreae, M. O.: Rainforest aerosols as biogenic nuclei of clouds and precipitation in the Amazon., *Science*, 329, 1513–6, doi:10.1126/science.1191056, 2010.

Presto, A. A., Miracolo, M. A., Donahue, N. M. and Robinson, A. L.: Secondary Organic Aerosol Formation from High-NO_x Photo-Oxidation of Low Volatility Precursors: N-Alkanes, *Environ. Sci. Technol.*, 44, 2029–2034, doi:10.1021/es903712r, 2010.

Presto, A. A., Nguyen, N. T., Ranjan, M., Reeder, A. J., Lipsky, E. M., Hennigan, C. J., Miracolo, M. A., Riemer, D. D. and Robinson, A. L.: Fine particle and organic vapor emissions from staged tests of an in-use aircraft engine, *Atmos. Environ.*, 45, 3603–3612, doi:10.1016/j.atmosenv.2011.03.061, 2011.

Richters, S., Herrmann, H. and Berndt, T.: Gas-phase rate coefficients of the reaction of ozone with four sesquiterpenes at 295 ± 2 K, *Phys. Chem. Chem. Phys.*, 17, 11658–11669, doi:10.1039/C4CP05542J, 2015.

Rinne, H. J. I., Guenther, A. B., Greenberg, J. P. and Harley, P. C.: Isoprene and monoterpene fluxes measured above Amazonian rainforest and their dependence on light and temperature, *Atmos. Environ.*, 36, 2421–2426, doi:10.1016/S1352-2310(01)00523-4, 2002.

Robinson, A. L., Donahue, N. M., Shrivastava, M. K., Weitkamp, E. A., Sage, A. M., Grieshop, A. P., Lane, T. E., Pierce, J. R. and Pandis, S. N.: Rethinking Organic Aerosols: Semivolatile Emissions and Photochemical Aging, *Science*, 315, 1259–1262, doi:10.1126/science.1133061, 2007.

Rogge, W. F., Hildemann, L. M., Mazurek, M. A., Cass, G. R. and Simoneit, B. R. T.: Sources of fine organic aerosol. 1. Charbroilers and meat cooking operations, *Environ. Sci. Technol.*, 25, 1112–1125, doi:10.1021/es00018a015, 1991.

de Sá, S. S., Palm, B. B. and Al., E.: No Title, *Prep.*, 2017.

Salcedo, D., Onasch, T. B., Dzepina, K., Canagaratna, M. R., Zhang, Q., Huffman, J. A., DeCarlo, P. F., Jayne, J. T., Mortimer, P., Worsnop, D. R., Kolb, C. E., Johnson, K. S., Zuberi, B., Marr, L. C., Volkamer, R., Molina, L. T., Molina, M. J., Cardenas, B., Bernabé, R. M., Márquez, C., Gaffney, J. S., Marley, N. A., Laskin, A., Shutthanandan, V., Xie, Y., Brune, W., Leshner, R., Shirley, T. and Jimenez, J. L.: Characterization of ambient aerosols in Mexico City during the MCMA-2003 campaign with Aerosol Mass Spectrometry: results from the CENICA Supersite, *Atmos. Chem. Phys.*, 6, 925–946, doi:10.5194/acp-6-925-2006, 2006.

Sander, S. P., Abbatt, J. P. D., Barker, J. R., Burkholder, J. B., Friedl, R. R., Golden, D. M., Huie, R. E., Kolb, C. E., Kurylo, M. J., Moortgat, G. K., Orkin, V. L. and Wine, P. H.: Chemical Kinetics and Photochemical Data for Use in Atmospheric Studies Evaluation Number 17, JPL Publ. 10-6, Jet Propulsion Laboratory, California Institute of Technology, Pasadena, CA, USA, 2011.

Saukko, E., Lambe, A. T., Massoli, P., Koop, T., Wright, J. P., Croasdale, D. R., Pedernera, D. A., Onasch, T. B., Laaksonen, A., Davidovits, P., Worsnop, D. R. and Virtanen, A.: Humidity-dependent phase state of SOA particles from biogenic and anthropogenic precursors, *Atmos. Chem. Phys.*, 12, 7517–7529, doi:10.5194/acp-12-7517-2012, 2012.

Seinfeld, J. H. and Pandis, S. N.: Atmospheric chemistry and physics: from air pollution to climate change, 2nd ed., John Wiley & Sons, Inc., Hoboken, New Jersey, USA, 2006.

Shilling, J. E., Chen, Q., King, S. M., Rosenoern, T., Kroll, J. H., Worsnop, D. R., McKinney, K. A. and Martin, S. T.: Particle mass yield in secondary organic aerosol formed by the dark ozonolysis of α -pinene, *Atmos. Chem. Phys.*, 8, 2073–2088, doi:10.5194/acp-8-2073-2008, 2008.

Shrivastava, M., Thornton, J., Cappa, C., Fan, J., Goldstein, A., Guenther, A., Jimenez, J. L., Kuang, C., Laskin, A., Martin, S., Ng, N. L., Petaja, T., Pierce, J., Rasch, P., Roldin, P., Seinfeld, J., Shilling, J., Smith, J., Volkamer, R., Wang, J., Worsnop, D., Zaveri, R., Zelenyuk, A. and Zhang, Q.: Recent advances in understanding secondary organic aerosols: implications for global climate forcing, *Rev. Geophys.*, submitted, 2016.

Slowik, J. G., Stroud, C., Bottenheim, J. W., Brickell, P. C., Chang, R. Y.-W., Liggio, J., Makar, P. A., Martin, R. V., Moran, M. D., Shantz, N. C., Sjostedt, S. J., van Donkelaar, A., Vlasenko, A., Wiebe, H. A., Xia, A. G., Zhang, J., Leaitch, W. R. and Abbatt, J. P. D.: Characterization of a large biogenic secondary organic aerosol event from eastern Canadian forests, *Atmos. Chem. Phys.*, 10, 2825–2845, doi:10.5194/acp-10-2825-2010, 2010.

Smith, J. D., Kroll, J. H., Cappa, C. D., Che, D. L., Liu, C. L., Ahmed, M., Leone, S. R., Worsnop, D. R. and Wilson, K. R.: The heterogeneous reaction of hydroxyl radicals with sub-micron squalane particles: a model system for understanding the oxidative aging of ambient aerosols, *Atmos. Chem. Phys.*, 9, 3209–3222, doi:10.5194/acp-9-3209-2009, 2009.

Spittler, M., Barnes, I., Bejan, I., Brockmann, K. J., Benter, T. and Wirtz, K.: Reactions of NO_3 radicals with limonene and α -pinene: Product and SOA formation, *Atmos. Environ.*, 40, 116–127, doi:10.1016/j.atmosenv.2005.09.093, 2006.

Sun, Y. L., Zhang, Q., Anastasio, C. and Sun, J.: Insights into secondary organic aerosol formed via aqueous-phase reactions of phenolic compounds based on high resolution mass spectrometry, *Atmos. Chem. Phys.*, 10, 4809–4822, doi:10.5194/acp-10-4809-2010, 2010.

Surratt, J. D., Chan, A. W. H., Eddingsaas, N. C., Chan, M., Loza, C. L., Kwan, A. J., Hersey, S. P., Flagan, R. C., Wennberg, P. O. and Seinfeld, J. H.: Reactive intermediates revealed in secondary organic aerosol formation from isoprene., *P. Natl. Acad. Sci. USA*, 107, 6640–5, doi:10.1073/pnas.0911114107, 2010.

Tan, Y., Carlton, A. G., Seitzinger, S. P. and Turpin, B. J.: SOA from methylglyoxal in clouds and wet aerosols: Measurement and prediction of key products, *Atmos. Environ.*, 44, 5218–5226, doi:10.1016/j.atmosenv.2010.08.045, 2010.

Tan, Y., Lim, Y. B., Altieri, K. E., Seitzinger, S. P. and Turpin, B. J.: Mechanisms leading to oligomers and SOA through aqueous photooxidation: insights from OH radical oxidation of acetic acid and

methylglyoxal, *Atmos. Chem. Phys.*, 12, 801–813, doi:10.5194/acp-12-801-2012, 2012.

Tanaka, P. L., Allen, D. T. and Mullins, C. B.: An environmental chamber investigation of chlorine-enhanced ozone formation in Houston, Texas, *J. Geophys. Res.*, 108, 4576, doi:10.1029/2002JD003314, 2003.

Tang, M. J., Shiraiwa, M., Pöschl, U., Cox, R. A. and Kalberer, M.: Compilation and evaluation of gas phase diffusion coefficients of reactive trace gases in the atmosphere: Volume 2. Diffusivities of organic compounds, pressure-normalised mean free paths, and average Knudsen numbers for gas uptake calculations, *Atmos. Chem. Phys.*, 15, 5585–5598, doi:10.5194/acp-15-5585-2015, 2015.

Tasoglou, A. and Pandis, S. N.: Formation and chemical aging of secondary organic aerosol during the β -caryophyllene oxidation, *Atmos. Chem. Phys.*, 15, 6035–6046, doi:10.5194/acp-15-6035-2015, 2015.

Thalman, R., de Sá, S. S., Palm, B. B., Barbosa, H. M. J., Pöhlker, M. L., Alexander, M. L., Brito, J., Carbone, S., Castillo, P., Day, D. A., Kuang, C., Manzi, A., Ng, N. L., Sedlacek III, A. J., Souza, R., Springston, S., Watson, T., Pöhlker, C., Pöschl, U., Andreae, M. O., Artaxo, P., Jimenez, J. L., Martin, S. T. and Wang, J.: CCN activity and organic hygroscopicity of aerosols downwind of an urban region in central Amazonia: Seasonal and diel variations and impact of anthropogenic emissions, *Atmos. Chem. Phys. Discuss.*, 1–60, doi:10.5194/acp-2017-251, 2017.

Thornton, J. A., Wooldridge, P. J. and Cohen, R. C.: Atmospheric NO_2 : In Situ Laser-Induced Fluorescence Detection at Parts per Trillion Mixing Ratios, *Anal. Chem.*, 72, 528–539, doi:10.1021/ac9908905, 2000.

Timonen, H., Karjalainen, P., Saukko, E., Saarikoski, S., Aakko-Saksa, P., Simonen, P., Murtonen, T., Dal Maso, M., Kuuluvainen, H., Ahlberg, E., Svenningsson, B., Pagels, J., Brune, W. H., Keskinen, J., Worsnop, D. R., Hillamo, R. and Rönkkö, T.: Influence of fuel ethanol content on primary emissions and secondary aerosol formation potential for a modern flex-fuel gasoline vehicle, *Atmos. Chem. Phys. Discuss.*, 1–28, doi:10.5194/acp-2016-579, 2016.

Tkacik, D. S., Presto, A. A., Donahue, N. M. and Robinson, A. L.: Secondary organic aerosol formation from intermediate-volatility organic compounds: cyclic, linear, and branched alkanes., *Environ. Sci. Technol.*, 46, 8773–81, doi:10.1021/es301112c, 2012.

Tkacik, D. S., Lambe, A. T., Jathar, S., Li, X., Presto, A. A., Zhao, Y., Blake, D., Meinardi, S., Jayne, J. T., Croteau, P. L. and Robinson, A. L.: Secondary Organic Aerosol Formation from in-Use Motor Vehicle Emissions Using a Potential Aerosol Mass Reactor, *Environ. Sci. Technol.*, 48, 11235–11242, doi:10.1021/es502239v, 2014.

Tsigaridis, K., Daskalakis, N., Kanakidou, M., Adams, P. J., Artaxo, P., Bahadur, R., Balkanski, Y., Bauer, S. E., Bellouin, N., Benedetti, A., Bergman, T., Berntsen, T. K., Beukes, J. P., Bian, H., Carslaw, K. S., Chin, M., Curci, G., Diehl, T., Easter, R. C., Ghan, S. J., Gong, S. L., Hodzic, A., Hoyle, C. R., Iversen, T., Jathar, S., Jimenez, J. L., Kaiser, J. W., Kirkevåg, A., Koch, D., Kokkola, H., Lee, Y. H., Lin, G., Liu, X., Luo, G., Ma, X., Mann, G. W., Mihalopoulos, N., Morcrette, J.-J., Müller, J.-F., Myhre, G., Myriokefalitakis, S., Ng, N. L., O'Donnell, D., Penner, J. E., Pozzoli, L., Pringle, K. J., Russell, L. M., Schulz, M., Sciare, J., Seland, Ø., Shindell, D. T., Sillman, S., Skeie, R. B., Spracklen, D., Stavrou, T., Steenrod, S. D., Takemura, T., Tiitta, P., Tilmes, S., Tost, H., van Noije, T., van Zyl, P. G., von Salzen, K., Yu, F., Wang, Z., Wang, Z., Zaveri, R. A., Zhang, H., Zhang, K., Zhang, Q. and Zhang, X.: The AeroCom evaluation and intercomparison of organic aerosol in global models, *Atmos. Chem. Phys.*, 14, 10845–10895, doi:10.5194/acp-14-10845-2014, 2014.

Tsimpidi, A. P., Karydis, V. A., Zavala, M., Lei, W., Molina, L., Ulbrich, I. M., Jimenez, J. L. and Pandis, S. N.: Evaluation of the volatility basis-set approach for the simulation of organic aerosol formation in the

- Mexico City metropolitan area, *Atmos. Chem. Phys.*, 10, 525–546, doi:10.5194/acp-10-525-2010, 2010.
- Tunved, P., Hansson, H.-C., Kerminen, V.-M., Ström, J., Maso, M. D., Lihavainen, H., Viisanen, Y., Aalto, P. P., Komppula, M. and Kulmala, M.: High natural aerosol loading over boreal forests., *Science*, 312, 261–3, doi:10.1126/science.1123052, 2006.
- Ulbrich, I. M., Canagaratna, M. R., Zhang, Q., Worsnop, D. R. and Jimenez, J. L.: Interpretation of organic components from Positive Matrix Factorization of aerosol mass spectrometric data, *Atmos. Chem. Phys.*, 9, 2891–2918, doi:10.5194/acp-9-2891-2009, 2009.
- Vaden, T. D., Imre, D., Beranek, J., Shrivastava, M. and Zelenyuk, A.: Evaporation kinetics and phase of laboratory and ambient secondary organic aerosol, *P. Natl. Acad. Sci. USA*, 108, 2190–2195, doi:10.1073/pnas.1013391108, 2011.
- VanReken, T. M., Ng, N. L., Flagan, R. C. and Seinfeld, J. H.: Cloud condensation nucleus activation properties of biogenic secondary organic aerosol, *J. Geophys. Res.*, 110, D07206, doi:10.1029/2004JD005465, 2005.
- Vereecken, L. and Peeters, J.: Enhanced H-atom abstraction from pinonaldehyde, pinonic acid, pinic acid, and related compounds: theoretical study of C–H bond strengths, *Phys. Chem. Chem. Phys.*, 4, 467–472, doi:10.1039/b109370c, 2002.
- Volkamer, R., Jimenez, J. L., San Martini, F., Dzepina, K., Zhang, Q., Salcedo, D., Molina, L. T., Worsnop, D. R. and Molina, M. J.: Secondary organic aerosol formation from anthropogenic air pollution: Rapid and higher than expected, *Geophys. Res. Lett.*, 33, L17811, doi:10.1029/2006GL026899, 2006.
- Wagner, N. L., Dubé, W. P., Washenfelder, R. A., Young, C. J., Pollack, I. B., Ryerson, T. B. and Brown, S. S.: Diode laser-based cavity ring-down instrument for NO₃, N₂O₅, NO, NO₂ and O₃ from aircraft, *Atmos. Meas. Tech.*, 4, 1227–1240, doi:10.5194/amt-4-1227-2011, 2011.
- von der Weiden, S.-L., Drewnick, F. and Borrmann, S.: Particle Loss Calculator – a new software tool for the assessment of the performance of aerosol inlet systems, *Atmos. Meas. Tech.*, 2, 479–494, doi:10.5194/amt-2-479-2009, 2009.
- Williams, J., Keßel, S. U., Nölscher, A. C., Yang, Y., Lee, Y., Yáñez-Serrano, A. M., Wolff, S., Kesselmeier, J., Klüpfel, T., Lelieveld, J. and Shao, M.: Opposite OH reactivity and ozone cycles in the Amazon rainforest and megacity Beijing: Subversion of biospheric oxidant control by anthropogenic emissions, *Atmos. Environ.*, 125, 112–118, doi:10.1016/j.atmosenv.2015.11.007, 2016.
- Winterhalter, R., Herrmann, F., Kanawati, B., Nguyen, T. L., Peeters, J., Vereecken, L. and Moortgat, G. K.: The gas-phase ozonolysis of β -caryophyllene (C₁₅H₂₄). Part I: an experimental study, *Phys. Chem. Chem. Phys.*, 11, 4152, doi:10.1039/b817824k, 2009.
- Wolfe, G. M., Cantrell, C., Kim, S., Mauldin III, R. L., Karl, T., Harley, P., Turnipseed, A., Zheng, W., Flocke, F., Apel, E. C., Hornbrook, R. S., Hall, S. R., Ullmann, K., Henry, S. B., DiGangi, J. P., Boyle, E. S., Kaser, L., Schnitzhofer, R., Hansel, A., Graus, M., Nakashima, Y., Kajii, Y., Guenther, A. and Keutsch, F. N.: Missing peroxy radical sources within a summertime ponderosa pine forest, *Atmos. Chem. Phys.*, 14, 4715–4732, doi:10.5194/acp-14-4715-2014, 2014.
- Woody, M. C., West, J. J., Jathar, S. H., Robinson, a. L. and Arunachalam, S.: Estimates of non-traditional secondary organic aerosols from aircraft SVOC and IVOC emissions using CMAQ, *Atmos. Chem. Phys.*, 15, 6929–6942, doi:10.5194/acp-15-6929-2015, 2015.

Wyche, K. P., Ryan, A. C., Hewitt, C. N., Alfarra, M. R., McFiggans, G., Carr, T., Monks, P. S., Smallbone, K. L., Capes, G., Hamilton, J. F., Pugh, T. A. M. and MacKenzie, A. R.: Emissions of biogenic volatile organic compounds and subsequent photochemical production of secondary organic aerosol in mesocosm studies of temperate and tropical plant species, *Atmos. Chem. Phys.*, **14**, 12781–12801, doi:10.5194/acp-14-12781-2014, 2014.

Xu, W., Guo, S., Gomez-Hernandez, M., Zamora, M. L., Secret, J., Marrero-Ortiz, W., Zhang, A. L., Collins, D. R. and Zhang, R.: Cloud forming potential of oligomers relevant to secondary organic aerosols, *Geophys. Res. Lett.*, **41**, 6538–6545, doi:10.1002/2014GL061040, 2014.

Yatavelli, R. L. N., Stark, H., Thompson, S. L., Kimmel, J. R., Cubison, M. J., Day, D. A., Campuzano-Jost, P., Palm, B. B., Hodzic, A., Thornton, J. a., Jayne, J. T., Worsnop, D. R. and Jimenez, J. L.: Semicontinuous measurements of gas–particle partitioning of organic acids in a ponderosa pine forest using a MOVI-HRToF-CIMS, *Atmos. Chem. Phys.*, **14**, 1527–1546, doi:10.5194/acp-14-1527-2014, 2014.

Yu, J., Griffin, R. J., Cocker, D. R., Flagan, R. C., Seinfeld, J. H. and Blanchard, P.: Observation of gaseous and particulate products of monoterpene oxidation in forest atmospheres, *Geophys. Res. Lett.*, **26**, 1145–1148, doi:10.1029/1999GL900169, 1999.

Zhang, H., Worton, D. R., Lewandowski, M., Ortega, J., Rubitschun, C. L., Park, J.-H., Kristensen, K., Campuzano-Jost, P., Day, D. A., Jimenez, J. L., Jaoui, M., Offenberg, J. H., Kleindienst, T. E., Gilman, J., Kuster, W. C., de Gouw, J., Park, C., Schade, G. W., Frossard, A. A., Russell, L., Kaser, L., Jud, W., Hansel, A., Cappellin, L., Karl, T., Glasius, M., Guenther, A., Goldstein, A. H., Seinfeld, J. H., Gold, A., Kamens, R. M. and Surratt, J. D.: Organosulfates as Tracers for Secondary Organic Aerosol (SOA) Formation from 2-Methyl-3-Buten-2-ol (MBO) in the Atmosphere, *Environ. Sci. Technol.*, **46**, 9437–9446, doi:10.1021/es301648z, 2012.

Zhang, Q., Jimenez, J. L., Canagaratna, M. R., Allan, J. D., Coe, H., Ulbrich, I., Alfarra, M. R., Takami, A., Middlebrook, A. M., Sun, Y. L., Dzepina, K., Dunlea, E., Docherty, K., DeCarlo, P. F., Salcedo, D., Onasch, T., Jayne, J. T., Miyoshi, T., Shimojo, A., Hatakeyama, S., Takegawa, N., Kondo, Y., Schneider, J., Drewnick, F., Borrmann, S., Weimer, S., Demerjian, K., Williams, P., Bower, K., Bahreini, R., Cottrell, L., Griffin, R. J., Rautiainen, J., Sun, J. Y., Zhang, Y. M. and Worsnop, D. R.: Ubiquity and dominance of oxygenated species in organic aerosols in anthropogenically-influenced Northern Hemisphere midlatitudes, *Geophys. Res. Lett.*, **34**, L13801, doi:10.1029/2007GL029979, 2007.

Zhang, Q., Jimenez, J. L., Canagaratna, M. R., Ulbrich, I. M., Ng, N. L., Worsnop, D. R. and Sun, Y.: Understanding Atmospheric Organic Aerosols via Factor Analysis of Aerosol Mass Spectrometry: a Review., *Anal. Bioanal. Chem.*, **401**, 3045–67, doi:DOI:10.1007/s00216-011-5355-y, 2011.

Zhang, X., Cappa, C. D., Jathar, S. H., McVay, R. C., Ensberg, J. J., Kleeman, M. J. and Seinfeld, J. H.: Influence of vapor wall loss in laboratory chambers on yields of secondary organic aerosol., *P. Natl. Acad. Sci. USA*, **111**, 5802–7, doi:10.1073/pnas.1404727111, 2014.

Zhao, D. F., Kaminski, M., Schlag, P., Fuchs, H., Acir, I.-H., Bohn, B., Häsel, R., Kiendler-Scharr, A., Rohrer, F., Tillmann, R., Wang, M. J., Wegener, R., Wildt, J., Wahner, A. and Mentel, T. F.: Secondary organic aerosol formation from hydroxyl radical oxidation and ozonolysis of monoterpenes, *Atmos. Chem. Phys.*, **15**, 991–1012, doi:10.5194/acp-15-991-2015, 2015.

Zhao, Y., Kreisberg, N. M., Worton, D. R., Teng, A. P., Hering, S. V. and Goldstein, A. H.: Development of an In Situ Thermal Desorption Gas Chromatography Instrument for Quantifying Atmospheric Semi-Volatile Organic Compounds, *Aerosol Sci. Technol.*, **47**, 258–266, doi:10.1080/02786826.2012.747673,

2013.

Zhao, Y., Hennigan, C. J., May, A. A., Tkacik, D. S., de Gouw, J. A., Gilman, J. B., Kuster, W. C., Borbon, A. and Robinson, A. L.: Intermediate-Volatility Organic Compounds: A Large Source of Secondary Organic Aerosol, *Environ. Sci. Technol.*, 48, 13743–13750, doi:10.1021/es5035188, 2014.

Ziemann, P. J.: Aerosol products, mechanisms, and kinetics of heterogeneous reactions of ozone with oleic acid in pure and mixed particles, *Faraday Discuss.*, 130, 469, doi:10.1039/b417502f, 2005.

Ziemann, P. J. and Atkinson, R.: Kinetics, products, and mechanisms of secondary organic aerosol formation, *Chem. Soc. Rev.*, 41, 6582, doi:10.1039/c2cs35122f, 2012.